ELECTRON AND GAMMA RAY INDUCED COMPLEX PARTICLE EMISSION

Thesis

Submitted by

PENELOPE J. THORLEY, B.Sc.

for the degree of

DOCTOR OF PHILOSOPHY

University of Edinburgh,

MAY, 1981.

ABSTRACT

Data has been taken using the University of Glasgow 160 MeV electron linear accelerator. Energy spectra and angular distribution measurements of complex particles (alpha particles, tritons, deuterons and ^{3}He particles) emitted from nuclei $27 \lesssim A \lesssim 197$ at an electron energy of 120 MeV have been made for particle energies between 2.5 and 67 MeV. Excitation functions of complex particles emitted from ^{197}Au have been measured for both electron and bremsstrahlung excitation at three different particle energies for electron and bremsstrahlung end point energies between 40 and 130 MeV. A comparison of angular distribution data for electron and photon induced complex particle emission has been obtained for the nuclei ^{58}Ni, ^{60}Ni and ^{197}Au at electron and bremsstrahlung end point energies of 60 and 120 MeV.

The energy spectra have been analysed in terms of the statistical compound nucleus model and the pre-equilibrium exciton model. Formation factors were obtained from a comparison of the measured data and the exciton model calculated spectra. The low particle energy angular distributions were parameterised using Legendre polynomials and the high energy angular distribution data compared to the results of a simple kinematic calculation which assumes that the momentum of the incoming photon is shared by a small group of nucleons. An estimate of the proportions of E1 and E2 virtual photon absorption required for high energy complex particle emission was obtained from a comparison of angular distribution data for excitation of nuclei by electrons and bremsstrahlung radiation. The measured, bremsstrahlung induced excitation functions were unfolded to give particle emission spectra which were compared with the results of exciton model calculations. The unfolded cross sections were folded in with E1 and E2 virtual photon spectra in an attempt to reproduce the measured electron induced excitation functions.

DECLARATION

The data presented in this thesis was obtained by the Universities of Glasgow and Edinburgh Nuclear Structure Group. I made a substantial contribution to the acquisition and analysis of the data. This thesis has been composed by myself.

ACKNOWLEDGEMENTS

I would like to thank my two supervisors Dr. D. Branford and Dr. A. Shotter for their advice and encouragement during the course of this thesis work. I am grateful to Dr. A.G. Flowers, Dr. J.C. McGeorge, Dr. R.O. Owens, Dr. C.H. Zimmerman, Mr. I. Anthony and Mr. M.R. Sené for their help in acquiring the experimental data. In particular I would like to thank Dr. A.G. Flowers for his assistance with much of the computing involved in this work, especially the implementation of the computer code PREQEC and for his calculations of virtual photon spectra and the unfolded cross sections.

My thanks go to Dr. R.O. Owens and Professor J.M. Reid, respective directors of the Kelvin Laboratory for the use of the facilities there and similarly to Professors Cochran and Cowley, respective heads of the Physics Department. I acknowledge the receipt of an S.R.C. studentship. I am indebted to Mrs. Chester for her excellent typing of this thesis.

I would like to thank my husband for his sometimes much needed encouragement and support. I express my gratitude to the late G.E.M. Hinton.

CONTENTS

C O N T E N T S (Contd.)

C O N T E N T S (Contd.)

CHAPTER I

INTRODUCTION

1.1 General Introduction to Photonuclear Reactions

The first references to photonuclear reactions were in 1934 when Chadwick and Goldhaber observed the photodisintegration of the deuteron[1]. In the same year Szilard and Chalmers reported on the photodisintegration of ^{9}Be [2]. Gamma rays from naturally occurring radioactive isotopes, with a maximum energy of 2.62 MeV yielded by ^{208}Tl, were used in these studies. Within a few years gamma rays, produced by the capture of low energy protons, deuterons and alpha particles from the first cyclotrons, were being used extensively in photonuclear reactions. These early experiments concentrated on measuring particle thresholds using photographic emulsions or cloud chambers to detect the emitted particles. Gamma rays of energy up to 17.6 MeV could be obtained from the $^{7}Li(p,\gamma)$ reaction and the first unambiguous observation of alpha particles produced in a photon induced reaction was made by Hanni[3] in 1948 using photons from this reaction. The $^{12}C(\gamma,3\alpha)$ reaction was observed following irradiation by 17.6 MeV and 14.6 MeV photons, using the photographic emulsion technique.

Livingstone and Bethe[4] in 1936 were the first to suggest that a study of photoalpha reactions would be of interest. Levinger[5] suggested that the (γ,d) reaction should also be regarded as an important part of the study of photonuclear reactions. However, due to the high thresholds for deuteron and triton emission, (γ,d) and (γ,t) reactions were not observed until photons of energy $\geq$ 30 MeV were available in the late 1940's from betatrons.

Development of betatrons and later synchrotrons made available photon sources of energies well above the pion threshold (∿160 MeV). Electron linear accelerators were in use for the study of photonuclear reactions by the mid 1950's although they were limited, in general, to a maximum energy of ∿ 30 MeV. These accelerators enabled studies of photonuclear reactions in the giant resonance region. It was not until the mid 1970's that complex particle emission using incident electron beams was studied. The much lower count rate for electron induced reactions as compared to photon induced reactions, in which a thick bremsstrahlung radiator can be placed in the electron beam, meant that such experiments were not considered practical until the emitted particles could be detected in solid state detectors used in conjunction with magnetic spectrometers to reduce the high background associated with electrons beams.

Thus extensive measurements of electron and photon induced complex particle emission have been obtained in the giant resonance region (E_γ, E_e < 30 MeV) and for photon induced reactions above the pion threshold (E_γ ∿ 160 MeV). Very little data was available on the emission of complex particles between these two regions, and that being mainly (e,α) reaction data for ^{238}U and the nickel isotopes, until work at the Kelvin Laboratory was initiated. Measurements on the (e,α) reaction for nuclei 27 < A < 197 have been reported by Flowers et al.[6,7,8]. The work carried out for this thesis extends those studies to include an investigation of the (e,d), (e,t) and (e,^{3}He) reactions and a comparison between these and their corresponding photon induced reactions.

1.2 Historical Development of Photon and Electron Induced Alpha Emission.

Following Hanni's observation of the $^{12}C(\gamma,3\alpha)$ reaction[3] most of the early (γ,α) studies concentrated on measuring yields of alpha emission from light nuclei, e.g. ^{12}C, ^{14}N, ^{16}O and from silver and bromine. This reflected the ease of observation of alpha particles from these nuclei using photographic emulsions and the interest in the alpha particle cluster model.

Haslam obtained activation curves for the (γ,α) reactions on ^{87}Rb, ^{65}Cu, Ag and ^{81}Br [9,10,11] using photons in the energy range 15-26 MeV. A photon difference analysis technique[12] gave photon energy dependent (γ,α) cross sections which showed a pronounced resonance shape at 20-24 MeV excitation energy. Thus it appeared that (γ,α) reactions proceeded through giant resonance absorption and attempts were made to obtain alpha energy spectra for comparison with the evaporation theory of Blatt and Weisskopf[13] which had already been used to explain (γ,n) and (γ,p) reaction data in the giant resonance region. Using emulsion track studies energy spectra were obtained[11,14,15] which showed reasonable agreement with evaporation theory although the spectra were poorly resolved with high statistical errors due to experimental difficulties.

Erdös[16] presented a review of (γ,α) reactions in 1957 which showed alpha particle yields consistent with photon absorption to a giant resonance centred at an excitation energy of $80/A^{\frac{1}{3}}$ MeV for $40 < A \leq 235$ with the evaporation of alpha particles from the compound nucleus, in agreement with statistical model calculations, at least for light and medium weight nuclei. The high alpha yields for ^{203}Tl and ^{205}Tl could not be explained in terms of the statistical compound

nucleus model and led to the proposal of a direct alpha knock-out model for heavy nuclei[17]. Further experiments in the 1960's using solid state detectors measured alpha energy spectra for both medium and heavy nuclei for photon energies up to 35 MeV[18-23]. The data obtained for medium weight nuclei agreed with statistical model predictions, although normalisation to the data was required. The yields and energy spectra observed for heavy nuclei could not be explained in terms of the compound nucleus reaction model and, although a direct alpha emission process had been proposed, no theoretical predictions of direct emission alpha energy spectra were (or are) available.

Studies of electron induced alpha emission begun in the mid 1970's gave energy spectra similar to those obtained for the (γ,α) reaction. Statistical model calculations successfully explained the low energy alpha emission from medium weight nuclei[6,24] although a high energy tail, not predicted by compound nucleus theory, was observed in ^{60}Ni [6]. Recent experiments[7,8,25] show the presence of a pre-equilibrium reaction component in both medium and heavy weight nuclei. Alpha particle energy spectra have been explained in terms of the pre-equilibrium exciton model[7,8]. Experiments on electron induced alpha emission from ^{238}U and Ni have been carried out to investigate the giant resonance multipolarities involved in (e,α) and (γ,α) reactions. Surprisingly large alpha decay widths for the giant quadrupole resonance in ^{238}U and Ni have been reported[26,27]. Some of the data was later reported to be in error[28,29] and other experiments on these nuclei have not observed large decay widths[30,31,32]. There is, therefore, some doubt as to the value of these results.

1.3 Historical Development of Photon and Electron Induced Deuteron Emission.

Byerly and Stephens[33] were the first to report the existence of photodeuterons in 1951. They measured the energy distribution of protons from copper following excitation by photons of energies up to 24 MeV using an emulsion technique. An extra peak at 2.5 MeV was observed and attributed to the presence of photodeuterons. It was reported that single deuterons could be distinguished from protons by counting the last 40 μm of the photo-particle tracks in the nuclear emulsions used. However, attempts to repeat this experiment[34,35] found that deuterons and protons could not be separated using either common or fine grain nuclear emulsions and it seems probable that the reported peak was a background effect.

The first unambiguous experiment which showed the existence of photodeuterons was performed by Smith and Laslett in 1952[36]. A thick copper target was irradiated with photons of maximum energy 65 MeV and deuterons separated from protons using a magnetic cloud chamber. The measured deuteron yield to proton yield gave a ratio (R_{dp}) of 0.76 and, using the same experimental arrangement, Ring[37] obtained a value for R_{dp} of 0.15 for the irradiation of sulphur. These values are considerably higher than those later measured by Chizov[38], using a two crystal telescope technique. Thus, although cloud chamber experiments showed the existence of photodeuterons, the high yield values obtained must be discounted as being due to difficulties in the experimental technique.

Between 1952 and 1960 several experiments were carried out to investigate the photodeuteron reaction for photons of maximum energy ∿30 MeV, using either a particle track grain counting technique in

nuclear emulsions (for example, references (33) and (34)), or an activation method (for example, references (39) and (40)). Neither of these methods clearly distinguishes detected deuterons[35] and only the method of deflecting charged particles in a magnetic field and detecting them by nuclear emulsions developed by Forkman[35] could be used with confidence to investigate (γ,d) reactions (for $E_\gamma \sim 30$ MeV) until solid state semiconductor detectors were available in the 1960's.

Chizov[41] measured deuteron to proton yields for $6 < A < 197$, using photons of maximum energy 90 MeV. The particles were detected using the techniques of deflecting charged particles in a magnetic field and that of a two crystal telescope. Angular distributions and excitation functions were also measured for light nuclei, e.g. Li, Be and B. High values of the deuteron to proton yield ratio, associated with forward peaked angular distributions for $E_D > 15$ MeV meant that the data could not be explained in terms of the statistical model. A two stage reaction mechanism, where a photon is absorbed on a nucleon which is then captured by another nucleon with sufficient momentum to lead to the emission of a deuteron, was found to successfully explain the data. Low energy photodeuteron yields ($E_D < 15$ MeV) were consistent with those predicted by statistical model calculations.

Later work on photodeuteron emission has concentrated on light nuclei either in the giant resonance region[42,43] or above the pion threshold[44,45]. Studies of electron induced deuteron emission, below the pion threshold, have been limited to the measurement of angular distributions of end point deuterons from ^{6}Li and ^{12}C for electron energies between 40 and 60 MeV[46,47].

1.4 Historical Development of Photon and Electron Induced Triton Emission.

The phototriton reaction was first observed in 1956 when Heinrich and Wäffler[48] measured total triton yields for Aℓ, Co and Cu, following excitation by 31 MeV photons, using an activation technique. Further experiments by the Darmstadt Group[49-52] for photon energies up to about 60 MeV, showed that the total triton yield agreed well with evaporation theory for light and medium weight nuclei but was much larger than predicted by theory for high A nuclei. Total triton yields measured for a maximum photon energy of 90 MeV[53] were consistent with the results at lower photon energies.

Measurements on electron induced triton emission from ^{19}F and ^{15}N have been made for electron energies less than 30 MeV[54,55]. The triton cross section exhibits resonance behaviour in the giant dipole resonance region, while angular distributions of tritons in this region are isotropic about 90^{o}, typical of evaporation following photon absorption to the giant dipole resonance.

1.5 Overall Review of Complex Particle Emission

Most studies of photon induced complex particle emission below the pion threshold have measured the total yield of the emitted alpha particle, deuteron or triton. No data on photon induced ^{3}He particle emission is available in this energy region for $A > 4$. The compound nucleus statistical model successfully explains complex particle yields at low particle and gamma ray energies for light and medium weight nuclei but some form of direct reaction mechanism is required to explain the high yields observed for high energy particles at photon energies

above the giant resonance region.

Some electron induced alpha particle energy spectra and angular distributions have been measured for electron energies up to 120 MeV[6,7,8] The low energy data agrees with that predicted by statistical model calculations, while high energy alpha data appears to be explained in terms of the pre-equilibrium exciton model. This model is discussed in Section 1.10.

1.6 Relationship Between Real and Virtual Photon Spectra

The relationship between electron and photon induced disintegration reactions can be understood if both the electron and photon induced total cross-sections are expanded as multipole series, i.e.

$$\sigma_\gamma(k_\gamma) = \sum_{\omega\lambda} \sigma_{\omega\lambda\gamma}(k_\gamma) \tag{1.1}$$

for photon induced reactions and:-

$$\sigma_e(E_e) = \sum_{\omega\lambda} \int_0^{(E_e - m_o c^2)/\hbar c} \sigma_{\omega\lambda\gamma}(k_\gamma) \frac{N_{\omega\lambda}(E_e, k_\gamma)}{k_\gamma} \, dk_\gamma \tag{1.2}$$

where $\hbar k_\gamma$ is the momentum of a photon of energy $\hbar c k_\gamma$, E_e is the incident electron energy, m_o the electron rest mass and ω denotes an electric (E) or magnetic (M) transition of multipole λ. $N_{\omega\lambda}(E_e, k_\gamma)/k_\gamma \hbar c$ defines a virtual photon spectrum for multipole λ, type ω.

A real photon of energy E_γ and momentum k_γ transfers momentum q to a nucleus on absorption where, by conservation of momentum, $q = \hbar k_\gamma$. Neglecting the recoil energy of the nucleus the excitation energy of the

nucleus, $E_x = E_\gamma = \hbar c k_\gamma = \hbar c q$. This condition is known as 'on the energy shell'. An electron of initial momentum k_1, may however be scattered through any angle θ ($0^\circ < \theta < 180^\circ$), thus letting the final momentum k_2 have any value between 0 and k_1. Thus when an electron interacts with a nucleus the momentum transfer, q, and excitation energy of the nucleus E_x for a 'virtual' photon, have values different to those for real photon absorption as given by:

$$q = \hbar (k_1^2 + k_2^2 - 2k_1 k_2 \cos\theta)^{\frac{1}{2}}$$

and

$$E_x = \hbar c (k_1 - k_2).$$

The 'on shell' relationship, i.e. $E_x = \hbar c q$, is achieved at $\theta = 0^\circ$, when the electrons are forward scattered.

An electron has an associated Coulomb field, thus in electron induced reactions a Coulomb interaction, which is not present in a photon nucleus interaction, must be taken into account. The photon electromagnetic field is purely transverse, while the Coulomb interaction introduces a longitudinal term. The longitudinal Coulomb matrix elements can be replaced by transverse electric matrix elements using Siegert's Theorem[56] for 'on shell' interactions.

Thus for $\theta \sim 0^\circ$ the transition matrix elements will be equal for both electron and photon induced reactions and the two interactions can be compared, as in equations (1.1) and (1.2), without any information on the details of the nucleus, which could only be supplied by a model. The approximation $\theta \sim 0^\circ$ is valid at low momentum transfers.

A longitudinal field is composed of the same multipole terms as a transverse field, with the addition of an $L = 0$ term. Thus electrons can excite nuclei to monopole resonances, which is not possible using

real photons. A real photon spectrum consists of equal amounts of each multipole while virtual photon spectra are enhanced for the higher multipoles. Thus a comparison of data obtained in photon and electron induced reactions can yield information on the multipolarities associated with these reactions, particularly of the giant resonance states excited by real and virtual photons. However this relies on the validity of the virtual photon formalism. Limitations of this formalism are discussed in the next section.

1.7 Virtual Photon Formalism

The use of virtual photon spectra to explain the electron-nucleus interaction was first developed by Weizäcker[57] and Williams[58] in the 1930's. The plane wave Born approximation (P.W.B.A.) was used in these early calculations. This approximation neglects distortion of the electron wave due to the Coulomb charge of the nucleus and assumes that the electron does not penetrate the nucleus. Thus P.W.B.A. is only valid for low Z nuclei (minimal distortion) and for electron energies where the long-wavelength limit applies (finite nuclear size not important). For a nucleus with $A = 240$, E_e must be less than about 30 MeV for the virtual photon formula to be valid to within 10%. The long wavelength approximation means that $qR \ll 1$ and limiting $qR < 0.2$ leads to an accuracy for the virtual photon spectrum to within $\sim$10%. Thus for the early electron induced reactions, using electrons of energy $\sim$ 30 MeV which concentrated mainly on light nuclei, the P.W.B.A. formalism was quite adequate to describe the electron nucleus interaction.

Experiments were performed to investigate the multipole components in the electrodisintegration cross section and were analysed using the plane wave formalism[59-64] in terms of electric dipole (E1), electric

quadrupole (E2) and magnetic dipole (M1) virtual photon spectra. The results obtained for light and medium weight nuclei were consistent with mostly E1 photon absorption, with up to a 12% E2 component. For heavy nuclei an E2 component of 50% or more was indicated. These results were somewhat surprising, as theory suggested that photon absorption was primarily an E1 process. They were thus assumed to arise from inaccuracy of the plane wave virtual photon spectra at high Z values.

Virtual photon spectra in the distorted wave Born approximation (D.W.B.A.), which takes account of the distortion effects of the Coulomb field, were produced by Gargaro and Onley in 1971[65]. These calculations still assume that the Coulomb field is generated by a point nucleus, thus there will be discrepancies at electron energies where the long-wavelength approximation is not valid, i.e. above $\sim$ 30 MeV for heavy nuclei. Calculation of virtual photon spectra using the D.W.B.A. formalism required long computer calculations. Computational rounding errors were often introduced into the calculation of E1 spectra as the sum of the partial waves converges very slowly. An analytic expression for the E1 virtual photon spectrum was developed[66] to relieve these problems and was used in the exciton model calculations reported in Chapter 4. This formula agrees with D.W.B.A. calculations to within 6% for $E_e < 50$ MeV and to within 10% in the giant resonance region for $Z \sim 28$ at $E_e = 120$ MeV[8].

Reliable E1, E2, E3 and M1 virtual photon spectra can now be rapidly calculated, using a method developed a few years ago[67]. It was noted that only the first few partial waves are affected by the Coulomb distortion. Thus for a given sum of partial waves the difference between the plane wave and distorted wave results quickly becomes constant. An accurate distorted wave spectrum is obtained by adding the result of this difference, once it has converged, to the

analytic plane wave result.

Experimentally determined ratios of the cross sections for the disintegration of nuclei, using both electrons and positrons (σ^-/σ^+) (at E_e = 27 MeV) have been compared to ratios calculated using both P.W.B.A. and D.W.B.A. virtual photon spectra[66]. Coulomb distortion effects are much more important for electrons than for positrons as the electron passes closer to the nucleus. This results in the increase of the ratio σ^-/σ^+ with increasing Z which has been experimentally observed. Good agreement between the experimental data and D.W.B.A. calculations suggest that the theoretical treatment of Coulomb distortions is fundamentally correct.

As a second test of D.W.B.A. virtual photon theory the experimentally measured $\sigma(e,n)$ cross section for ^{238}U was compared to that obtained from the (γ, n) cross section using an E1 D.W.B.A. virtual photon spectrum[68]. The two cross sections were found to agree to within 3%. Both these tests refer only to the E1 virtual photon spectrum and no tests have been made of the spectra for higher multipoles. Large differences between plane wave and distorted wave virtual photon spectra are observed, especially (as predicted) for high Z nuclei. The difference between the two calculations is more pronounced for the higher multipoles.

At high electron energies where the long-wavelength limit is not satisfied, it is expected that the virtual photon spectra will not be correct unless some correction, which takes account of the finite size of the nucleus, is applied. Shotter[69] has used the generalized Helm model[70,71] in conjunction with plane wave virtual photon spectra to estimate changes in the spectra due to the finite size of the nucleus. For an E1 virtual photon spectrum the difference between the two calculations for a finite and point nucleus is very small (< 10%) even for

uranium isotopes and can be effectively ignored. The longitudinal component of virtual photon spectra is much more strongly influenced by finite nuclear size effects. This component is dominant in the case of E2 transitions and for A = 240, E_e = 100 MeV, E_γ = 10 MeV effects due to the finite size of the nucleus cause a factor of five reduction in the E2 virtual photon spectrum calculated assuming a point charge. Even for light nuclei, A $\sim$ 10, finite nuclear size effects cannot be neglected in the calculation of E2 virtual photon spectra at electron energies above $\sim$ 50 MeV.

Thus it seems that D.W.B.A. E1 virtual photon spectra can be used with some confidence for electron energies up to 120 MeV. No tests on the accuracy or applicability of E2 virtual photon spectra have been carried out. At present the best available E2 virtual photon spectrum calculation is the D.W.B.A. calculation of Soto Vargas et al.[67] combined with correction factors due to the finite size of the nucleus as calculated by Shotter[69]. E2 virtual photon spectra calculated in this way were used in this thesis, although their accuracy is not known.

At energies < 40 MeV photon absorption is dominated by absorption on to the giant dipole resonance (G.D.R.). Sum rules, i.e. model independent conservation laws which give the total integrated absorption cross sections, for photon absorption to the lowest electric (E1,E2, E3) giant resonances, together with their centroid energies, are given in Table 1.1.

Above the giant resonance region photon absorption appears to be dominated by absorption onto a correlated neutron proton pair, a quasideuteron, which is a dipole process. Thus for most of this thesis work only E1 virtual photon spectra, which can be easily and accurately calculated, are required.

TABLE 1.1

Giant Resonance Centroids and Sum Rules

	$E_c A^{1/3}$	$\int_E \frac{\sigma dE}{2\lambda-2}$
E1 isovector	80	$60 \frac{NZ}{A^{1/3}}$ mb. MeV
E2 isoscalar	63	$0.22 \frac{Z^2}{A^{1/3}}$ μb/MeV
E2 isovector	130	$0.22 \frac{NZ}{A^{1/3}}$ μb/MeV
E3 isoscalar	∿30	$0.31Z \cdot A^{1/3}$ pb/MeV^3
E3 isovector	∿110	$0.31Z \cdot A^{1/3}$ pb/MeV^3

1.8 Bremsstrahlung Spectrum

The real photon cross section was given in equation (1.1) as $\sigma_\gamma(k_\gamma) = \sum_{\omega\lambda} \sigma_{\omega\lambda_\gamma}(k_\gamma)$. In this thesis work a bremsstrahlung spectrum, produced by placing a radiator in the electron beam, was used as the source of real photons. A bremsstrahlung spectrum consists of photons of all energies up to the electron energy and is given by:

$$\sigma_{br}(E_e) = \sum_{\omega\lambda} \int_0^{E_e - m_o c^2} \sigma_{\omega\lambda_\gamma}(E_\gamma) \frac{k(E_e,E_\gamma)}{E_\gamma} dE_\gamma$$

where $\frac{k(E_e,E_\gamma)}{E_\gamma}$ is the bremsstrahlung spectrum of real photons, which is the same for all multipolarities. The bremsstrahlung formula for $k(E_e,E_\gamma)$ used in this thesis work was the extreme-relativistic Bethe-Heitler formula with the Coulomb correction and intermediate screening[72]. The calculations of Deck et al.[73] were used at the end point as the Bethe-Heitler formula, being a Born-approximation formula, is not valid in this region. The end point cross section was joined to the Bethe-Heitler cross section with a straight line tangential to this curve at the point of contact to produce a complete spectrum since a gap of $\sim$1 MeV is left between the two theories[74].

1.9 Quasi-deuteron Absorption

Total photon absorption cross sections have not been measured for photon energies above $\sim$ 30 MeV except for a few recent measurements on heavy nuclei for photons of energy up to $\sim$ 110 MeV[75,76]. A theoretical estimate of the absorption cross section is necessary before the cross

section for the emission of complex particles due to high energy photons can be calculated using a suitable model. Levinger[77] proposed that photon absorption took place on a correlated neutron proton pair (quasideuteron) in the nucleus and calculated the photon absorption cross section in terms of the deuteron photodisintegration cross section.

High energy nucleons emitted from a nucleus have momenta far above the Fermi momentum. In a photonuclear reaction the incoming photon has considerable energy $\hbar\omega$, but comparatively little momentum $\hbar\omega/c$, thus the emitted particles can gain little momentum from the photon. Assuming that momentum transfer cannot occur after photon absorption (the Born approximation), the nucleon must have had a high momentum in the ground state. This is possible if the nucleon is acted on by strong forces due to the proximity of other nucleons. If two nucleons are much closer than the average internucleon distance, it is likely that no other nucleons will be close to these two nucleons. Thus nucleons of high momentum are likely to be emitted from a nucleus following photon absorption onto a two nucleon cluster. The dipole term is dominant in the photodisintegration of nuclei at high photon energies, thus the two nucleons must be a neutron, proton pair. Complex particles can be emitted from the nucleus by a further interaction process occurring after quasideuteron absorption of the initial real or virtual photon.

Levinger showed that the quasideuteron wave function is proportional to the ground state deuteron wave function, for small values of the neutron-proton separation. The maximum possible number of neutron-proton pairs in a nucleus is NZ which leads to the value of the quasideuteron photon absorption cross section given by

$$\sigma_{\gamma_{Q\to D}}(E_\gamma) = L\left(\frac{NZ}{A}\right)\cdot\sigma_D(E_\gamma) \qquad (1.3)$$

where $\sigma_D(E_\gamma)$ is the deuteron photodisintegration cross section and L is the Levinger parameter, a factor which takes account of the momentum distributions of the neutron and proton. This parameter was first given a value of 6.4 by Levinger in his original work and later amended to a value of 8[5].

The photon absorption cross section as given by equation (1.3) will be an overestimate at photon energies below $\sim$ 150 MeV. It was assumed, in the derivation of the quasideuteron cross section, that high energy photons only interact with closely correlated nucleons of separation r and low relative momenta k, i.e. $kr << 1$. Also no allowance was made for the Pauli blocking of many neutron and proton final states at low photon energies. The addition of a 'quenching factor' to the expression given in equation (1.3) to account for these effects is discussed further in Section 4.1.5.

1.10 Pre-equilibrium Exciton Model

Several reaction models have been developed to try to explain the high energy cross section observed in particle induced reactions[78,79] which is not predicted by statistical model calculations. The calculations which have been most successful in predicting this high energy tail involve some form of intranuclear interaction following the initial photon absorption[80,81]. Complex particles may be emitted from a nucleus in a process where the particle is formed from nucleons which have been excited in a cascade process within the nucleus. The pre-equilibrium exciton model is based on such a reaction mechanism. Energy spectra and excitation functions of complex particles emitted following particle excitation have been successfully explained using this model[79,82]. The pre-equilibrium exciton model was first proposed by Griffin[83]

in 1966 and has since been developed by a number of authors[84].

A computer code has been developed to perform exciton model calculations of energy spectra for complex particles emitted in electron induced reactions[80]. The experimentally measured energy spectra have been compared to spectra calculated using this computer code. The results of this comparison are discussed in Chapter 4, together with a more detailed review of the exciton model.

1.11 Experimental Data

Energy spectra, angular distributions and excitation functions for the emission of complex particles from nuclei $12 < A < 197$ following excitation by electrons and gamma rays at energies between the giant resonance region and the pion threshold ($40 \lesssim E_e, E_\gamma \lesssim 130$ MeV) have been measured during the course of this thesis study. This work extends that already reported for alpha emission[6,7,8], to include measurements for the emission of deuterons, tritons and ^{3}He particles. Energy spectra have been measured at one particular angle (30° to the beam direction) for the nuclei ^{12}C, ^{27}Aℓ, Ni, ^{92,94}Mo, Sn, Ta and Au to establish the systematics of electron induced complex particle emission at $E_e = 120$ MeV. Angular distributions have been obtained at the same electron energy for the nuclei ^{12}C, ^{27}Aℓ, Ni, Sn and Au, for up to five different particle energies between 2.5 and 50 MeV. A comparison between the angular distributions of particles emitted following excitation by both real and virtual photons for electron and bremsstrahlung end point energies of 60 and 120 MeV has been made for the nuclei ^{58}Ni, ^{60}Ni and Au. Excitation functions at three different particle energies have been measured for both electron and bremsstrahlung excitation,

at energies $40 \leq E_e \leq 130$ MeV, using a gold target.

The experimental data has been analysed in terms of the statistical and pre-equilibrium exciton models in an attempt to more fully understand the mechanisms involved in photonuclear reactions. Data obtained for both electron and photon excitation is compared in the hope that more information on the multipolarity of the virtual photon absorption process can be deduced.

CHAPTER 2

EXPERIMENTAL SYSTEM

2.1 Introduction

A diagram of the experimental arrangement is shown in Fig. 2.1. Target nuclei in a range from ^{12}C to ^{197}Au were bombarded with electrons and photons of energies between 40 and 140 MeV. The incident electrons were produced in an electron linear accelerator and passed through an energy compression system, to reduce the momentum spread, before being bent through a total of 90^{o} and energy analysed by energy defining slits. The electron beam then passes into the heavily shielded experimental area.

The electrons are then incident either on a target positioned inside the scattering chamber or on a bremsstrahlung radiator situated 10 cm upstream from the target, in the case of photon induced reactions. The complex particles emitted from the target (i.e. alphas, deuterons, tritons and ^{3}He particles), are detected by an array of ten silicon surface barrier detectors mounted in the focal plane of a magnetic spectrometer at angles between 30^{o} and 150^{o} to the beam. The amount of charge delivered to the target or bremsstrahlung radiator is monitored using a toroid system. The signals from the detectors are then pulse height analysed. The pulse height spectra were transferred to a P.D.P.10 computer so that further analysis could be carried out.

2.2 Accelerator and Energy Compression System

The electron linear accelerator is a pulsed r.f. travelling wave (s-band) type. It is made up of three sections, each powered by a 25 MW klystron. The first two sections consist of four cylindrical wave guides of

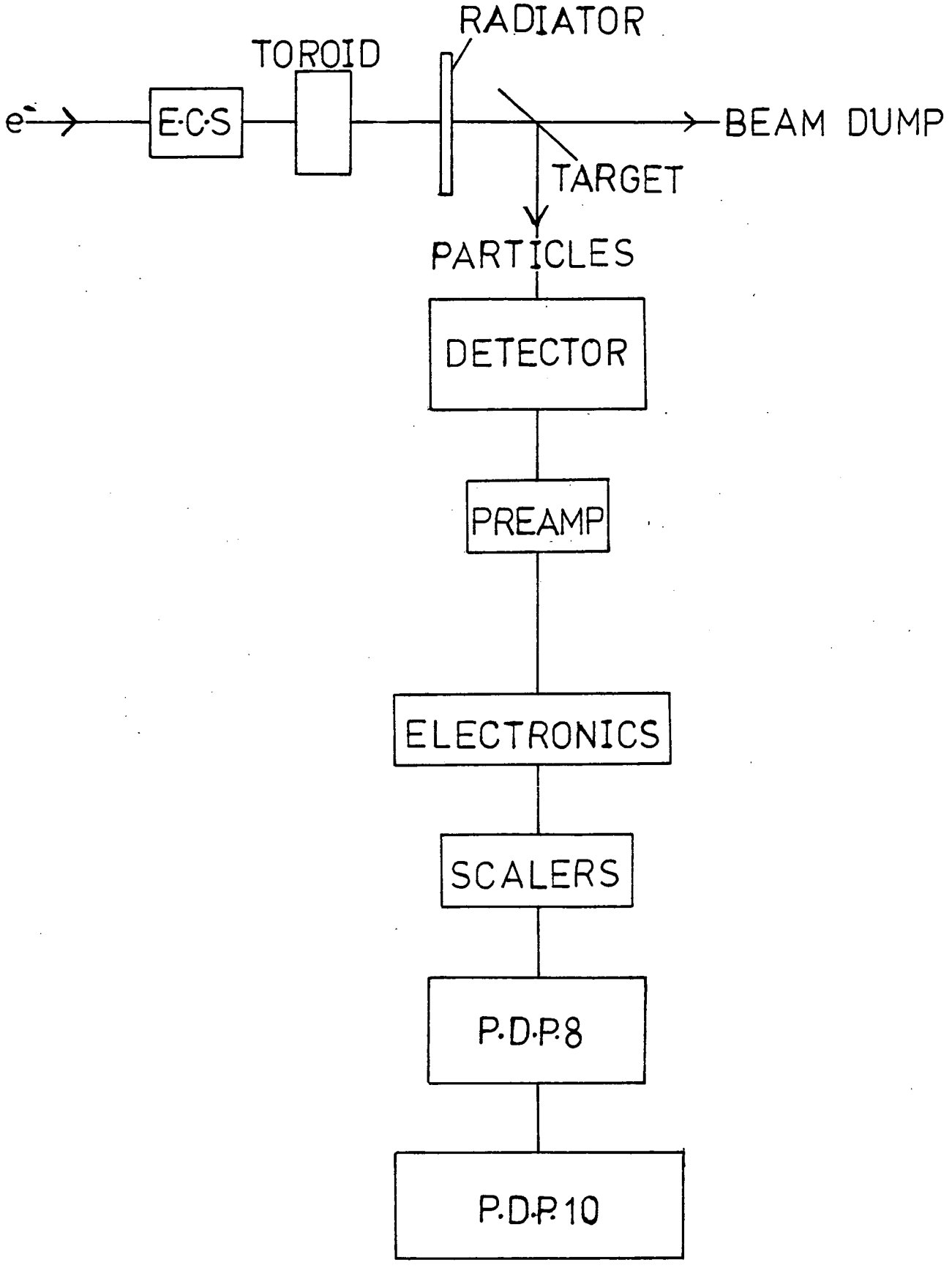

Fig. 2.1 Block diagram of the experimental arrangements.

length 1.5m, and the final section of four wave guides, each 2m long. A maximum beam energy of approximately 160 MeV can be obtained from the accelerator, the first two sections imparting about 40 MeV to the electron beam and the third approximately 80 MeV.

The accelerator is pulsed at 100 p.p.s. with a pulse length of 3.25 μs giving a duty cycle of 3.25×10^{-4}. The voltage pulses applied across the klystrons are charged from 3 phase 50 Hz power supplies which are phase rectified but have some 300 Hz frequency ripple on the outputs, despite being smoothed. There is also 300 Hz frequency ripple from the electron gun 50 Hz A.C. power supply. This ripple can lead to a modulation of the beam energy if the phases of the firing pulses are not the same. This results in a substantial loss of current in the energy analysis system due to two distinct energies of electrons being produced. The accelerator is adjusted such that the klystron and electron gun power supplies are all locked in phase to prevent this occurring.

Peak currents of approximately 80 ma are used, giving a mean current on the target of between 12 and 15 μA at 120 MeV, with an energy analysis of 0.5%. Attenuation of the r.f. power in some of the accelerator sections means that electron energies down to 80 MeV can be obtained. Below this energy it is necessary to 'back-phase' the second section, thus decelerating the beam in this part of the accelerator. The deceleration ensures beam stability throughout the accelerator and thus beam energies between 20 and 140 MeV can be readily obtained at mean currents on the target of 7 μa or more.

At the accelerator exit the beam passes through an energy compression system (E.C.S.) which reduces the momentum spread of the electron beam leaving the accelerator. The improved energy resolution thus provided by the E.C.S. facilitates beam handling and allows higher currents to be transmitted through the beam handling system, resulting in a lower background.

There is also an improvement in beam stability after energy analysis as the compression system automatically corrects for small changes in beam energy. The operation of such a system is described fully by Kaiser[85].

The E.C.S. consists of three dipole magnets, a schematic view of which is shown in Fig. 2.2, plus a section of r.f.wave guide. The sharply bunched electron beam emitted from the accelerator passes through the magnet system which makes the low energy electrons take a longer route, resulting in a 'sheared' bunch, shown as area II of Fig. 2.3. The initial electron beam is represented in the longitudinal phase space by area I, drawn there as a rectangle although the real accelerator emittance closely approximates an ellipse. The beam has width b and length $\delta\rho_1$, where b is the electron bunch length and $\delta\rho_1$ the momentum spread.

On leaving the magnet system there is a linear relationship between the momentum of an electron and its position in the bunch. The debunched beam of low momentum spread, area III of Fig. 2.3, is produced by passing the beam through a short section of accelerating wave guide. The r.f. field is adjusted such that the higher energy electrons at the head of the bunch are decelerated, while the lower energy electrons at the tail of the bunch are accelerated. The final compressed beam is slightly distorted due to the inherent non-linearity of the r.f. sinusoidal field.

Thus the bunched beam of momentum spread $\delta\rho_1$, which entered the compression system, emerges with the much lower momentum spread of $\delta\rho_2$, i.e. the momentum has been compresed by a factor:

$$F_c = \frac{\delta\rho_1}{\delta\rho_2}$$ which is typically about 10.

Small drifts in beam energy are automatically corrected by the E.C.S. due to the action of the r.f. field which holds the centroid of phase area III fixed on the Z axis for small drifts of the centroid of area I

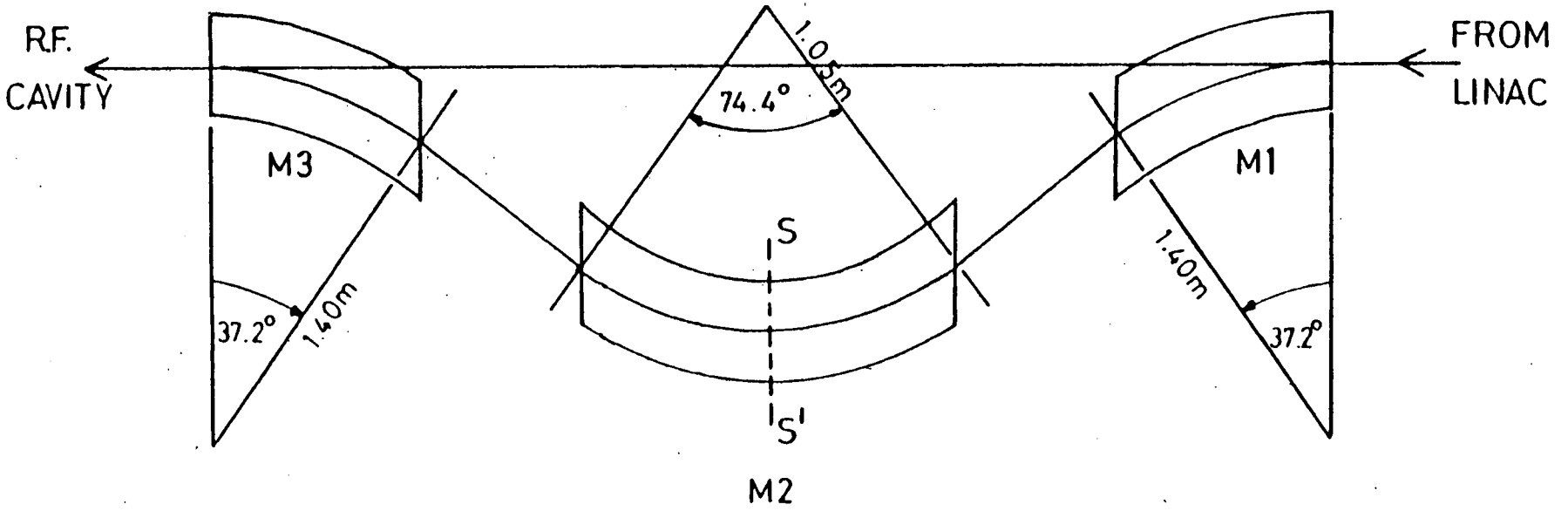

Figure 2.2. GEOMETRY OF E.C.S.

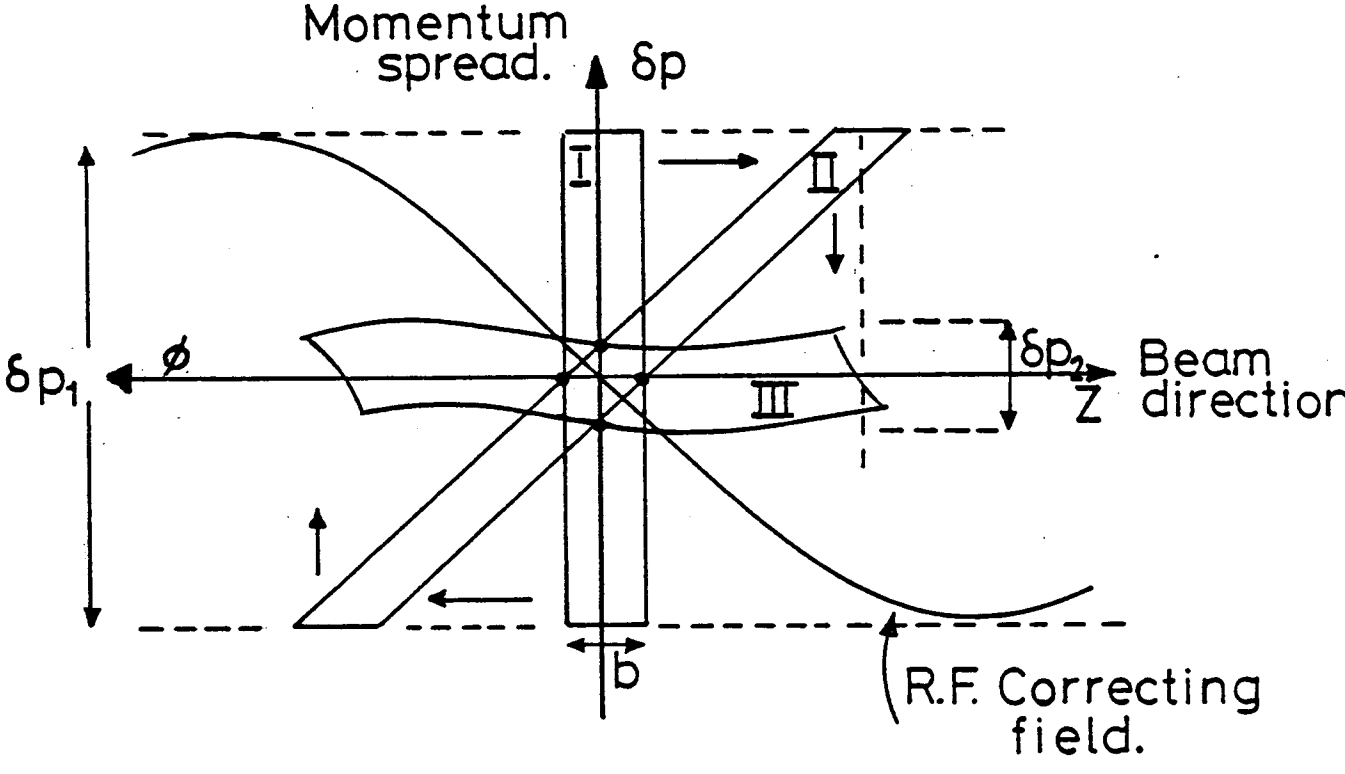

Fig. 2.3 Schematic view of the momentum compression of the electrón beam.

away from the momentum axis.

2.3 Beam Handling System

After the beam has been compressed by the E.C.S. it enters the beam handling and energy analysis system shown in Fig. 2.4. Quadrupole magnets M1 and M2 focus the beam through two sets of adjustable slits, C1 and C2 which form a rectangular collimating aperture - the object for the energy analysis system. These slits are water cooled as the spread of the incident electron beam is usually greater than the aperture.

The energy analysis system consists of a 45^{o} bending magnet D1 and the energy defining slit C3. The energy resolution is a function of the width of the energy defining slit and the size of the collimating aperture C1, C2. An energy resolution of 0.5% was used throughout these experiments. The second 45^{o} bending magnet D2, a mirror image of D1, has as its object the slit C3. The beam which has been turned through a total of 90^{o} is further focused by quadrupoles H3 and H4 to produce an approximately parallel beam.

The beam then travels a distance of approximately 2.5m between the beam deflection room and the experimental area and is finally steered and focused on to the target, using steering magnets S1, S2 and quadrupoles H5, H6.

A nuclear magnetic resonance (N.M.R.) probe situated within the first bending magnet D1 is used to measure the energy of the electron beam by assuming that the electron momentum is linearly related to the measured magnetic field. The position of the N.M.R. is reproducible to 0.5mm - the equivalent of 0.003% constancy in the magnetic field as measured by the N.M.R. Once the system is calibrated (see Appendix 1)

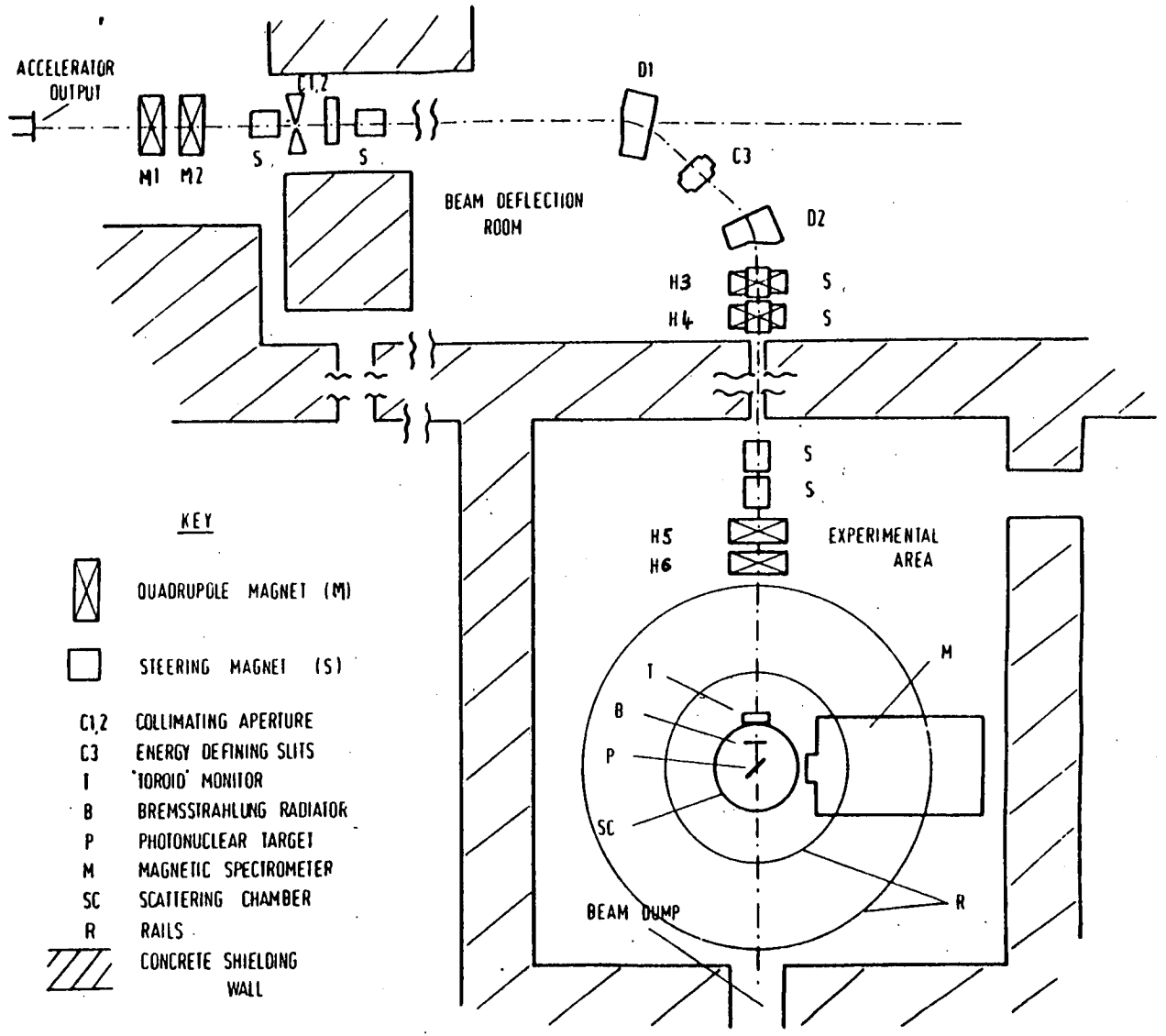

Fig. 2.4 Beam handling and energy analysis system.

the frequency of the r.f. oscillator at resonance measures the electron energy.

2.4 Toroid Charge Monitor

The charge monitor system used in this work was a non intercepting beam current integrator[86]. This system uses the signal from a toroidal transformer to drive a current integrator. The toroid is positioned just upstream of the scattering chamber (Fig. 2.1). The core and windings together with the preamplifier are mounted within a copper shield which is located inside the vacuum system but electrically isolated from the beam tube. A toroidal mu-metal core acts as a current transformer, its primary being the electron beam. The signal from the secondary windings is amplified by a low input impedance preamplifier, before being transmitted to the control room where the linear gate and current integrator are situated. The preamplifier is heavily shielded with lead to prevent radiation damage.

A block diagram of the charge monitor system is given in Fig. 2.5. The linear gate is opened only for the duration of a beam pulse to remove the undershoot, which has an area equal to that of the main pulse, and to help reduce the pickup. The output of the toroidal transformer is A.C. coupled to the preamplifier input. Similarly the preamplifier output is A.C. coupled to the linear gate. The A.C. coupling of the preamplifier limits D.C. drift. The digital output of the current integrator is accumulated by a scalar which has an automatic stop facility. Thus for each experimental run the same amount of charge is incident on the target.

The toroid system was calibrated against a Faraday cup and showed no deviations from linearity, or instability for mean currents up to

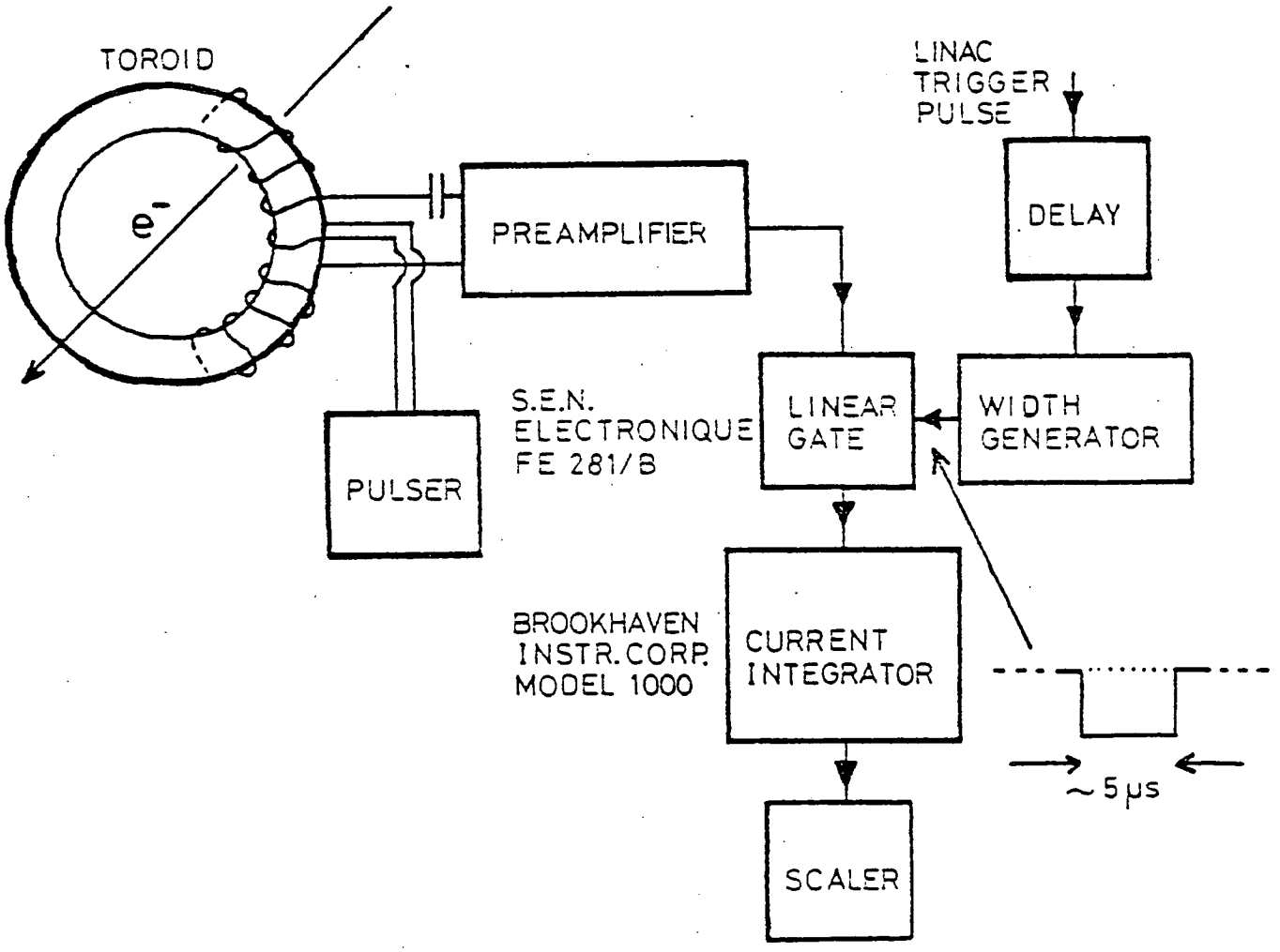
CHARGE MONITOR
TOROID
e⁻
PREAMPLIFIER
LINAC
TRIGGER
PULSE
DELAY
PULSER
S.E.N.
ELECTRONIQUE
FE 281/B
LINEAR
GATE
WIDTH
GENERATOR
BROOKHAVEN
INSTR. CORP.
MODEL 1000
CURRENT
INTEGRATOR
~5 μs
SCALER

Fig. 2.5.

19 μA within 0.6% (see Appendix 2). The beam pulse shape is not rectangular and frequently varies quite considerably in shape, thus linearity in the toroid system is very important. The efficiency of the Faraday cup was 0.996 for electron energies above 70 MeV, decreasing by 1% at 40 MeV due to multiple scattering between the toroid and the Faraday cup[86].

A single turn calibration loop is wound round the toroid, along with the twenty turns of signal winding, and is fed by a precision pulser. This 'calibration' circuit was used after every two or three experimental runs to check that there had been no drift in the toroid system. Balance adjustments to the D.C. voltages in the linear gate and current integrator, monitored with a digital voltmeter, were made at similar time intervals.

2.5 Scattering Chamber and Bremsstrahlung Radiators

The scattering chamber, which is an aluminium cylinder 10" high with a diameter of 18" is shown in Fig. 2.6. The target ladder is situated at the centre of the scattering chamber and the bremsstrahlung radiator 10 cm downstream. The chamber has mountings for windows every $7\frac{1}{2}^{o}$ such that complex particles can be detected by the spectrometer in 15^{o} intervals from 30 to 150 degrees. A glass window on the opposite side of the chamber to the spectrometer is used to enable the targets to be directly viewed and also to be observed by a television camera which displays an image on a screen in the control room.

The chamber was evacuated to approximately 10^{-5} torr. and vacuum coupled to the magnetic spectrometer. An aluminium foil, of thickness 150 or 180 μg cm^{-2}, was used as a vacuum isolator between the chamber and

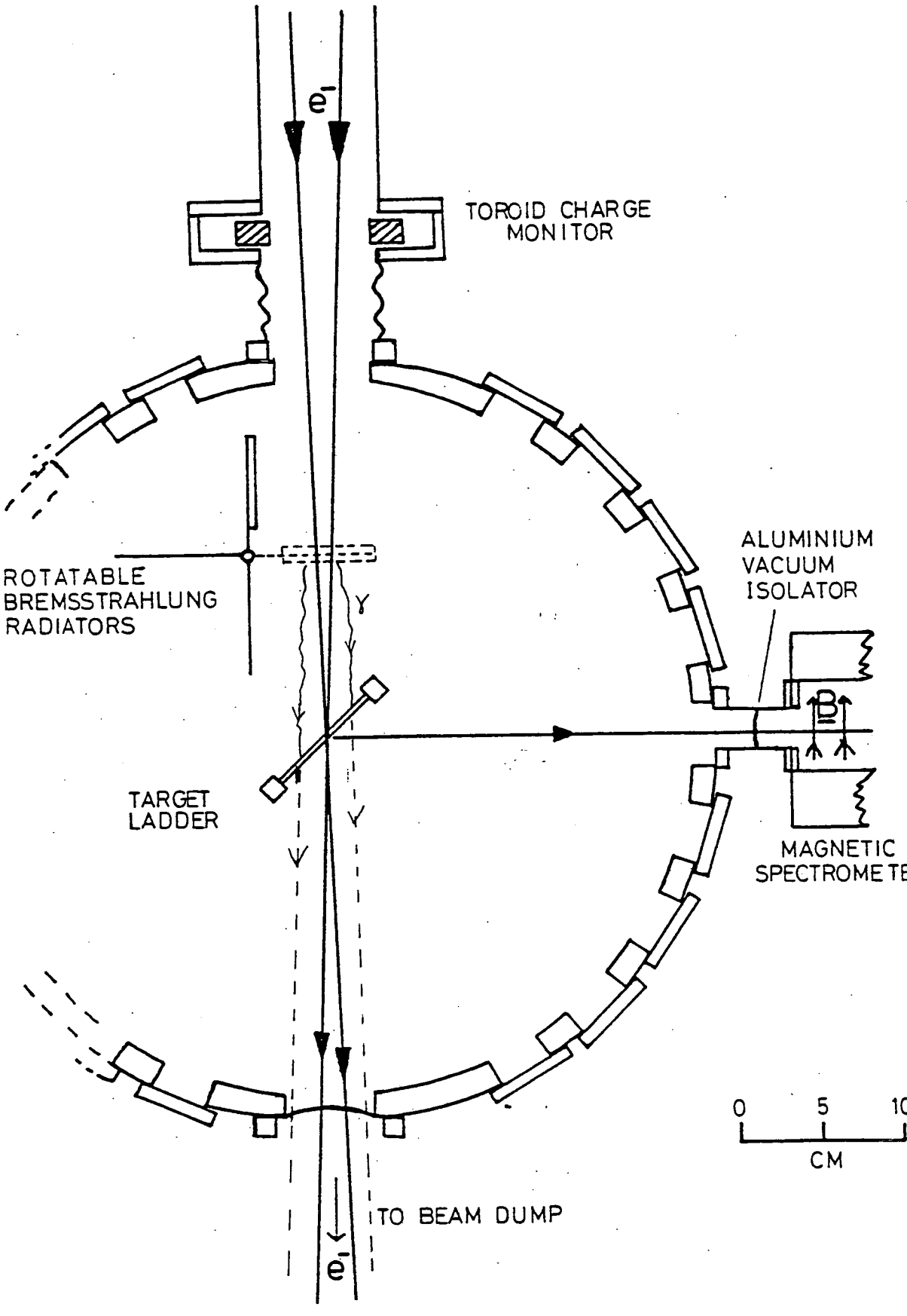

Figure 2.6 Scattering chamber.

spectrometer as the pressure in the spectrometer, approximately 10^{-4} torr., was not as low as that in the scattering chamber. The exit port of the scattering chamber is of 0.01" aluminium foil after which the beam travels through air for approximately 2m to the beam dump entrance. The beam dump consists of a pile of iron at the end of a 0.6m square and 4m long tunnel.

The bremsstrahlung radiators were mounted on a rotator consisting of four radiator holders positioned at 90^{o} to each other on a vertical shaft. The shaft is rotated by means of an electric motor which lies on top of the scattering chamber. Any of the four radiator positions can be moved into the beam path as required.

The radiator position is changed by remote control, using a Wheatstone bridge arrangement which is accurate to 1^{o} or 0.02% in radiator thickness. One variable resistor is mounted on the motor shaft so that the resistance varies as a function of radiator angle , while the other resistor of the bridge system is in the control room. This resistor was adjusted until a balance was achieved at certain switch positions corresponding to each of the radiator mountings being in a position of 90^{o} to the electron beam.

Two tantalum radiators of thicknesses 0.1694 ± 0.0012 g/cm^2 and 0.0813 ± 0.0009 g/cm^2 were used, leaving two blank positions to enable electron induced reactions to be carried out and also to enable visual checks of the beam spot size and position using a BeO scintillator as target.

The radiators were chosen to be as thick as possible, while keeping the size of the beam spot on the target less than $\sim$ 10 mm in diameter. This ensures that all of the particles emitted will be detected by the counters of width 40 mm. The enlargement of the beam spot due to multiple scattering in the bremsstrahlung radiator was calculated using the

approximate formula[87]

$$\theta_{ms} = \frac{20}{E}\sqrt{t} \quad ,$$

where θ_{ms} = mean square spread of the bremsstrahlung spectrum.

E = electron energy (MeV)

t = thickness of radiator (radiation lengths)

and $\theta_{ms} \approx \tan \theta_{ms} = \frac{x/2}{l}$

where x = increase in spot size in cm and $l = 10$ cm is target to radiator distance.

It has been shown[32] that the loss in detected particles due to the finite size of the detectors is below 1% in all cases.

2.6 Targets

The target thicknesses were chosen so that the energy loss of alpha particles was less than 5% for all the measured particle energies. Thus it was necessary to use several targets of differing thickness over the whole particle energy range to ensure that some particles could be detected at high energy whilst restricting the energy loss at low energies. Although the energies of the tritons and deuterons detected are $\frac{1}{3}$ and $\frac{1}{2}$, respectively, of the corresponding alpha energy, the much lower energy loss for these particles means that the above 5% criterion is quite adequate.

Table 2.1 gives the target thicknesses and purity for the range of nuclei used in these experiments.

The target thicknesses were determined by measuring the area and weighing except for thin ^{12}C and thin ^{27}Al targets where this method would be inaccurate. The thicknesses of these targets were determined using an alpha energy loss technique. For these measurements a ^{238}Pu

TABLE 2.1

Target	Thickness mg/cm^2	% Purity
^{12}C	0.386 ± 0.019	Unknown
Polythene	10.6 ± 0.2	"
$^{27}A\ell$	0.197 ± 0.010	99.6
$^{27}A\ell$	7.9 ± 0.2	99.5
$^{27}A\ell$	30.1 ± 0.9	99.0
^{58}Ni	4.5 ± 0.1	Unknown
^{60}Ni	5.4 ± 0.2	"
^{NAT}Ni	3.1 ± 0.1	99.95
^{NAT}Ni	5.7 ± 0.1	99.95
^{NAT}Ni	11.3 ± 0.2	99.9
^{NAT}Ni	39.4 ± 1.6	99.9
^{92}Mo	42 ± 2	99
^{94}Mo	48 ± 1	99
^{NAT}Sn	5.7 ± 0.1	99.75
^{NAT}Sn	15.6 ± 0.3	99.75
^{181}Ta	15.5 ± 0.3	99.9
^{197}Au	21.0 ± 0.8	99.9
^{197}Au	29.7 ± 0.3	99.9

alpha source was placed directly behind the required target in the scattering chamber. The number of alphas observed by three detectors at the centre of the ladder were counted on scalars as the magnetic field of the spectrometer was altered, one Rawson unit at a time, to sweep across the whole energy range of the detected alpha particles. In this way alpha energy spectra are obtained for the two targets.

The ^{238}Pu source consists of two alpha lines very close together at energies 5.4565 and 5.4992 MeV. Thus by fitting two gaussian curves to the alpha line spectra the energy loss for the mean of the alpha lines can be calculated for each target. From Zeigler's[88] alpha energy loss tables the target thicknesses can then be directly obtained.

The cross section for the energy spectra and angular distributions of ^{12}C, for alpha energies greater than 30 MeV, was measured using a polythene target due to difficulties in obtaining a thick carbon foil. As the beam intensity is slowly increased on the polythene target it gradually blackens as the oxygen and hydrogen atoms are 'burnt' off to leave almost pure ^{12}C as the target.

Despite using a defocused beam spot of a quarter of the normal beam current (i.e. $\sim$ 0.25 μA) it was found that the polythene target had melted and split after completion of angular distributions taken at alpha energies of 30 and 50 MeV. The two sets of distributions had similar, irregular shapes, suggesting that certain of the data points were too low due to the melting of the target. At each angle data was obtained for both particle energies, the angle then changed and data measured again at the two energies. Thus the low data points will be at the same angle for both sets of angular distributions and so only the one for 30 MeV alpha particle energy was repeated using a different target for each angle.

Each target, after being irradiated, was placed in a holder sandwiched between two Ge (Li) detectors to ascertain the activity of the 478 keV gamma ray (half life 53.4 days) from ^{7}Be. The target holder was arranged in such a way that the position of each target was exactly reproducible, so that a direct comparison could be easily made between the total counts in the gamma ray peak for each target. Corrections for time of counting and delay between irradiation and counting were taken into account using the formula:

$$N_o = \frac{N}{(e^{-\lambda T_1} - e^{-\lambda T_2})}$$

where N = Number of counts measured

N_o = Activity $/ \lambda$

T_1 = Time of starting counting after end of irradiation

T_2 = Time of ending counting after end of irradiation

λ = Disintegration constant of ^{7}Be

Thus by normalising the activities to the results of two targets which remained intact and gave the same counts, within statistical inaccuracy, factors can be obtained which, on multiplying with the spectra from the surface barrier detectors, give the cross sections for the angular distributions at E_α = 30 MeV. The cross sections for the 50 MeV alpha energy angular distributions were obtained by multiplying each data point by the ratio of the 'new', corrected cross section to the original value at each corresponding angle for the 30 MeV angular distribution.

Tin has a low melting point (232^{o}C) and thus for the thick target (15.6 mg/cm^2) it was necessary to use half the normal beam current ($\sim$ 0.5 μA) to prevent the target from melting. This was not necessary with the thin target as the heat produced in the target is dissipated

quickly for a thin foil and so there is less likelihood of melting.

The targets are mounted vertically in five positions on a target ladder which is at the centre of the scattering chamber. The lowest target position has a BeO scintillator permanently fixed in place which is used for viewing the beam spot. Various groupings of the targets listed in Table 2.1 are used as required for particular experiments. The target holders used are made of thin aluminium 3" long by 1½" high, with either a 1 cm diameter hole for the target at the centre, for electron induced reactions or a 2½" by 1" rectangular hole for the bremsstrahlung induced reactions. A larger target is required due to the increase in spot size because of multiple scattering of electrons in the radiator.

The target ladder is operated remotely, being raised and lowered by a pneumatic piston bringing each target into position in the beam line, with an accuracy of 0.1 mm in the vertical direction. Using a telescope mounted on the spectrometer the targets are accurately aligned as they are put on to the target ladder. This is necessary in the case of the BeO scintillator which is used when setting up the electron beam. A change in the position of the beam spot on the target means a change in the position of the focused particles in the focal plane of the spectrometer, i.e. an energy shift. The accuracy of positioning $\pm$ 0.1mm is equivalent to a change in energy of 0.01%, which is a negligible shift.

The angular position of the targets is set so that the normal to the target ladder is at 45^{o} to the beam direction when particles are detected at backward angles in the spectrometer, and at 135^{o} to the beam direction for particles emitted at forward angles. These angles are chosen to minimize the energy losses of complex particles produced in the targets, whilst ensuring that the beam does not hit the target ladder. A correction is applied during the cross section calculation

to account for the loss in energy of complex particles in the target itself (see Section 3.2).

2.7 Magnetic Spectrometer

The magnetic spectrometer is an $n = \frac{1}{2}$, 80 cm radius, 'magic angle' spectrometer based on a design of Penner[89]. Fig. 2.7 shows the spectrometer and the position of the counter ladder. The spectrometer is motor driven on a carriage running on two concentric circular tracks, with the scattering chamber at the centre. The evacuated scattering chamber is vacuum coupled to the spectrometer which is pumped to a vacuum of approximately 10^{-4} torr. At this pressure energy losses and scattering are minimal even for the lowest energy particles detected, deuterons of energy about 2.5 MeV.

Complex particles of the same magnetic rigidity will be detected together in the focal plane of the spectrometer. For constant magnetic rigidity (momentum/charge) the energy of the detected particles is proportional to Z^2/A where Z = charge of the complex particle and A is the nuclear mass. Thus for each alpha particle energy ($Z^2/A = 1$), tritons of energy $E_\alpha/3$, deuterons of energy $E_\alpha/2$ and ^{3}He particles of energy $E_\alpha \cdot \frac{4}{3}$ will also be detected. The maximum magnetic rigidity of a particle which can be focused by the spectrometer is approximately 375 MeV/c, which corresponds to an alpha particle energy of 67 MeV. The current for the spectrometer magnet windings is provided by a 170V, 700 A power supply stable to 3 parts in 10^5. Both the power supply and windings are water cooled.

An array of ten silicon surface barrier detectors is mounted in the focal plane of the spectrometer. The detector ladder spans a range of 6% in momentum, each detector having a momentum bite of 0.45% with

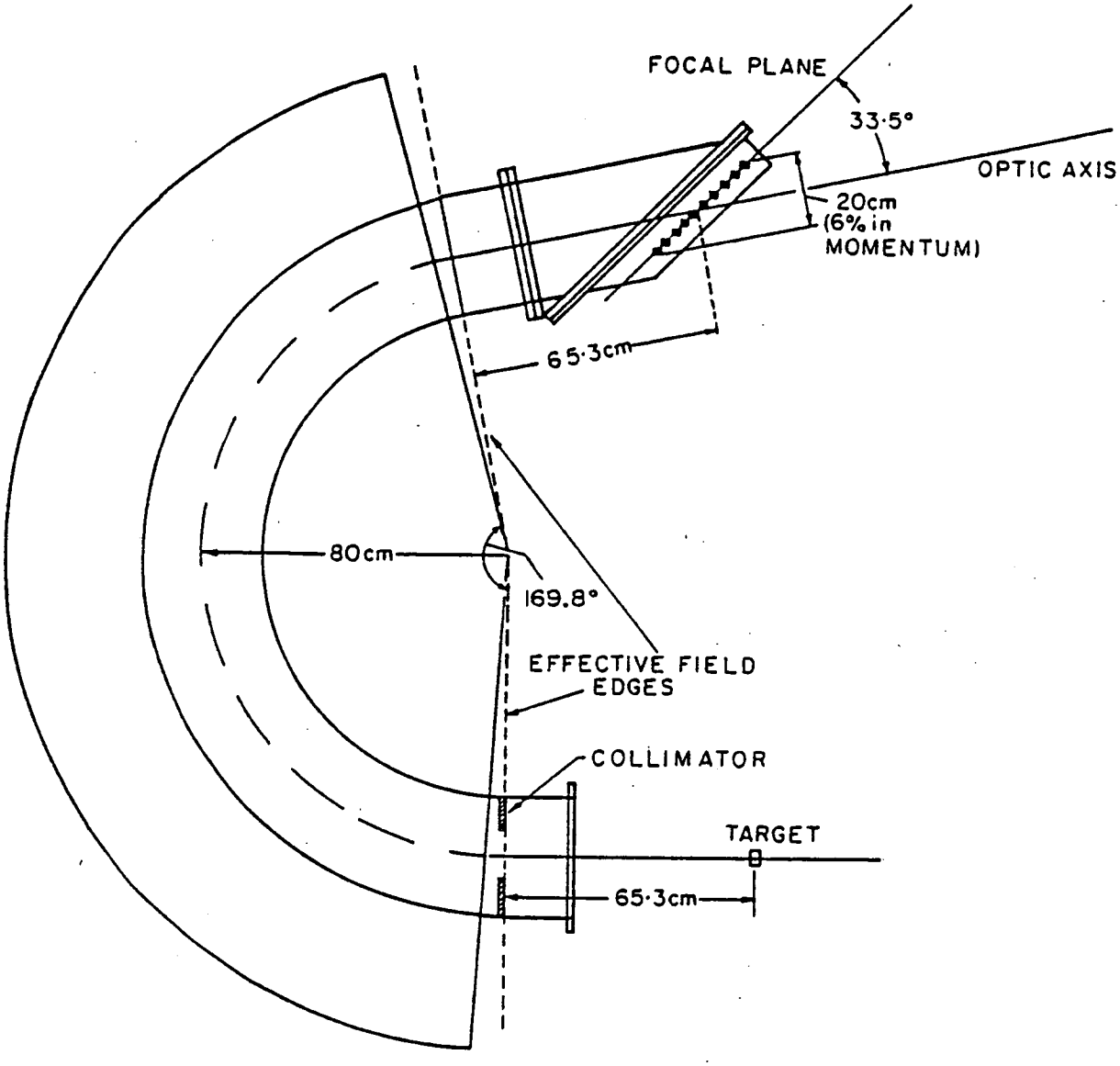

Fig. 2.7 Magnetic Spectrometer.

0.6% spacing between counters. Due to the large momentum span there is some loss of quality of the images produced for the detectors at either end of the ladder. Relative counter efficiencies (see Appendix 4) are used to eliminate this effect.

The effective solid angle subtended by the spectrometer at the target is 9.94 millisteradians. A brass collimator, placed at the effective pole edge of the spectrometer magnet, defines the solid angle as 10.00 ms. This is reduced due to the presence of the probe of a Rawson-Lush rotating coil gaussmeter, near the outer edges of the pole pieces. The gaussmeter has a stability of approximately 1 part in 10^5.

2.8 Detectors

Ten n-type silicon surface barrier detectors are mounted on a detector ladder positioned in the focal plane of the magnetic spectrometer. The counters, which are housed in a casing of dimensions 22mm × 55mm × 12mm, have a sensitive area of (nominal specifications) 15mm by 40 mm. The resistivity varies with each counter within a range 4000-6000 ohm.cm. Operating at voltages between 8 and 180V gives depletion depths from 100 μm to 500 μm, breakdown occurring above 200V. The highest energy of alpha particles which can be fully stopped by the detectors is about 33 MeV. For particle energies above this maximum the energy deposited in the detectors will be less than the incident energy. Despite this the different complex particles, apart from ^{3}He particles which cannot be detected above 40 MeV, can still be easily differentiated right up to the energy limit of the spectrometer, since discrete peaks are still observed for each particle.

Protons and alpha particles of the same energy will be focused to

the same place on the focal plane by the spectrometer and thus be detected together. Protons, however, require a much greater thickness of detector to be fully stopped than alpha particles of the same energy. Thus by adjusting the depletion depth of the detectors such that alpha particles will be stopped but protons will only deposit a small amount of energy in the detectors, the alpha and proton peaks can be easily separated in the pulse height spectrum. The depletion depth is related to the applied voltage as

$$d \sim 0.5(pV)^{\frac{1}{2}}$$

where d = depletion depth in μm

p = resistivity of silicon in $\Omega \cdot cm$

V = bias applied to detector in volts.

Thus at each particle energy the bias applied to the individual detectors must be set according to the resistivity of each detector such that the proton peak is positioned near, or below, the threshold of the pulse height spectrum so that distinct peaks are obtained for the other, complex, particles detected. The lowest bias settings at which the above condition is met are generally used to limit background caused by neutron induced reactions in the sensitive area of the detectors.

The resolution of the detectors is 40 keV or better, with a leakage current of less than 2 μA.

Several of the older counters have narrow strips of film attached to the sides of the detectors to act as collimators due to slight variations in uniformity at the counter edges. A low energy tail is observed in the spectrum obtained using an alpha particle test source, as a result of these variations. The use of collimators results in a lower relative efficiency of the specific detectors,

for which a correction is made.

The counters are mounted with their centres 2 cm apart along the ladder, symmetrically about the central orbit and numbered 0 to 9 inclusive. The lowest-energy particles are detected in counter 0 for a given magnetic field. The ratio of counter bite to counter spacing is 0.75 for the non-collimated detectors which have a sensitive width of $\sim$ 1.5 cm and 0.6 for the collimated detectors of sensitive width $\sim$ 1.2 cm. The value of 0.75 is used throughout the data analysis, a correction for the lower ratio for the collimated detectors being introduced by the relative efficiency values. From the alpha calibration (Appendix 3) the relative momenta at the centre of each detector are 0.6% in momentum for counter spacing and 0.45% for the momentum bite, for any one spectrometer field setting.

Each counter has a particular relative efficiency; a counter if placed at position 4½ on the ladder, having by definition a relative efficiency of one, the other detectors having varying values - as low as 0.7 at the ends of the detector ladder. The relative efficiency is dependent on the efficiency of the individual counter, variations in dispersion across the focal plane and changes in the solid angle (see Appendix 4).

In order to reduce the background at the counters it is necessary to have considerable shielding around the detectors and around the sources of background radiation. The shielding around the counters consists of 10 to 15 cm of lead and 30 cm of borated paraffin wax. An additional 8 cm of lead and 20 cm of paraffin is placed on top of the scattering chamber which lies directly below the counter ladder. Paraffin wax is placed around the beam pipe as it enters the experimental area, and at the entrance to the beam dump. Also pulses are only accepted from the counters for the duration of the beam burst

which further reduces background. This, in combination with the shielding, ensures that the background is reduced to almost negligible proportions over the whole range of particle energies detected.

2.9 Electronics

A block diagram of the electronics for one counter in the detector ladder is shown in Fig. 2.8. There are ten identical channels as ten counters are used.

The pulse from the counter passes first to a pre-amplifier positioned within the shielding, as close as possible to the detector. This signal is then transmitted to the control room where it is amplified and split, one portion feeding a discriminator, the other a gated digitizer. The discriminator cuts out small background pulses while the digitizer produces a train of output pulses, the number of pulses in the train being proportional to the height of the input pulse. This number, when recorded by a scalar, gives the pulse height spectrum.

The digitizer is gated by the output of the discriminator after it has been fed through the dead time generator. This is a device which reproduces at the output its input pulse (which must be short), only if there has not been a similar pulse present in the last 50 μsec. As the duration of the beam burst is only 3 μsec this ensures that only one counter pulse above the discriminator threshold is digitized every beam pulse. The delay preceding the input of the digitizer compensates for the delay of the other signal portion in passing through the second amplifier, discriminator and dead time generator.

The outputs of the discriminator (total counts) and dead time generator (accepted counts) were read by scalars. The ratio of these

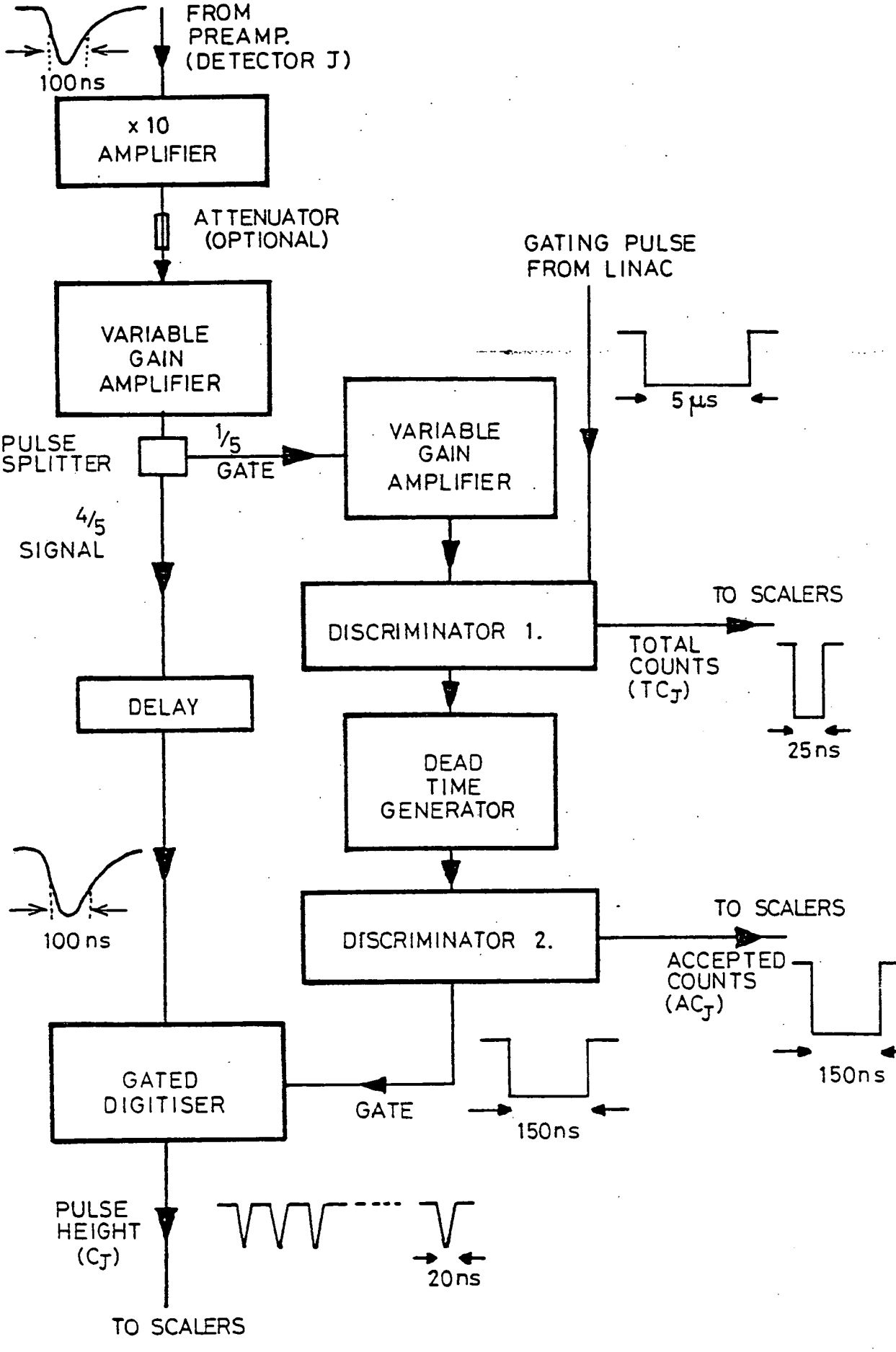

Fig. 2.8 Electronics

two numbers gives the dead time correction which must be applied to the data. For most of the experimental runs reported in this work the dead time corrections were kept below 3%. Thus there are thirty numbers - three for each detector - which characterise the response of the counter ladder. These numbers are stored in a Lecroy type 150 scaling system. Scalers 1 - 10 contain the pulse height information, 11 - 20 the accepted counts and 21 - 30 the total counts.

The scalars are interfaced to a D.E.C. P.D.P.8 computer, using a system composed of commercial CAMAC modules and a custom built LECROY/CAMAC interface. The computer controls the CAMAC controller as a peripheral device. After each beam burst an interrupt signal, the accelerator trigger pulse delayed by 50 μsecs, is sent through the interrupt-mixer to the computer and the scalars are inhibited so that no further counts can be accumulated. The number contained in each scalar is in turn presented to the Lecroy data bus and read by the computer. The scalars are then reset to zero to await the next beam burst.

The computer stores and displays a 200 channel spectrum, plus the total and accepted counts, for each of the ten detectors. On receiving an interrupt from the LECROY/CAMAC interface, the computer reads the scalars and then returns to the display mode. The contents of the scalars are deposited in the accumulator and the memory updated each time the scalars are read.

The spectrum of each counter can be displayed on the oscilloscope screen as it accumulates. A typical pulse height spectrum showing alpha particles, tritons, deuterons and ^{3}He's is shown in Fig. 3.2.

Three canberra type 1492 scalars are used to record the charge delivered to the target, as measured by the toroid, the number of beam pulses and the time for each experimental run. The inhibit

line of one of the scalars is linked to the inhibit line of the LECROY system so that starting this scalar enables the whole data collection system. Using the automatic stop facility of the scalars, the data collection is stopped after a specified amount of charge has passed.

At the end of each experimental run the ten spectra are transferred from the computer memory to storage on DEC-tape and directly onto disk of a D.E.C. P.D.P. 10 computer so that the pulse height spectra can be analysed.

CHAPTER 3

ANALYSIS AND PRESENTATION OF THE EXPERIMENTAL DATA

3.1 Determination of Complex Particle Peak Areas

The first part of the data analysis procedure is to determine the number of complex particles incident on the detectors, i.e. the raw data. This is achieved by obtaining the areas of the peaks in the pulse height spectra for each complex particle. One counter spectrum, from the set of ten spectra recorded for each experimental run, is displayed on a visual display unit (V.D.U.) using the interactive graphics of the D.E.C. P.D.P. 10 computer. Cursors are set, by eye, at either side of a peak to obtain the peak area.

The peaks, in most of the experimental runs, sit on a background which must be subtracted from the peak area to give the true counts. A second order Legendre polynomial is fitted simultaneously to a background region on either side of the peak. These background regions are set by eye using the cursors.

The fitted background curve is then drawn on the V.D.U. screen and the χ^2 of the fit is also displayed. If this value is close to 1 and the fitted curve appears to give a good fit to the background, the next peak in the spectrum is integrated in this manner. However, if this is not the case the background regions can be altered until a good fit is achieved.

Each counter has a 200 channel spectrum, the data being scaled to map channels 0-200 onto the real axis between -1 and +1 such that the Legendre polynomials, which are orthogonal over the interval $[-1, +1]$ are approximately orthogonal over the background fitted

region. It was found that it was necessary only to go to a second order polynomial to get a good background fit, i.e. the function fitted was:

$$a_o P_o + a_1 P_1 + a_2 P_2 \quad .$$

The background is thus interpolated under the peak (see Fig. 3.1) and then is subtracted from the peak area to give the actual number of counts in the peak. For each spectrum a maximum of four different peaks can be integrated in this manner. Thus, if all the complex particles, i.e. alphas, tritons, deuterons and ^{3}He's are present, forty peak areas are measured for each experimental run.

The procedure of setting the peak limits and background regions by eye is necessarily a subjective operation. However tests have been carried out which show that the change in peak area, for a peak being integrated by several different people, lies within the associated error on the peak area. Most of the integrations were carried out personally so this is only a minor problem.

The procedure outlined above gives the raw data for electron induced reactions. For reactions induced by bremsstrahlung the radiator was placed in the electron beam path before the target so that real photons as well as electrons were incident on the target. The number of electrons reaching the target is the same as for runs without the bremsstrahlung radiator, assuming small scattering effects. Thus, to obtain the number of complex particles detected which are produced by the bremsstrahlung spectrum, it is necessary to subtract the 'radiator out' data from that for the radiator positioned in the beam path. The subtraction is performed by taking the difference of corresponding counter spectra, normalized to the same charge delivered to the target or bremsstrahlung radiator, for 'radiator in' and 'radiator out' runs and then evaluating

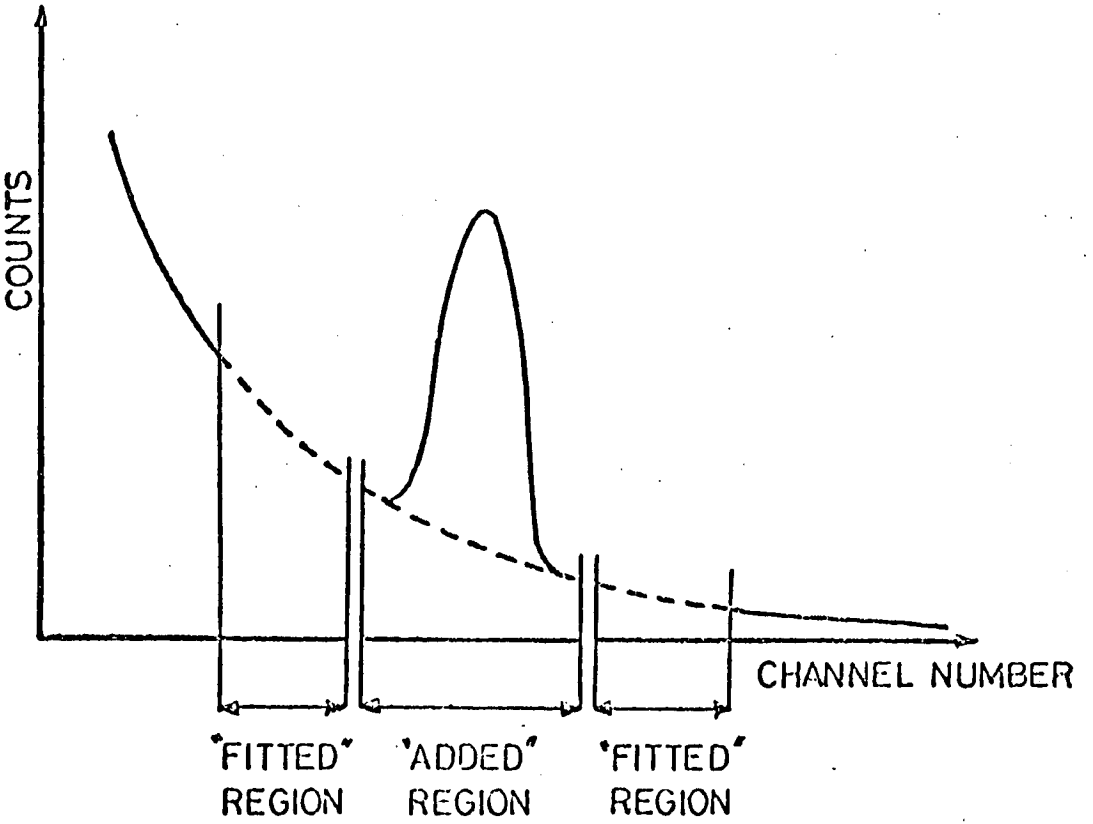

Fig. 3.1 Idealized pulse height spectrum.

the peak areas as described previously. This means that only one background fitting is necessary, most of the background in fact cancels out, and the same channel numbers are used for defining the peak limits. Thus as long as there are no gain shifts between experimental runs this method is far better than evaluating both sets of peak areas and then subtracting.

The pulse height spectra collected for low particle energies contain, in general, four sharp, easily distinguishable peaks. These peaks correspond to deuterons of energy $\frac{E_\alpha}{2}$, tritons of energy $\frac{E_\alpha}{3}$, ^{3}He particles of energy $E_\alpha \cdot \frac{4}{3}$ and alpha particles (see Fig. 3.2). All the detected particles have the same magnetic rigidity. As the energy of the particles detected increases the deuterons cannot deposit all their energy in the detectors, causing the deuteron peak to move closer to the triton peak in the pulse height spectra. The positions of the deuteron and triton peaks become reversed for alpha energies above 30 MeV - as shown in Fig. 3.3. Alpha particles and ^{3}He particles are not fully stopped in the detectors above energies of approximately 28 MeV. This results in the broadening of the peaks. Above 40 MeV so little of the ^{3}He energy is deposited in the detectors that the peak becomes very flat and is lost in the background.

The actual number of counts in each peak is multiplied by a factor to correct for the dead time. The error associated with each peak area is derived from combining the statistical uncertainty with a factor which takes account of the goodness of fit of the background curve.

The output from the integration programme consists of a peak area and error for the ten counters, for each complex particle. These numbers are then sorted, using a computer programme, into files containing the run number, target name, name of particle, electron energy, spectrometer angle and Rawson setting plus the corresponding peak areas and errors

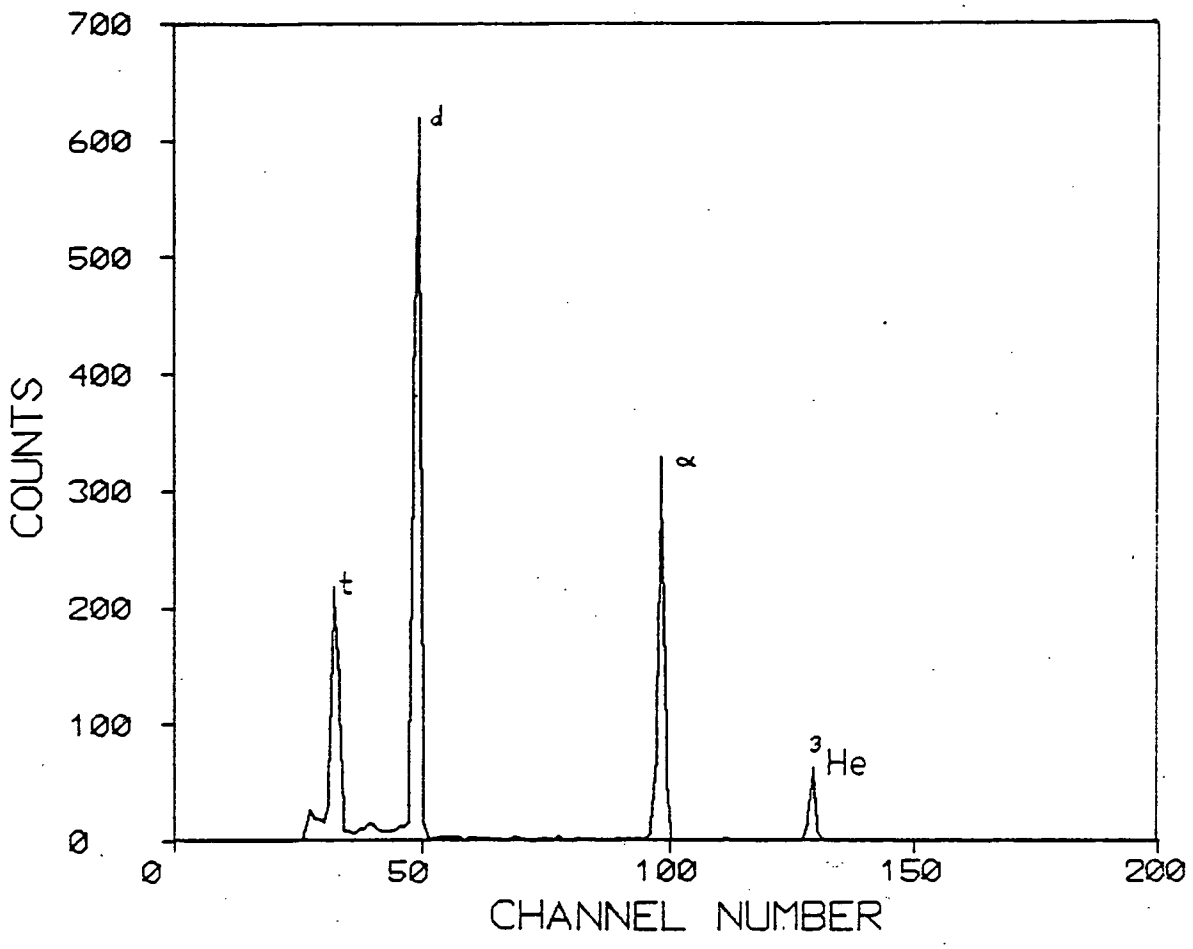

Fig. 3.2 Pulse height spectrum at E_α < 30 MeV. All particles fully stopped in the detector.

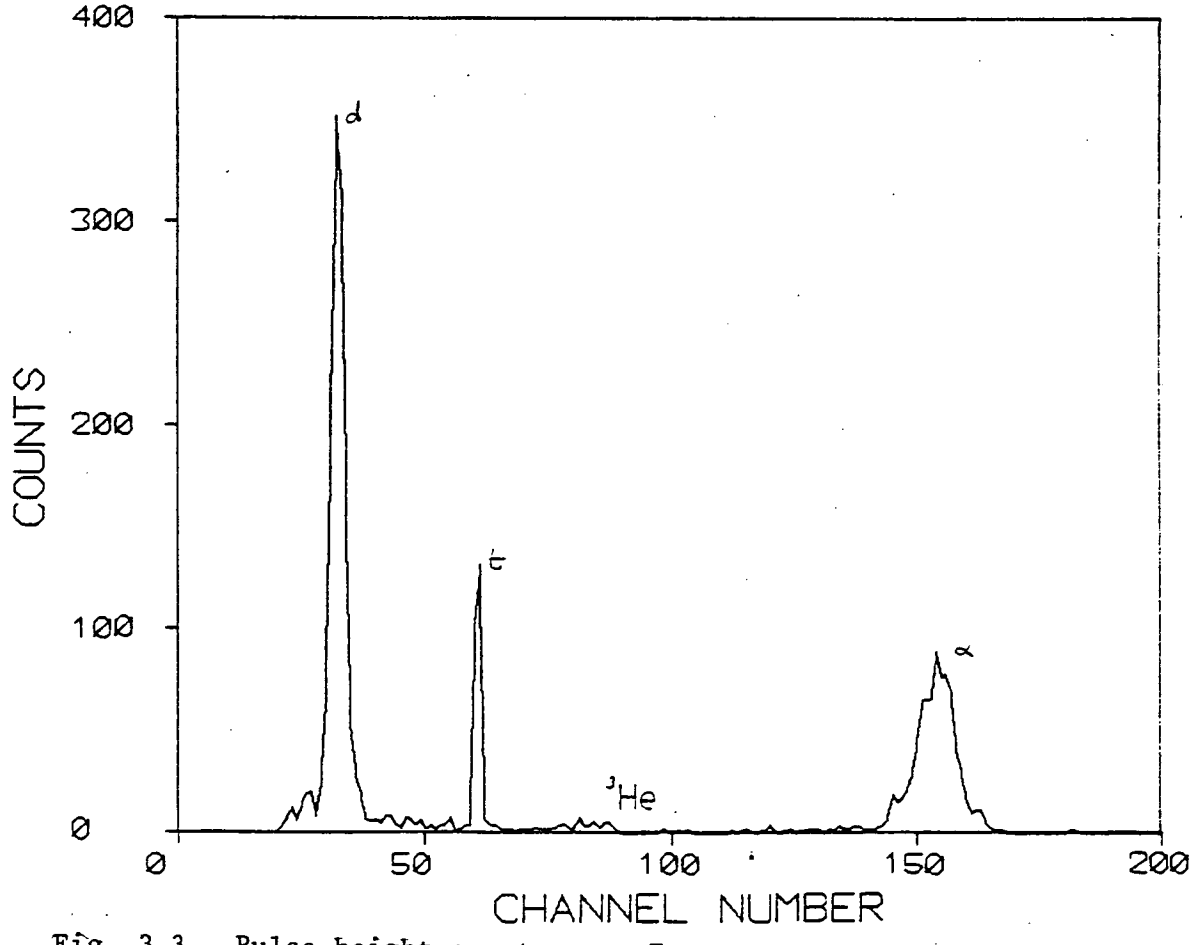

Fig. 3.3 Pulse height spectrum at E_α > 30 MeV. Alphas, deuterons and ^3He particles not fully stopped.

for each of the ten counters*. These files are the inputs for NSIGZ - the computer programme which calculates the double differential cross section, $\frac{d^2\sigma}{dE \cdot d\Omega}$ for the emitted particles.

3.2 Calculation of Double Differential Cross Sections

The areas of the alpha particle, triton, deuteron and ^{3}He peaks from each pulse height spectrum were obtained as described in Section 3.1. From this data the double differential cross sections (differential in energy and solid angle), for the emission of the various complex particles, i.e. $\frac{d^2\sigma}{dE \cdot d\Omega}$ (μb/MeV.sr) were calculated.

The cross section is related to the peak area (C), for a particular counter J (where J varies from 0 - 9 (see Section 2.8)) by the equation:

$$\frac{d^2\sigma}{dE \cdot d\Omega} \propto C_J / \Delta E_J \cdot \Delta\Omega_J$$

where C_J = peak area for counter J

$\Delta\Omega_J$ = solid angle for counter J

ΔE_J = energy bite of counter J.

The alpha calibration (App. 3) gives the momenta at each counter for a particular spectrometer field setting as:

$$P_J = F(J)\bar{p}(R) \quad . \qquad (3.1)$$

---

* The spectrometer field is measured using a Rawson-Lush gaussmeter which is calibrated to give the energy of a particular particle focused onto the detector ladder for a fixed spectrometer field, i.e. fixed Rawson setting. It is convenient to use the Rawson settings rather than particle energies at this stage. The particle energies are calculated in the cross section programme where corrections for energy losses in the target and vacuum isolater are applied.

Thus it is necessary to evaluate the energy bite (ΔE_J) in terms of the momentum bite Δp_J.

Using relativistic formulae:

$$\Delta E' = \frac{p \cdot c^2}{E'} \cdot \Delta p$$

where E' = total energy of particle

p = momentum of particle

m_o = rest mass of particle

$E' = E + m_o c^2$

where

E = kinetic energy of particle

$\therefore \Delta E = \Delta E'$

and

$$\Delta E_J = \frac{p_J c^2 \cdot \Delta p_J}{E + m_o c^2} .$$

The momentum bite Δp_J can be written

$$\Delta p_J = \frac{dp_J}{dJ} \Delta J ,$$

where ΔJ = width of counter in counter number space. Differentiating eqn. (3.1) with respect to J gives

$$\frac{dp_J}{dJ} = \frac{dF_J}{dJ} \cdot \bar{p}(R)$$

$\frac{dF_J}{dJ}$ is obtained from the α-calibration and $\bar{p}(R)$ is the momentum on the central orbit for a particular Rawson setting (R).

Thus, substituting for p_J and Δp_J gives

$$\Delta E_J = \frac{\bar{p}^2(R) F(J)}{E + m_o c^2} \cdot \frac{dF_J}{dJ} \cdot c^2 \cdot \Delta J$$

Using $\bar{p}^2c^2 = \bar{E}'^2 - m_o^2c^4$

i.e. $\bar{p}^2c^2 = (\bar{E} + m_oc^2)^2 - m_o^2c^4$

$\bar{p}^2c^2 = \bar{E}^2 + 2\bar{E}\, m_oc^2$

where $\bar{E}$ = kinetic energy at central orbit.

$$\Delta E_J = \frac{\bar{E}^2 + 2\bar{E}\, m_oc^2}{E + m_oc^2} F(J) \cdot \frac{dF_J}{dJ} \cdot \Delta J$$ in terms of

the particle energy. Rearranging gives:

$$\Delta E_J = 2\bar{E} \frac{(1 + \frac{\bar{E}}{2m_oc^2})}{1 + \frac{E}{m_oc^2}} F(J) \cdot \frac{dF_J}{dJ} \cdot \Delta J$$

$$\therefore \frac{d^2\sigma}{dE \cdot d\Omega} = C_J\Big(2\bar{E} \frac{(1 + \frac{\bar{E}}{2m_oc^2})}{1 + \frac{E}{m_oc^2}} \cdot F(J) \frac{dF_J}{dJ} \cdot \Delta J \cdot \Delta\Omega_J\Big)^{-1}$$

The magnification of the spectrometer varies across the focal plane causing changes in $\Delta\Omega$ away from the central orbit. Near the edges of the pole pieces the field deviates from the theoretical shape also causing changes in $\Delta\Omega$. The dispersion across the focal plane is not constant causing changes in $\frac{dF}{dJ}(J)$ across the counter ladder. These effects are grouped together into a factor dependent on counter number and particle energy - the relative efficiency $(\eta(\bar{E}))$ which has a defined value of 1 for the central orbit, i.e. $J = 4.5$. Thus:

$$\frac{d^2\sigma}{dE \cdot d\Omega} = C_J\Big(2\bar{E} \frac{(1 + 2\frac{\bar{E}}{m_oc^2})}{(1 + \frac{E}{m_oc^2})} \cdot F(J=4.5)\left(\frac{dF}{dJ}\right)_{J=4.5} \cdot \Omega_{J=4.5} \cdot \Delta J \cdot \eta_J(\bar{E})\Big)^{-1}$$

where:

$F(J = 4.5)$, $\left(\frac{dF}{dJ}\right)_{J=4.5}$, $\Omega_{J=4.5}$ and ΔJ have definite values (see App. 3 and Section 2.7).

The number of electrons incident on the target of thickness t (mg/cm^{-2}) for one experimental run is N_e. Thus the final expression for the cross section is

$$\frac{d^2\sigma}{dE \cdot d\Omega} = C_J \left(2\bar{E} \frac{(1 + \frac{\bar{E}}{2m_o c^2})}{(1 + \frac{E}{m_o c^2})} (F \cdot (\frac{dF}{dJ}) \cdot \Omega)_{J=4.5} \cdot \Delta J \cdot \eta_J(\bar{E}) \right.$$

$$\left. \cdot \frac{N_e \cdot t \cdot N_A}{A \cdot \sin(45^o)} \cdot D_J \right)^{-1} \qquad (3.2)$$

where:

N_A = Avagadro's number

A = Atomic mass of target

D_J = Dilation factor.

The target is set at an angle of 45^o to the beam direction so the actual thickness of target 'seen' by the electron beam is $\frac{t}{\sin(45^o)}$.

The emitted particles lose energy in the target itself and in the aluminium vacuum isolator. The particle energies in the above equation are energy loss corrected and a dilation factor D_J corrects for the change in energy bite between the target and the detectors (see Ref. (8)).

Two reasonable assumptions are made in calculating the energy loss of the complex particles:

i) All the particles are produced at the centre of the target.

ii) The energy loss can be expressed as

$$\frac{dE}{dx} = AE^B \qquad (3.3)$$

where x = target thickness

E = particle energy.

A and B are parameters which are obtained by fitting the above expression to the energy loss values as tabulated by Williamson[90] for deuterons, tritons and ^{3}He, and by Ziegler[88] for alpha particles.

The energy of the particle at the centre of the target, E_p, is obtained by integrating equation (3.3), i.e.

$$\int_{E_p}^{E_t} \frac{E^{-B}}{A} \cdot dE = \int_0^{t/2} dx$$

$$\therefore \quad \left[\frac{E^{-B+1}}{(1-B)\cdot A}\right]_{E_p}^{E_t} = \frac{t}{2}$$

$$\text{giving} \quad E_p = \left[A(1-B)\frac{t}{2} - E_t^{(1-B)}\right]^{1/1-B}$$

where E_t = energy of particle outside target. E_t is obtained in terms of the particle energy measured at the detectors (E_m), using the above procedure to calculate the energy loss through the aluminium window. Thus E_p can be calculated from the measured energy E_m.

The error on the calculated cross section values is a combination of the errors on the individual measured values. The two factors which contribute most to the final error are the error in the target thickness measurement and the statistical error on the number of counts.

3.3 Corrections Necessary Due to Au Targets Acting as Bremsstrahlung Radiators.

The ^{197}Au targets used in these experiments were of thickness 21.00 mg cm^{-2} and 29.68 mg cm^{-2}. Thus the targets themselves act as bremsstrahlung radiators and it is necessary to subtract from the calculated differential cross sections the number of particles emitted due to the bremsstrahlung produced in the targets. In the case of the excitation functions and angular distributions this is a straightforward procedure since measurements have been made for both electron and bremsstrahlung induced reactions.

At each excitation energy or angle a factor, f, is subtracted from both the electron induced cross sections and the bremsstrahlung yields where f is given by

$$f^{(\theta,E_e)} = \left(\frac{N}{E}\right)_{\text{Target}} / \left(\frac{N}{E}\right)_{\text{Ta. radiator}} \cdot \sigma_{\text{brem.}}(\theta,E_e)$$

$\frac{N}{E}$ is bremsstrahlung spectrum (see Section (1.8).

From Fig. 3.4 it can be seen that $\left(\frac{N}{E}\right)_{\text{target}} / \left(\frac{N}{E}\right)_{\text{Ta. radiator}}$ can be given by a single number, 0.131 for the thicker Au target, 0.0927 for the other, for all gamma energies. This approximation is correct to << 1% except at the end point.

The energy spectra for gold have only been measured for electron induced reactions. However for each complex particle except ^{3}He, a three point bremsstrahlung induced energy spectrum can be obtained from the excitation functions. Thus corrections to the energy spectra are calculated for these three particle energies and the corrections at other particle energies obtained by extrapolation from these values. The corrections necessary to the ^{3}He data are estimated from those calculated

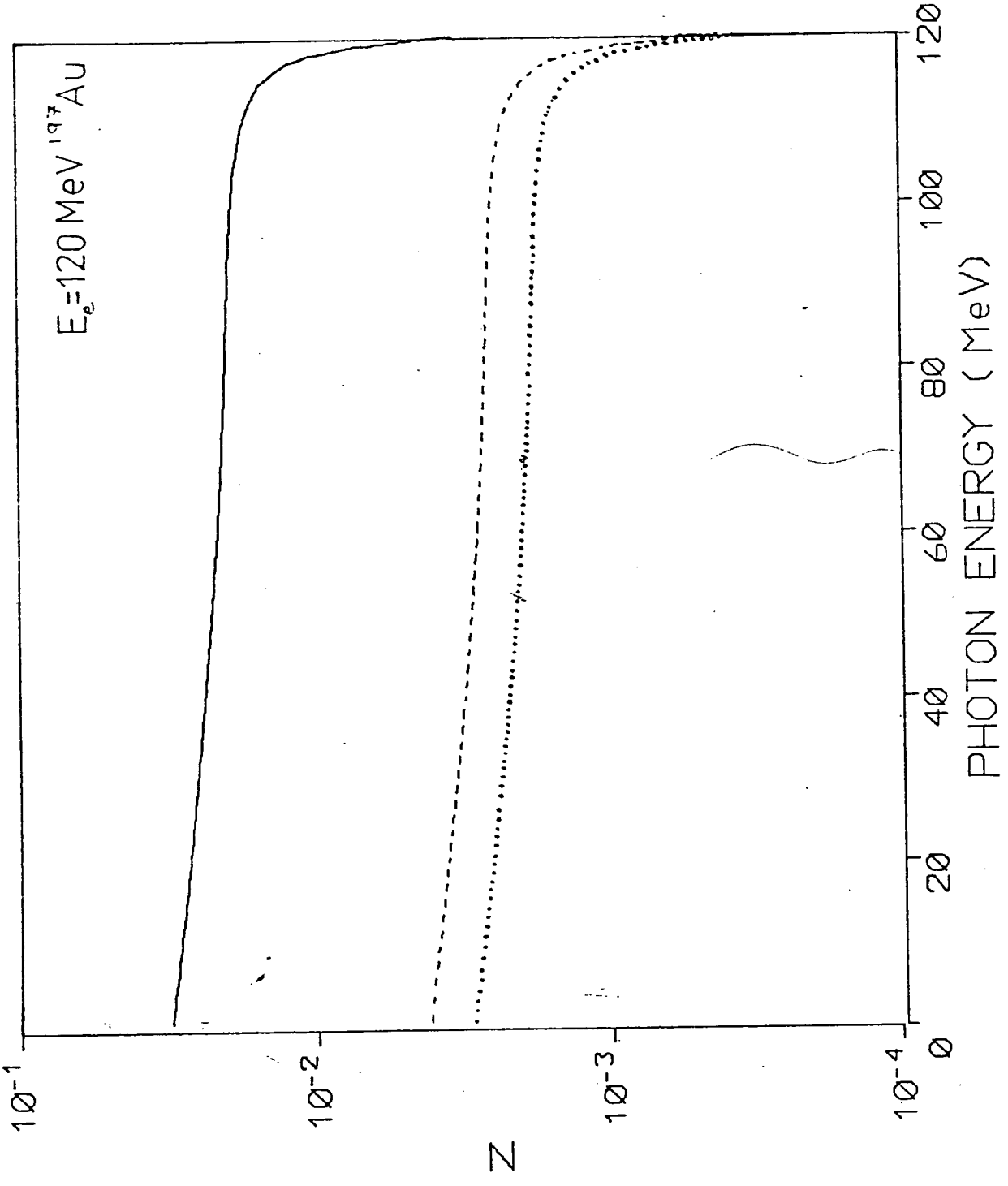

Fig. 3.4 Bremsstrahlung spectra for an electron energy of 120 MeV. The solid line is the bremsstrahlung radiation produced by a 169 mg/cm^2 Ta radiator, the dashed line shows that produced in the 29.68 mg/cm^2 ^{197}Au target and the dotted line the radiation produced by the 21.00 mg/cm^2 ^{197}Au target.

for the other complex particles. The thickness of the Au targets acting as a bremsstrahlung radiator is assumed to be $\frac{t}{2\sin 45^{o}}$ i.e. half the thickness of the target 'seen' by the electron beam.

3.4 Experimental Data

The measured data can be divided into three distinct groups, i.e. i) energy spectra, ii) angular distributions and iii) excitation functions, where the cross section for the emission of complex particles from nuclei is measured as the particle energy, angle or electron or bremsstrahlung end point energy, respectively, are varied. The data taken during the course of this thesis are summarised in Tables 3.1, 3.2 and 3.3. Energy spectra are presented in Figures 3.5 - 3.13, angular distributions in Figures 3.14 - 3.39 and excitation functions in Figures 3.40 - 3.44.

3.4.1 Energy spectra

The deuteron data has been divided by 10 and the ^{3}He data by 100 in order more easily to distinguish the spectral shapes of the energy spectra for ^{12}C (Fig. 3.5). Similarly, the triton data has been divided by 10 to separate it from the ^{3}He data for the energy spectra of complex particles emitted from ^{27}Aℓ (Fig. 3.6). Only the low energy (up to 15 MeV) part of the alpha energy spectrum was measured for ^{27}Aℓ, the rest of the spectrum, also marked on Fig. 3.6 having been previously measured by Flowers[7].

Due to the low coulomb barrier of ^{12}C not all of the low energy peaks can be observed, due to experimental limitations. The coulomb

TABLE 3.1

Target	Particle	Particle Energy E_x (MeV)	Electron Energy (MeV)	Angle to Beam (θ^o)	Electron or bremsstrahlung induced	Fig. No.
^{12}C	α	$3.0 < E_\alpha < 56.0$	120	30	Electron	3.5
^{12}C	d	$2.7 < E_D < 33.6$	120	30	Electron	3.5
^{12}C	t	$2.6 < E_T < 23.8$	120	30	Electron	3.5
^{12}C	^3He	$3.7 < E_{^3He} < 14.3$	120	30	Electron	3.5
^{27}Al	α	$3.3 < E_\alpha < 14.9$	120	30	Electron	3.6
^{27}Al	d	$2.7 < E_D < 22.6$	120	30	Electron	3.6
^{27}Al	t	$3.6 < E_T < 21.2$	120	30	Electron	3.6
^{27}Al	^3He	$4.2 < E^3He < 47.9$	120	30	Electron	3.6
^{NAT}Ni	d	$7.8 < E_D < 24.5$	120	30	Electron	3.7
^{NAT}Ni	t	$5.3 < E_T < 21.3$	120	30	Electron	3.7
^{NAT}Ni	^3He	$20.5 < E < 46.5$	120	30	Electron	3.7
^{92}Mo	d	$12.1 < E_D < 24.6$	120	30	Electron	3.8
^{92}Mo	t	$8.9 < E_T < 21.2$	120	30	Electron	3.8
^{92}Mo	^3He	$34.3 < E < 48.8$	120	30	Electron	3.8
^{94}Mo	d	$12.7 < E_D < 24.6$	120	30	Electron	3.9
^{94}Mo	t	$9.0 < E_T < 21.2$	120	30	Electron	3.9
^{94}Mo	^3He	$34.9 < E < 49.0$	120	30	Electron	3.9

TABLE 3.1 (Contd.)

Target	Particle	Particle Energy E_x (MeV)	Electron Energy (MeV)	Angle to Beam (θ^o)	Electron or bremsstrahlung induced	Fig. No.
^{NAT}Sn	α	$5.6 < E_\alpha < 50.3$	120	30	Electron	3.10
^{NAT}Sn	d	$5.0 < E_D < 33.5$	120	30	Electron	3.10
^{NAT}Sn	t	$7.1 < E_T < 22.7$	120	30	Electron	3.10
^{NAT}Sn	^3He	$11.8 < E < 52.0$	120	30	Electron	3.10
^{181}Ta	α	$17.0 < E_\alpha < 63.7$	120	30	Electron	3.11
^{181}Ta	d	$11.5 < E_D < 33.5$	120	30	Electron	3.11
^{181}Ta	t	$8.0 < E_T < 22.6$	120	30	Electron	3.11
^{181}Ta	^3He	$22.1 < E < 46.5$	120	30	Electron	3.11
^{181}Ta	α	$17.3 < E_\alpha < 56.7$	120	150	Electron	3.12
^{181}Ta	d	$7.4 < E_D < 33.3$	120	150	Electron	3.12
^{181}Ta	t	$8.3 < E_T < 22.7$	120	150	Electron	3.12
^{197}Au	d	$7.7 < E_D < 27.1$	120	30	Electron	3.13
^{197}Au	t	$8.1 < E_T < 20.7$	120	30	Electron	3.13
^{197}Au	^3He	$19.8 < E < 40.9$	120	30	Electron	3.13

TABLE 3.2 Angular distributions

Target Nucleus	Particle	Particle Energy (MeV)	Electron Energy (MeV)	θ	Electron/ Photon Induced	Fig.
^{12}C	α	5.6	120	$30 < \theta < 150^{o}$	Electron	3.14
^{12}C	α	8.0	120	"	"	3.14
^{12}C	α	15.0	120	"	"	3.14
^{12}C	α	31.9	120	"	"	3.14
^{12}C	α	50.7	120	"	"	3.14
^{12}C	d	2.7	120	"	"	3.15
^{12}C	d	4.0	120	"	"	3.15
^{12}C	d	7.5	120	"	"	3.15
^{12}C	d	15.5	120	"	"	3.15
^{12}C	d	24.0	120	"	"	3.15
^{12}C	t	2.5	120	"	"	3.16
^{12}C	t	5.0	120	"	"	3.16
^{12}C	t	10.7	120	"	"	3.16
^{12}C	t	16.5	120	"	"	3.16
^{12}C	^{3}He	7.2	120	"	"	3.17
^{12}C	^{3}He	10.7	120	"	"	3.17
^{12}C	^{3}He	20.0	120	"	"	3.17
^{12}C	^{3}He	41.6	120	"	"	3.17
^{27}Al	α	4.9	120	"	"	3.18
^{27}Al	α	7.9	120	"	"	3.18
^{27}Al	α	14.9	120	"	"	3.18
^{27}Al	α	32.7	120	"	"	3.18
^{27}Al	α	51.8	120	"	"	3.18
^{27}Al	d	2.7	120	"	"	3.19
^{27}Al	d	3.8	120	"	"	3.19
^{27}Al	d	7.6	120	"	"	3.19
^{27}Al	d	16.1	120	"	"	3.19
^{27}Al	d	23.0	120	"	"	3.19
^{27}Al	t	5.0	120	"	"	3.20
^{27}Al	t	10.5	120	"	"	3.20
^{27}Al	t	17.8	120	"	"	3.20
^{27}Al	^{3}He	7.2	120	"	"	3.21
^{27}Al	^{3}He	10.2	120	"	"	3.21
^{27}Al	^{3}He	20.0	120	"	"	3.21
^{27}Al	^{3}He	41.0	120	"	"	3.21

TABLE 3.2 (Contd.)

Target Nucleus	Particle	Particle Energy (MeV)	Electron Energy (MeV)	θ	Electron/ Photon Induced	Fig.
^{NAT}Ni	d	15.3	120	$30 < \theta < 150^{o}$	Electron	3.22
^{NAT}Ni	d	24.5	120	"	"	3.22
^{NAT}Ni	t	10.5	120	"	"	3.23
^{NAT}Ni	t	17.3	120	"	"	3.23
^{NAT}Ni	^{3}He	41.5	120	"	"	3.24
^{NAT}Sn	^{3}He	20.0	120	"	"	3.24
^{NAT}Sn	α	15.0	120	"	"	3.25
^{NAT}Sn	α	31.0	120	"	"	3.25
^{NAT}Sn	α	50.3	120	"	"	3.25
^{NAT}Sn	d	7.5	120	"	"	3.26
^{NAT}Sn	d	15.1	120	"	"	3.26
^{NAT}Sn	d	24.5	120	"	"	3.26
^{NAT}Sn	t	10.5	120	"	"	3.27
^{NAT}Sn	t	16.8	120	"	"	3.27
^{197}Au	d	24.3	120	"	"	3.28
^{197}Au	t	17.0	120	"	"	3.28
^{58}Ni	α	30.3	120	$30 < \theta < 150$	Electron	3.29
^{58}Ni	α	30.3	120	$30 < \theta < 135$	Photon	3.29
^{58}Ni	α	30.3	60	$30 < \theta < 150$	Electron	3.29
^{58}Ni	α	30.3	60	"	Photon	3.29
^{58}Ni	d	15.1	120	"	Electron	3.30
^{58}Ni	d	15.1	120	$30 < \theta < 135$	Photon	3.30
^{58}Ni	d	15.1	60	$30 < \theta < 150$	Electron	3.30
^{58}Ni	d	15.1	60	"	Photon	3.30
^{58}Ni	t	10.2	120	"	Electron	3.31
^{58}Ni	t	10.2	120	$30 < \theta < 135$	Photon	3.31
^{58}Ni	t	10.2	60	$30 < \theta < 150$	Electron	3.31
^{58}Ni	t	10.2	60	"	Photon	3.31
^{58}Ni	^{3}He	40.2	120	"	Electron	3.32
^{58}Ni	^{3}He	40.2	120	$30 < \theta < 135$	Photon	3.32
^{60}Ni	α	30.4	120	$30 < \theta < 150$	Electron	3.33
^{60}Ni	α	30.4	120	"	Photon	3.33
^{60}Ni	α	30.4	60	"	Electron	3.33
^{60}Ni	α	30.4	60	"	Photon	3.33

TABLE 3.2 (Contd.)

Target Nucleus	Particle	Particle Energy (MeV)	Electron Energy (MeV)	θ	Electron/ Photon Induced	Fig.
^{60}Ni	d	15.1	120	$30 < \theta < 150$	Electron	3.34
^{60}Ni	d	15.1	120	"	Photon	3.34
^{60}Ni	d	15.1	60	"	Electron	3.34
^{60}Ni	d	15.1	60	"	Photon	3.34
^{60}Ni	t	10.3	120	"	Electron	3.35
^{60}Ni	t	10.3	120	"	Photon	3.35
^{60}Ni	t	10.3	60	"	Electron	3.35
^{60}Ni	t	10.3	60	"	Photon	3.35
^{60}Ni	^{3}He	40.3	120	"	Electron	3.36
^{60}Ni	^{3}He	40.3	120	"	Photon	3.36
^{197}Au	α	31.3	120	"	Electron	3.37
^{197}Au	α	31.3	120	"	Photon	3.37
^{197}Au	α	31.3	60	"	Electron	3.37
^{197}Au	α	31.3	60	"	Photon	3.37
^{197}Au	d	15.4	120	"	Electron	3.38
^{197}Au	d	15.4	120	"	Photon	3.38
^{197}Au	d	15.4	60	"	Electron	3.38
^{197}Au	d	15.4	60	"	Photon	3.38
^{197}Au	t	10.4	120	"	Electron	3.39
^{197}Au	t	10.4	120	"	Photon	3.39
^{197}Au	t	10.4	60	"	Electron	3.39
^{197}Au	t	10.4	60	"	Photon	3.39

TABLE 3.3 Excitation Functions

Target Nucleus	Particle	Particle Energy (MeV)	Electron Energy (MeV)	θ	Electron or Photon Induced	Fig.
^{197}Au	α	26.3	$40 < E_e < 130$	30^o	Electron	3.40
^{197}Au	α	26.3	"		Photon	3.40
^{197}Au	α	36.1	$50 < E_e < 130$	"	Electron	3.40
^{197}Au	α	36.1	"	"	Photon	3.40
^{197}Au	α	46.0	$60 < E_e < 130$	"	Electron	3.40
^{197}Au	α	46.0	"	"	Photon	3.40
^{197}Au	d	12.8	$40 < E_e < 130$	"	Electron	3.41
^{197}Au	d	12.8	"	"	"	3.41
^{197}Au	d	17.8	$60 < E_e < 130$	"	"	3.41
^{197}Au	d	17.8	$40 < E_e < 130$	"	Photon	3.42
^{197}Au	d	22.7	"	"	"	3.42
^{197}Au	d	22.7	$60 < E_e < 130$	"	"	3.42
^{197}Au	t	8.8	$40 < E_e < 130$	"	Electron	3.43
^{197}Au	t	8.8	"	"	"	3.43
^{197}Au	t	12.1	$60 < E_e < 130$	"	"	3.43
^{197}Au	t	12.1	$40 < E_e < 130$	"	Photon	3.44
^{197}Au	t	15.4	"	"	"	3.44
^{197}Au	t	15.4	$60 < E_e < 130$	"	"	3.44

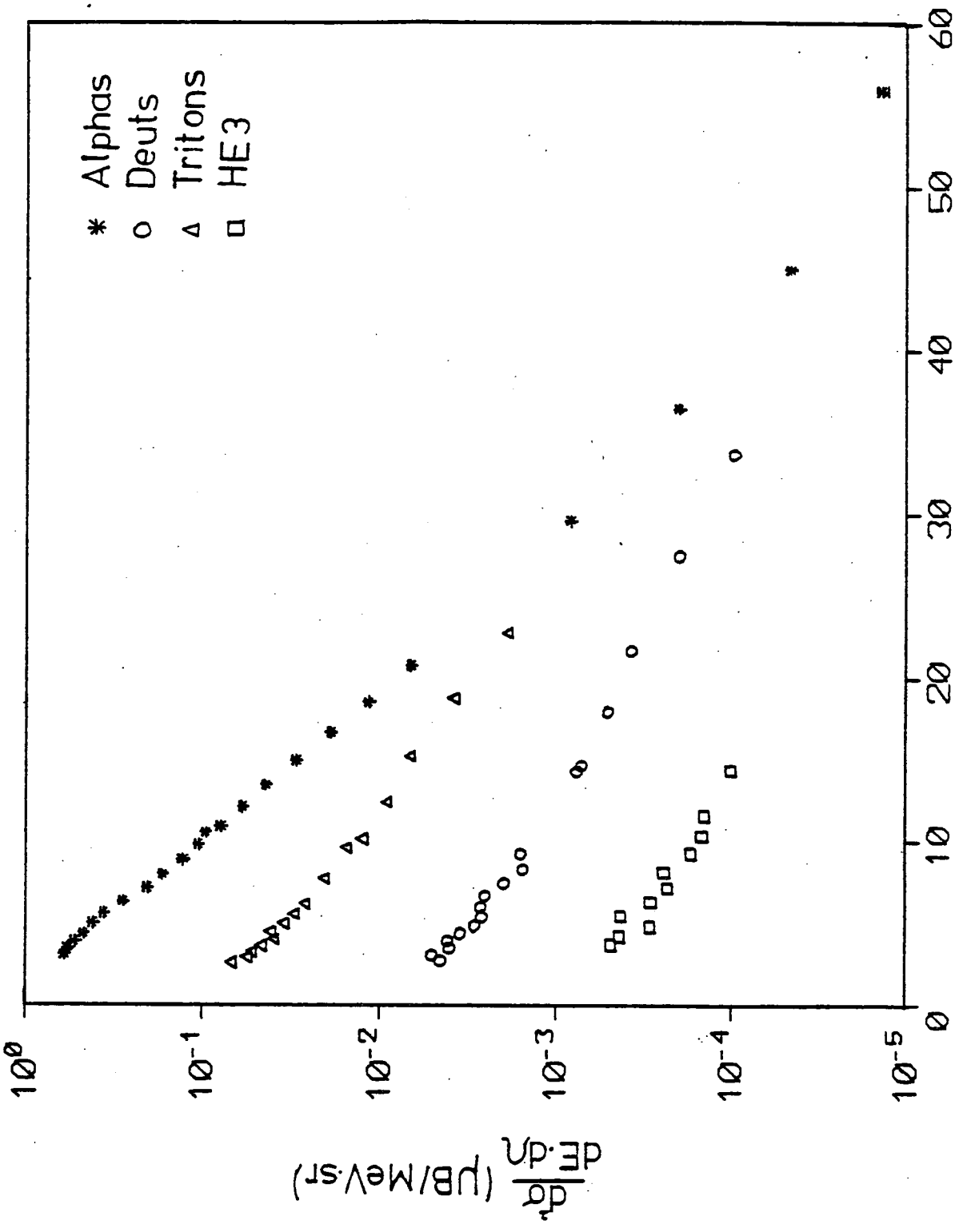

Fig. 3.5 Energy spectra for ^{12}C at E_e = 120 MeV, $\theta = 30^{o}$. Deuteron data has been divided by 10 and ^{3}He data by 100.

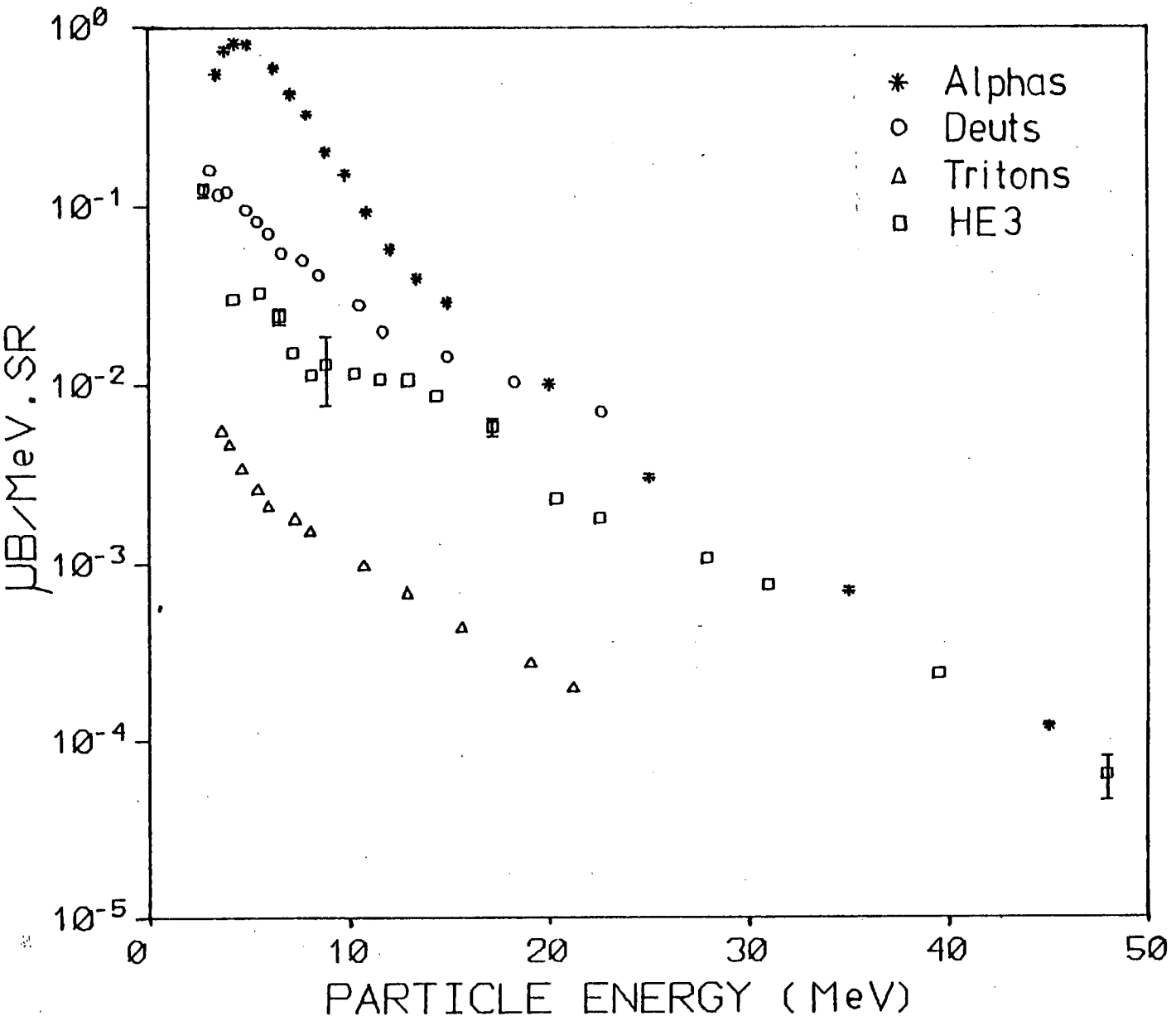

Fig. 3.6 Energy spectra for ^{27}Al at E_e = 120 MeV, $\theta = 30^{o}$. Triton data has been divided by 10.

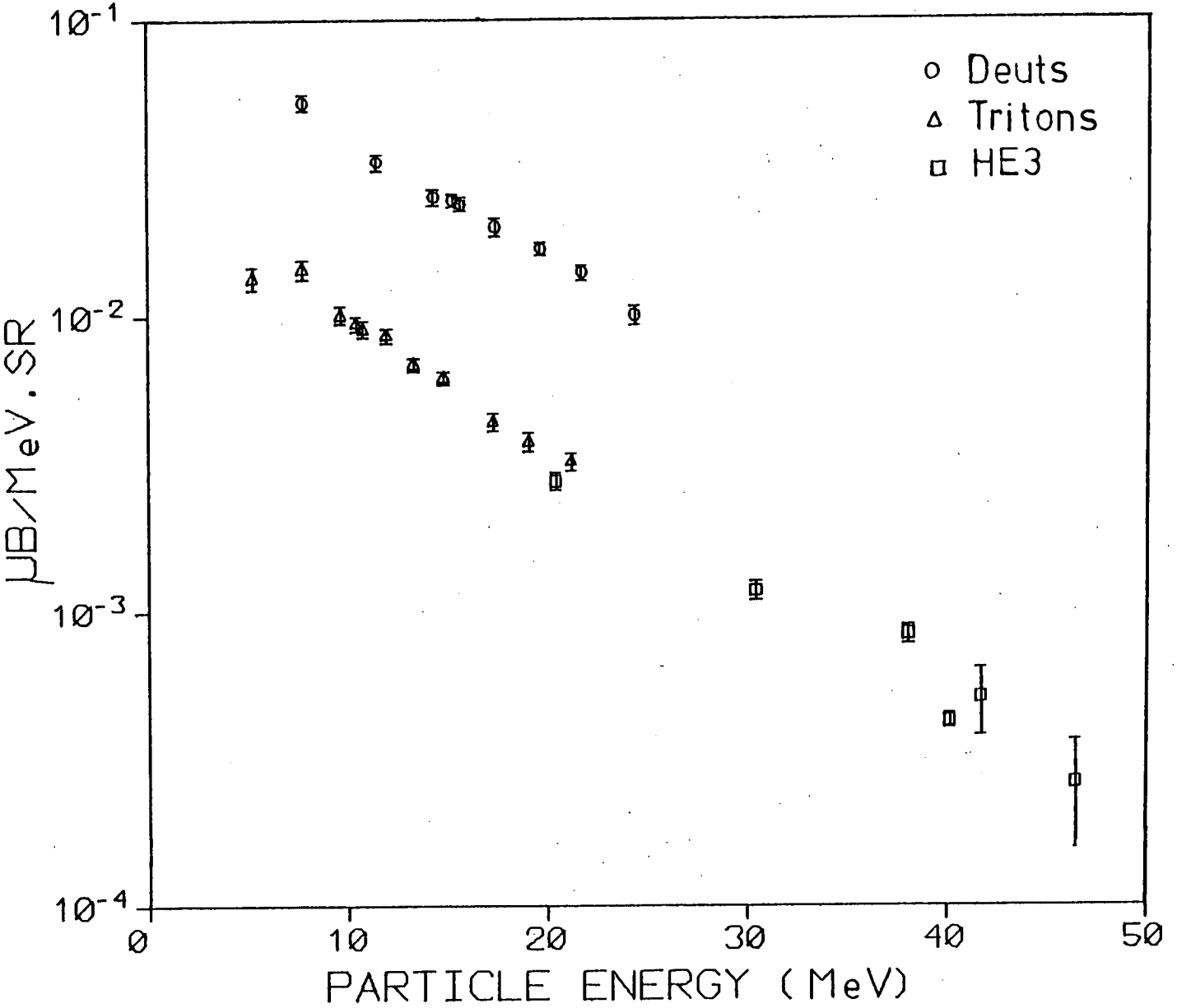

Fig. 3.7 Energy spectra for $^{NAT}_{Ni}$ at E_e = 120 MeV, θ = 30°.

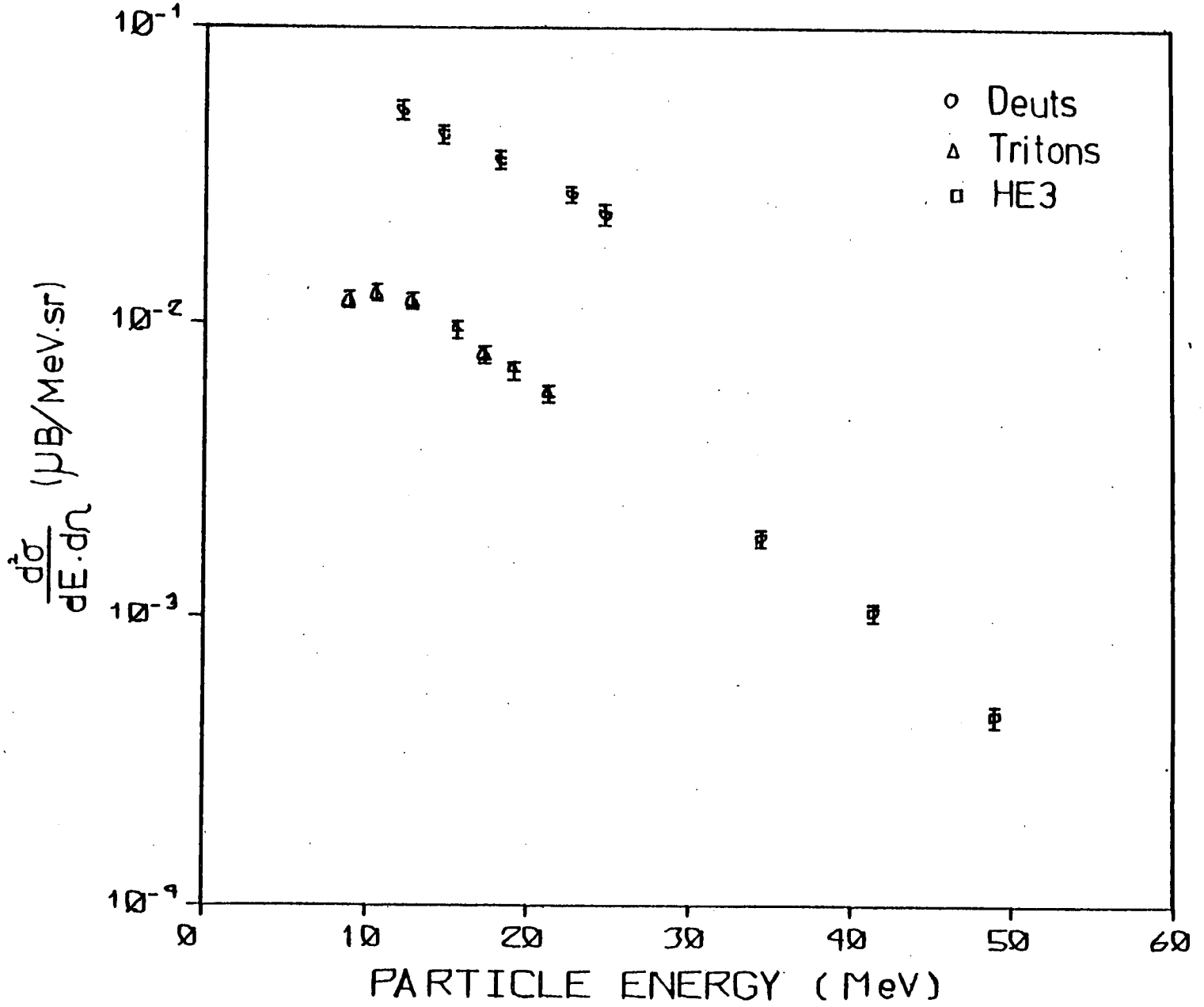

Fig. 3.8 Energy spectra for ^{92}Mo at E_e = 120 MeV, θ = 30°.

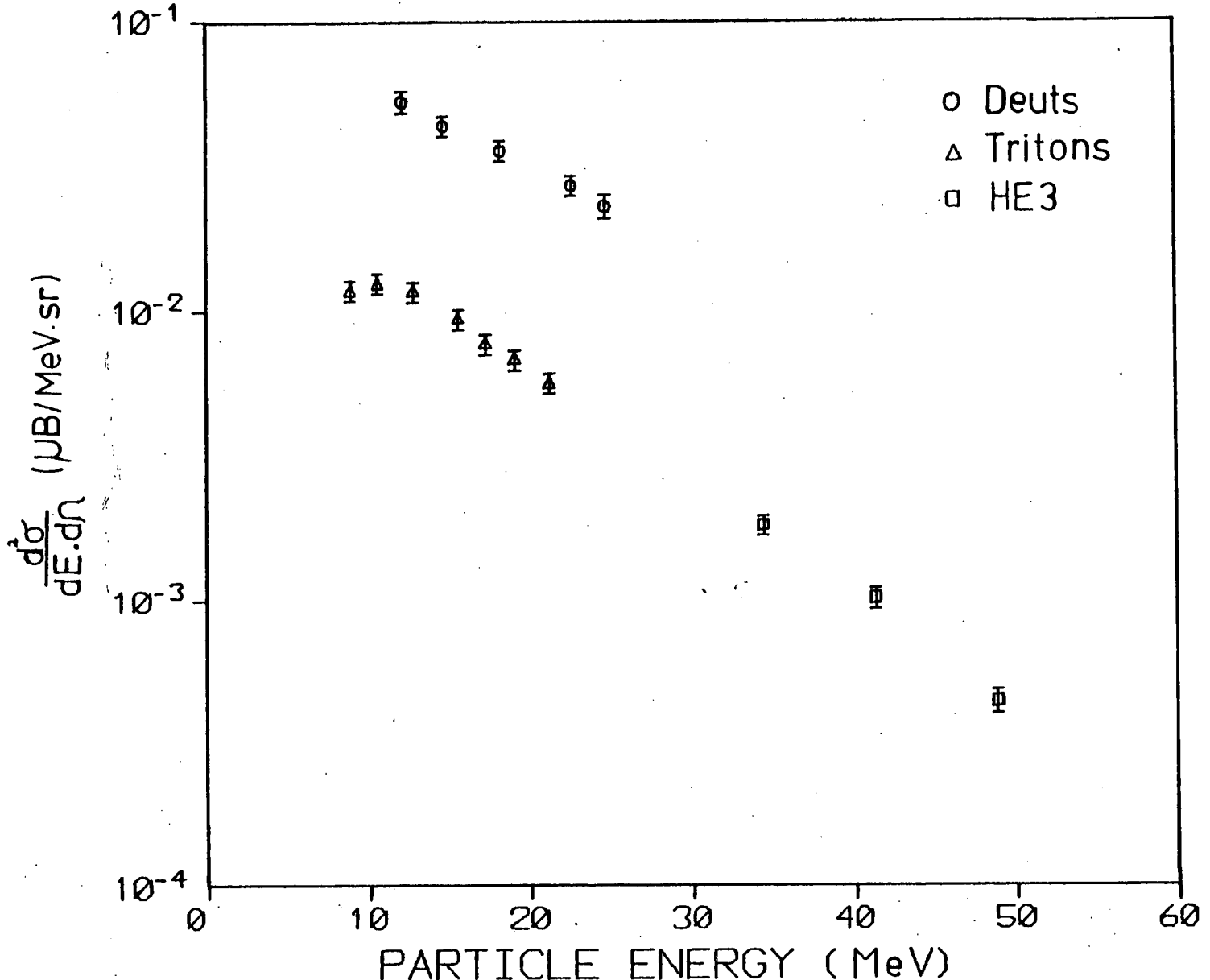

Fig. 3.9 Energy spectra for ^{94}Mo at E_e = 120 MeV, θ = 30°.

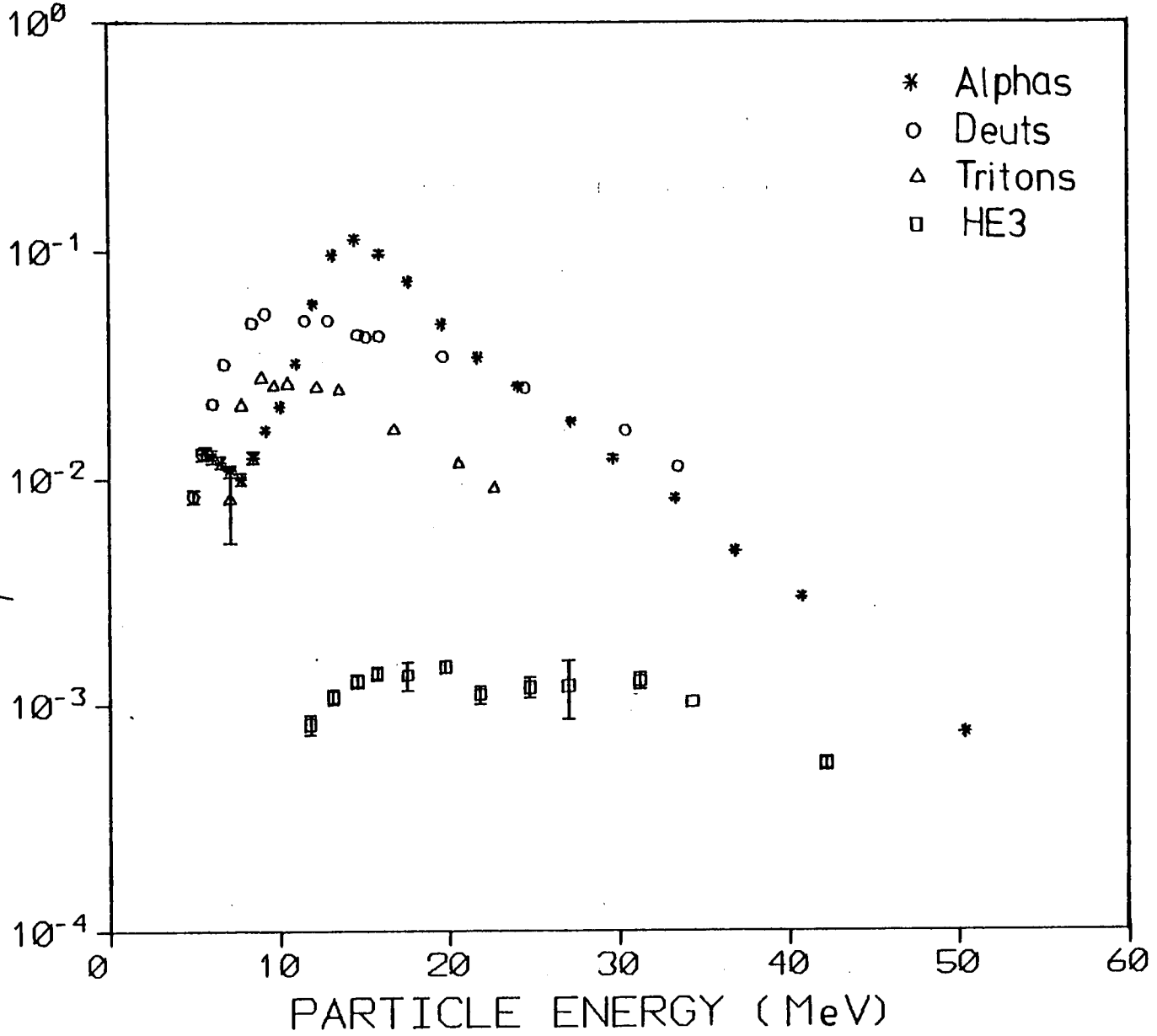

Fig. 3.10 Energy spectra for ^{NAT}Sn at E_e = 120 MeV, θ = 30°.

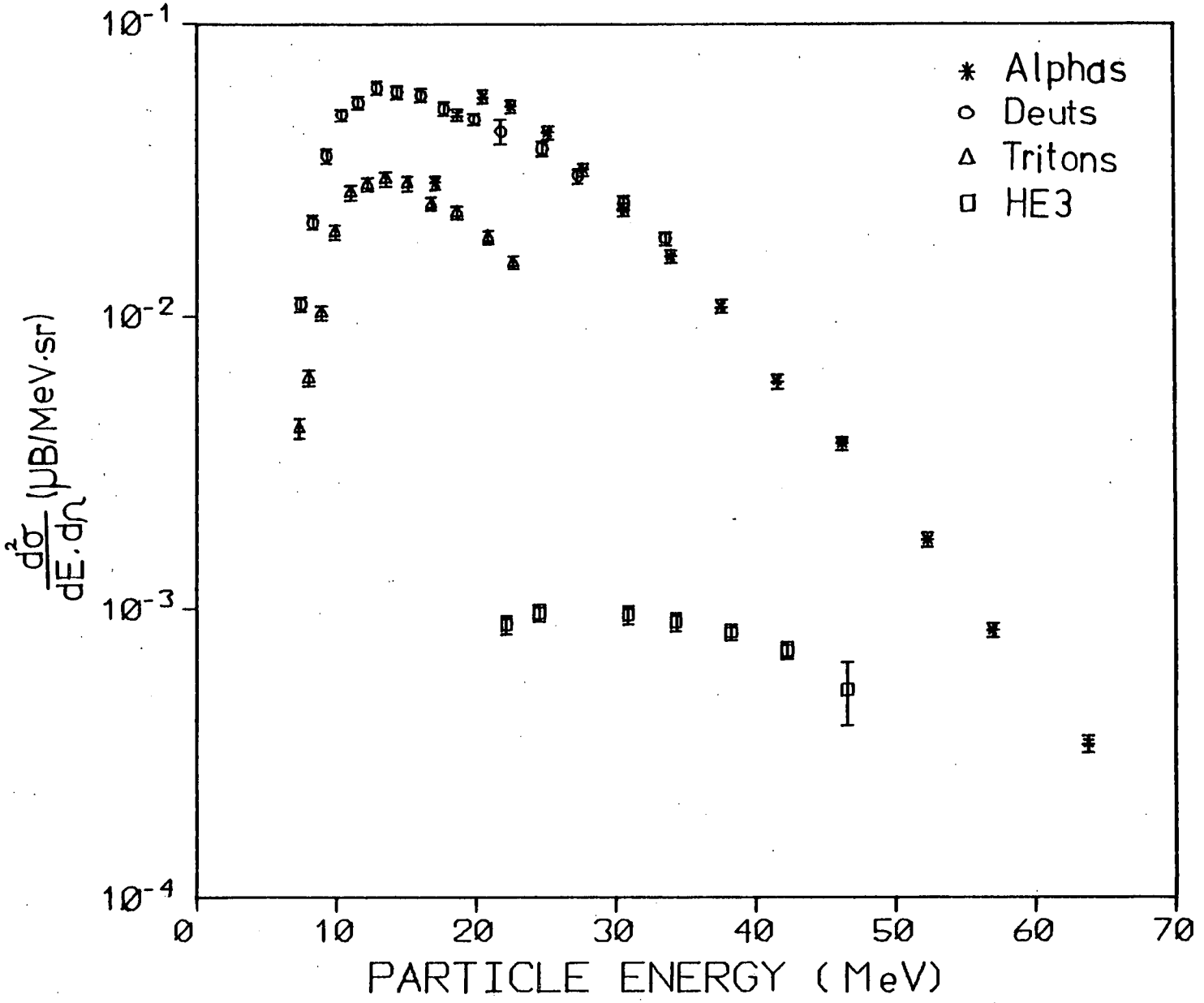

Fig. 3.11 Energy spectra for ^{181}Ta at E_e = 120 MeV, θ = 30°.

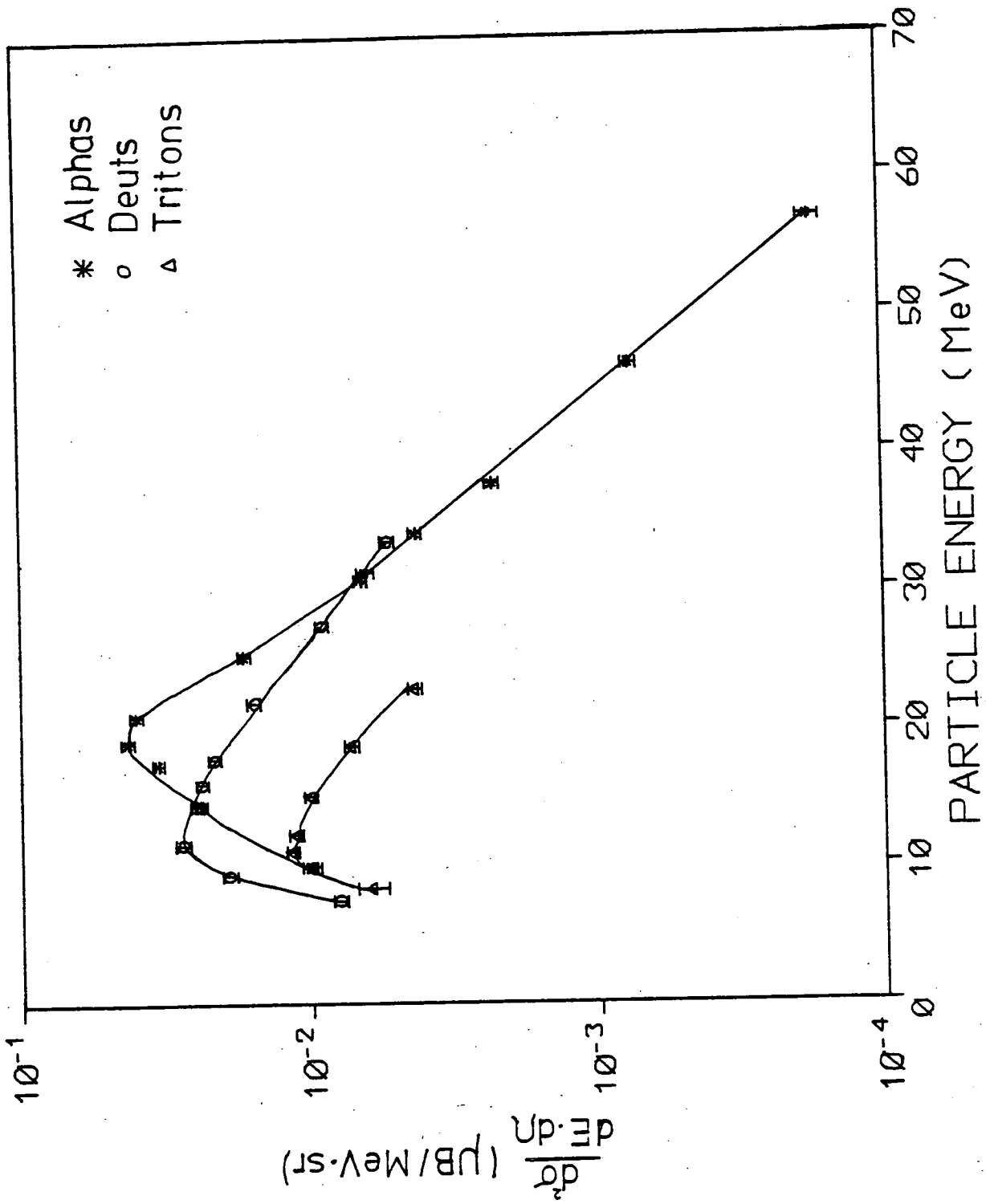

Fig. 3.12 Energy spectra for ^{181}Ta at E_e = 120 MeV, $\theta = 150^{o}$. Lines drawn to guide the eye.

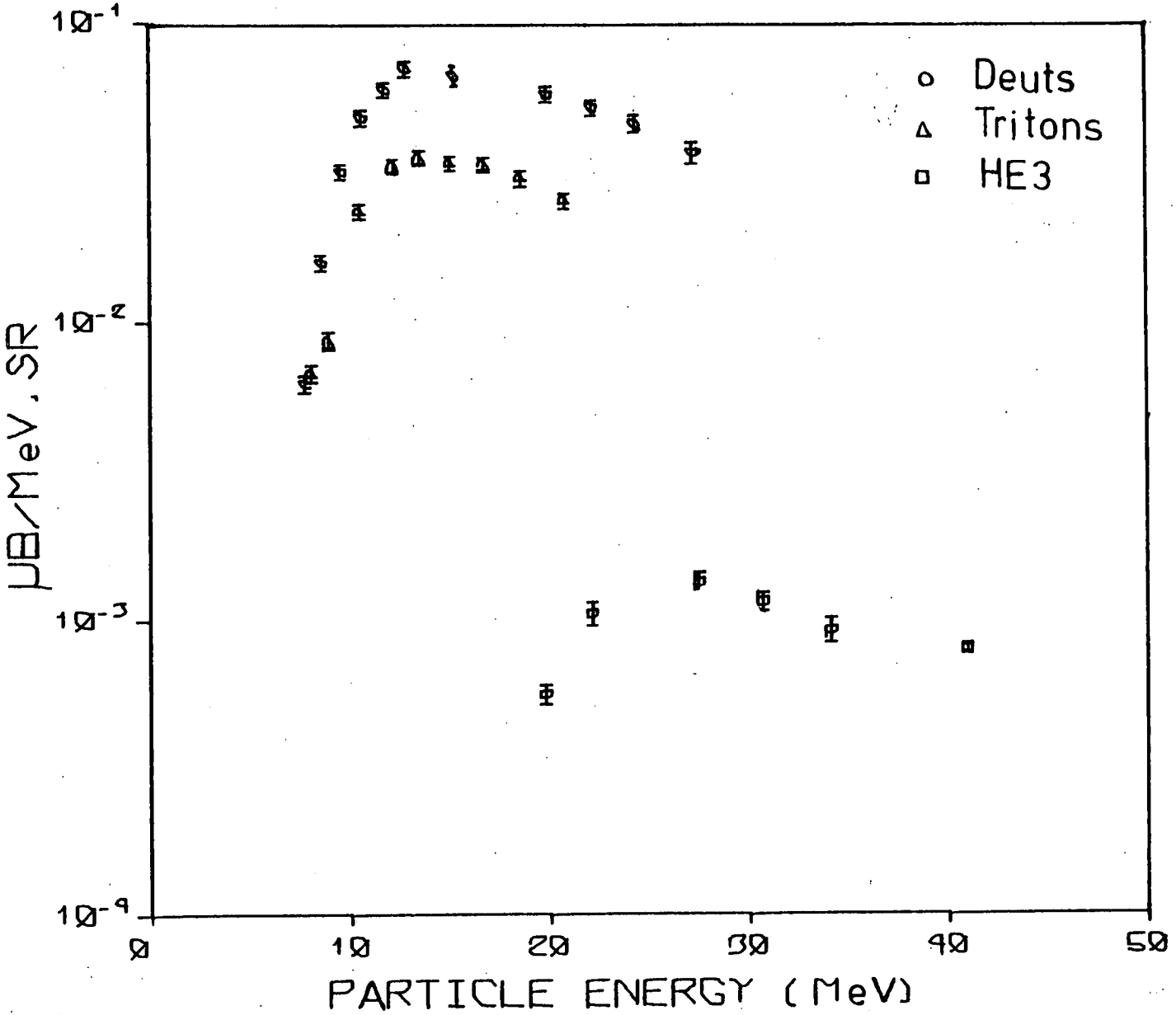

Fig. 3.13 Energy spectra for ^{197}Au at E_e = 120 MeV, θ = 30°.

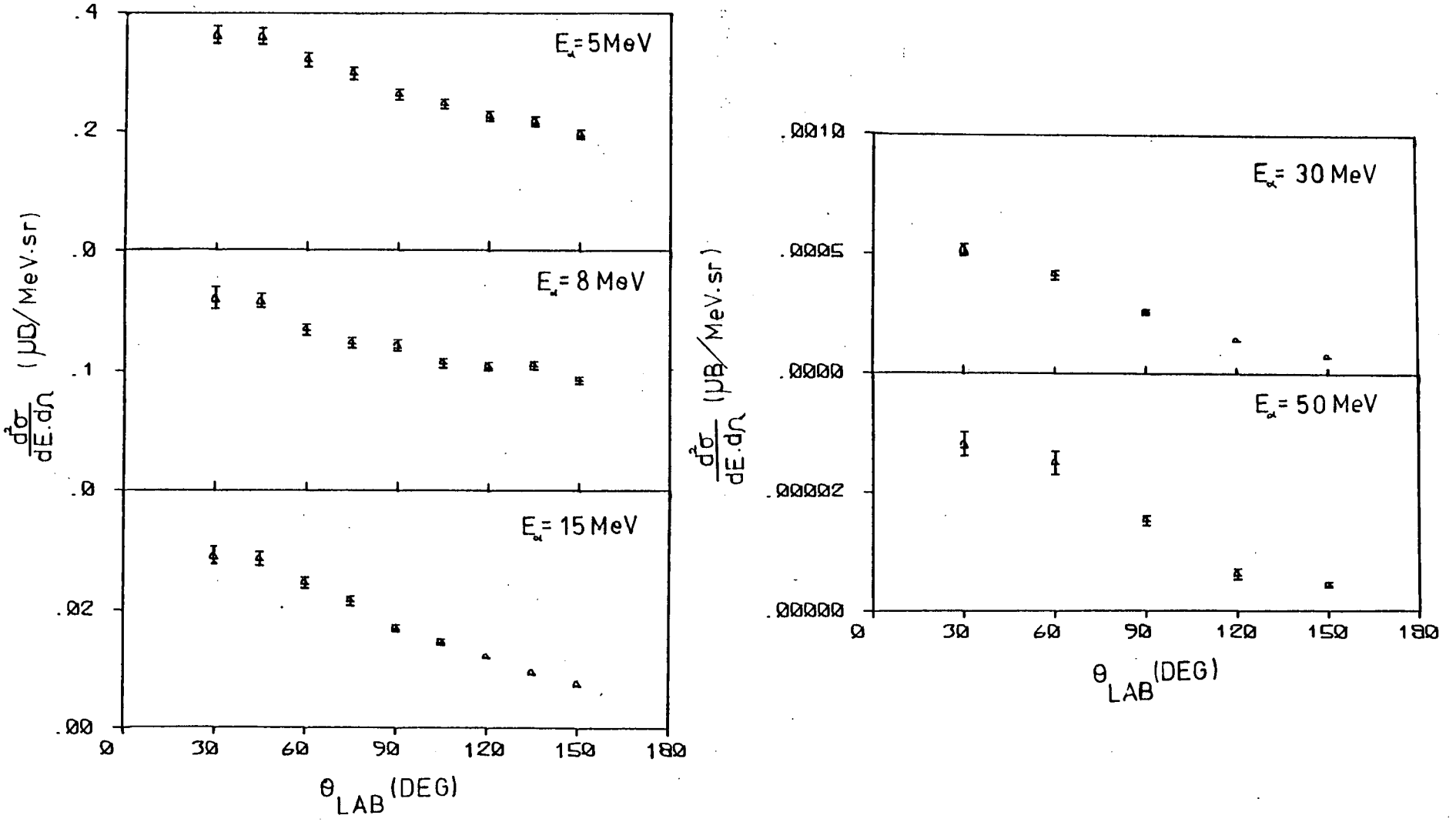

Fig. 3.14 Angular distributions for alphas from ^{12}C at E_e = 120 MeV.

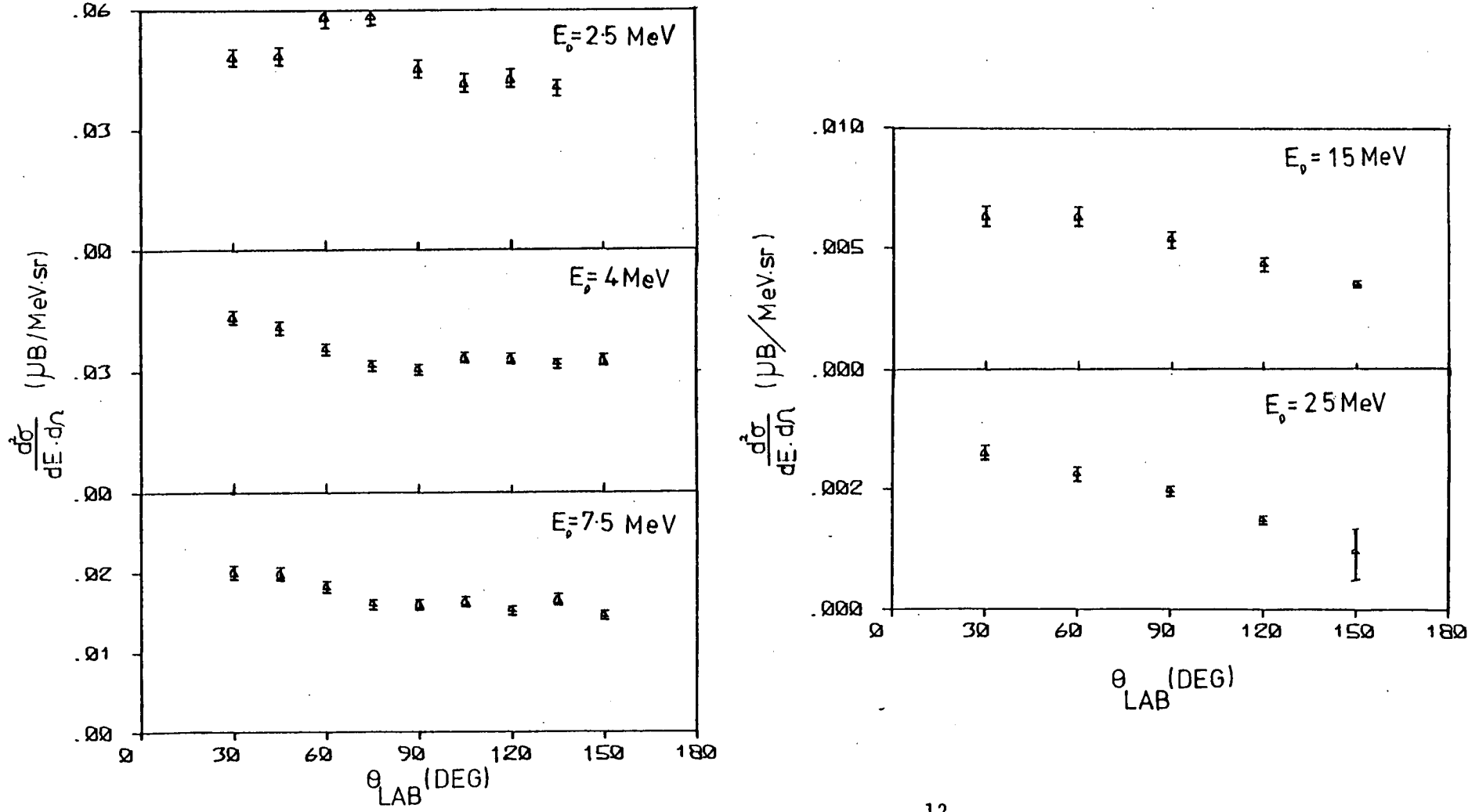

Fig. 3.15 Angular distributions for deuterons from ^{12}C at E_e = 120 MeV.

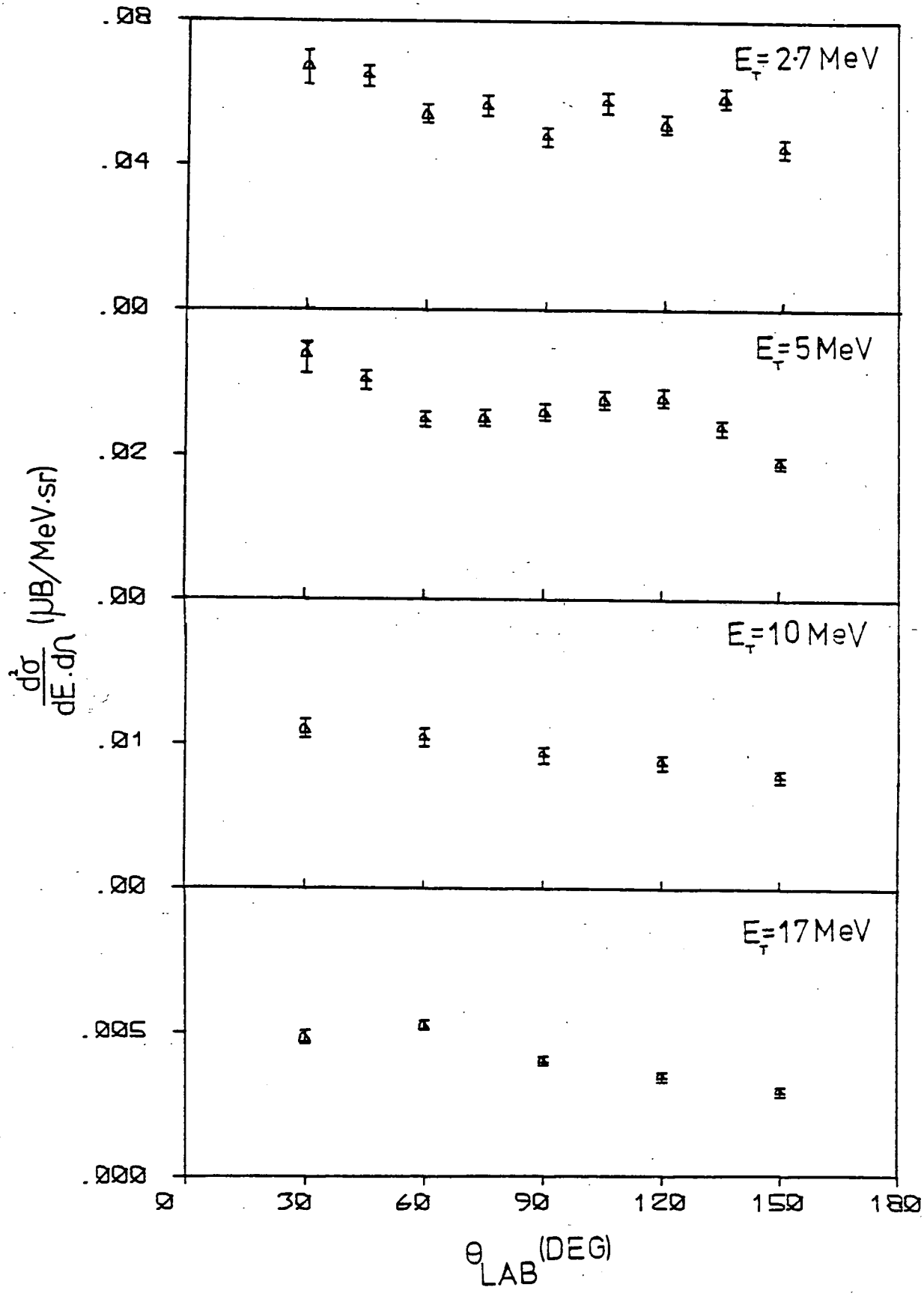

Fig. 3.16 Angular distributions for tritons from ^{12}C at E_e = 120 MeV.

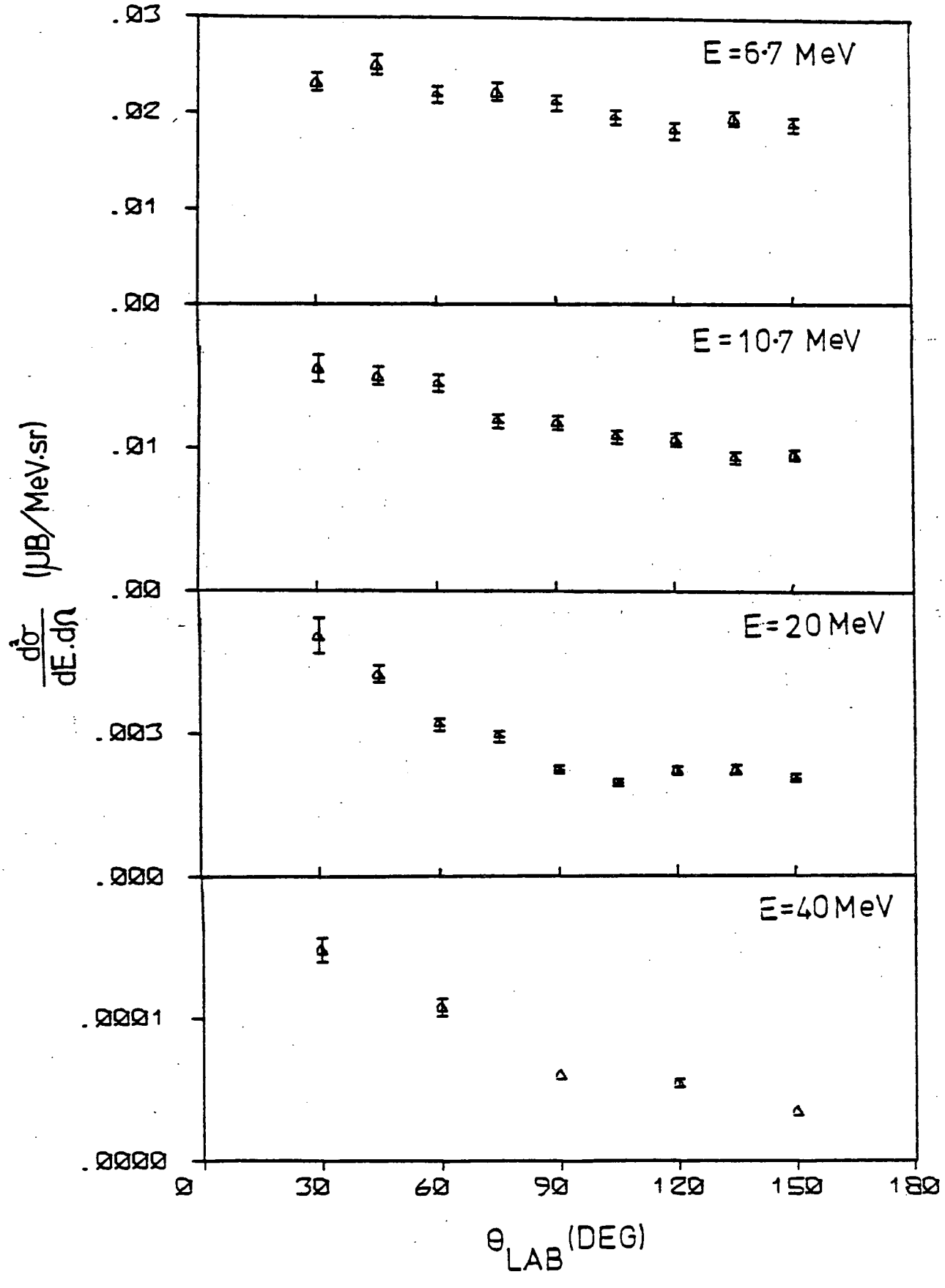

Fig. 3.17 Angular distributions for ^{3}He's from ^{12}C at E_e = 120 MeV.

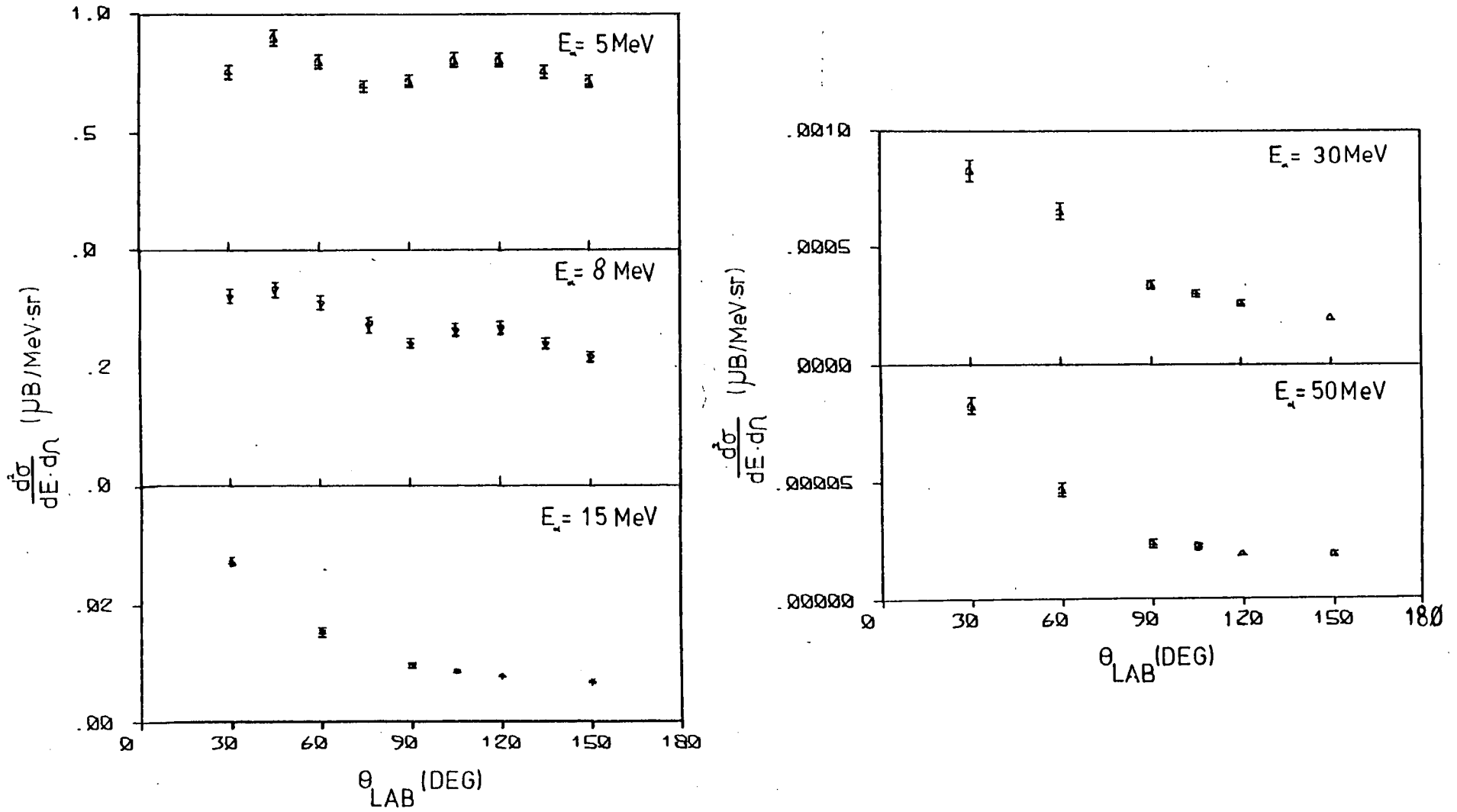

Fig. 3.18 Angular distributions for alphas from ^{27}Aℓ at E_e = 120 MeV.

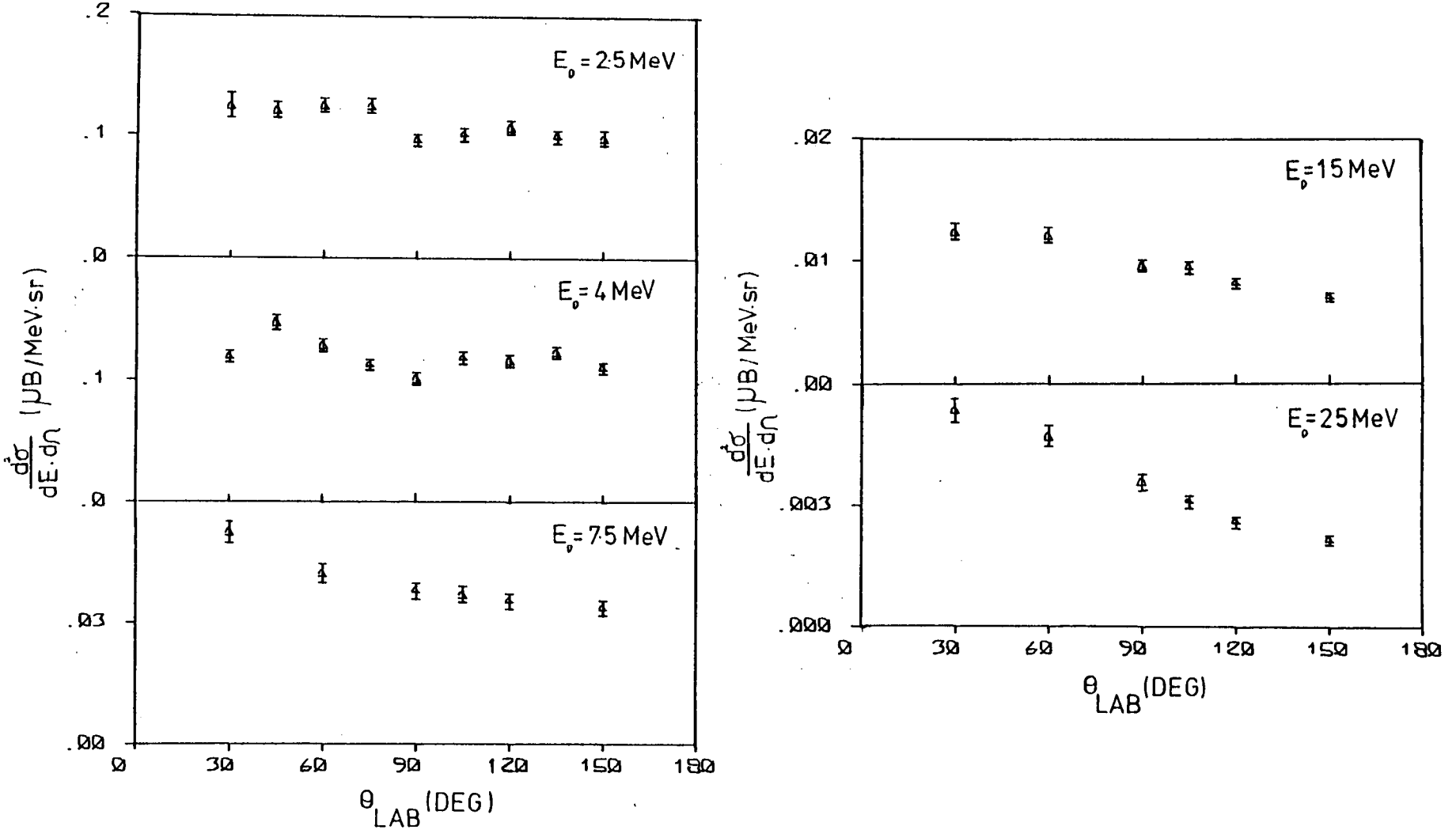

Fig. 3.19 Angular distributions for deuterons from ^{27}Al at E_e = 120 MeV.

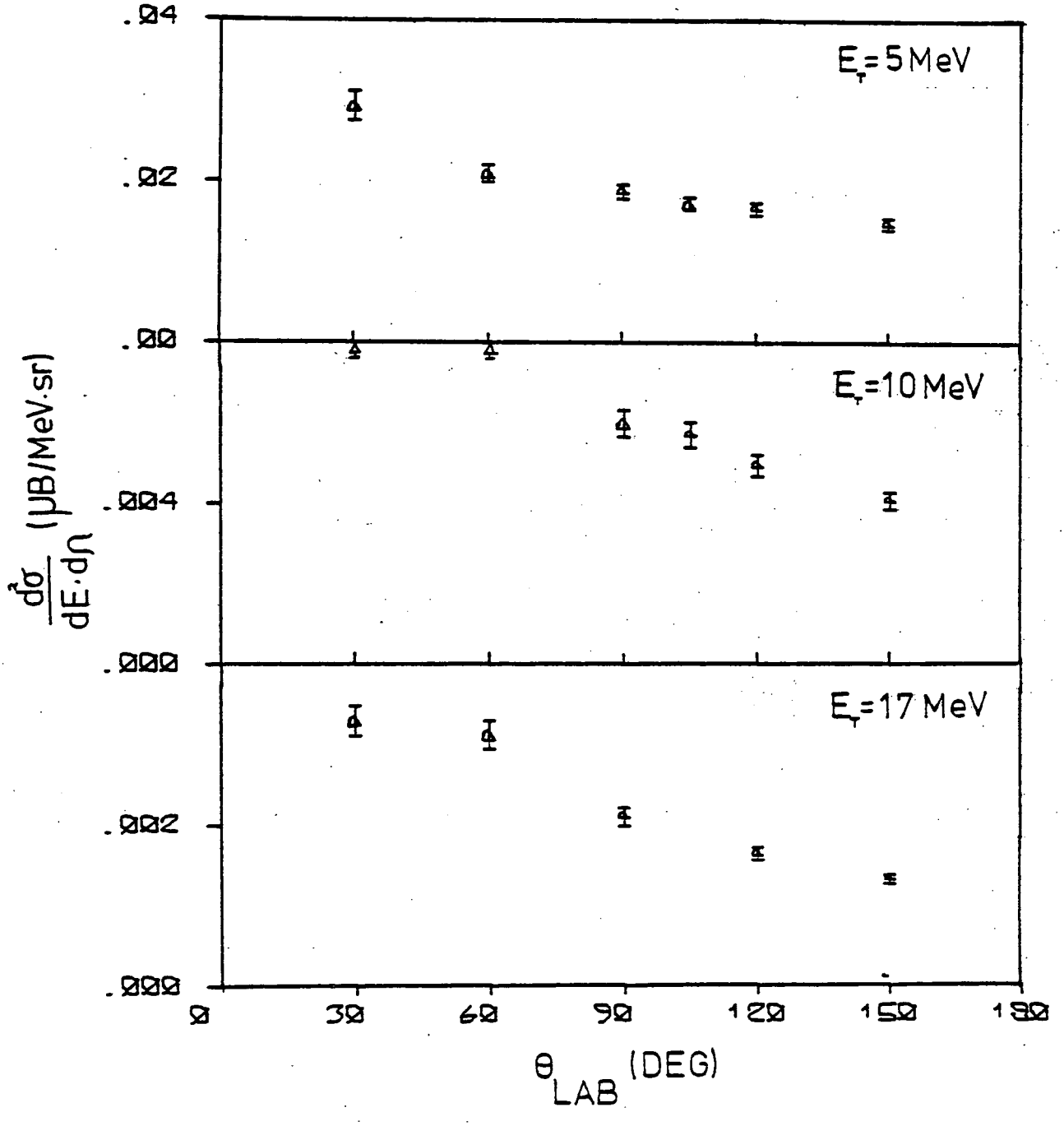

Fig. 3.20 Angular distributions for tritons from ^{27}Aℓ at E_e = 120 MeV.

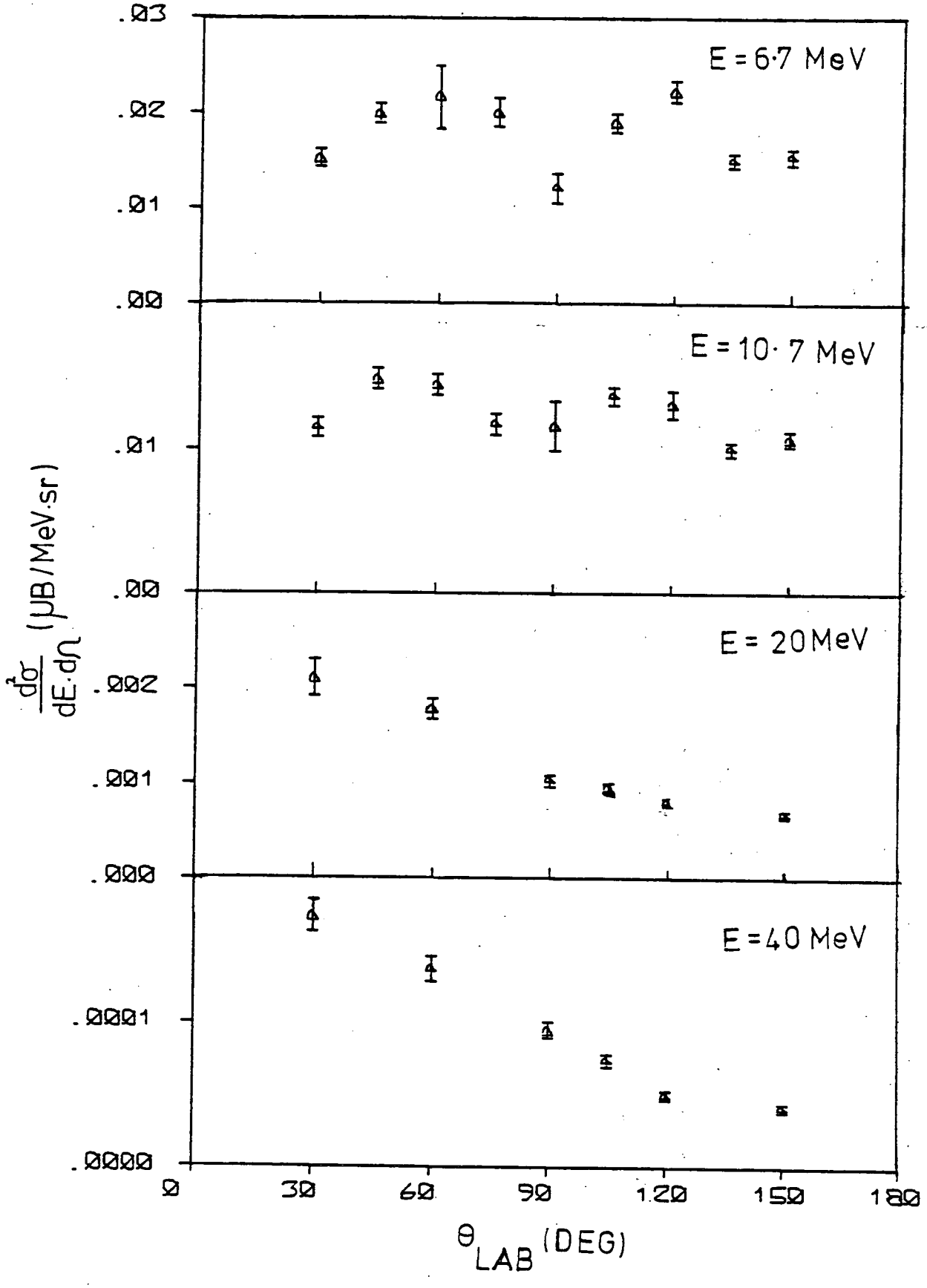

Fig. 3.21 Angular distributions for ^{3}He's from ^{27}Al at E_e = 120 MeV.

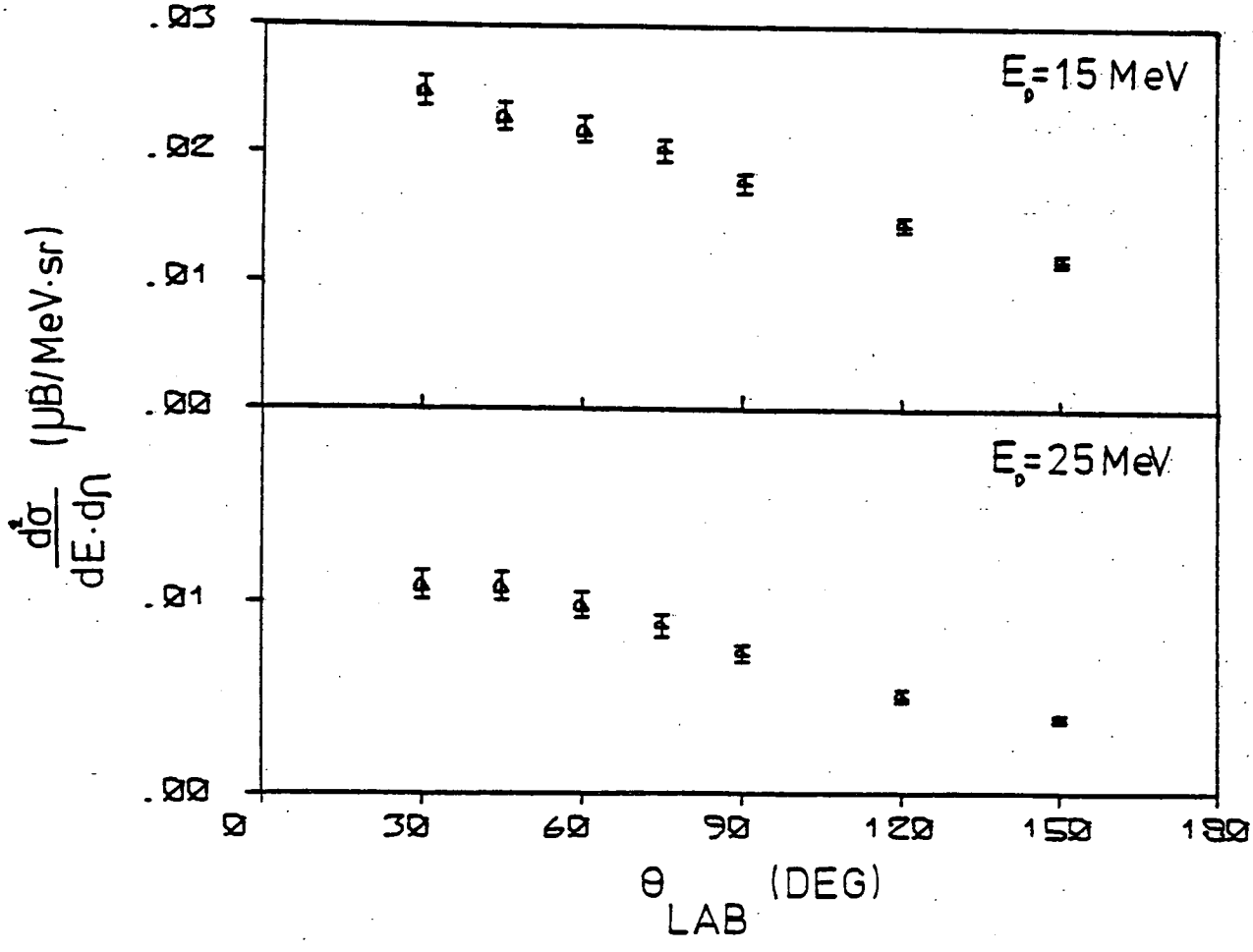

Fig. 3.22 Angular distributions for deuterons from ^{NAT}Ni at E_e = 120 MeV.

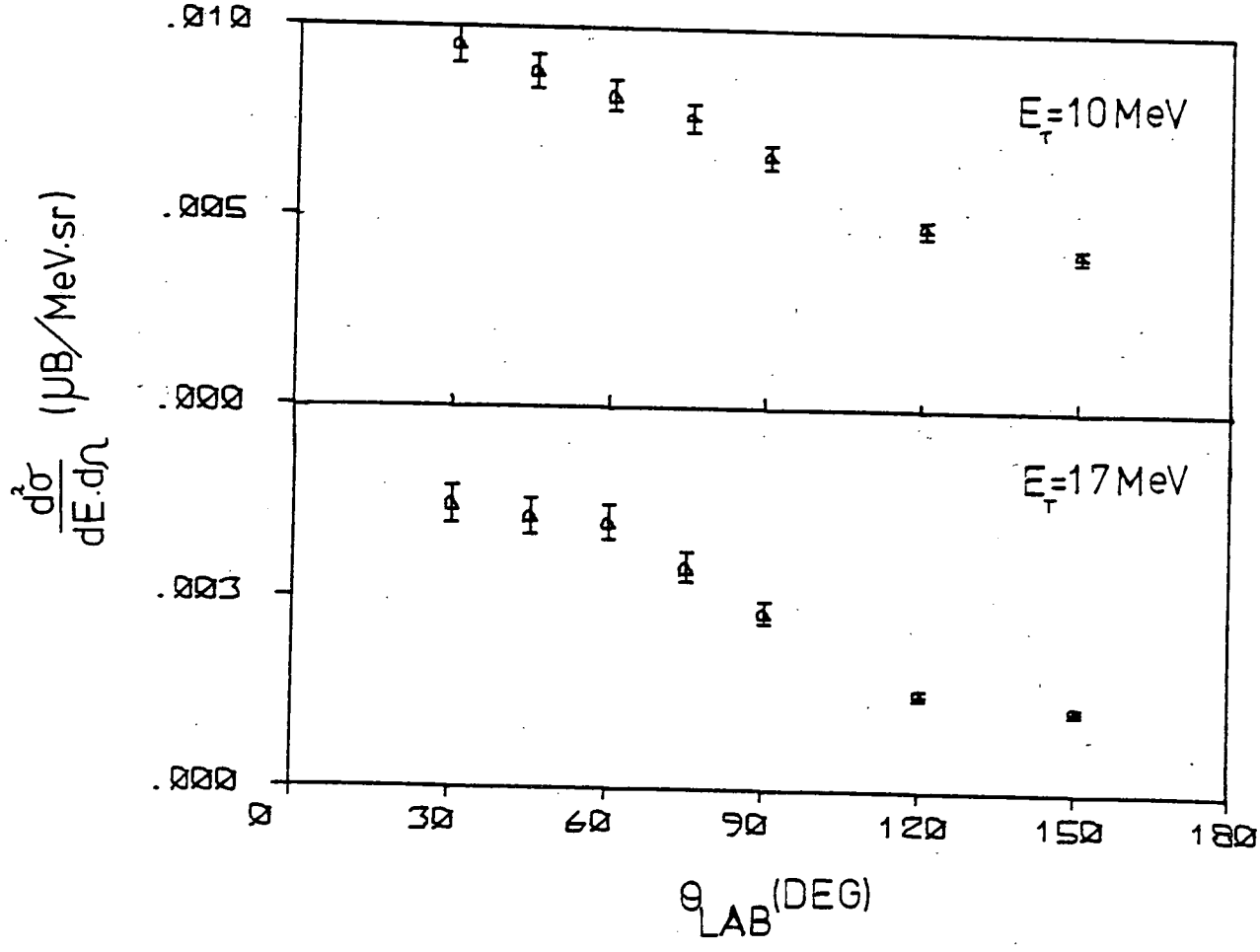

Fig. 3.23 Angular distributions for tritons from ^{NAT}Ni at E_e = 120 MeV.

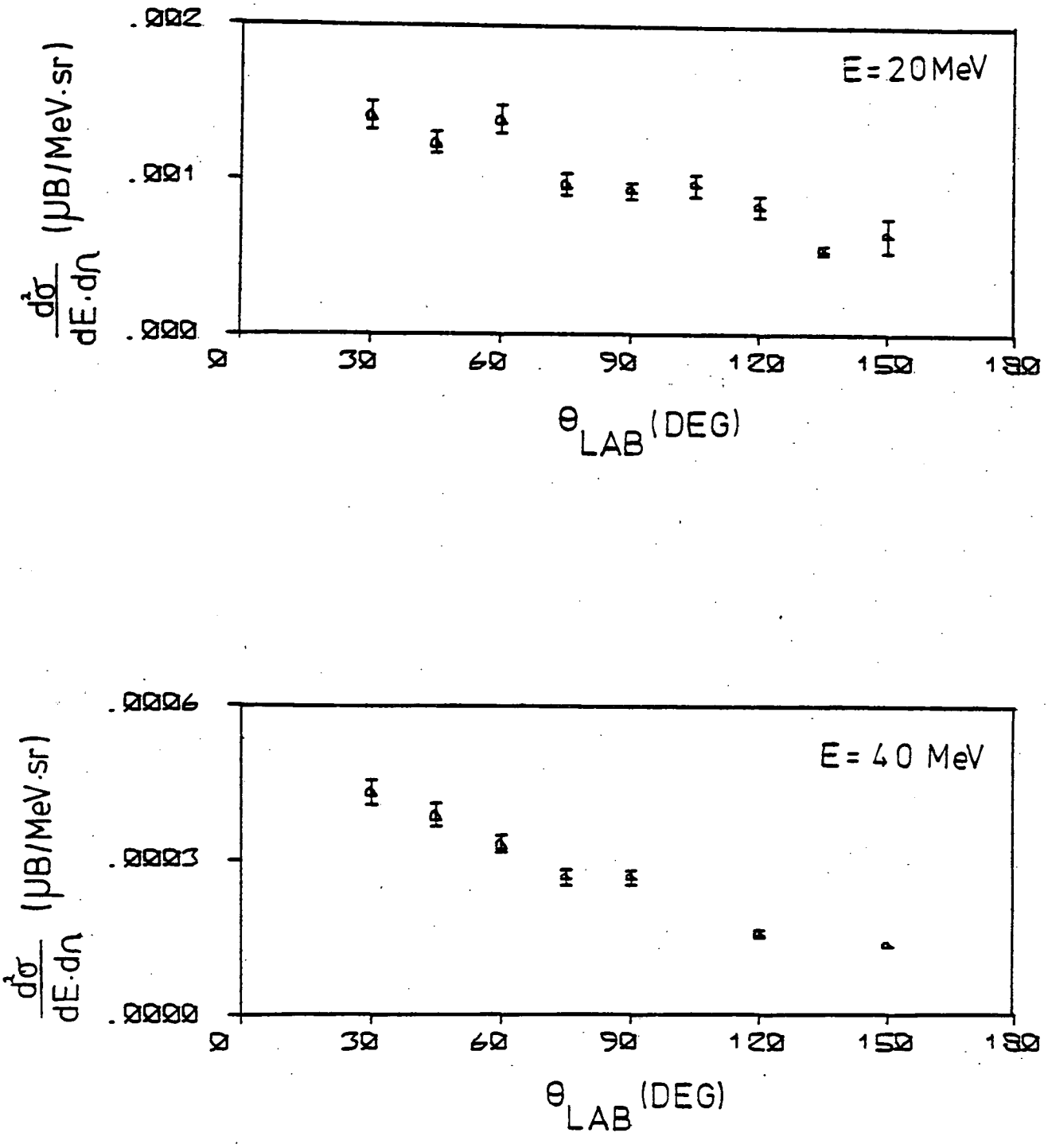

Fig. 3.24 Angular distributions for ^{3}He's from ^{NAT}Sn and ^{NAT}Ni at E_e = 120 MeV.

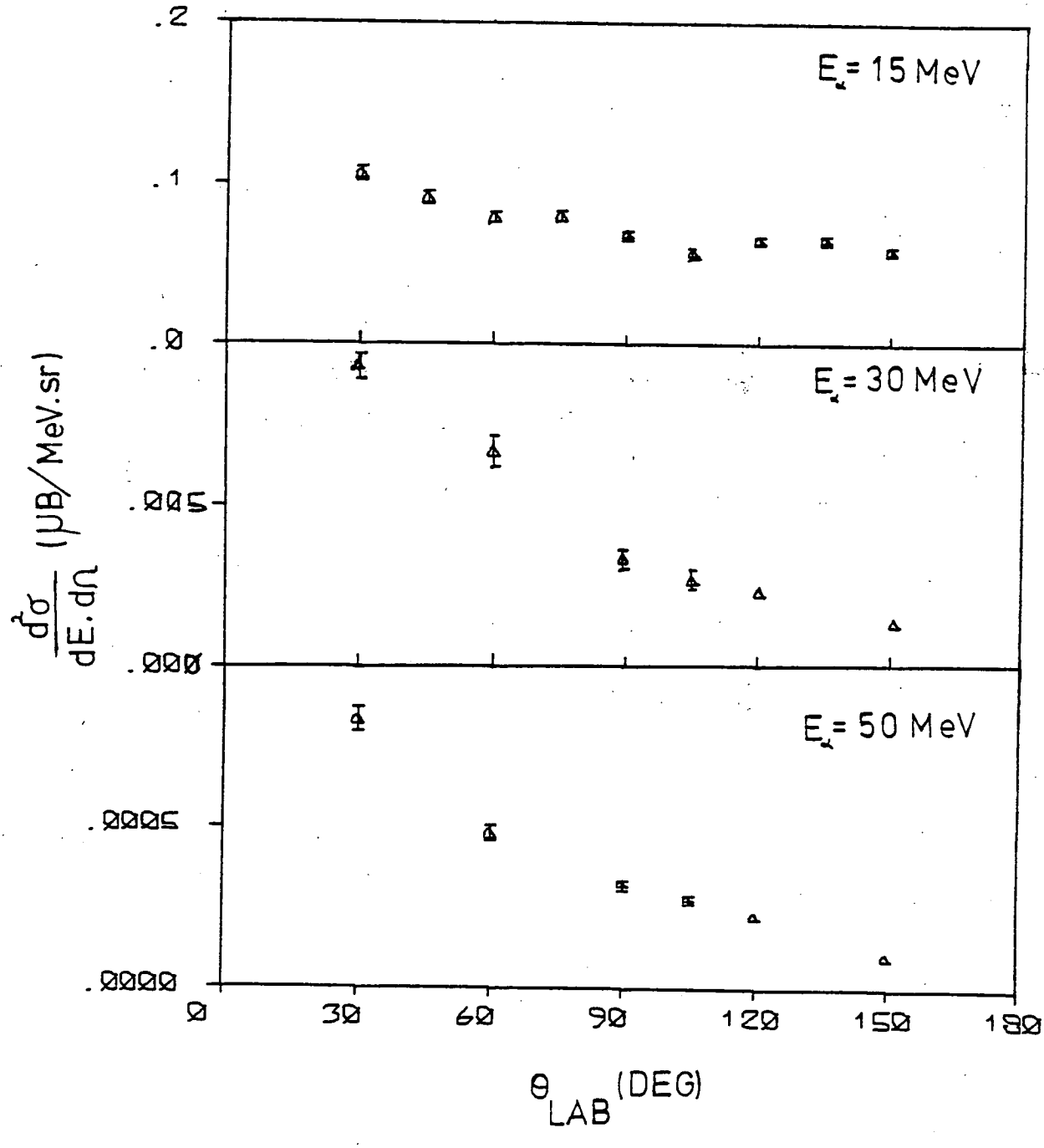

Fig. 3.25 Angular distributions for alphas from ^{NAT}Sn at E_e = 120 MeV.

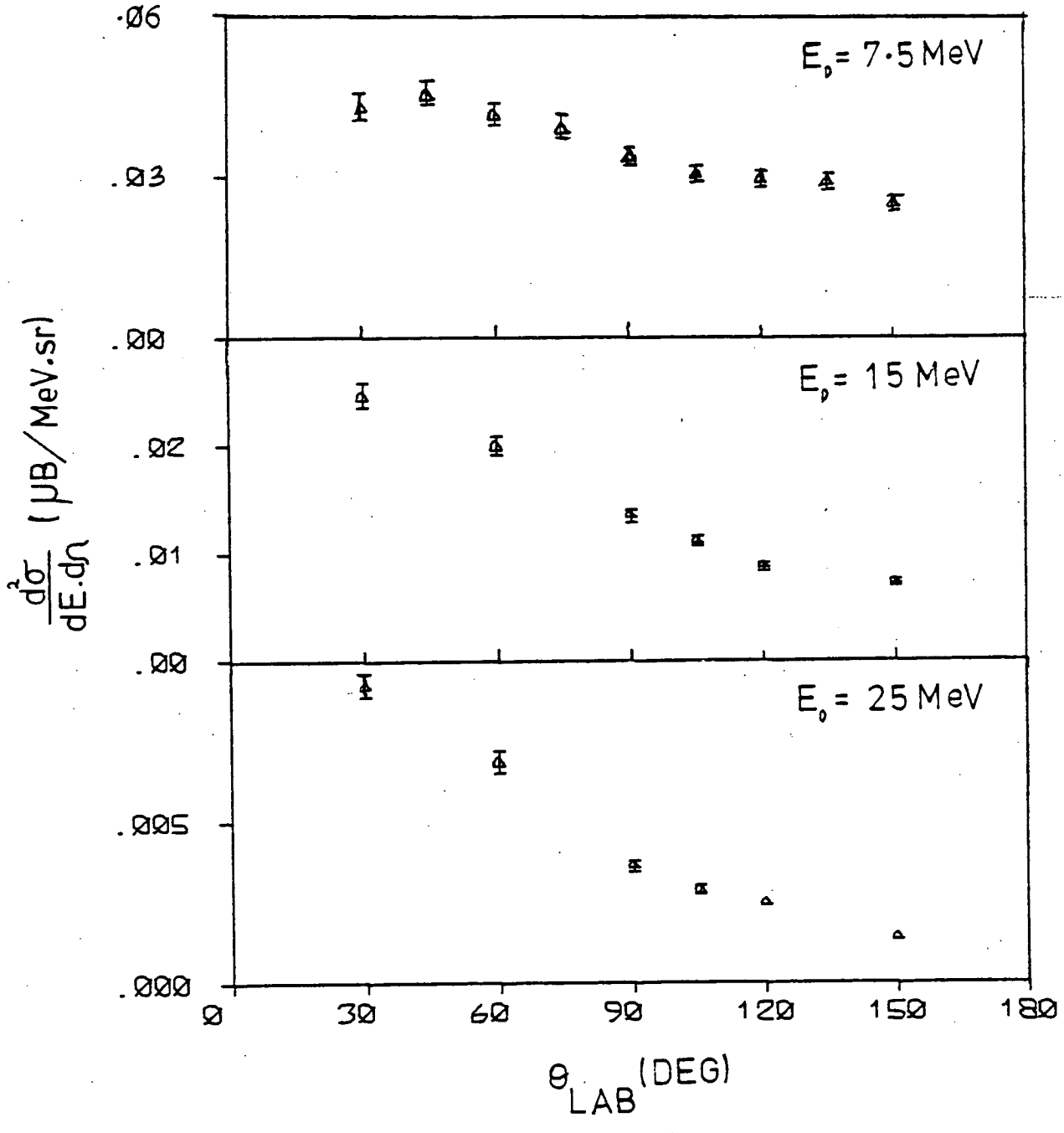

Fig. 3.26 Angular distributions for deuterons from ^{NAT}Sn at E_e = 120 MeV.

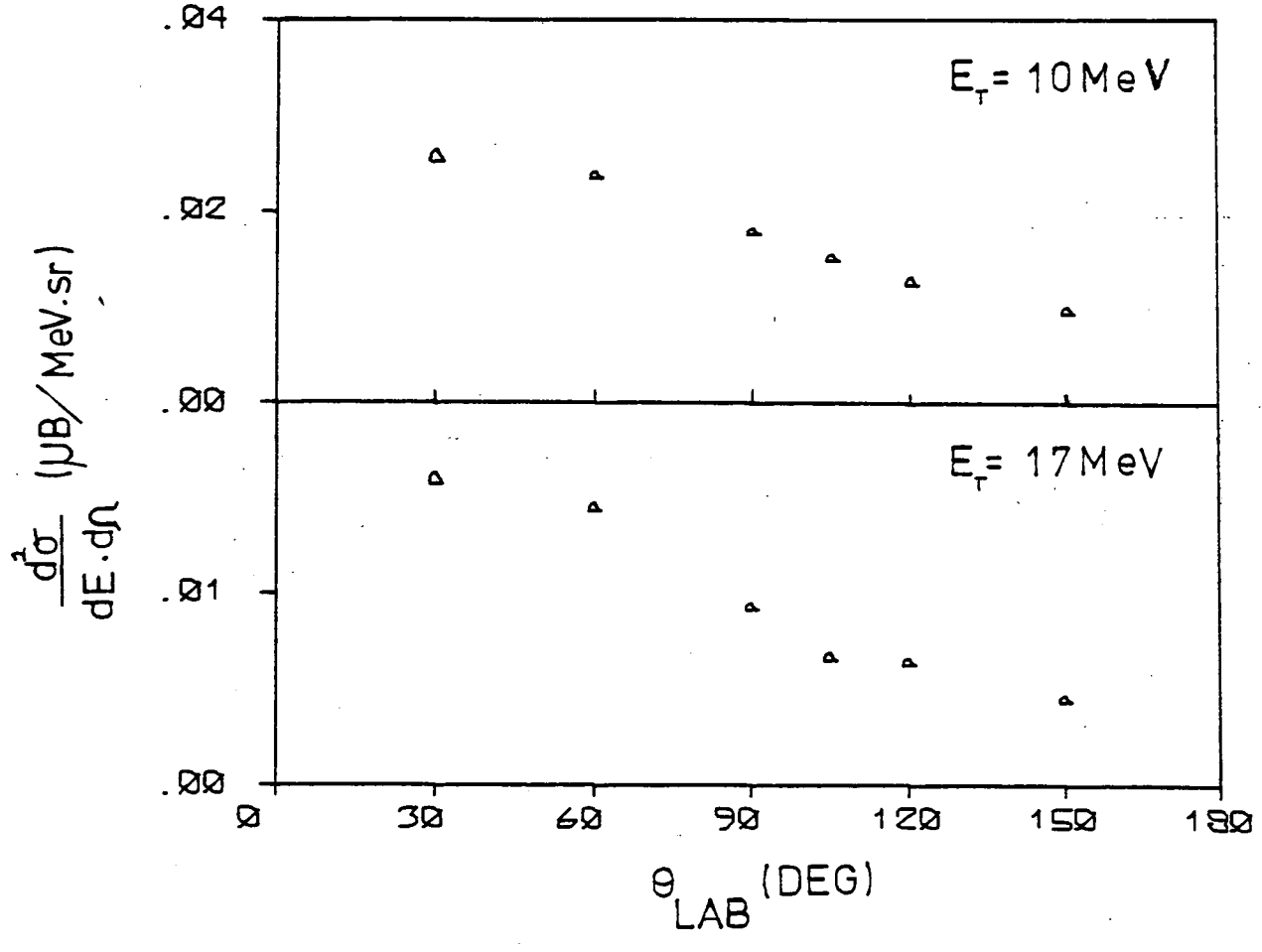

Fig. 3.27 Angular distributions for tritons from ^{NAT}Sn at E_e = 120 MeV.

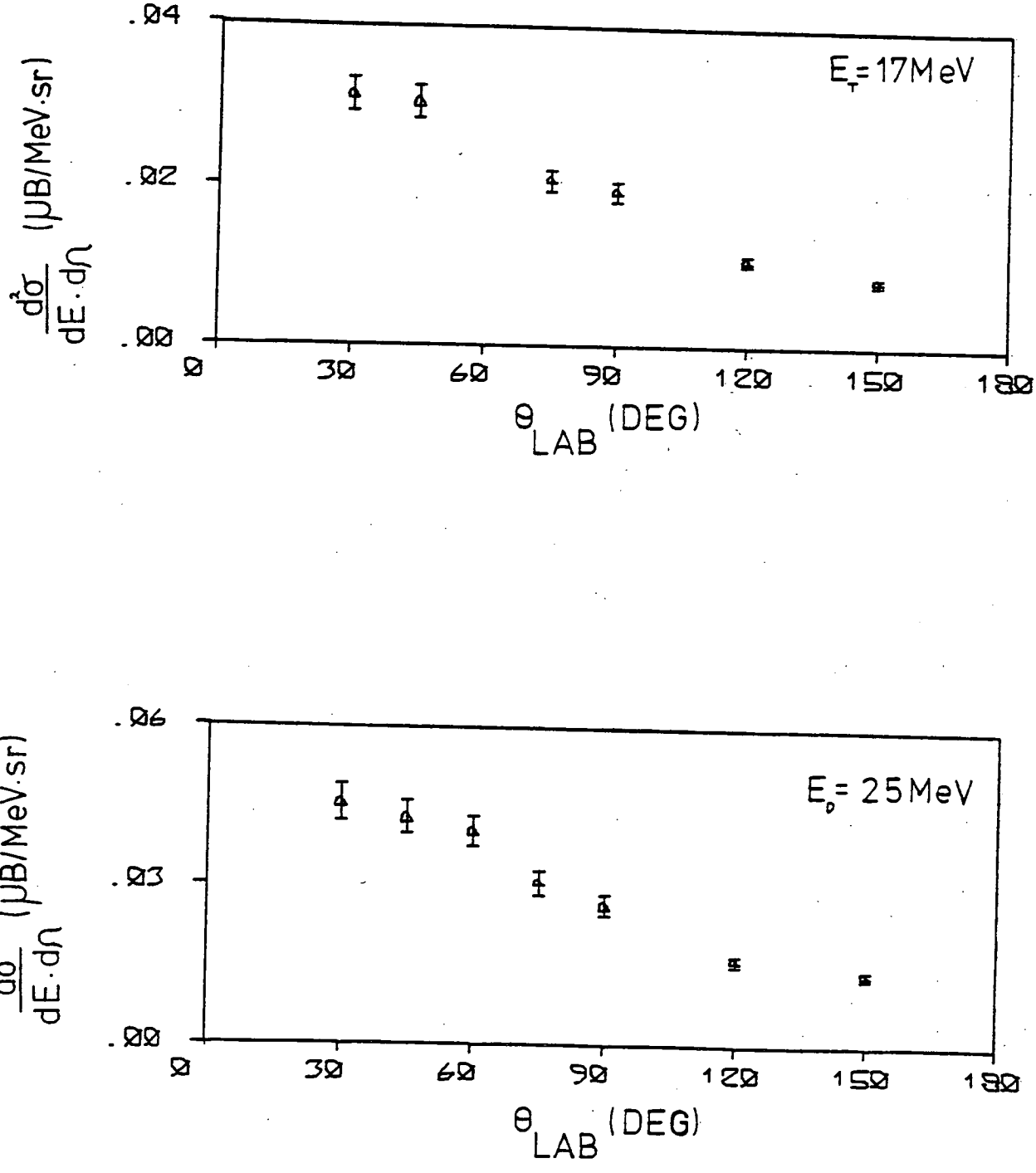

Fig. 3.28 Angular distributions for tritons and deuterons from ^{197}Au at E_e = 120 MeV.

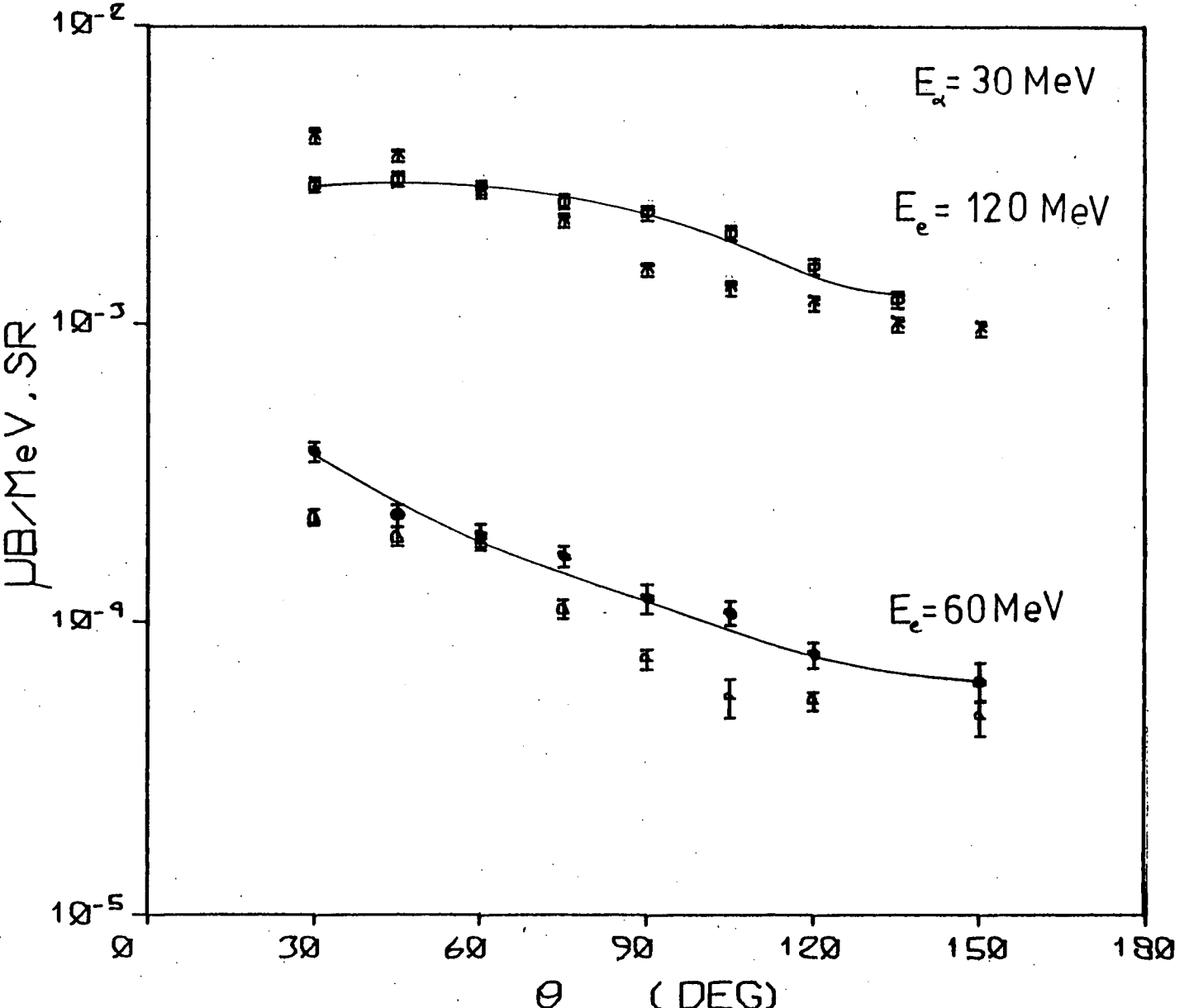

Fig. 3.29 Angular distributions for alphas from ^{58}Ni. Solid lines to guide the eye for bremsstrahlung yields.

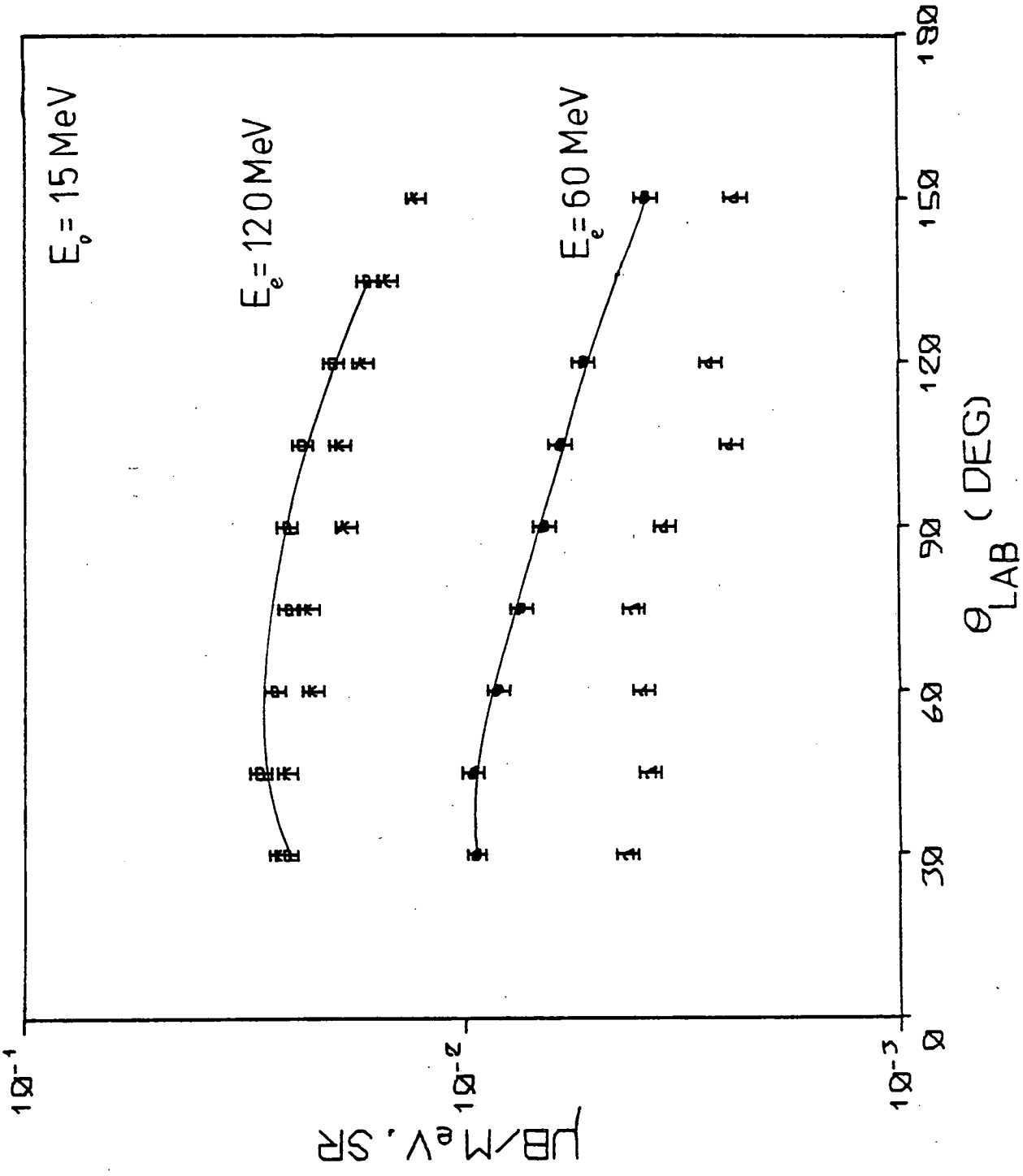

Fig. 3.30 Angular distributions for deuterons from ^{58}Ni. Solid lines to guide the eye for bremsstrahlung yields.

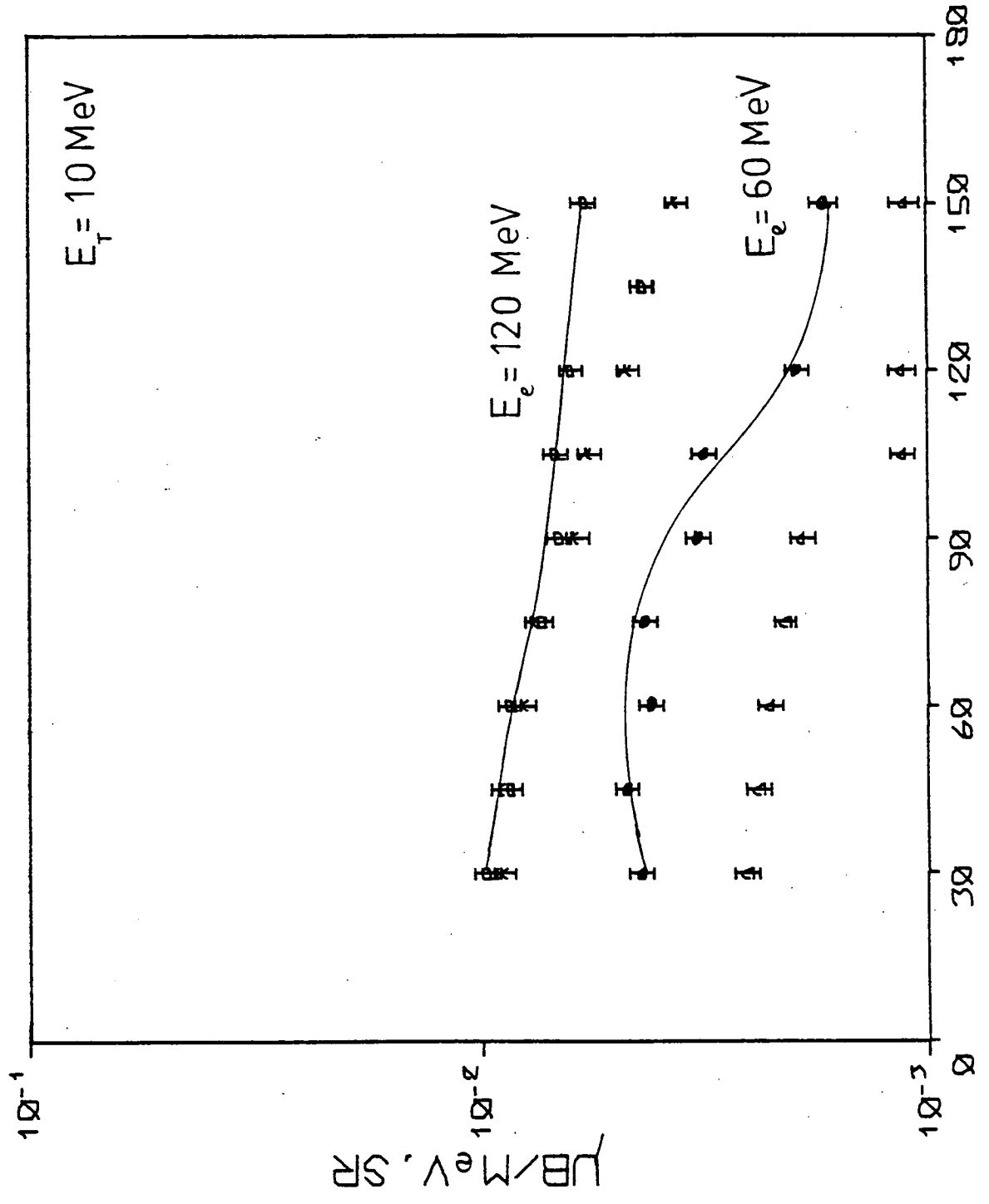

Fig. 3.31 Angular distributions for tritons from ^{58}Ni. Solid lines to guide the eye for bremsstrahlung yields.

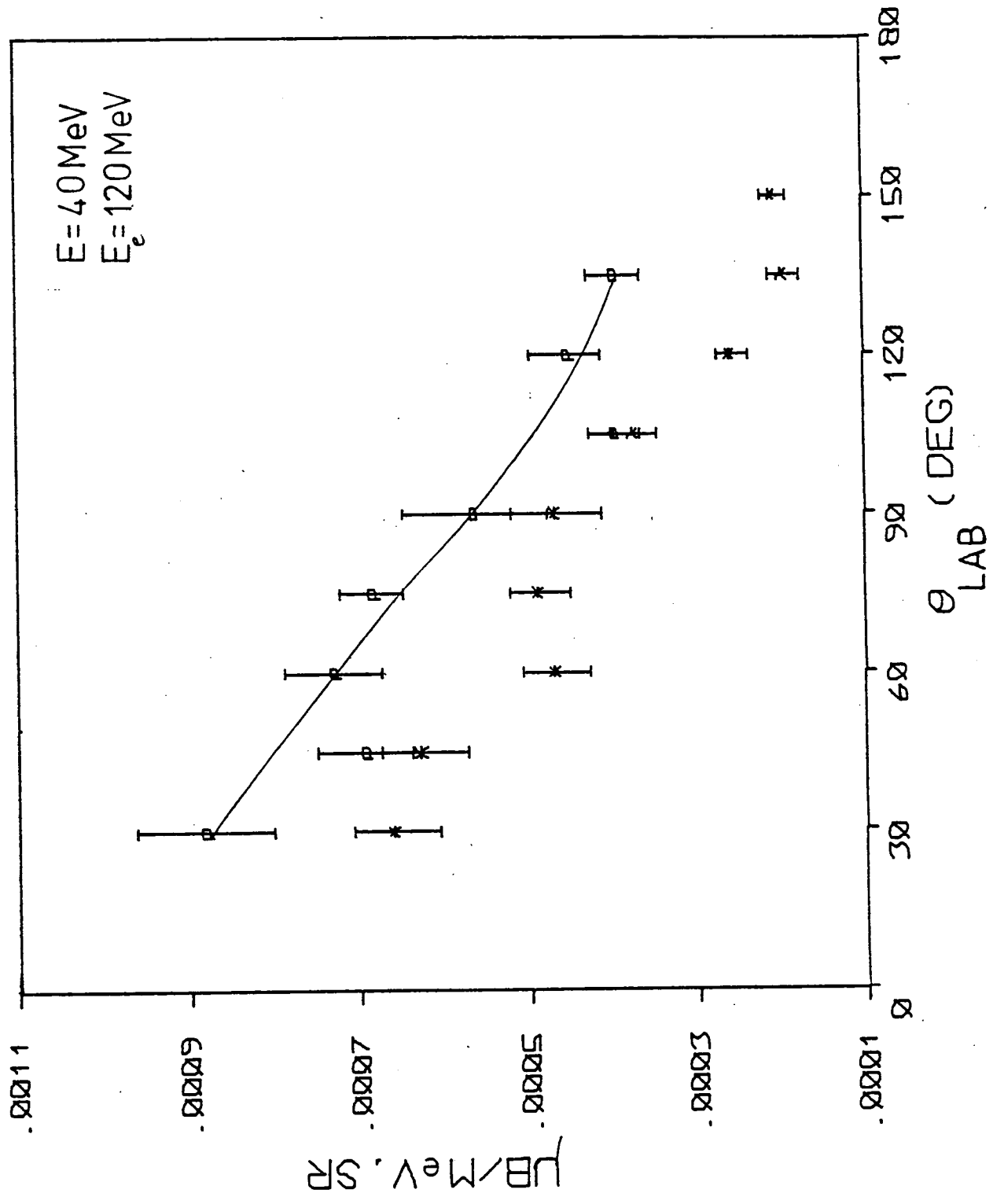

Fig. 3.32 Angular distributions for ^{3}He's from ^{58}Ni. Solid line to guide the eye for bremsstrahlung yields.

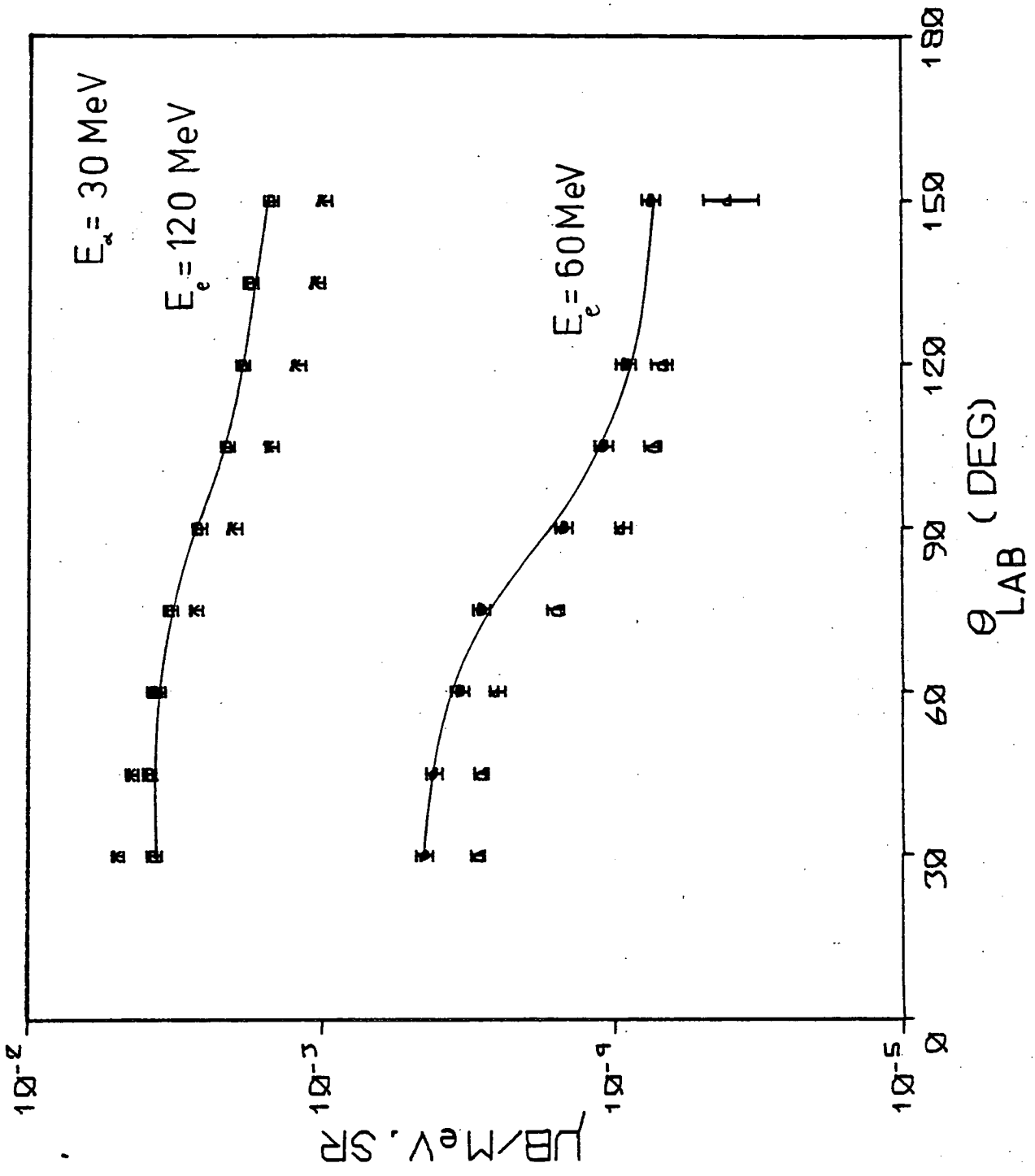

Fig. 3.33 Angular distributions for alphas from ^{60}Ni. Solid lines to guide the eye for bremsstrahlung yields.

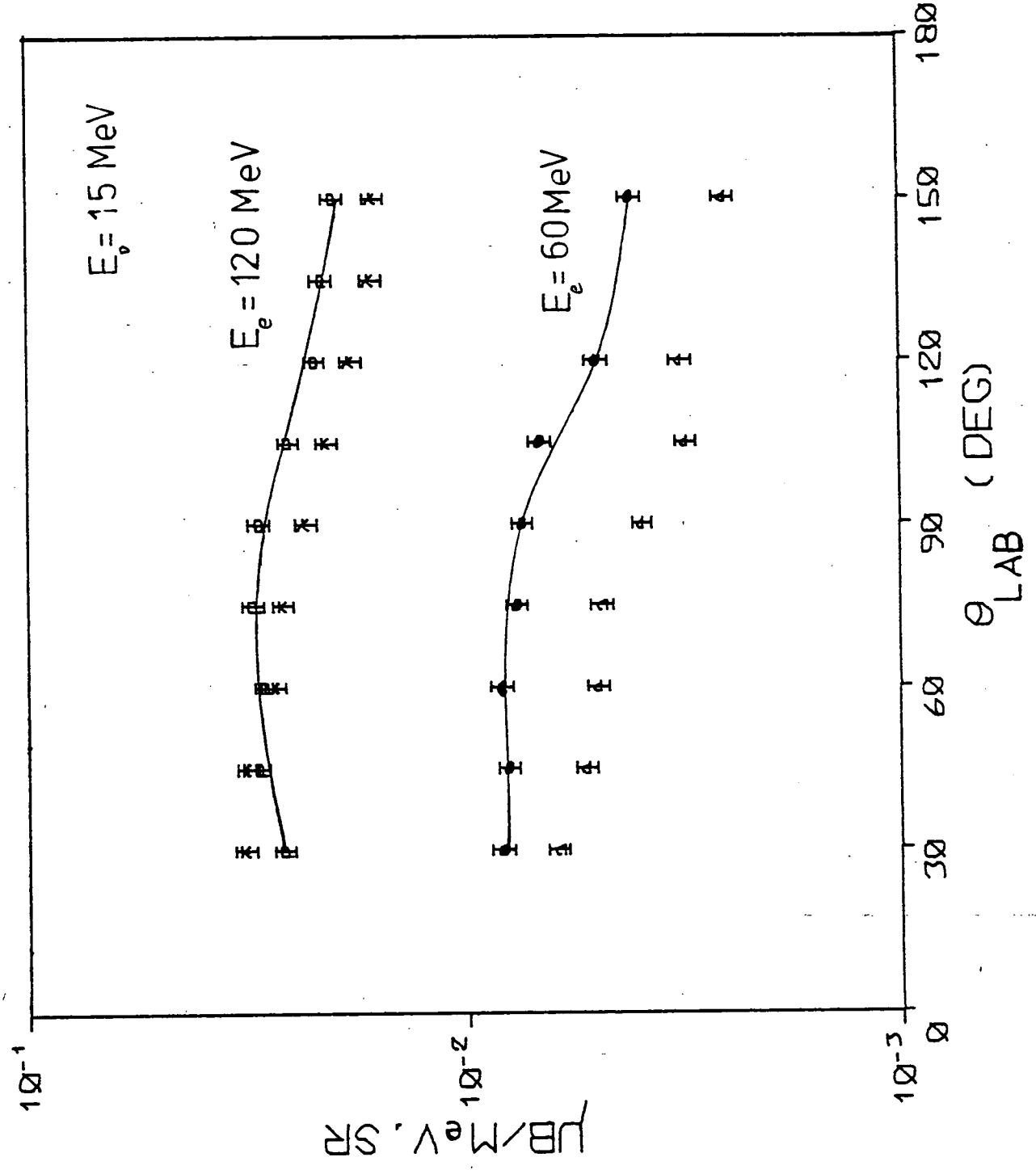

Fig. 3.34 Angular distributions for deuterons from ^{60}Ni. Solid lines to guide the eye for bremsstrahlung yields.

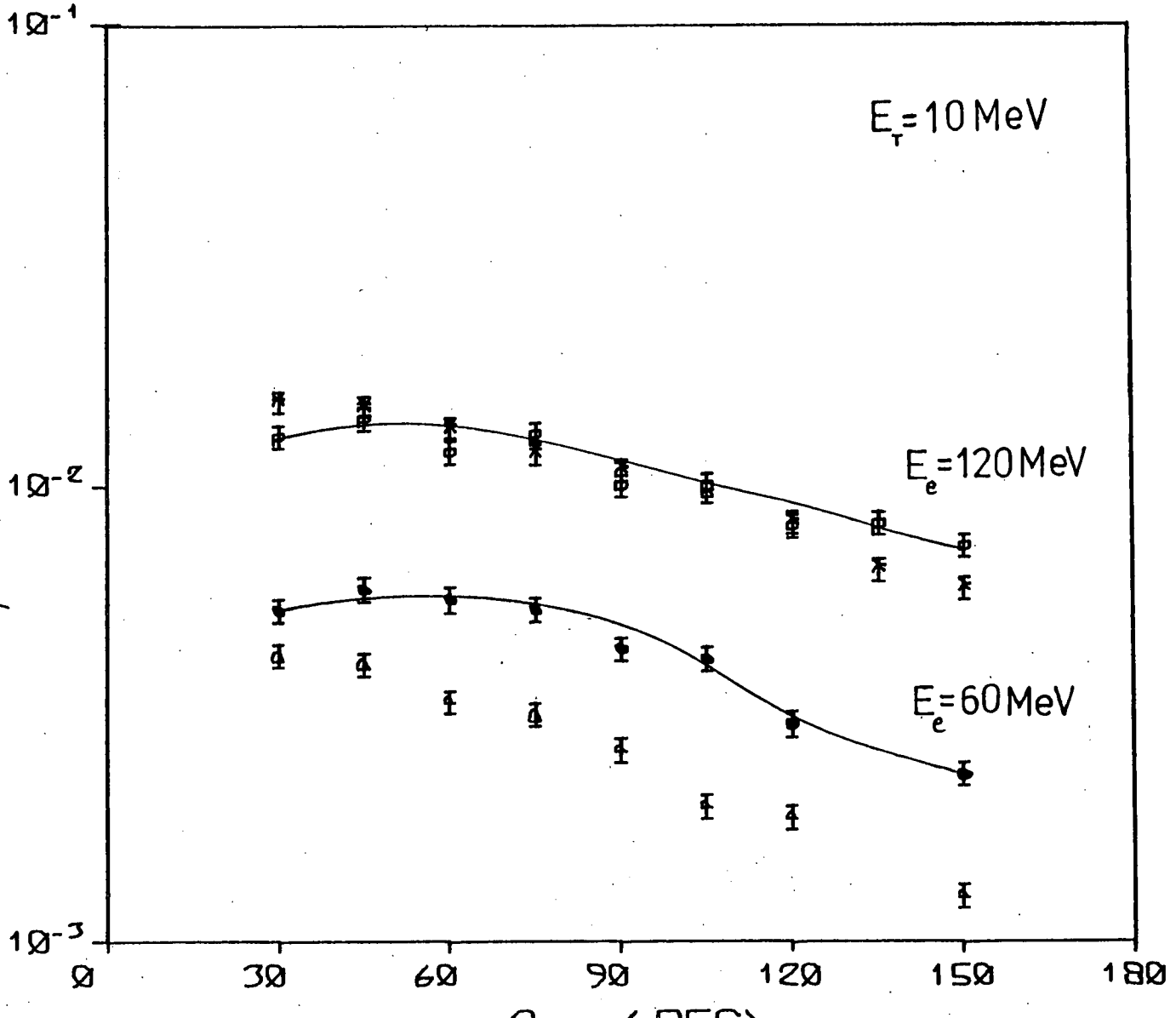

Fig. 3.35 Angular distributions for tritons from ^{60}Ni. Solid lines to guide the eye for bremsstrahlung yields.

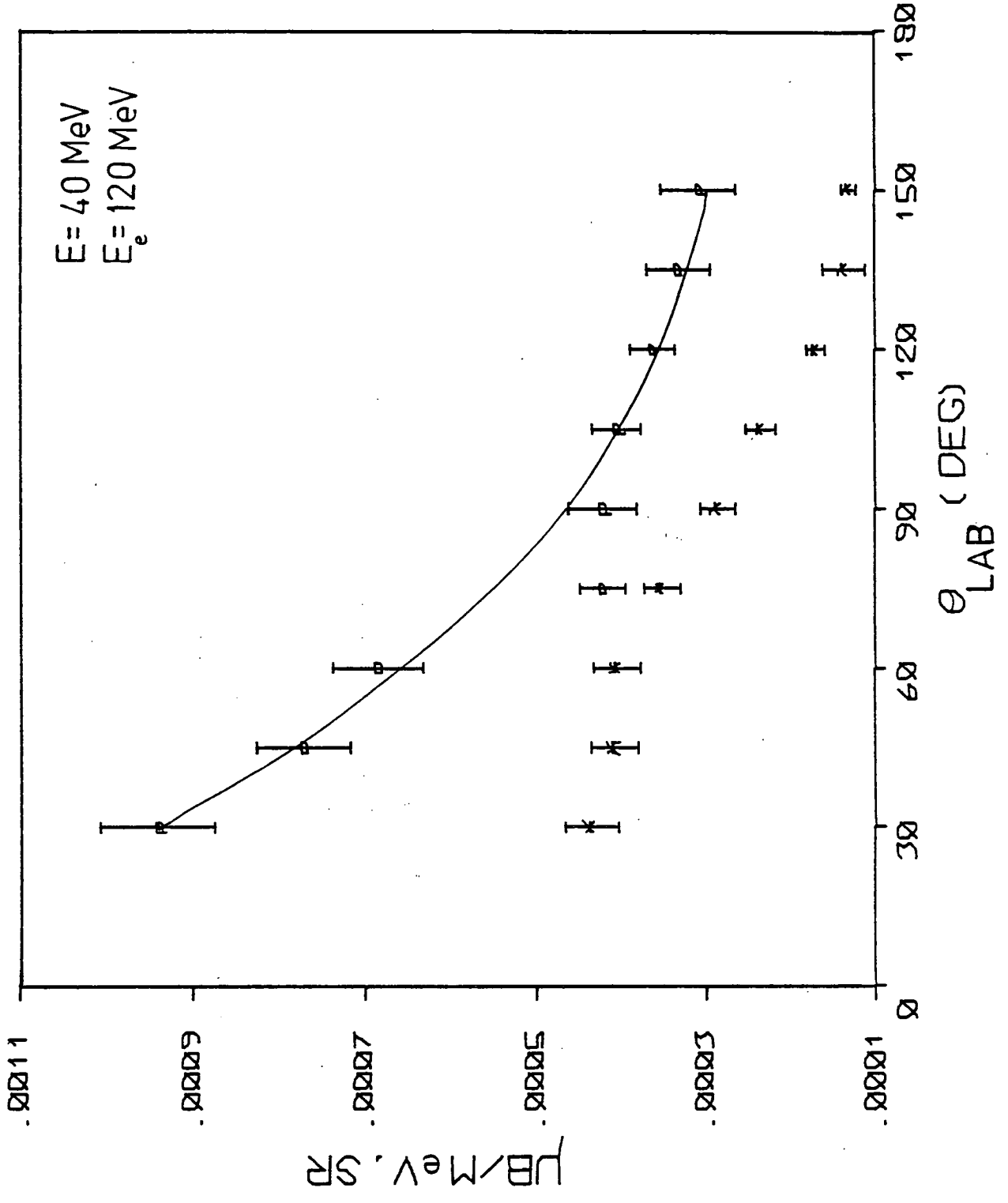

Fig. 3.36 Angular distributions for ^{3}He's from ^{60}Ni. Solid line to guide the eye for bremsstrahlung yields.

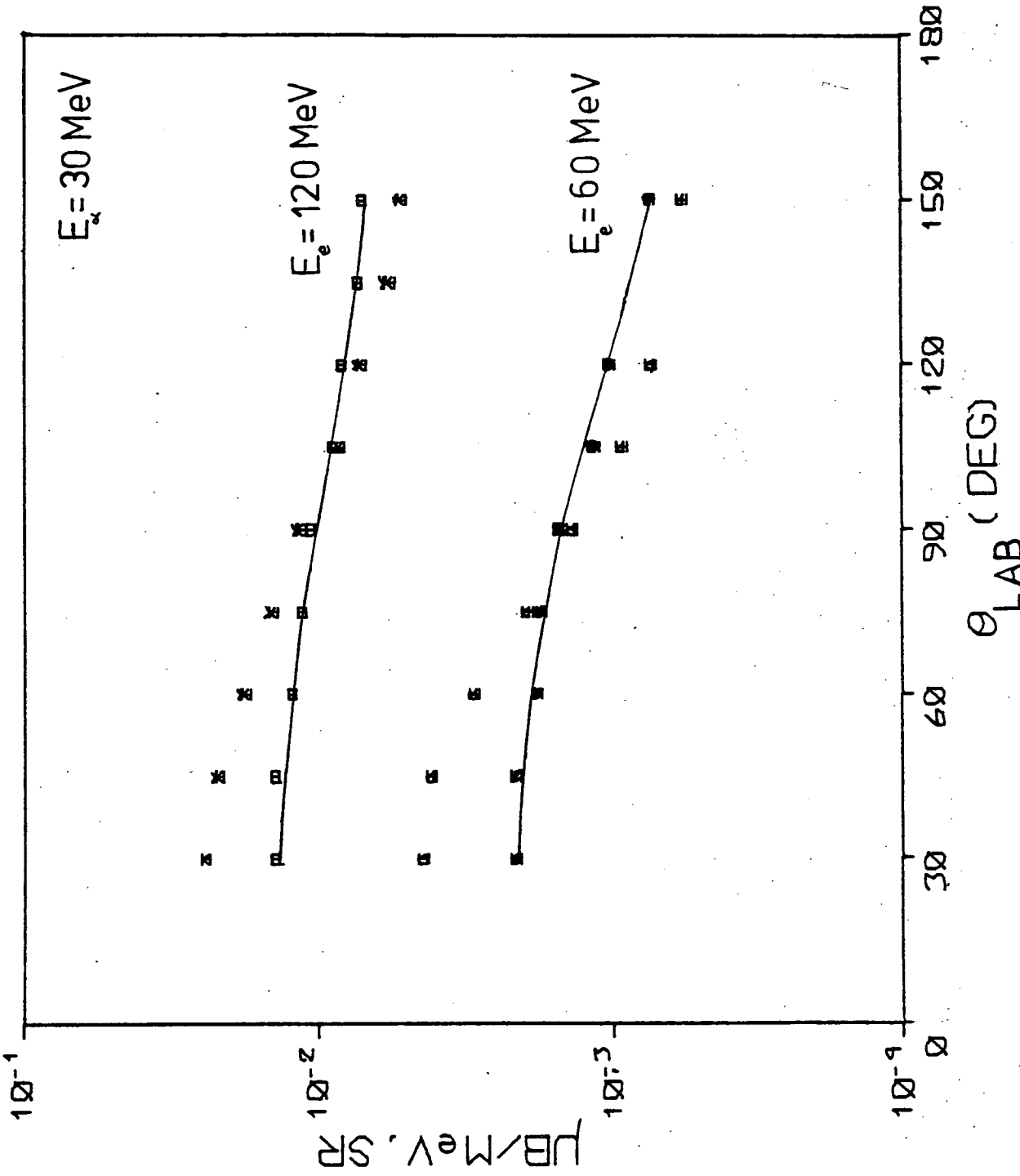

Fig. 3.37 Angular distributions for alphas from ^{197}Au. Solid lines to guide the eye for bremsstrahlung yields.

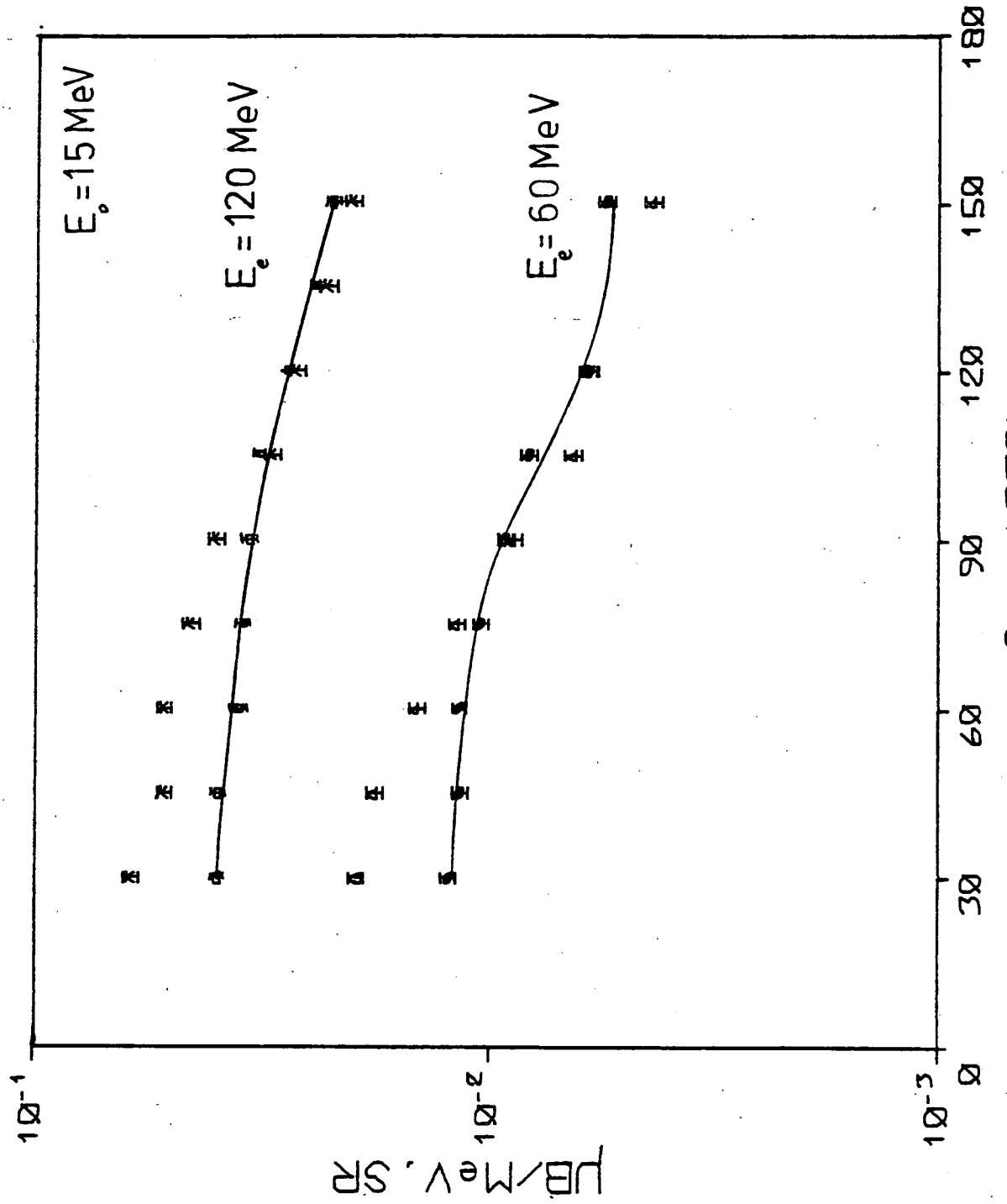

Fig. 3.38 Angular distributions for deuterons from ^{197}Au. Solid lines to guide the eye for bremsstrahlung yields.

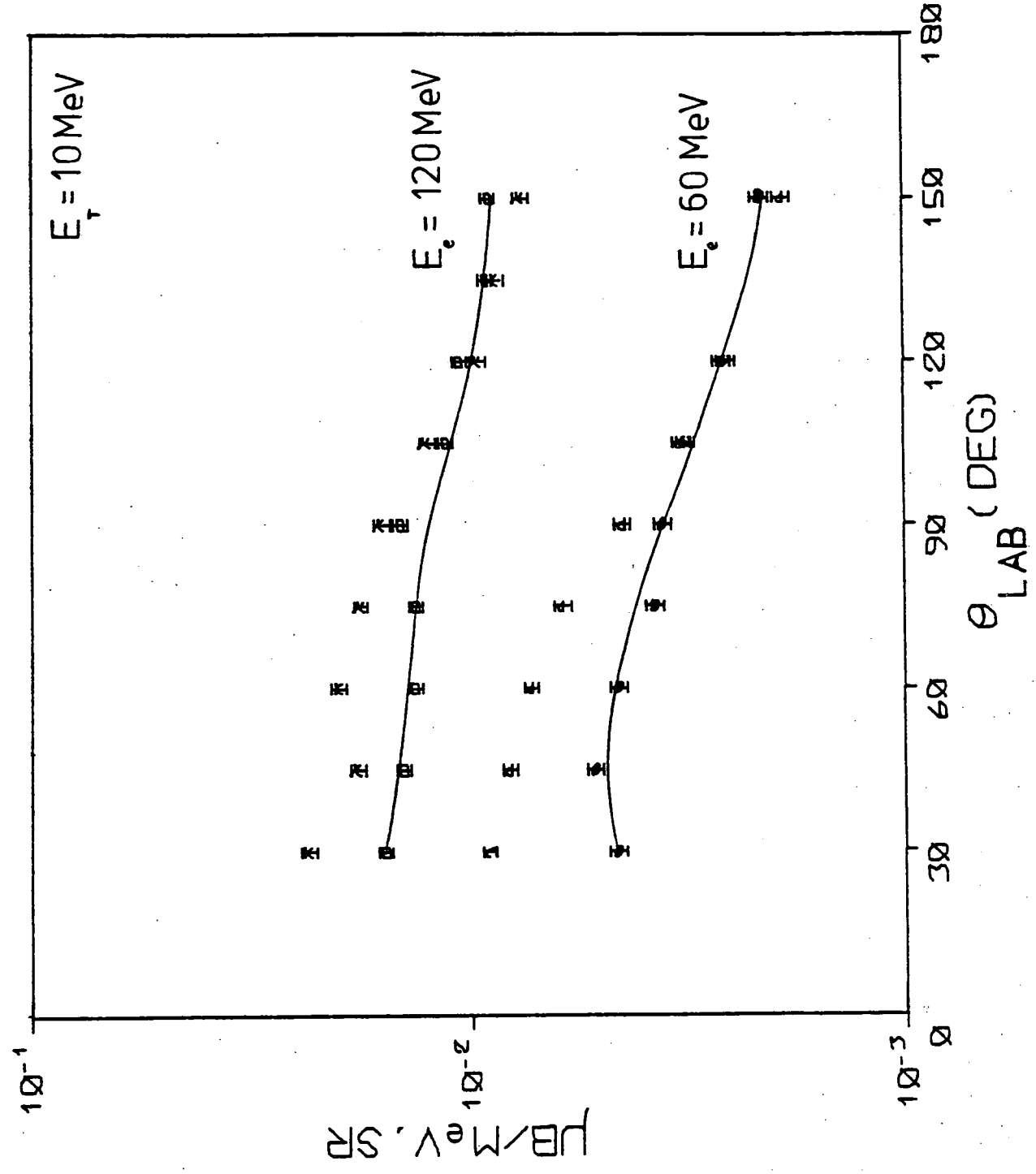

Fig. 3.39 Angular distributions for tritons from ^{197}Au. Solid lines to guide the eye for bremsstrahlung yields.

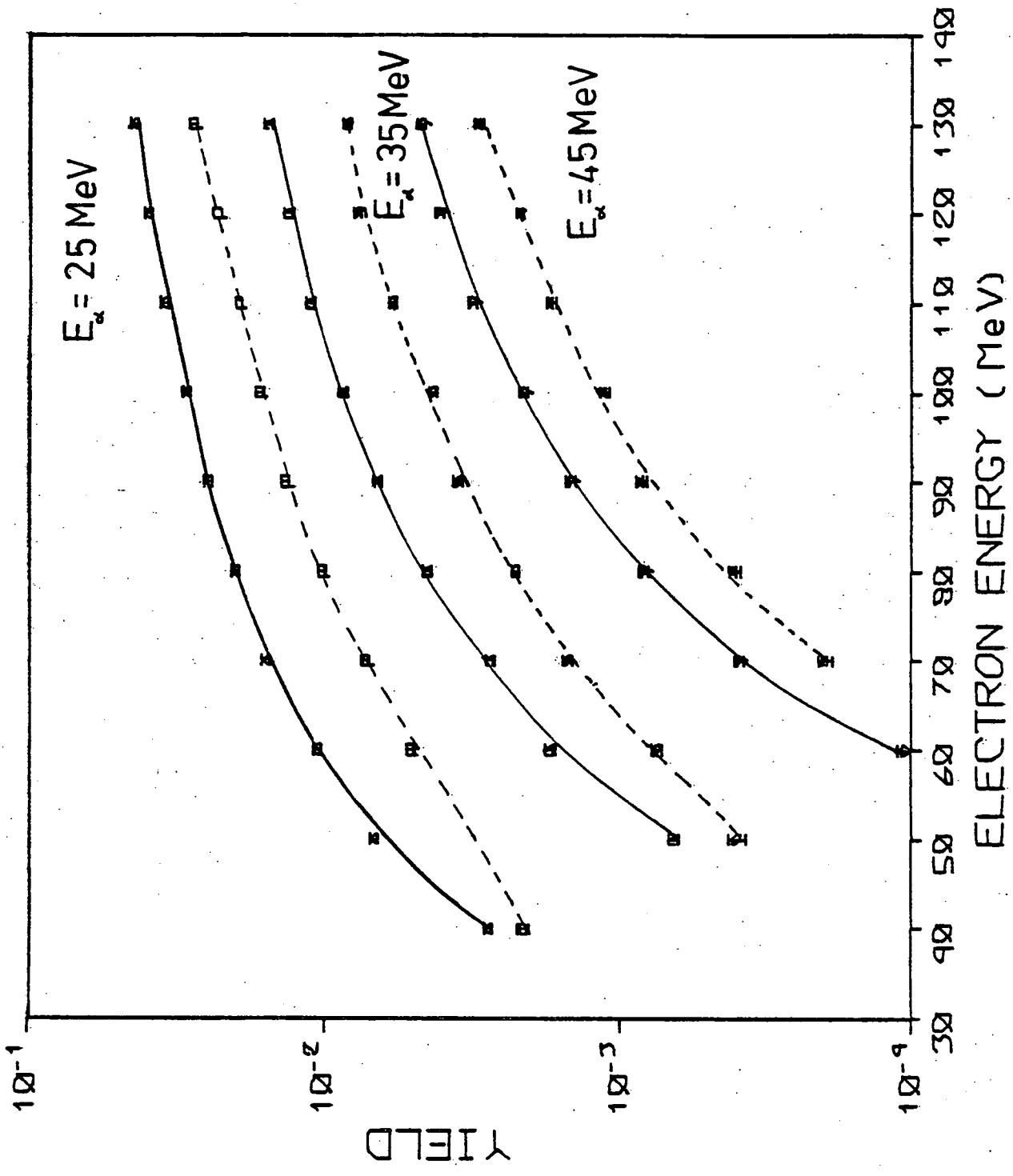

Fig. 3.40 Excitation functions for alphas from ^{197}Au at $\theta = 30^{\circ}$. Dashed lines to guide the eye for bremsstrahlung yields and solid lines for electron cross sections.

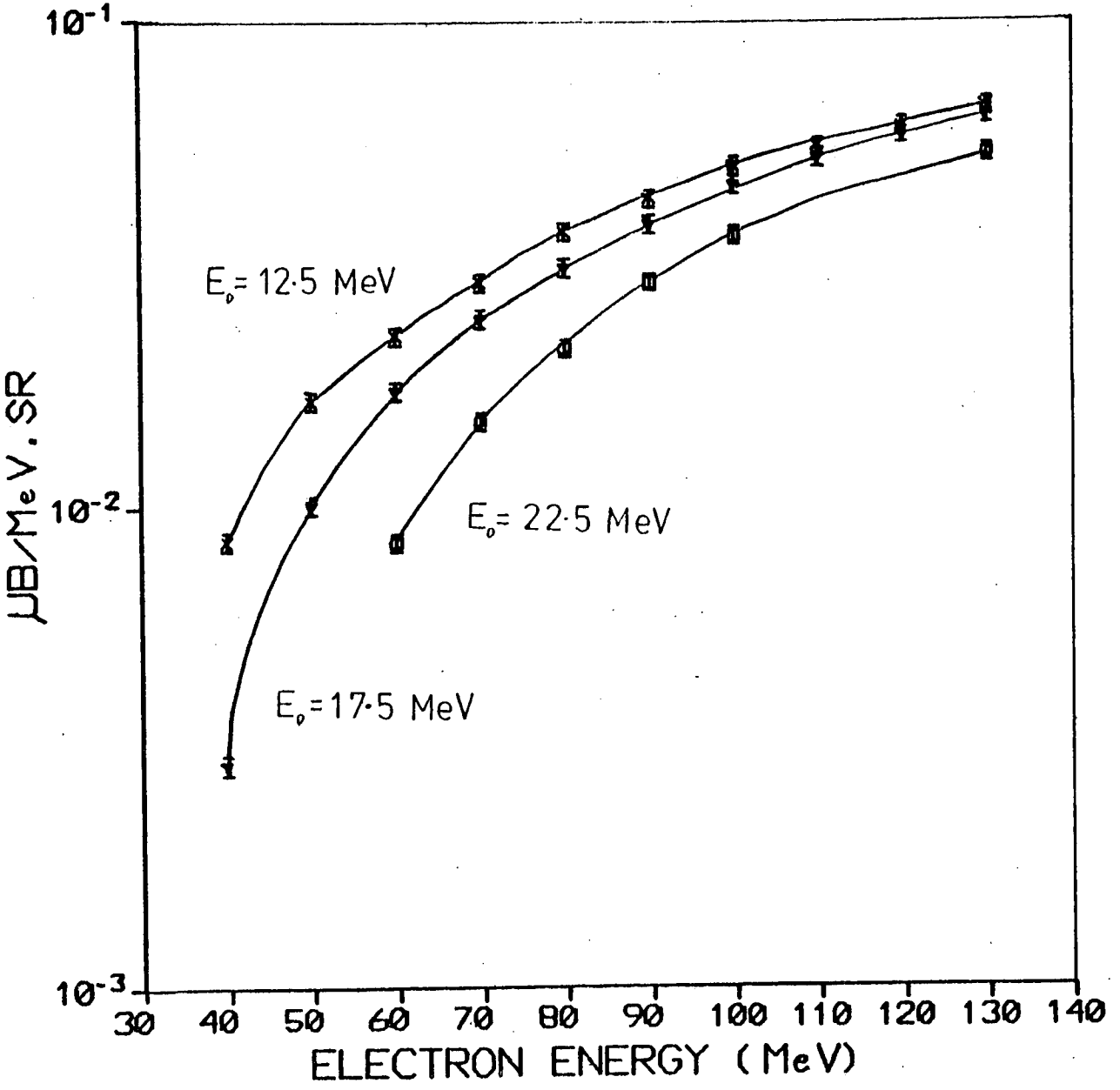

Fig. 3.41 Excitation functions for deuterons from ^{197}Au for electro-excitation. Lines drawn to guide the eye.

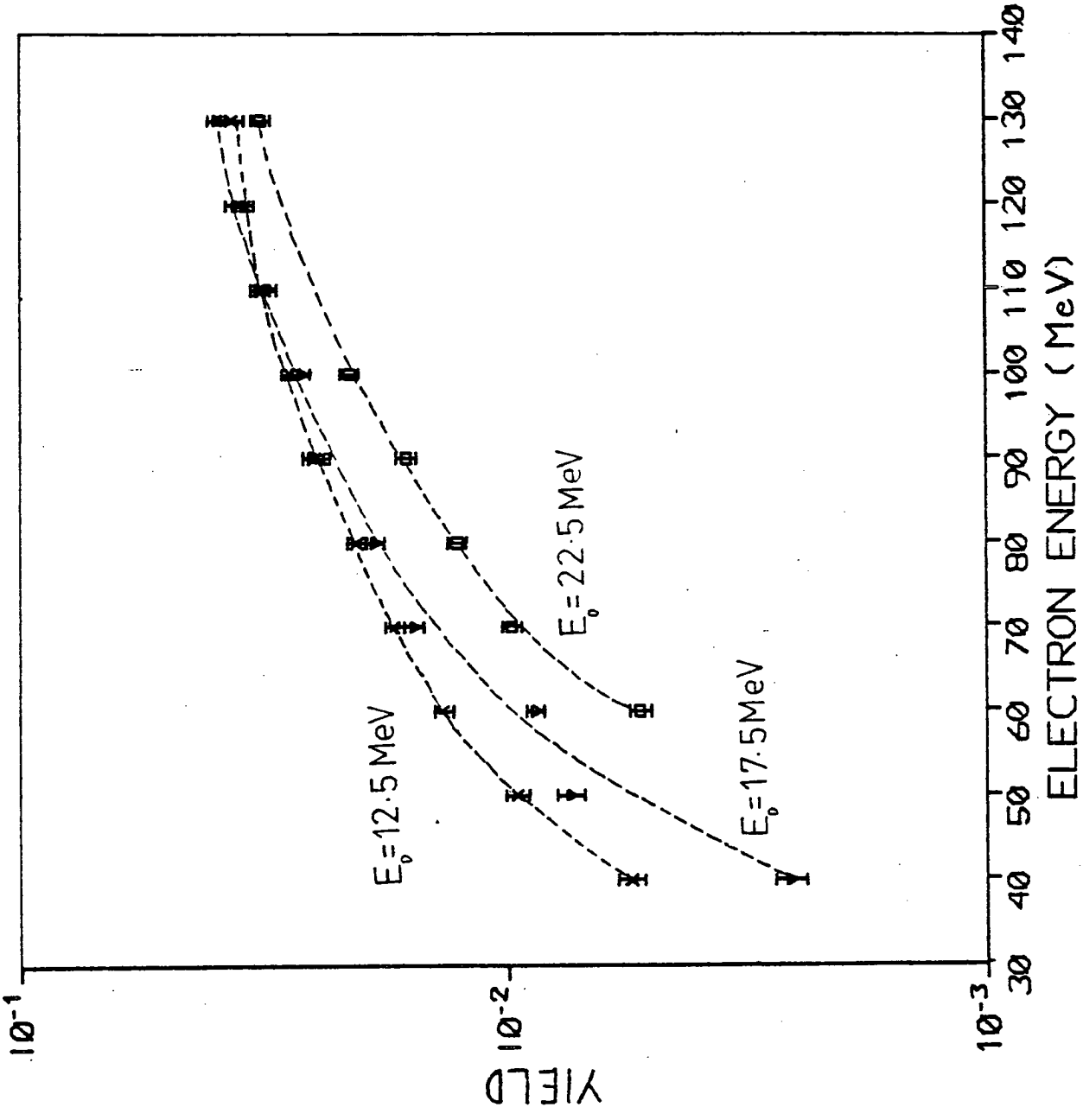

Fig. 3.42 Excitation functions for deuterons from ^{197}Au for photo excitation. Lines drawn to guide the eye.

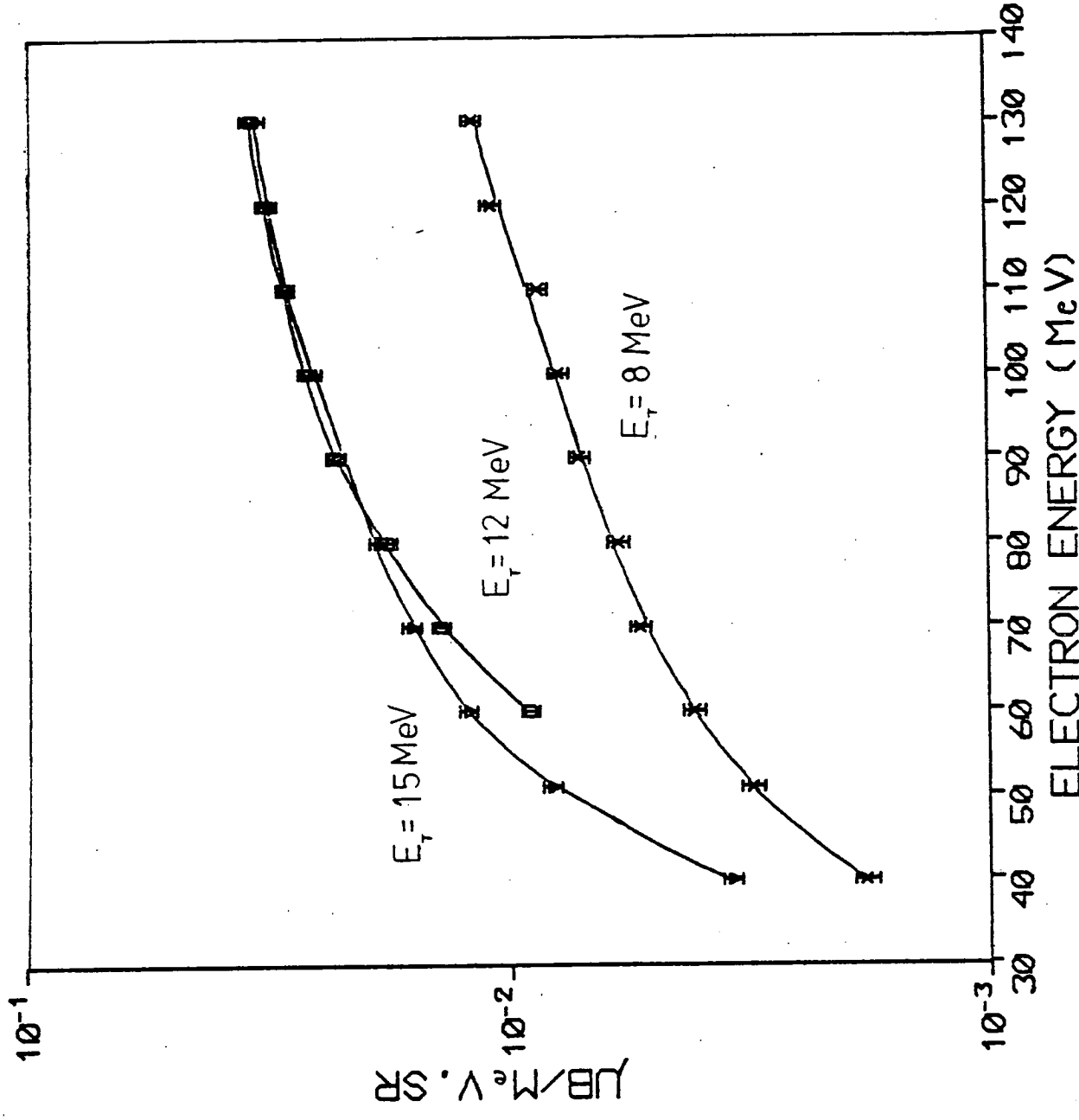

Fig. 3.43 Excitation functions for tritons from ^{197}Au for electro excitation. Lines drawn to guide the eye.

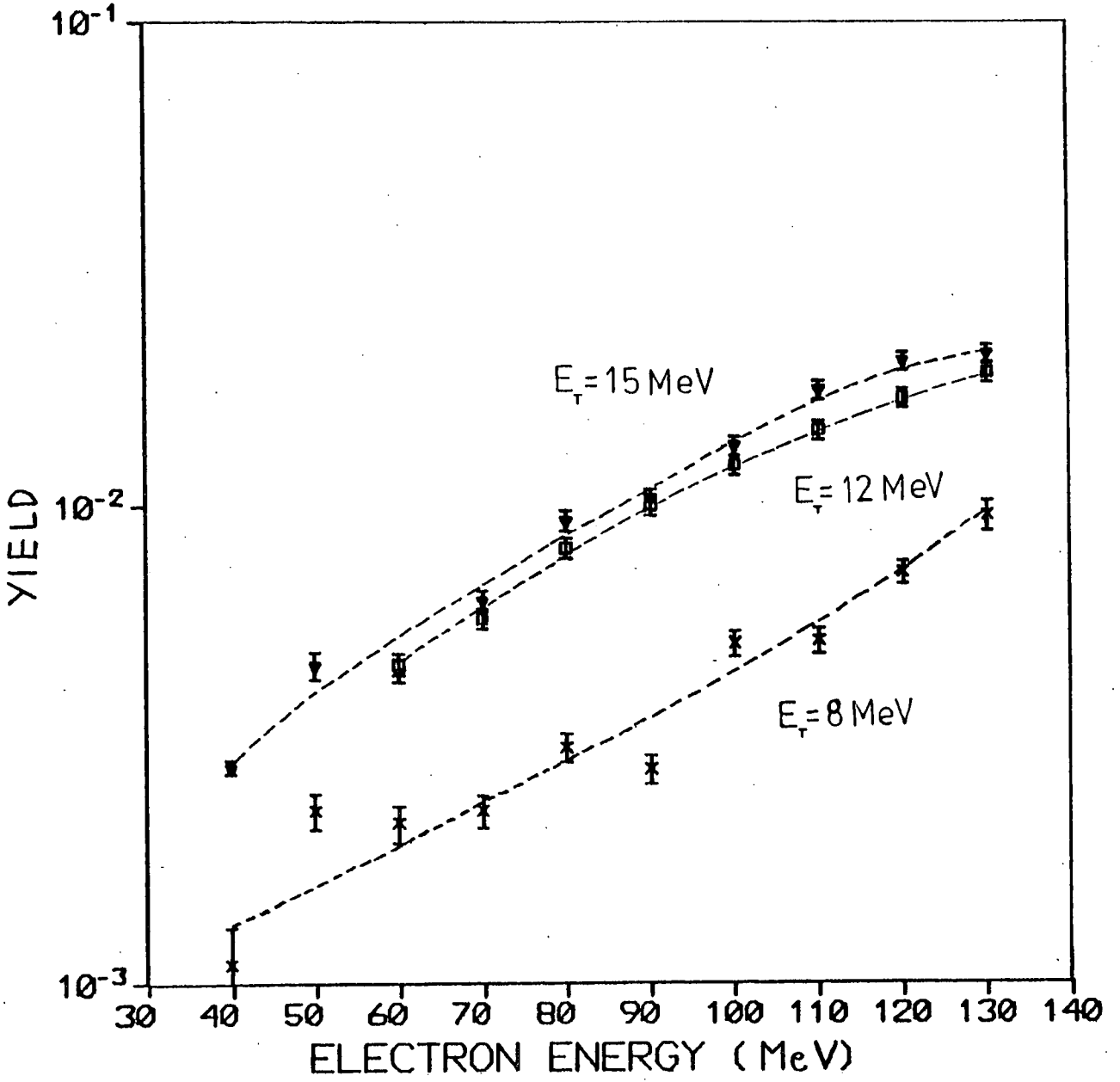

Fig. 3.44 Excitation functions for tritons from ^{197}Au for photo excitation. Lines drawn to guide the eye.

barrier heights were calculated, using the formula

$$E_c(\text{MeV}) = \frac{1.45\ Z_1 Z_2}{r_o(A_1^{1/3} + A_2^{1/3})} \quad (91)$$

and positions of the giant dipole resonance (G.D.R.) at $77A^{-1/3}$ MeV[92] are given in Table 3.4. At values below A = 40 the G.D.R. position is not given accurately by the above formula.

The experimental measurements are probably not accurate enough to pick out any possible structure due to the emission of particles from the low lying states of ^{12}C.

The alpha particle data for ^{NAT}Ni, ^{92}Mo, ^{94}Mo and ^{197}Au have been previously measured by Flowers[7] and are not included in the respective energy spectra diagrams. The high alpha cross section observed for ^{NAT}Sn (Fig. 3.10) below 8 MeV alpha particle energy is most probably due to oxygen contamination of the target and is thus not considered further.

Due to the very low cross section it was not possible to obtain measurements for the emission of ^3He particles from ^{181}Ta at 150° (Fig. 3.12).

3.4.2 Angular distributions

Angular distribution measurements were made at alpha particle energies of 5, 8, 15, 30 and 50 MeV for ^{12}C and ^{27}Al, at 15, 30 and 50 MeV for ^{NAT}Sn, at 30 and 50 MeV for ^{NAT}Ni and at 50 MeV for ^{197}Au. It was not possible to obtain data for the emission of 1.7 MeV tritons (E_α = 5 MeV) or 66.7 MeV ^3He particles (E_α = 50 MeV) due to the very small cross sections. Similarly data could not be obtained for the

TABLE 3.4

Nucleus	Coulomb Barrier (MeV)				Q value (MeV)[122]				Peak Energy (MeV)				G.D.R. Energy (MeV)
	α	t	d	^{3}He	α	t	d	^{3}He	α	t	d	^{3}He	
^{12}C	3.74	1.94	2.04	3.88	-7.4	-27.4	-25.2	-26.3	3	-	-	-	
^{27}Aℓ	5.6	2.9	3.1	5.7	-10.1	-18.2	-17.1	-23.7	5	-	3	-	
^{NAT}Ni	10.0	5.15	5.33	10.3	-6.3 (^{60}Ni) (^{119}Sn)	-20.1	-17.8	-19.2	-	8	-	-	19.7
^{NAT}Sn	15.1	7.7	7.9	15.4	-4.4	-16.8	-14.3	-16.3	15	10	11	17	15.6
^{181}Ta	19.7	10.1	10.3	20.1	1.4	-11.1	-11.3	-13.3	21	13	13	-	13.6
^{197}Au	20.9	10.7	10.9	21.3	0.9	-11.4	-11.5	-13.6	-	13	13	27	13.2

emission of 2.7 MeV tritons (E_α = 8 MeV) from $^{27}A\ell$ and of 40 MeV ^{3}He particles (E_α = 30 MeV) from both ^{NAT}Ni and ^{NAT}Sn. Angular distribution measurements for the emission of alpha particles from ^{NAT}Ni and ^{197}Au have been reported previously[7]. Measurements of angular distributions for complex particles emitted from ^{58}Ni, ^{60}Ni and ^{197}Au following both electro and photo excitation have also been made.

3.4.3 Excitation functions

Excitation functions have been measured for the emission of complex particles from ^{197}Au following both electron and photon excitation. Data were obtained at electron and bremsstrahlung end point energies between 40 and 130 MeV at alpha particle energies of 25, 35 and 45 MeV. Measurements were taken in 10 MeV steps. A ^{181}Ta bremsstrahlung radiator of thickness 0.0813 g.cm^{-2} was used at electron energies of 40 and 50 MeV and the data normalized to the thicker ^{181}Ta radiator (0.169 g.cm^{-2}) used at higher electron energies. No data was obtained for the emission of ^{3}He particles due to the very low cross section.

CHAPTER 4

DISCUSSION OF EXPERIMENTAL RESULTS

4.1 Energy Spectra

4.1.1 Introduction

The experimentally observed energy spectra reported in Section 3.4.1 all show a basic similarity in shape - i.e. a low energy peak plus an exponential decrease in cross section with increasing particle energy. The cross sections for the emission of tritons, deuterons and ^{3}He particles are of approximately the same magnitude in the case of ^{12}C but for the other nuclei studied the cross sections generally increase in magnitude as $^{3}He < t < d < \alpha$ for low particle energies. The alpha particle spectrum falls off more rapidly with increasing particle energy as compared to the other complex particles. The relative deuteron to alpha particle cross section for $^{27}A\ell$ is typical. Although the deuteron cross section is a factor of ten lower than the alpha cross section in the peak, the deuteron cross section exceeds that for alpha emission above about 20 MeV.

The high energy part of the measured energy spectra does not appear to be a continuation of the tail of the low energy peak. This is most marked in the spectrum of alpha particles emitted from ^{12}C. There appears to be a change in slope of the energy spectrum at an alpha energy of approximately 7 MeV with the cross section remaining higher than an extrapolation of the low energy peak would predict. This can be interpreted as a two component reaction mechanism, a statistical component which gives rise to the low energy peak and some form of direct component which accounts for the high energy cross section.

The statistical compound nucleus model has been used successfully to give good agreement with low energy data for many particle induced

and photonuclear reactions - see the review articles of Berman, Thomas and Bodansky, references (93), (94) and (95) respectively and references (20) and (22). Statistical model calculations accurately predict energy spectra, angular distributions and excitation functions, particularly for emitted particles of low energy, on the basis that these particles are 'evaporated' from the target nuclei. Good agreement between statistical model calculations and the low energy alpha peak following electro-excitation of ^{60}Ni has also been observed[6].

The angular distribution of complex particles emitted in a statistical reaction is predicted to be symmetric about 90^{o}. However, if the particles are emitted in some form of direct or pre-equilibrium reaction, a forward peaked angular distribution is predicted. The angular distributions for the emission of complex particles from Sn and Au, presented in Section 3.4.2, are all forward peaked, even when measured at the peaks of the particle energy spectra. This suggests that the low energy peaks are not statistical in nature, as expected for Au due to the high coulomb barrier. In the case of Sn, however, the coulomb barrier for alpha particles is at approximately the energy of the G.D.R. (see Table 3.4).

A comparison between the two sets of energy spectra measured for ^{181}Ta at 30^{o} and 150^{o} to the beam direction show that the two sets of spectra are not identical as would be expected if the complex particle emission was due wholly to a statistical mechanism. Only at the lowest measured particle energies are the cross sections at the two angles comparable. The cross section measured at 150^{o} becomes increasingly lower than that measured at 30^{o} as the particle energy increases, consistent with an angular distribution which becomes increasingly forward peaked as the particle energy increases. This indicates that a pre-equilibrium reaction mechanism is necessary to explain all but the lowest

energy data.

A statistical model calculation was carried out to estimate the alpha particle energy spectrum for Sn due to a compound nucleus reaction. This nucleus was chosen as being the heaviest nucleus for which energy spectra were measured where the coulomb barriers for particle emission were not too high to almost entirely inhibit the evaporation of particles from the nucleus. Wu and Chang[82] have observed that in the case of proton induced reactions nearly all of the energy spectra for tritons and deuterons emitted from Sn can be explained by pre-equilibrium calculations, although for alpha emission the low energy peak cannot be predicted. Thus a statistical model calculation was performed for the emission of alpha particles from Sn although the coulomb barrier is higher for alpha emission than for the emission of tritons and deuterons.

Statistical model calculations were performed to estimate the differential energy spectra for the emission of alphas and tritons from Aℓ. These calculations should indicate whether the low energy peaks in the energy spectra of complex particles emitted from light nuclei can be explained by the evaporation of complex particles from a compound nucleus. The experimental data for Ni and both Mo isotopes did not extend to low energies so a statistical model calculation was not carried out for a medium weight nucleus.

There is evidence[7,20] that for heavy nuclei (Au and In respectively), statistical model calculations greatly underestimate the peak cross section for alpha particles emitted following bremsstrahlung and electron excitation. In heavy nuclei the coulomb barrier height exceeds the energy of alpha particles emitted following giant resonance excitation (see Table 3.4) - effectively inhibiting statistical emission of alphas. Statistical model calculations cannot predict the

high energy tail observed in the energy spectra reported here, or the high energy cross section observed in (p,X) (where X = p, d, t, ^{3}He, α) reactions for a range of nuclei[78]. Several reaction models have been developed in an attempt to explain the high energy continuum of emitted particles observed in particle and photon induced reactions.

Two main types of model have been developed to explain the emission of high energy particles for photon or electron induced reactions. A one step direct knock out process has been suggested by Carver[17] who showed that ratios of (γ, α) to (γ, p) yields for heavy nuclei were comparable to those calculated on the basis of direct particle knockout. The other type of model assumes some form of intranuclear interaction following photon absorption on to a quasideuteron. Calculations, including intranuclear interactions[80,81], give good agreement with experimental measurements of high energy photonucleon spectra while calculations omitting such interactions overestimate the data.

The intranuclear interaction may involve:

i) A Quasi-free scattering (Q.F.S.) process.

ii) One step pick up of a cluster of nucleons by a nucleon.

iii) Formation of a complex particle after the constituent nucleons have been excited in a cascade (Quasi equilibrium process).

Bertini[96] and Gabriel, Alsmiller[81] have developed Monte-Carlo cascade calculations for nucleon and photon induced reactions based on the quasi-free scattering model, which have been successfully applied for nucleon emission. The equilibration proceeds via a series of two body collisions in the nucleus. Complex particle emission is only considered in the evaporative stage of the calculations of Gabriel and Alsmiller and Barashenkov et al.[97] and these are the only two cascade calculations at present applicable to photon induced reactions. Thus, such calculations cannot explain the high energy particle spectra

presented in Section 3.4.1 of this thesis.

An alternative quasi-free scattering model in which particle decay rates are calculated by considering the phase space available, and is thus not geometry dependent, has been successfully applied to (p, α) reactions[98,99] by Scobel, Blann and Mignerey. This model has not as yet been applied to photonuclear reactions.

Pick up reaction amplitudes leading to low lying final states in (p, α) reactions have been shown to dominate knock-out components[100] and this may be important in the emission of high energy complex particles following a nucleon cascade. Experimentally observed (p, X) spectra, (where X = α, d, t, ^{3}He), have been predicted by combining calculated pick-up spectra with exciton model results[101]. However normalisation factors are required in these calculations and the inclusion of a pick-up component contradicts the calculations of Scobel[98], who assumes that cascade nucleons interact with a pre-formed complex particle. Alpha particle energy spectra obtained by Scobel using this assumption agree reasonably well with experimental data. There are therefore doubts as to the validity of the pick-up model which is also at present inapplicable in the case of photon and electron induced reactions.

In a pre-equilibrium reaction particles are emitted during equilibration of the nucleus, while a quasi-equilibrium condition assumes particle emission from a particle-hole state which is itself at equilibrium. The pre-equilibrium exciton model uses a quasi-equilibrium condition in its formalism. The pre-equilibrium exciton model first proposed by Griffin[83] and since developed by a number of authors[84] has been used successfully to explain energy spectra and excitation functions of complex particles emitted following excitation by protons, neutrons and alpha particles[80,82,102] and references therein.

Wu and Chang[80] have had some success in predicting neutron cross sections for bremsstrahlung induced reactions and have developed an exciton model code PREQEC, which will calculate energy spectra differential in energy for electron and bremsstrahlung induced complex particle emission. Using this code good agreement between experimental alpha particle energy spectra for electro excitation of Au and Ni and exciton model calculated results has been obtained[7].

Exciton model calculations use an equispacing approximation to the Fermi gas model to calculate the level densities in the nuclei. This approximation is obviously invalid for such a light nucleus as ^{12}C, thus exciton model calculations were not attempted for ^{12}C. Exciton model calculations of particle energy spectra were performed for Aℓ, ^{NAT}Ni, ^{92}Mo, ^{94}Mo, ^{NAT}Sn, Ta and Au for the emission of alphas, deuterons, tritons and ^{3}He particles.

Comparisons between the results of statistical and exciton model calculations and experimental data are made in the following sections.

4.1.2 Statistical model

The statistical compound nucleus model, as applied to photonuclear reactions, assumes the formation of an excited nucleus, due to the absorption of either a real or virtual photon, which then de-excites by evaporation of one or more particles. It is assumed, for electron induced reactions, that E1 virtual photon absorption is the dominant process. This assumption is valid to approximately 10% for photon energies up to about 120 MeV[6,32]. The (γ, X) cross section is usually given in terms of the total reaction cross section. It can, however, be given in terms of the total photoneutron cross section, which has

been experimentally measured for many nuclei. This is the form used in the statistical model calculations carried out for this thesis work, i.e.

$$d\sigma_{\gamma,X}(E_\gamma,E_X) = \frac{\sigma_{\gamma,n}(E_\gamma)\Gamma_X(E_\gamma,E_X)dE_X}{\int\Gamma_n(E_\gamma,E_n)dE_n} \quad (103) \qquad (4.1)$$

where Γ_X = complex particle channel exit width

Γ_n = neutron channel exit width.

The total photoneutron absorption cross section is approximated by the measured single photoneutron cross section $[\sigma(\gamma,n) + \sigma(\gamma,pn)]$. The values used for the photoneutron cross sections in the statistical model calculations performed are shown in Fig. 4.1. In the energy region used in these calculations ($E_\gamma \sim 10 - 30$ MeV) the (γ, pn) cross section is very small, thus the approximation is valid. The photoneutron cross sections are known for most cases only up to a photon energy of about 30 MeV. Thus a limit of 30 MeV is imposed on the calculation of the particle emission cross sections.

The (e,X) cross section is then calculated from the (γ, X) cross section using the expression:

$$d\sigma_{e,X}(E_e,E_X) = \int_{-Q_n}^{30} d\sigma_{\gamma,X}(E_\gamma,E_X)N^{E1}(E_e,E_\gamma)E_\gamma^{-1}dE_\gamma$$

assuming only E1 virtual photon absorption.

Q_n = photoneutron Q value

N^{E1} = electric-dipole virtual photon intensity spectrum calculated using analytic expression of Nascimento[66] (see Section 1.7).

The neutron and complex particle channel widths were calculated using a modified form[104] of the computer coder HAUSER[105]. The

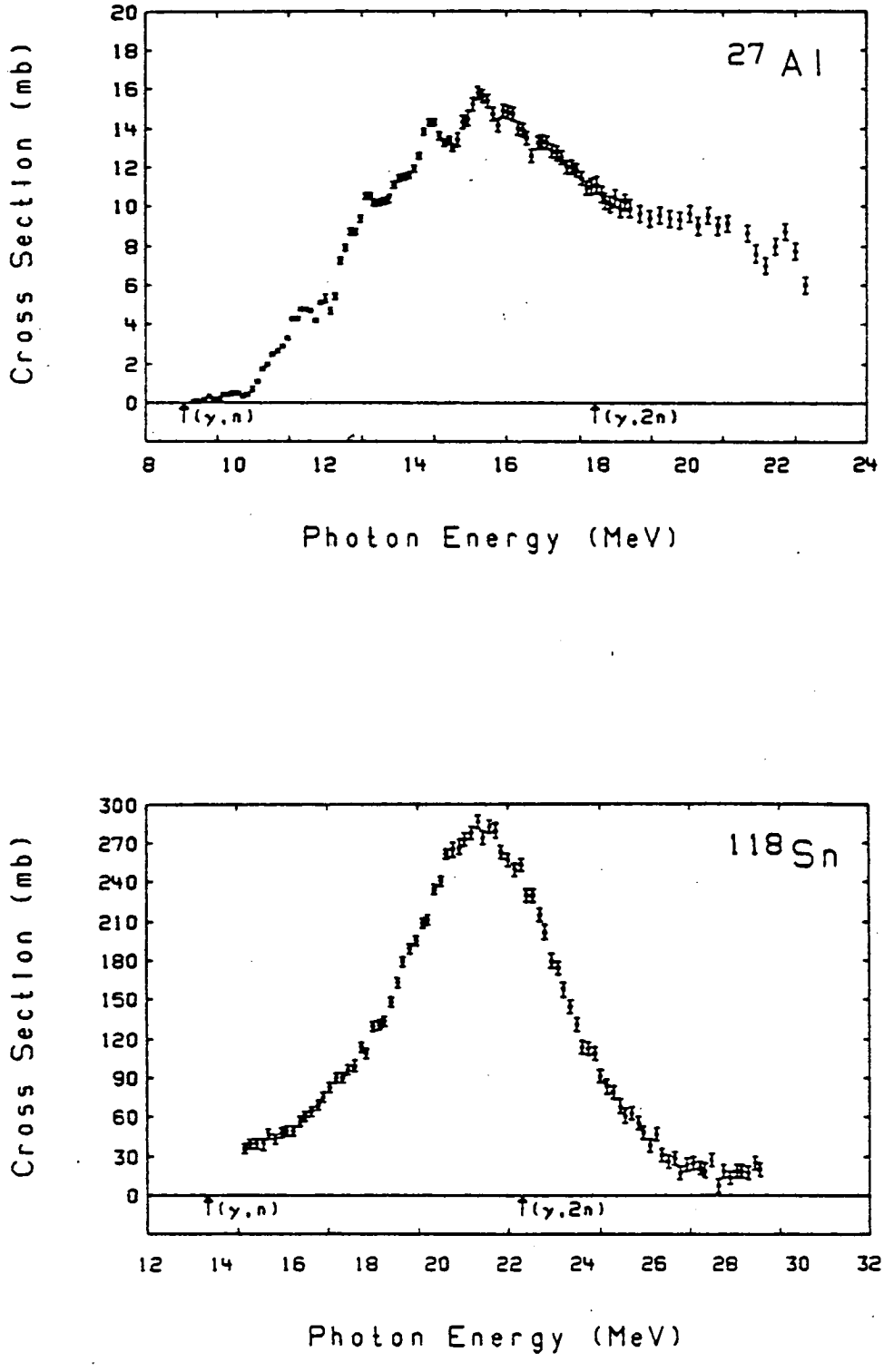

Fig. 4.1 Measured single photoneutron cross sections for ^{27}Aℓ and ^{118}Sn.

transmission coefficients which give these exit channel widths were calculated, using the relevant optical potentials for the various decay channels. The optical model parameters used in these calculations were taken from the tabulation by Perey[106] and are given in Table 4.1 where

V,R,A are real optical potential, radius and diffuseness.

W,RW,AW - Imaginary volume potential, radius, diffuseness.

WD,RD,AD - Imaginary surface potential, radius, diffuseness

VSO,RSO,ASO - spin orbit potential, radius, diffusness.

RC - Coulomb radius parameter.

The transmission coefficients must be summed over all possible decay channels. However, the individual levels of the residual nucleus are only known fully up to a certain, low excitation energy (typically 3 MeV). Above this energy the level density formulae of Gilbert and Cameron[107] are used to estimate the energy levels. Gilbert and Cameron use an enpirical formula, which gives a good fit to the experimental data, up to an excitation energy of approximately 10 MeV. For high excitation energies, a level density formula derived from the Fermi Gas model of the nucleus is used. These two formulas are represented as curves and fitted tangentially to give values for the level density over the complete range of excitation energy. The parameters used to calculate these level densities are taken from Gilbert and Cameron and given in Table 4.2.

The cross section formula (equation (4.1)) applies for target nuclei of spin zero. Thus, in calculating the (e, α) cross section for ^{NAT}Sn (A = 118.69) the optical model parameters, level density parameters and Q value for a ^{118}Sn target nucleus, a spin zero nucleus, are used. The inherent uncertainty in the whole evaporation calculation (± 50%) is so large that the approximation of using the

TABLE 4.1

Optical Model Parameters

	V	R	A	ω	Rω	Aω	ωD	RD	AD	VSO	RSO	ASO	RC
^{27}Aℓ(e,α)	54.94	1.656	0.589	10.36	1.656	0.589	0	0	0	0	0	0	1.2
^{27}Aℓ(e,t)	126.0	1.4	0.64	34.6	1.4	0.64	0	0	0	0	0	0	1.25
^{27}Aℓ(e,n)	49.9	1.22	0.65	0	0	0	7.14	1.24	0.48	8.0	1.22	0.65	1.2
Sn(e,α)	46.2	1.523	0.574	11.8	1.523	0.574	0	0	0	0	0	0	1.3
Sn(e,n)	46.0	1.35	0.4	4.6	1.35	0.4	0	0	0	0	0	0	1.2

TABLE 4.2

	Pairing energy corrections P(Z) + P(N)	Level Density Parameter a	Excitation Energy E_x
^{26}Al	4.26	3.65	6.8
^{23}Na	5.13	3.68	11.9
^{24}Mg	5.13	3.82	13.0
^{117}Sn	2.51	16.7	4.3
^{114}Cd	2.68	17.43	7.5

^{118}Sn isotope in the calculations is valid. The ground state of ^{27}Aℓ is of spin $\frac{5^+}{2}$, thus there are three possible spins of the compound nucleus state following E1 virtual photon absorption, namely $\frac{3}{2}$, $\frac{5}{2}$, $\frac{7}{2}$. Calculations for the ^{27}Aℓ (e, α) evaporation spectrum are carried out for the $\frac{3}{2}$ and $\frac{7}{2}$ compound nucleus states. A comparison of the two calculated spectra with the experimental data, is shown in Fig. 4.2. The two calculated spectra are within ± 50% and it is assumed that the calculated (e, α) spectrum, when all three compound nucleus states are taken into account, would lie somewhere between the two spectra. It was thus only felt necessary to perform the evaporation calculation of the Aℓ(e,t) spectrum for one of the compound nucleus states (namely $\frac{3}{2}$ spin state).

To ensure that the evaporation calculation only considered particles resulting from excitation of the giant dipole resonance region, a cut off of ∿ 30 MeV photon energy was imposed on the virtual photon absorption. Above this energy the cross section for photon absorption resulting in compound nucleus formation is uncertain - the dominant mechanism for photon absorption being the quasideuteron process at higher photon energies (∿ 40 to 150 MeV).

Isospin selection rules state that excitation of the G.D.R. results in a change of isospin of $\Delta T = 1$ for $N = Z$ nuclei and $\Delta T = 0 \pm 1$ for $N \neq Z$ nuclei. On the basis of isospin allowed transitions both the $T_<$ and $T_>$ giant resonance states may neutron decay but only the $T_<$ states may alpha decay where $T_< = T_o$ and $T_> = T_o + 1$ for $N \neq Z$. Thus only the $T_<$ neutron channel should be considered in the application of equation 4.1. However there is evidence of almost complete isospin mixing of the $T_<$ and $T_>$ states in medium and heavy nuclei[108]. Statistical model calculations performed, assuming complete isospin mixing, agree well with experimental (e, α) energy spectra[8] and

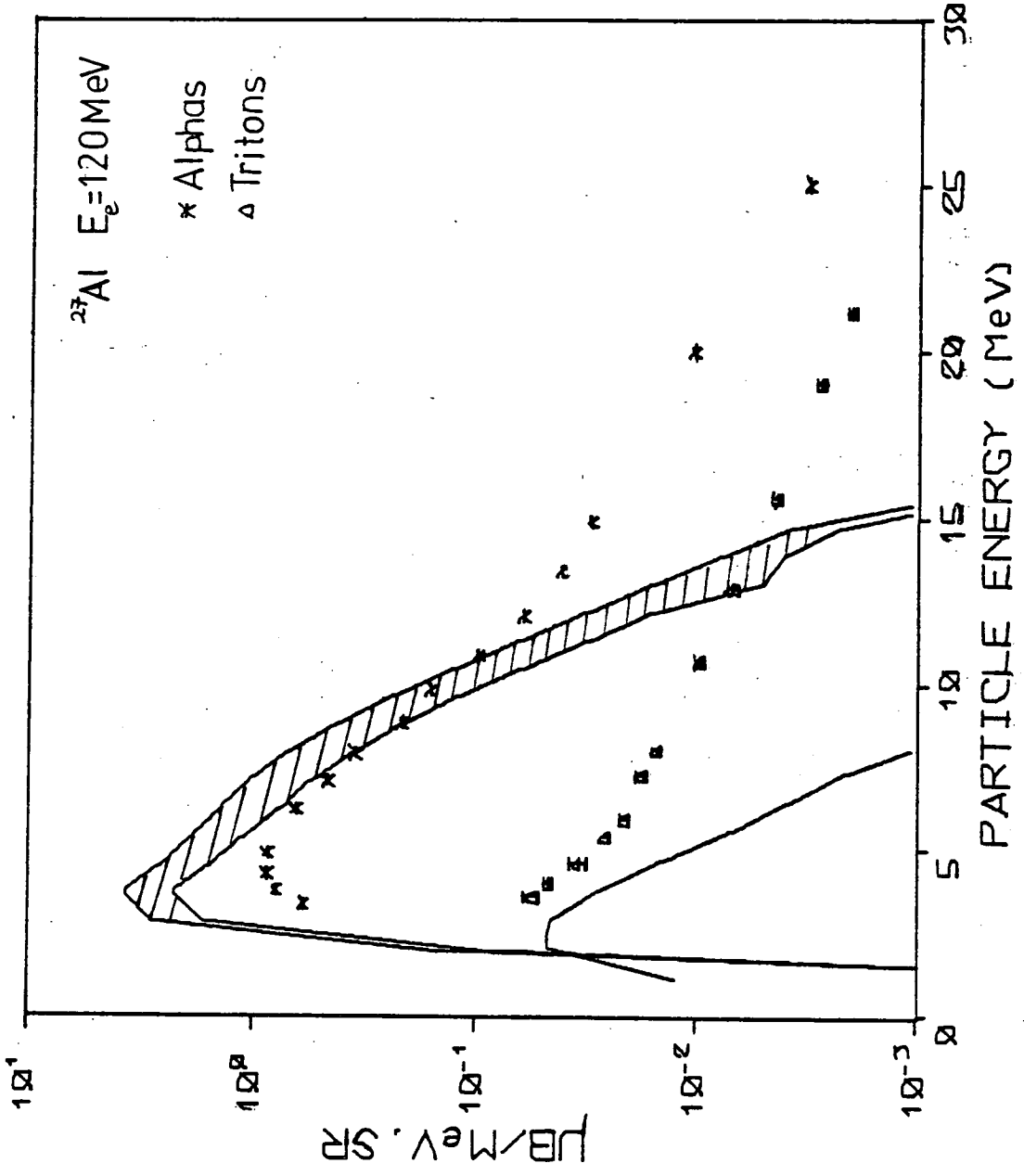

Fig. 4.2 Comparison of data and statistical model calculations for tritons and alphas from ^{27}Aℓ. Solid line is the triton statistical model result. Hatched area shows the probable alpha statistical model result, i.e. between the results obtained for a $^{3}/_{2}^{-}$ and a $^{7}/_{2}^{-}$ excited state.

thus total isospin mixing is assumed in these calculations and the total (γ, n) cross section is used.

4.1.3 Comparison of the results of statistical model calculations with experimental data.

Fig. 4.2 shows the experimental energy spectra for alphas and tritons emitted from $^{27}A\ell$ together with statistical model calculation results. The statistical model calculations give angle integrated cross sections which are divided by 4π, assuming an isotropic angular distribution, to enable comparison with double differential cross sections, as in this case, where data has been taken at 30°. The position of the calculated alpha peak is about 1 MeV below the measured result, while its magnitude is a factor of 3 times greater than the experimental data. The fit to the alpha peak is reasonable considering the large uncertainties in the calculation. Above E_{α} = 10 MeV, the discrepancy between the measured and calculated results becomes increasingly marked as the alpha energy increases. Some other reaction mechanism clearly dominates at high alpha energies. Attempts have been made to predict this high energy component using the pre-equilibrium exciton model. This is discussed further in Section 4.1.4.

Measurements of the cross section for tritons emitted from $^{27}A\ell$ with energies < 3 MeV could not be obtained due to experimental limitations. Thus the position of the peak of the triton energy spectrum could not be ascertained. The coulomb barrier for the emission of tritons from $^{27}A\ell$ is at an energy of $\sim$ 3MeV. The peak of the triton spectrum is thus expected to be positioned at about this energy, and from a consideration of the data, it appears likely that the magnitude of the peak will not exceed 10^{-2} μb/MeV.sr.

Thus it seems that the statistical model calculation result gives good agreement with both the position and magnitude of the peak, within the uncertainty of the calculation. Above E_t = 7 MeV there is a large discrepancy, increasing with triton energy, between the calculated results and the data. Pre-equilibrium exciton model calculations have been carried out in an attempt to explain this high energy tail (see Section 4.1.4).

A comparison of the statistical model calculation for the emission of alpha particles from ^{NAT}Sn with the experimental data is shown in Fig. 4.3. It can be seen that neither the peak position nor the magnitude are explained by the statistical model results.

The predicted peak position ($\sim$ 11 MeV) is in good agreement with the calculations of Menneghetti and Vitale[20] who predicted peak positions of 11 MeV and 12 MeV for Ag and In, A = 107.9 and 114.8, respectively. The energy of alphas emitted following giant resonance excitation is approximately the same as the coulomb barrier height for Sn. Thus the statistical component will be much reduced as in Fig. 4.3.

Some other reaction mechanism is therefore required to explain both the peak and high energy tail. The results of pre-equilibrium exciton model calculations for Sn are discussed in the following sections.

4.1.4 Pre-equilibrium exciton model

The pre-equilibrium exciton model first developed by Griffin[83] and extended by many authors[84] assumes that equilibrium between target and projectile is achieved by a succession of two body interactions. A composite nucleus is formed in an initial particle hole state which then proceeds to a series of more complex states via energy conserving two body interactions until statistical equilibrium is attained. Particles

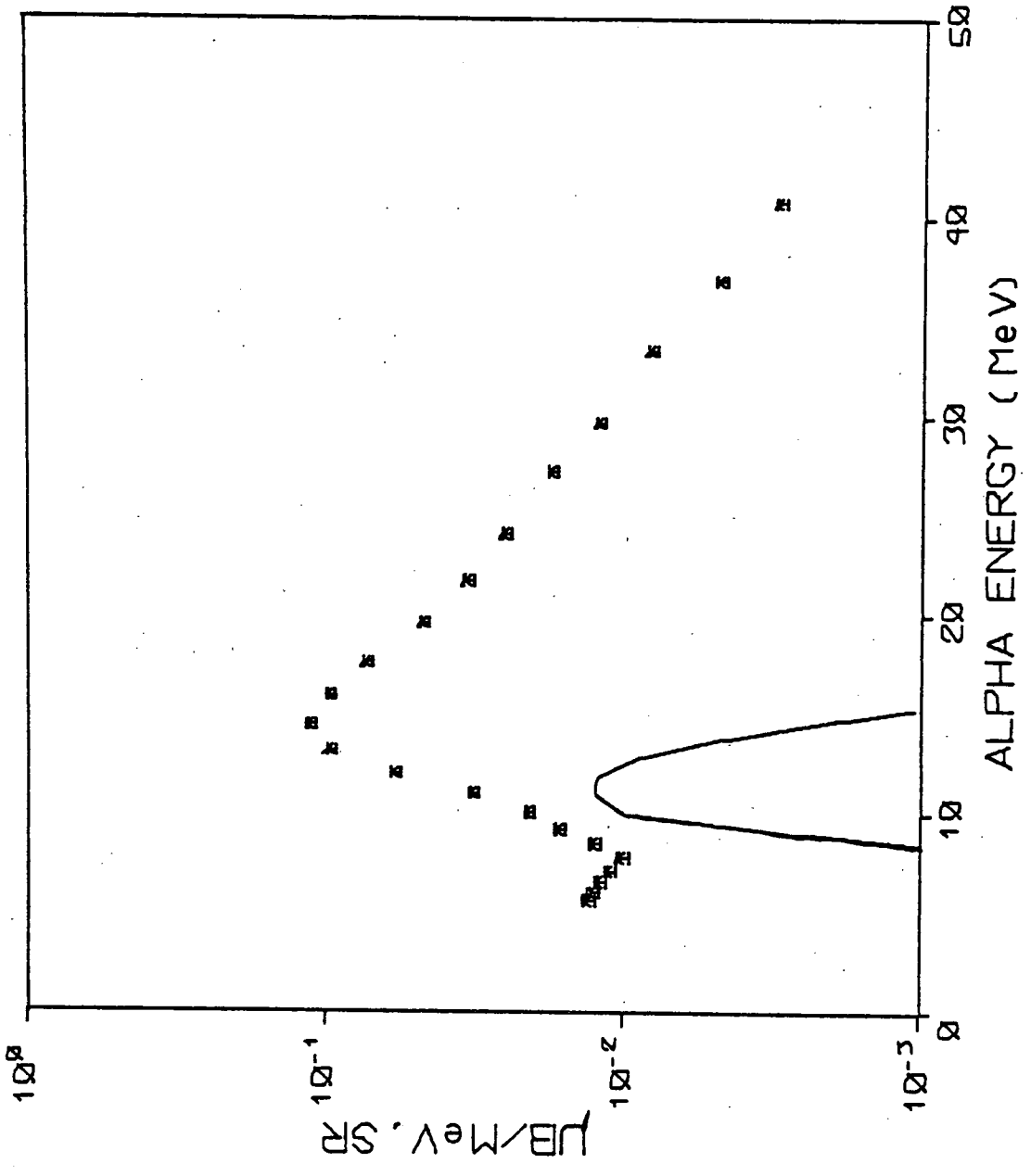

Fig. 4.3 Comparison of data and statistical model calculation for alphas from ^{NAT}Sn. Solid line is the statistical model result.

may be emitted from each intermediate state during the equilibration process. The exciton model calculation used in this work is that of Wu and Chang and a detailed description of the model is given in references (80) and (82).

The general expression for the pre-compound decay probability per unit time of a particle B of channel energy ε, from a given particle (p) hole (h) state is given by[82]

$$\omega_B(p,h,E,\varepsilon)d\varepsilon = \frac{\Gamma_B(p,h,E,\varepsilon)}{\hbar} d\varepsilon$$

$$= \left[\frac{\omega(p-p_B,h,U)}{\omega(p,h,E)} R_B(p)\gamma_B\omega(p_B,0,E-U)dE\right] \lambda_B^C(\varepsilon)$$

$$= \frac{2S_B+1}{\pi^2\hbar^3} \mu_B\sigma_B(\varepsilon)d\varepsilon \frac{\omega(p-p_B,h,U)}{\omega(p,h,E)} \frac{\omega(p_B,0,E-U)}{g_B} R_B(p)\gamma_B \quad (4.2)$$

$\lambda_B^C(\varepsilon)$ is the emission rate of particle B at energy ε into the continuum. S_B, μ_B, σ_B and g_B are the spin, the reduced mass, the inverse cross section and single particle state density for the emitted particle B. U and E are the excitation energies of the residual and composite nuclei and ω the particle-hole state densities. $R_B(p)$ gives the probability that any random p_B nucleons from p excited particles, have the right neutron proton combination to form the emitted particle B. γ_B is the formation probability of particle B, i.e. the probability that a particle formed from the excited nucleons has the right momentum to be emitted as a particle B.

The transition widths for creating a particle-hole pair ($\Delta p = \Delta h = +1$), annihilating a particle-hole pair ($\Delta p = \Delta h = -1$), and for remaining in a given (p,h) state are given respectively by:

$$\Gamma_+(p,h,E) = \pi \cdot |M|^2 \frac{g}{(p+h+1)} (gE - C_{p+1,h+1})^2$$

$$\Gamma_-(p,h,E) = \pi \cdot |M|^2 \, gph(p+h-2)$$

$$\Gamma_o(p,h,E) = \pi \cdot |M|^2 \, g(gE - C_{p,h}) \cdot \left\{ \frac{p(p-1)+4ph+h(h-1)}{p+h} \right\}$$

where $C_{p,h}$ is a correction due to the Pauli exclusion principle and is given by:

$$C_{p,h} = \tfrac{1}{2}(p^2 + h^2)$$

and $|M|^2$ is the square of the average two body transition matrix.

The term $\lambda_B{}^C(\varepsilon)$ in equation (4.2) is given by[80]

$$\lambda_B{}^C(\varepsilon) = \sigma_B(\varepsilon)\nu_B P_B{}^C(\varepsilon)/g_B{}^V$$

where $\nu_B = \left(\frac{2\varepsilon}{\mu_B}\right)^{\frac{1}{2}}$ is the velocity of particle B

and $P_B{}^C(\varepsilon) = \left(\frac{V}{4\pi^2\hbar^3}\right)(2S_B+1)(2\mu_B)^{3/2}\,\varepsilon^{1/2}$

is the density of states of the particle B in the continuum. V is the laboratory volume.

The dominant process for the interaction of photons with a nucleus in the energy range between the giant resonances and the pion threshold ($\sim$ 40 - 150 MeV) (see Section 1.9) is thought to be the absorption of a photon by a neutron-proton pair (or quasideuteron). The quasideuteron mechanism first proposed by Levinger[77] is thus used as the initial interaction in exciton model calculations of photo and electro induced reactions for energies E_e, $E_\gamma \lesssim 150$ MeV. For electron and bremsstrahlung end point energies below $\sim$ 30 MeV, the dominant mechanism for photon

interaction is absorption to the giant resonance region. The total photoabsorption cross section for $E_e, E_\gamma < 35$ MeV is approximated by the experimental photoneutron cross sections obtained with monoenergetic photons as in the statistical model calculations (Section 4.1.2). The input parameters to the exciton model calculation are the Lorentz parameters E_m, σ_m and Γ_m obtained by fitting the experimental cross section to a Lorentz curve, i.e.

$$\sigma(E_\gamma) = \sum_{m=1}^{2} \sigma_m E_\gamma^2 / (E_\gamma^2 + \Gamma_m^{-2}(E_\gamma^2 - Em^2)^2)$$

where E_m = resonance energy

σ_m = peak cross section

Γ_m = full width at half maximum.

It is not possible to accurately fit a Lorentz shape resonance line to the Aℓ data, thus the experimental data is used as a direct input. In the statistical model calculations, this is also the case, Lorentz parameters being used for the photoabsorption cross section for Sn while for Aℓ the experimental data itself is used.

Two slight alterations to the computer code PREQEC were made. One was the amending of the quasideuteron cross section used, as described in the next section, the other the substitution of a distorted wave E1 virtual photon spectrum calculated using the analytic formula of Nascimento[66] in place of the E1 plane wave formula used by Wu and Chang[82]. Finite nuclear size effects[69] on the virtual photon spectrum were ignored. The expected change in spectrum shape and absolute magnitude is negligible (< 10%) for an E1 virtual photon spectrum (see Section 1.7).

The inverse reaction cross sections are calculated from empirical formulas[109]. No essential differences have been found for the inverse

reaction cross sections calculated using the empirical formulas of Wu or from optical model calculations[80], thus the empirical formulas are used to give all the inverse cross sections required. An initial exciton number of $n_o = 4$ is used, corresponding to the formation of a two-particle, two-hole state after absorption of a photon onto a quasideuteron. The choice of the initial exciton number n_o, is very important in determining the shape of the pre-equilibrium spectrum[110], the division of the excitons into particles and holes being much less important. As the initial exciton number is increased the relative number of high energy particles decreases rapidly. High energy particles tend to be emitted early in the equilibration process, coming mainly from states of low exciton number, thus a reasonably low initial exciton number is necessary to predict the data discussed here, which show a pronounced high energy tail. Use of a lower initial exciton number would result in a flatter spectrum shape which would not improve the fits obtained to the data in this case. In the giant resonance region the initial exciton number is $n_o = 2$ due to interaction of the incident photon with the dipole moment of the target nucleus. However to simplify the calculations an initial 2-particle, 2-hole state was used over the whole electron energy range. No significant changes in the calculated energy spectra are seen[80] if a 1p - 1h initial state is assumed over the giant resonance region.

The square of the average two-body transition matrix element $|M|^2$, used to calculate exciton state decay rates, is approximated using the empirical formula of Cline[111], i.e.

$$|M|^2 = K A^{-3} E^{-1}$$

where A and E are the mass number and excitation energy respectively, of the system. The value of K used for electron induced reactions was

100 in all cases. Various values of k were used[80] for exciton model calculations of photon induced neutron emission. A value of $k = 100$ was chosen as giving good agreement to the data over a large range of A values. Due to uncertainties in the value of k, and in the formation factors, absolute cross section values cannot be accurately calculated for electron induced reactions.

The particle binding energies are either taken from the tabulations of Mattauch, Thiele and Wapstra[112] or calculated using a semi-empirical mass formula of Wing and Fong[113]. The particle-hole state density is given by

$$\omega(p,h,E) = \frac{g(gE - A_{p,h})^{p+h-1}}{p!h!(p+h-1)!} \qquad (114)$$

where $A_{p,h} = \frac{1}{4}(p^2 + h^2 + p - 3h)$ is a correction term which takes into account first order effects of the Pauli exclusion principle. g is the single particle state density in the equi-spacing model and is given by $g = \frac{6a}{\pi^2}$, where a is the level density parameter and is taken to be $\frac{A}{8}$ where A is the mass number of the composite nucleus.

Small changes in the single particle state density, g, will not affect the calculated pre-equilibrium spectra[110]. Thus this approximation for a is quite adequate for all the exciton model calculations considered here.

4.1.5 Quasideuteron cross section

The process of absorption of real and virtual photons onto a proton neutron pair, or quasideuteron, first proposed by Levinger[77], is now thought to be the dominant mechanism for photon absorption above the giant resonance (Section 1.9). Levinger showed that the cross section for the absorption of a photon onto a quasideutron within a nucleus ($\sigma_{Q\cdot D}$), is proportional to the cross section for the photodisintegration of a free deuteron (σ_D), i.e.

$$\sigma_{Q\cdot D} = \alpha\sigma_D$$

$$= L\frac{NZ}{A}\sigma_D \qquad (4.3)$$

where α = proportionality constant.

L = Levinger parameter.

NZ = No. of proton-neutron pairs in the nucleus.

Values of 6.4 and 10.3 have been obtained for L by Levinger and Garvey et al.[115] respectively. Several authors, including Levinger[77] and Wu and Chang[80], have suggested that some quenching of the quasideuteron cross section should be introduced as the photon energy decreases. Thus the reduction of the quasideuteron cross section at low energies has been taken into account by multiplying equation (4.3) by an appropriate quenching factor. Levinger originally proposed a value of e^{-30/E_γ} [77] which he has recently amended to a value of e^{-60/E_γ} [116] to take account of blocking of some of the final states of protons or neutrons directly emitted by the quasideuteron, due to the Pauli exclusion principle. In the computer code PREQEC Wu and Chang use a quenching factor of $(1 - e^{-0.1(E_\gamma-40)})$ which assumes a low energy cut off of 40 MeV for the quasideuteron process. This is

a somewhat arbitrary cut off value[117] so a calculation based on Fermi energy level considerations was carried out to determine a quenching value.

4.1.5.1 Fermi gas model considerations

At low photon energies not all of the protons and neutrons in the nucleus can be excited to sufficient energy levels to produce a quasi-deuteron. In the case of either a proton or a neutron the energy available for excitation is $\frac{E_\gamma}{2}$ (see diagram 4.4). The number of energy levels in the nucleus up to the Fermi energy, E_F, is $\frac{N}{2}$ where N = number of neutrons. If the number of levels up to the energy of $(E_F - \frac{E_\gamma}{2})$ is X then the number of neutrons within the energy range of $\frac{E_\gamma}{2}$ is $2(\frac{N}{2} - X)$. The Fermi gas model gives the number of levels in a momentum range $p \rightarrow p + dp$ as

$$\frac{V 4\pi p^2 dp}{h^3}$$

where V = volume of nucleus

$= \frac{4}{3}\pi r_o^3 \cdot A$ assuming a spherical nucleus.

$E = p^2/2m$ $\therefore$ $p^2 = E \cdot 2m$ and $dp = \frac{m \cdot dE}{\sqrt{2mE}} = \frac{E^{-\frac{1}{2}} m^{\frac{1}{2}} \cdot dE}{\sqrt{2}}$

m = mass of neutron.

Thus the number of levels up to the energy $(E_F - \frac{E_\gamma}{2})$ (i e X) is given by

$$\int_o^{E_F - \frac{E_\gamma}{2}} \frac{V \cdot 4\pi}{h^3} E^{1/2} m^{3/2} \frac{2}{\sqrt{2}} \cdot dE$$

$$= \frac{32\sqrt{2}\pi^2 r_o^3 \cdot A}{9h^3} m^{3/2} (E_F - \frac{E_\gamma}{2})^{3/2}$$

Fig. 4.4 Fermi gas well

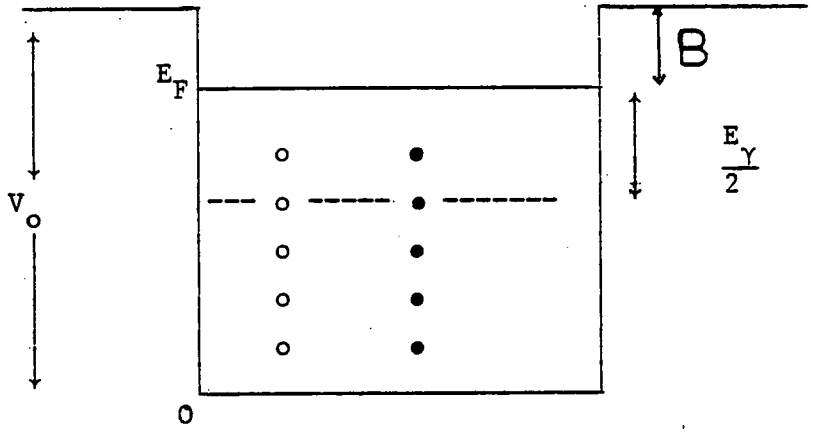

o - neutron

● - proton

E_F = Fermi energy

V_o = Depth of well

E_γ = Energy of incident γ ray

B = Binding energy

where the Fermi energy is given by $E_F = \left(\frac{3h^3 \cdot N}{8\pi \cdot 4\frac{\pi}{3} \cdot Ar_o^3}\right)^{2/3} \frac{1}{2m}$

from the Fermi Gas Model.

Using values of $r_o = 1.24$ fm and $m = \frac{939.55}{C^2}$ MeV

$$X = 0.00143 \cdot A(E_F - \frac{E_\gamma}{2})^{3/2}$$

and $$E_F = 49.63 \left(\frac{N}{A}\right)^{2/3} \text{ MeV.}$$

If N' = number of neutrons excited by photons of energy $\frac{E_\gamma}{2}$ then

$N' = N - 2X$

i.e. $$N' = (N - 0.00286A(49.63 \left(\frac{N}{A}\right)^{2/3} - \frac{E_\gamma}{2})^{3/2}$$

carrying out a similar procedure for protons leads to

$$Z' = (Z - 0.00286A(49.7 \left(\frac{Z}{A}\right)^{2/3} - \frac{E_\gamma}{2})^{3/2}$$

and gives a quasideuteron cross section of

$$\sigma_{Q \cdot D} = L \frac{N'Z'}{A} \sigma_D \qquad (4.4)$$

This method of calculating the quasideuteron cross section uses the Fermi gas model, which gives a reasonable approximation to the nuclear energy levels of the nuclei for which these exciton model calculations are carried out. The nucleus is assumed to be spherical, which will not be true for heavy nuclei such as Au, However these approximations should not invalidate the method.

The Oak Ridge cascade evaporation code (PICA) calculates quasideuteron quenching factors using a Monte Carlo technique. The calculation uses the formula:

$$\sigma_\gamma = 10.3 \frac{NZ}{A} \sigma_D$$

and discounts any excitation process which is forbidden by the Pauli exclusion principle. Table 4.3 gives a comparison of the quenching factors calculated, using the code and those obtained using the method described here, for the nucleus ^{197}Au. The main differences between the methods are i) the factors calculated using the Fermi gas model are considerably higher at all photon energies and ii) using this model quenching is not taken into account above $\sim$ 60 MeV, while with the PICA code some quenching is apparent even at 120 MeV.

The experimental cross section data of Partovi[118] for the photodisintegration of a free deuteron was fitted, using an exponential function, i.e.

$$\sigma_D = e^{(a + bE_\gamma + cE_\gamma^2 + dE_\gamma^3 + eE_\gamma^4)}$$

where the factors a, ... e are given by:

$$a = 7.927 \qquad b = -0.0949 \qquad c = 0.00104$$

$$d = -0.0000058 \qquad e = 0.0000000125$$

to an accuracy of 2%.

Fig. 4.5 gives a comparison of the quasideuteron cross-section calculated using the above exponential approximation to the photodeuteron cross section, and a value of 6.4 for the Levinger parameter with the following quenching factors:

i) factor calculated as outlined above using the Fermi Gas Model.

ii) quenching factor of Wu and Chang[80], i.e. $(1 - e^{-0.1(E_\gamma - 40)})$

iii) e^{-30/E_γ}

iv) e^{-60/E_γ} (Ref. 119)

v) no quenching factor

All calculations are for the nucleus ^{118}Sn.

TABLE 4.3

Comparison of quenching factors calculated by PICA and using equation (4.4) for ^{197}Au.

E_γ	Q from PICA	Q from equation (4.4)
40	0.254	0.533
60	0.494	1.09
80	0.649	1.01
100	0.767	0.99
120	0.883	0.92

TABLE 4.4

f'

Target Nucleus	α	d	t	^3He
^{27}Al	0.00336	0.00112	0.00121	0.000735
^{NAT}Ni	0.000639	0.000935	0.000510	0.000500
^{92}Mo	0.000658	0.001304	0.000555	0.000428
^{94}Mo	0.000474	0.000922	0.000355	0.000353
^{NAT}Sn	0.000660	0.00123	0.000555	0.000251
^{181}Ta	0.000382	0.00111	0.000372	0.000145
^{197}Au	0.000218	0.00122	0.000562	0.000145

f

Target Nucleus	α	d	t	^3He
^{27}Al	-	0.0086	0.0103	0.0075
^{NAT}Ni	0.00393	0.0087	0.0036	0.0032
^{NAT}Sn	0.00313	0.0100	0.0043	-
^{197}Au	0.00126	0.0092	0.0042	0.0012

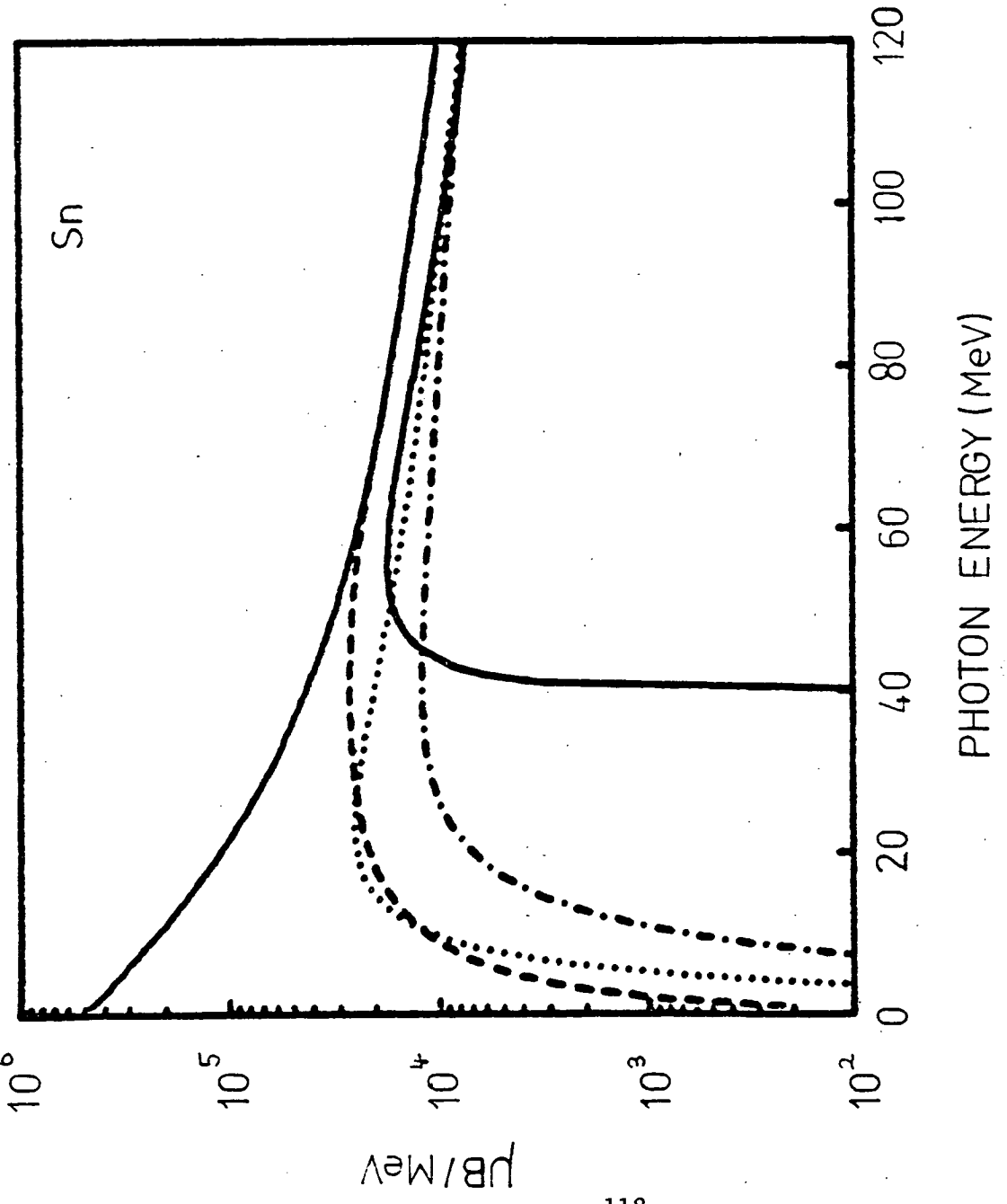

Fig. 4.5 Quasideuteron cross section for ^{118}Sn. The upper solid line shows no quenching and the dashed line is calculated using equation (4.4). The calculations using quenching factors of e^{-30/E_γ}, e^{-60/E_γ} and $(1 - e^{-0.1(E_\gamma - 40)})$ are given by the dotted, dot-dash and lower solid lines respectively.

At energies above ~ 40 MeV the quasideuteron cross section, calculated using the Fermi Gas Model, is higher than any of the other quenched cross sections which still quench the cross section even at 120 MeV. Below 40 MeV the quasideuteron cross section of Wu and Chang is zero by definition. A comparison of the $Pb(\gamma, xn)$ data of Lepetre[75] and the quasideuteron cross section calculated by the above method shows good agreement at high photon energies, although the calculation predicts somewhat more cross section at low photon energies (< 60 MeV) than experimentally observed.

Fig. 4.6 shows the exciton model calculated results of electron induced deuteron emission for ^{197}Au, using the quasideuteron cross section of equation (4.4) and that of Wu and Chang, - the results being normalized at E_d = 22 MeV. From a comparison of the spectral shapes, it is seen that the calculation using the quasideuteron cross section of equation (4.4) gives a better fit to the experimental data than the cross section calculated using the quasideuteron formula of Wu and Chang. This is also true for the other nuclei considered here, as the use of equation (4.4) increases the cross section at low particle energies producing a spectrum which is not as flat as that obtained using the original computer code.

The quasideuteron cross section calculated using equation (4.4) was used for all the exciton model calculations performed for the data presented here. This method gives some cross section below 40 MeV, in agreement with reference (119) and has no quenching above 100 MeV photon energy, in agreement with measured (γ, xn) data at high photon energies[75]. Intuitively, it seems unreasonable to have a low energy cut off at 40 MeV; also a spectrum shape is obtained which is in more agreement with the experimental data. A value of 6.4 was used for the Levinger parameter for all the calculations carried out, although a change in magnitude

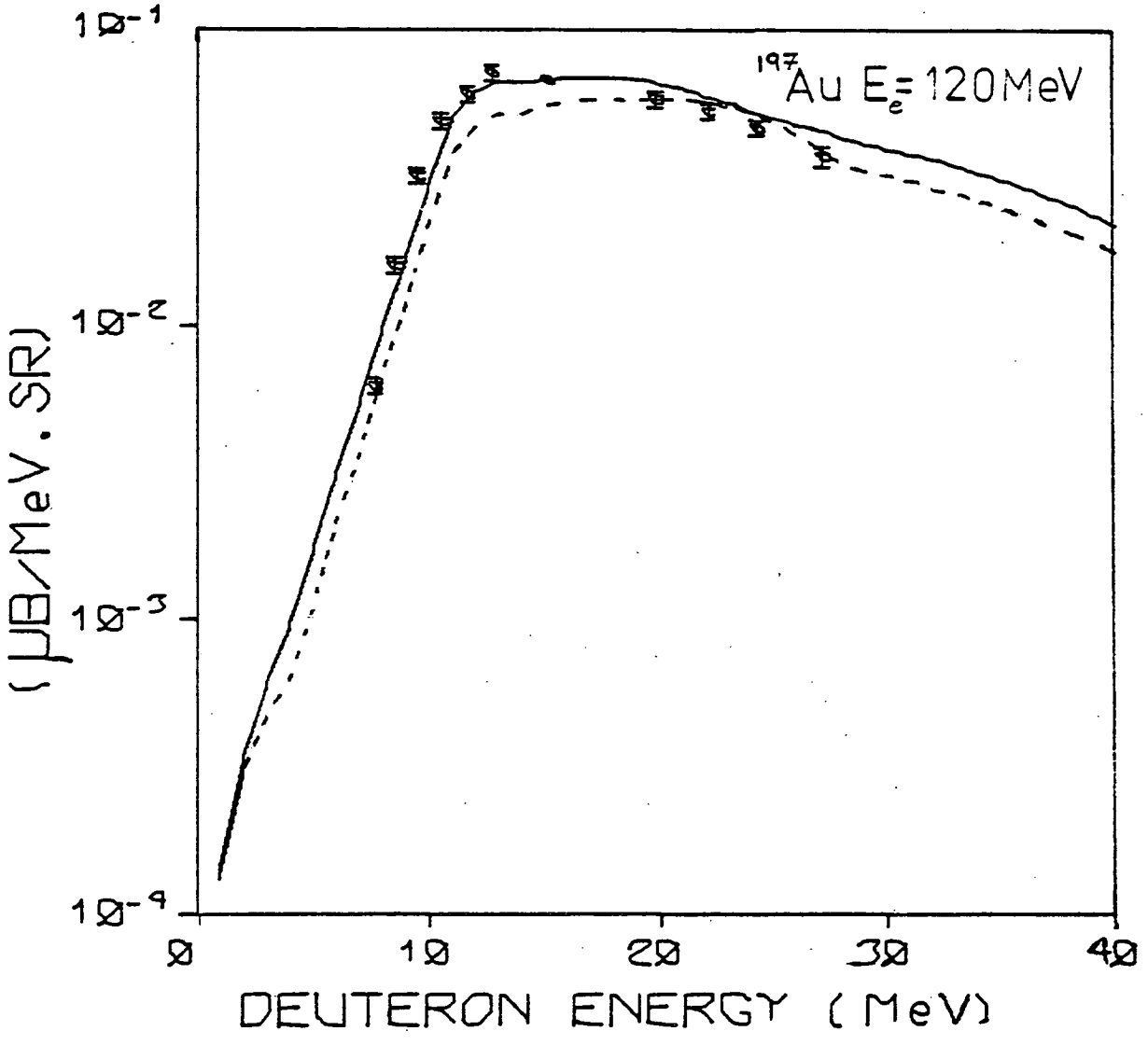

Fig. 4.6 Comparison of data and exciton model results for deuterons from ^{197}Au. Solid line is the exciton model result using the quasideuteron cross section as given by eqn. (4.4). Dashed line is the result obtained using the quasideuteron cross section given in reference 80.

will not alter the calculated spectral shapes.

4.1.6 Formation factors

Within the exciton model code PREQEC formation factors ($\frac{\gamma_B \cdot g}{g_B}$) are used to describe the probability of a certain complex particle B being formed from among the excited nucleons. Wu and Chang[82] have obtained formation factors for the emission of alpha particles, deuterons, tritons and ^{3}He particles from nuclei in particle induced reactions. They define the formation factor as the probability that a particular state has the correct combination of neutrons and protons with the right momentum to form a complex particle.

The high energy section of a particle energy spectrum is made up of particles emitted mainly during the early stages of equilibration - when only a few simple particle-hole states are involved. Assuming that the highest section of a measured differential energy spectrum is a result of particle emission from the simplest particle-hole state from which that particular particle can be emitted, Wu and Chang obtain a factor relating the exciton model calculated energy spectrum for the simplest (p,h) state to the experimental data at one particular particle emission energy.

The constant N_B, which is a function of all the formation factors and transition widths, of the equation:

$$\frac{d\sigma_B^{emp}}{d\varepsilon}(p,h,E,\varepsilon) = N_B \frac{2S_B + 1}{\pi^2\hbar^3} \mu_B \sigma_B(\varepsilon)\varepsilon \frac{\omega(p - p_B, h, U)}{\omega(p,h,E)} \times \frac{\omega(p_B,0,E - U)}{g_B} R_B(p)$$

$$= N_B \phi_B(p,h,E,\varepsilon)/\hbar$$

is obtained by setting $\frac{d\sigma_B^{emp}}{d\varepsilon}(p,h,E,\varepsilon)$ equal to the experimentally measured value of the differential energy spectrum of particle B at a high particle emission energy ε. This equation is derived from the general expression for the pre-compound decay probability of particle B, with energy ε from a certain (p,h) state, given in Section 4.1.4. Values for the state densities (ω) and g_B are given in reference (80), S_B, μ_B, and σ_B are the spin, reduced mass and inverse reaction cross section for particle B. $R_B(p)$ is a combinatorial probability and E and U are excitation energies of the residual and composite nuclei.

The total reaction cross section for the emission of a particle B from the simplest (p,h) state is obtained by integrating $\phi_B(p,h,E,\varepsilon)$ over ε, i.e. $\sigma_B^{emp}(p,h,E) = N_B \Phi_B(p,h,E)/\hbar$. The empirical estimate of the fraction of the total reaction cross section, resulting from this simplest (p,h) state is defined as $f_B^{emp}(p,h,E) = \sigma_B^{emp}(p,h,E)/\sigma_R(E)$. Using the values of f_B^{emp} obtained in this way, the values of γ_B, the formation factors, for the emission of complex particles from a range of nuclei are calculated using:

$$\gamma_B = \frac{f_B^{emp}(p,h,E)\left[\sum_\nu \gamma_\nu \Phi_\nu(p,h,E) + \Gamma_+(p,h,E) + \Gamma_-(p,h,E)\right]}{\Phi_B(p,h,E)\left[P(p,h,E) - \sum_\mu f_\mu^{emp}(p,h,E)\right]} \qquad (4.5)$$

where particle B is a particle with p_B nucleons, the sum ν is over all particles which can be emitted from the $(p-1, h-1)$ state, the sum μ is over all particles which have the state (p,h) as the simplest state from which they can be emitted and $P(p,h,E)$ is the probability of populating the (p,h) state. Γ_+ and Γ_- are transition widths, as given in Section 4.1.4.

The experimental differential energy spectra of Bertrand and Peele[78] at a bombarding energy of E_p = 62 MeV were used by Wu and Chang

to obtain formation factors for the emission of alpha particles, deuterons, tritons and ^{3}He particles from ^{12}C, ^{16}O, $^{27}A\ell$, ^{54}Fe, ^{89}Y, ^{120}Sn, ^{197}Au and ^{209}Bi, using the above method.

The formation factors are dependent on the type of particle emitted and the target nucleus but assumed to be independent of particle and projectile energy. From comparisons of data and calculations for several different bombarding energies it appears that the formation factors are nearly independent of proton bombarding energy but may not be independent of emitted particle energy. Good agreement between exciton model calculated results and data for proton induced reactions, using formation factors obtained in this way, has been observed in those cases that have been studied.

For electron induced reactions the factor $f_B^{emp}(p,h,E)$ the empirical estimate of the fraction of the reaction cross-section resulting from the simplest (p,h) state is very small (typically ~ 0.001). Thus it can be seen from equation (4.5) that the formation factors enter linearly into the exciton model calculations of cross sections. Tests, using the computer code PREQEC, showed that the formation factors (entered as $\frac{\gamma_B g}{g_B}$ in the code) caused linear changes in the high energy portion of the cross section for a factor of ten change in the value of the formation factors in the case of deuterons and about a factor of 3 change for the other complex particles. Deuterons can be emitted from the initial two particle two hole state, unlike the other complex particles, thus simplifying the calculation of $\frac{\gamma_B g}{g_B}$.

Thus, for this thesis work it was decided to calculate the formation factors from a direct comparison of the calculated and experimental high energy section of the energy spectra. This process allows formation factors to be quickly and easily calculated for electron induced reactions.

An initial calculation is performed for one particular nucleus using the formation factors required for the proton induced reaction and the calculated spectra normalized to the high energy part of the experimental energy spectra. The calculation is then repeated using new formation factors obtained from the normalization, assuming the formation factors enter linearly into the calculation and a renormalization to the data is performed if required. Once a set of formation factors is obtained for one nucleus, these can then be used as the initial factors required in the calculations for other target nuclei. If the normalization to the data then required is less than a factor of ten for deuterons and less than a factor of three for the other particles, the new formation factors can be calculated directly from this normalization. If this is not the case the exciton model calculation must be repeated once more to obtain the correct formation factors.

The exciton model calculations yield angle integrated energy spectra which have been directly compared to experimental data taken at $\theta = 30^{\circ}$ and 150°. Thus the formation factors obtained in this way must be adjusted before comparison with formation factors calculated for proton and alpha particle induced complex particle emission. If f is the formation factor obtained by comparison of angle integrated experimental data to angle integrated calculated results and f' the formation factor obtained by comparing double differential experimental cross sections to the calculated exciton model results then:

$$\frac{d\sigma}{dE}\,(\text{calc})\cdot f' = \frac{d^2\sigma}{dE\cdot d\Omega}$$

and

$$\frac{d\sigma}{dE}\,(\text{calc})\, f = \frac{d\sigma}{dE}$$

dividing gives

$$f = \frac{d\sigma}{dE} \cdot f' \,\frac{1}{\frac{d^2\sigma}{dE\cdot d\Omega}}$$

$\frac{d\sigma}{dE}$ is obtained from angular distribution measurements since:

$$\frac{d\sigma}{d\Omega} = \sum_{\nu=0}^{4} A_\nu P_\nu(\cos\theta)$$

where $P_\nu(\cos\theta)$ are Legendre Polynomials

$\frac{d\sigma}{dE}$ is given by $4\pi A_o$.

If f differed from f' by $\sim$ a factor of 10 (as with tritons and ^{3}He particles), corrections had to be made to f to account for the slight nonlinearity of f' in the exciton model code.

Thus values of f, formation factors which can be directly compared to the values of the formation factors $\frac{\gamma_B g}{g_B}$ calculated for proton induced reactions can be calculated from a comparison of the measured double differential cross sections and exciton model calculated angle integrated spectra.

Exciton model calculated spectra which have been normalized, using the formation factors f' as a parameter, to the high energy part of the experimental spectra, are compared to the measured energy spectra in the next section.

4.1.7 Comparison of energy spectra to exciton model calculated results

Figures 4.7 to 4.10 show the comparison between angle integrated exciton model calculation results and experimental energy spectra measured at $\theta = 30^o$ for the emission of alpha particles, deuterons, tritons and ^{3}He particles, respectively. It can be seen that the exciton model calculations predict most of the cross section above the low energy peak. For heavy nuclei such as ^{181}Ta and ^{197}Au where the

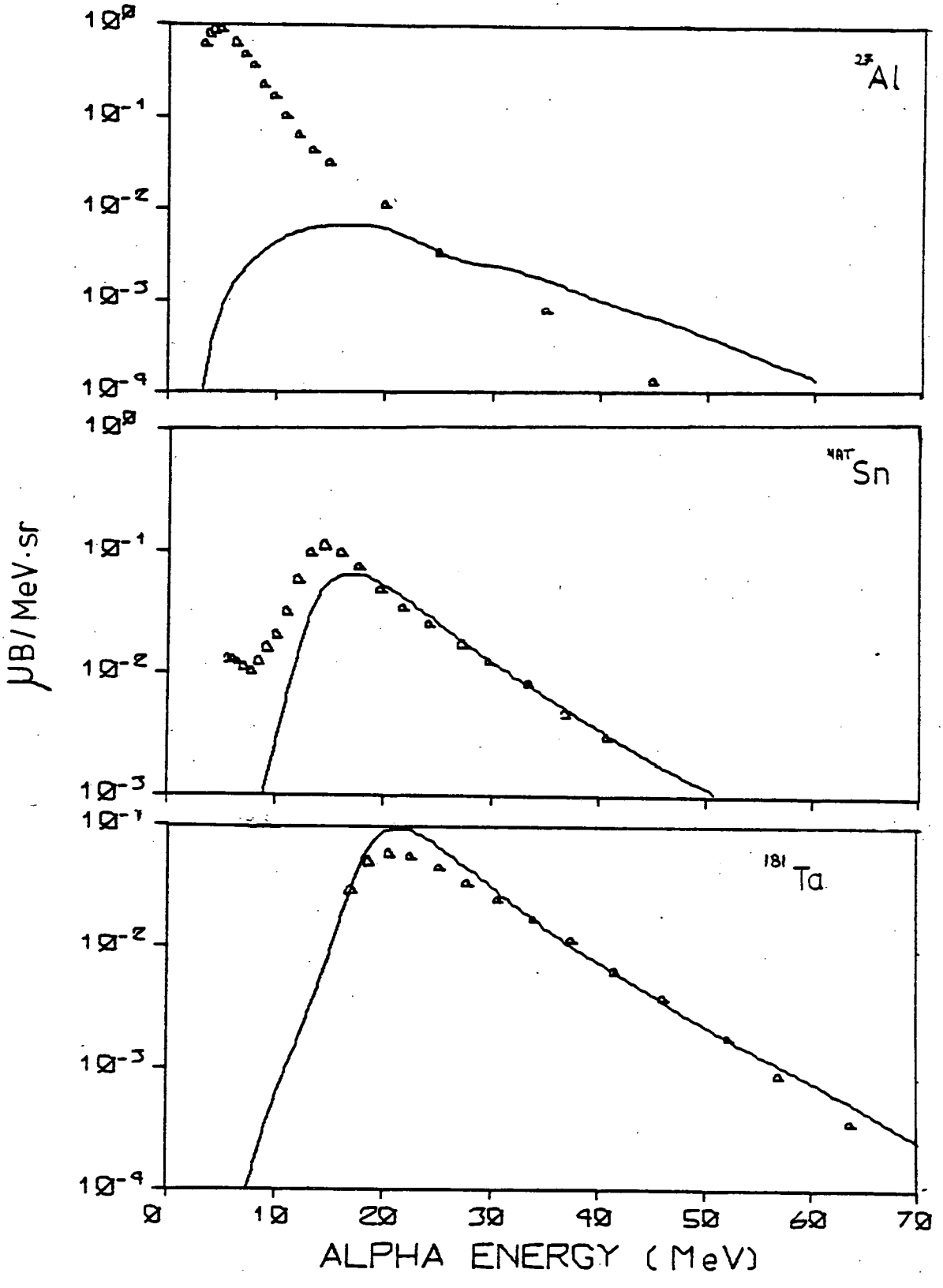

Fig. 4.7 Comparison of measured energy spectra and exciton model calculations for alpha particles. Solid lines are the exciton model results.

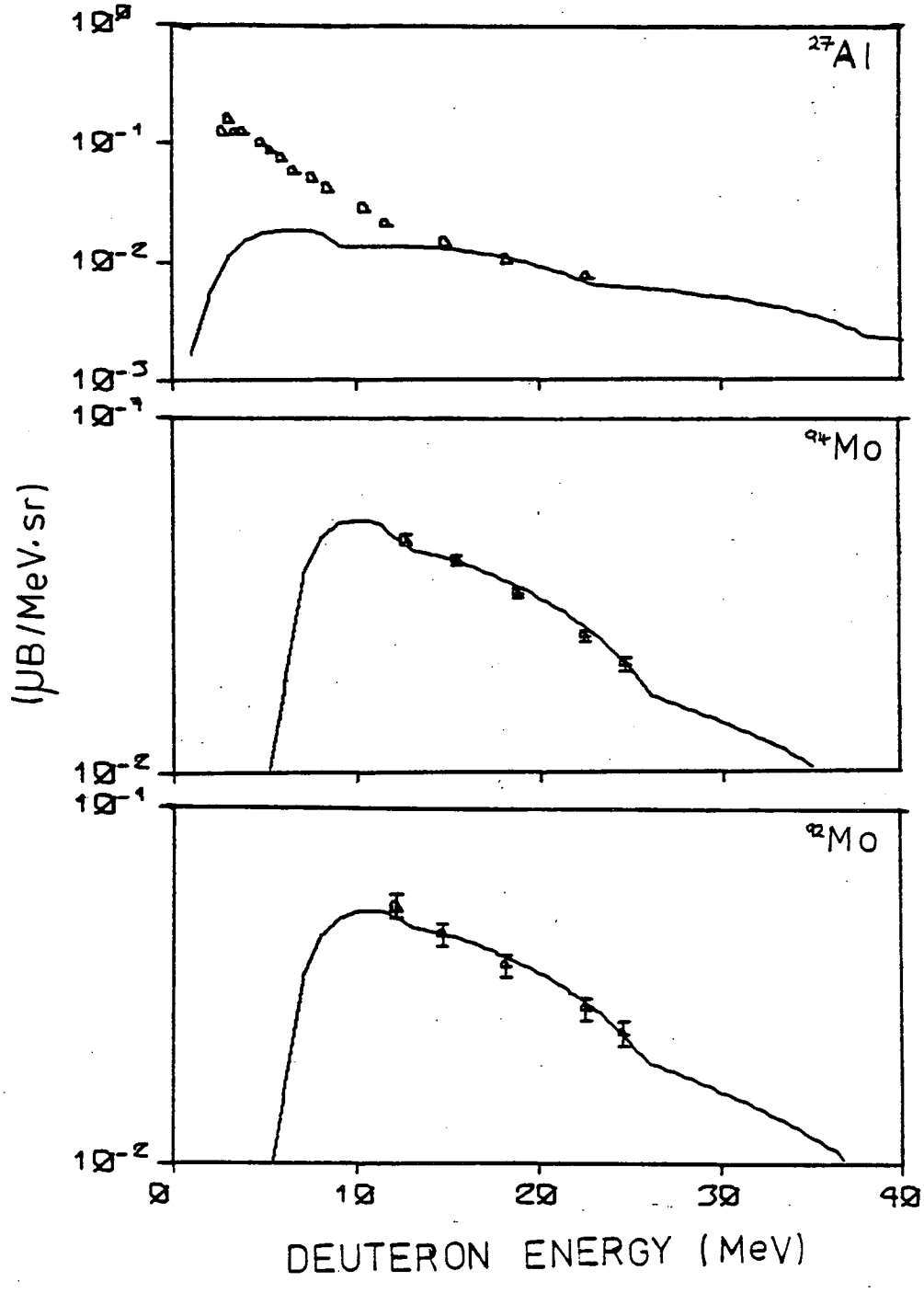

Fig. 4.8(a) Comparison of measured energy spectra and exciton model calculations for deuterons. Solid lines are the exciton model results.

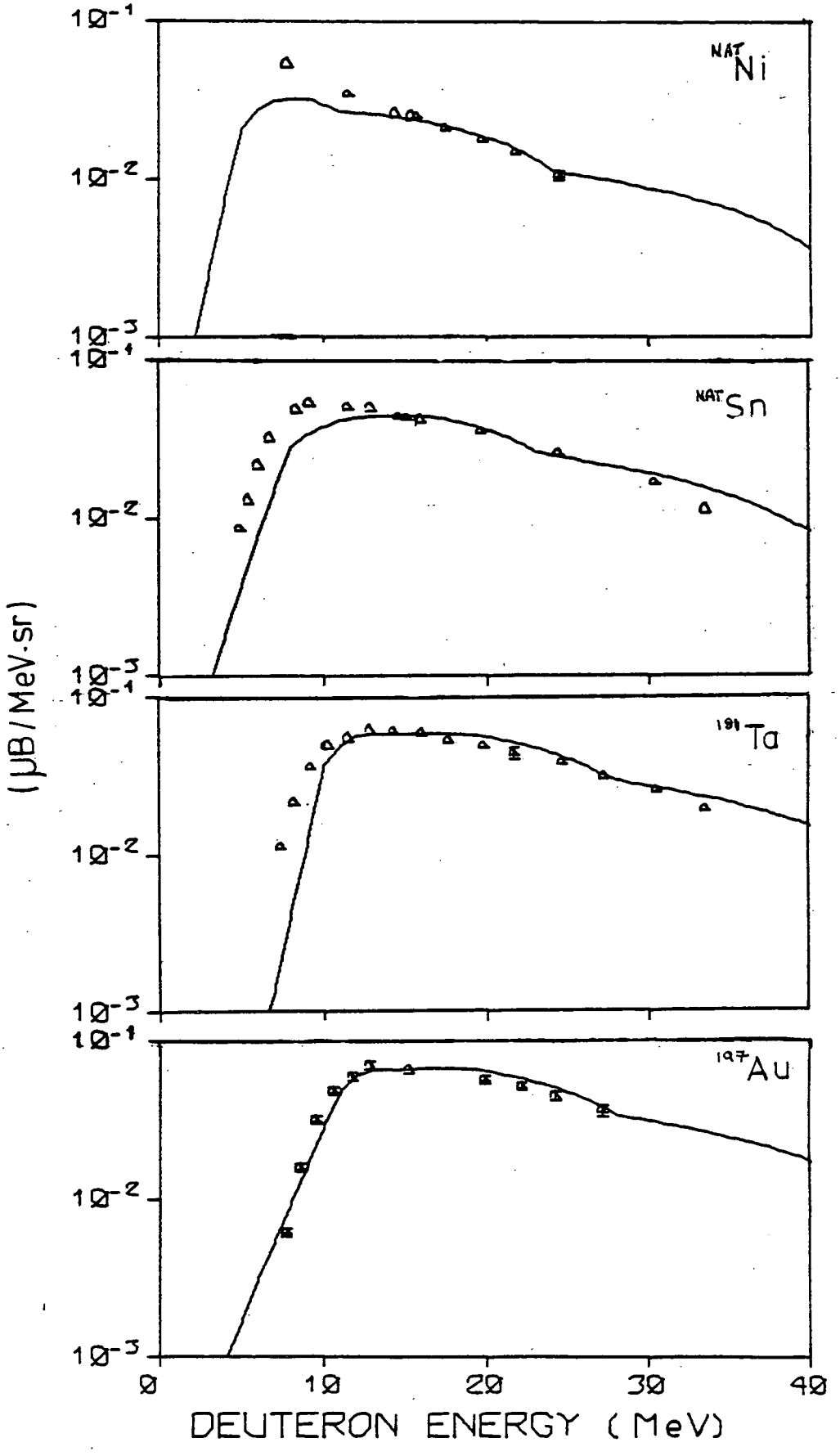

Fig. 4.8(b) Comparison of measured energy spectra and exciton model calculations for deuterons. Solid lines are the exciton model results.

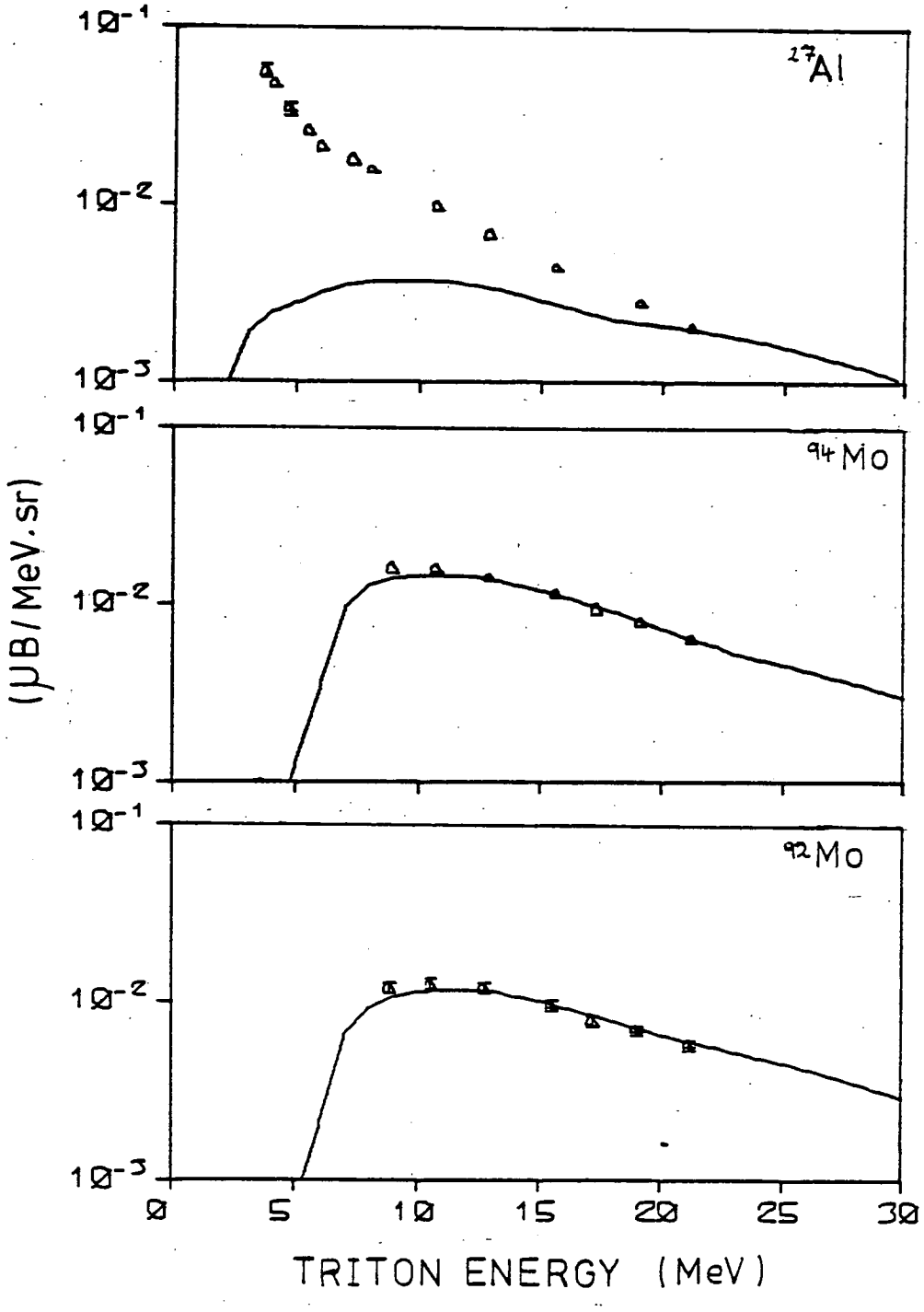

Fig. 4.9(a) Comparison of measured energy spectra and exciton model calculations for tritons. Solid lines are the exciton model results.

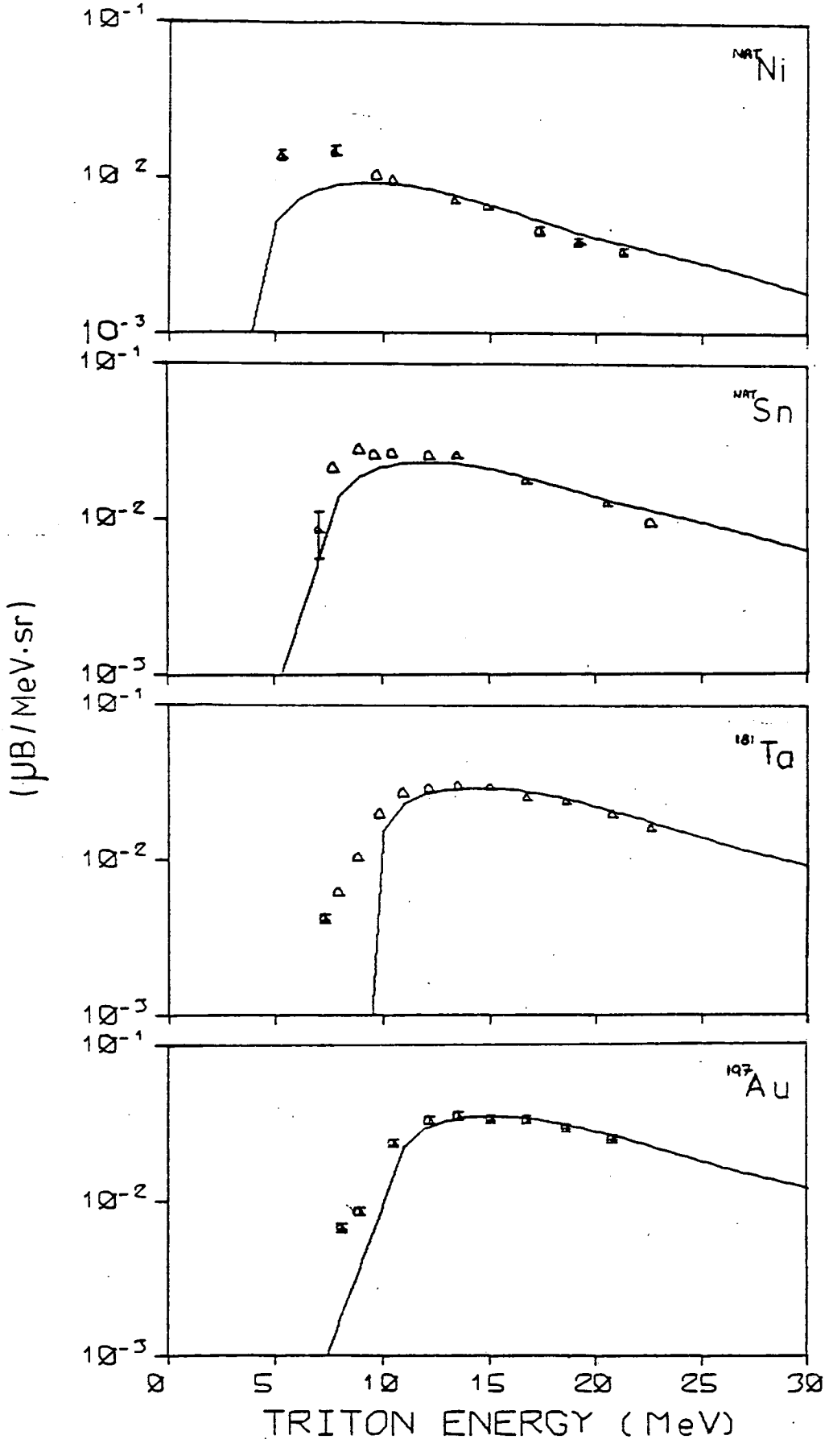

Fig. 4.9(b) Comparison of measured energy spectra and exciton model calculations for tritons. Solid lines are the exciton model results.

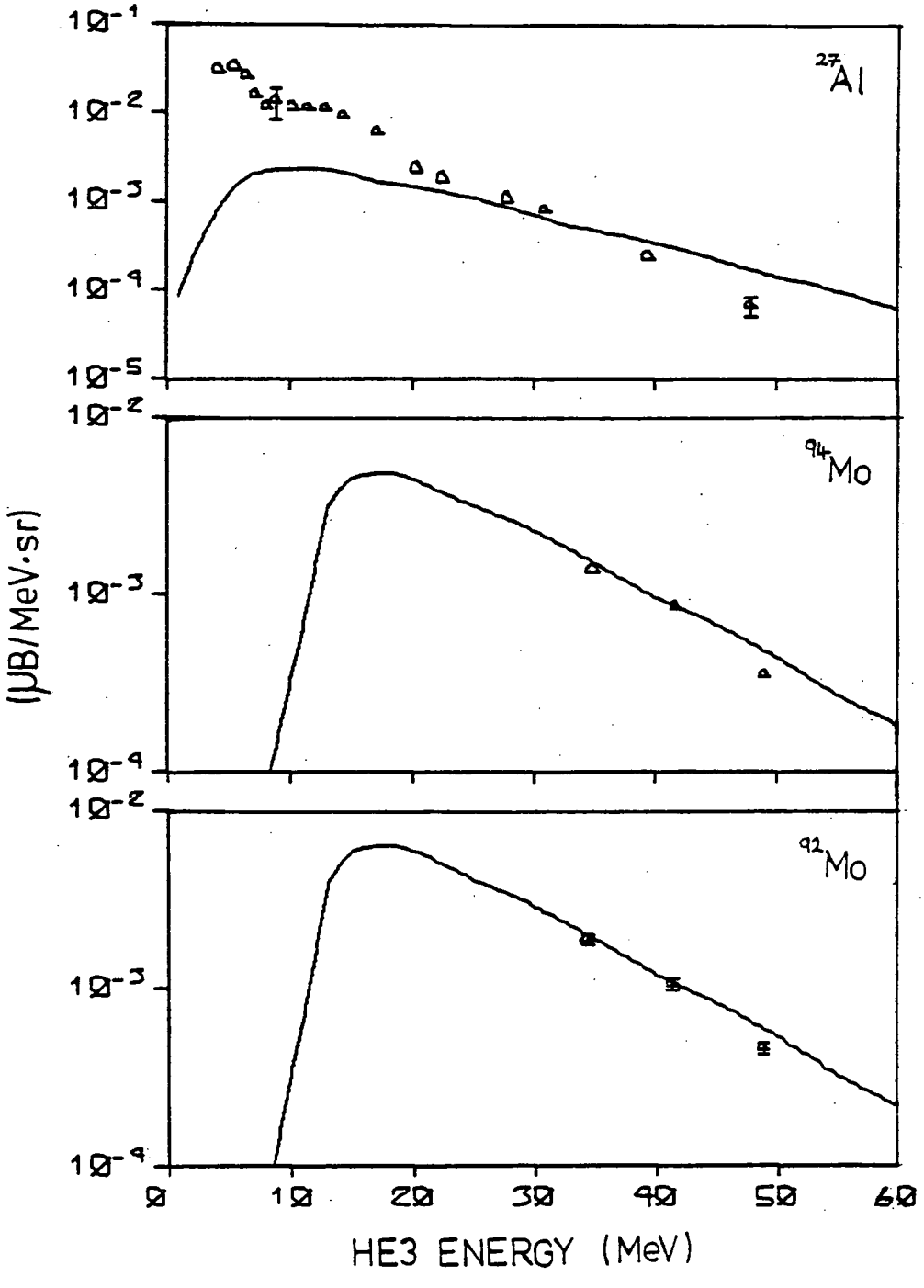

Fig. 4.10(a) Comparison of measured energy spectra and exciton model calculations for ^{3}He's. Solid lines are the exciton model results.

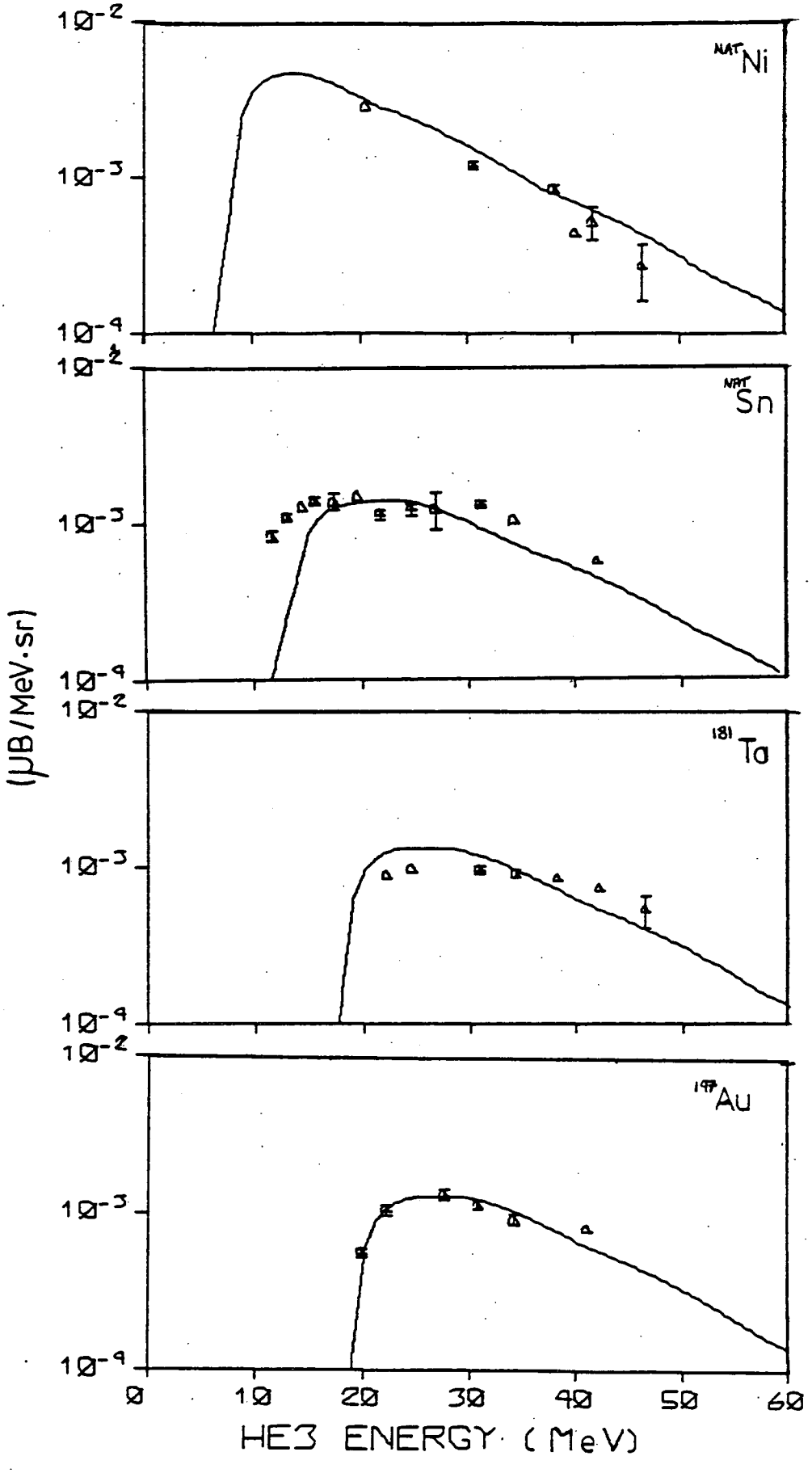

Fig. 4.10(b) Comparison of measured energy spectra and exciton model calculations for ^{3}He's. Solid lines are the exciton model results.

high coulomb barrier inhibits evaporation from the giant resonance region, nearly all of the cross section is predicted by the exciton model calculations. A light nucleus such as ^{27}Al is expected to have a large statistical reaction component, as discussed in Section 4.1.2. At high particle energies statistical model calculations cannot predict the measured cross section and it is expected that these parts of the energy spectra can be explained in terms of the exciton model. However, the calculated exciton model spectra do not predict the high energy portions of the measured energy spectra for ^{27}Al except possibly for the high energy deuterons. This is discussed further in Section 4.1.9.

Exciton model calculations for the emission of deuterons appear to predict the energy spectra for all the nuclei studied here somewhat better than for the emission of other complex particles. This may be because deuterons can be emitted from simpler particle hole states. In the case of alpha emission the exciton model results predict a peak of greater magnitude than the experimental data. This is not really a problem though, as the high energy part of the calculated spectra agrees with the measured cross section. Similar characteristics are observed in the comparison of the exciton model predictions and experimental data for proton induced complex particle emission presented by Wu and Chang[80].

Table 4.4 lists the formation factors f' used to produce the exciton model fits shown in Figures 4.7 to 4.10 plus the values of f obtained by fitting Legendre polynomials to the angular distributions measured at E_α = 50 MeV, E_D = 25 MeV, E_T = 17 MeV and $E_{^3He}$ = 40 MeV for certain of the target nuclei. The A dependence of the formation factors f' and f are determined from plots of $\ell n(f)$ against $\ell n(A)$ and $\ell n(f')$ against $\ell n(A)$, Figures 4.11 and 4.12 respectively. From these plots it seems that the curves follow a power law, i.e. $f = kA^x$ where k and x are constants. Thus $\ell nf = k + x\ell n(A)$ and the slope

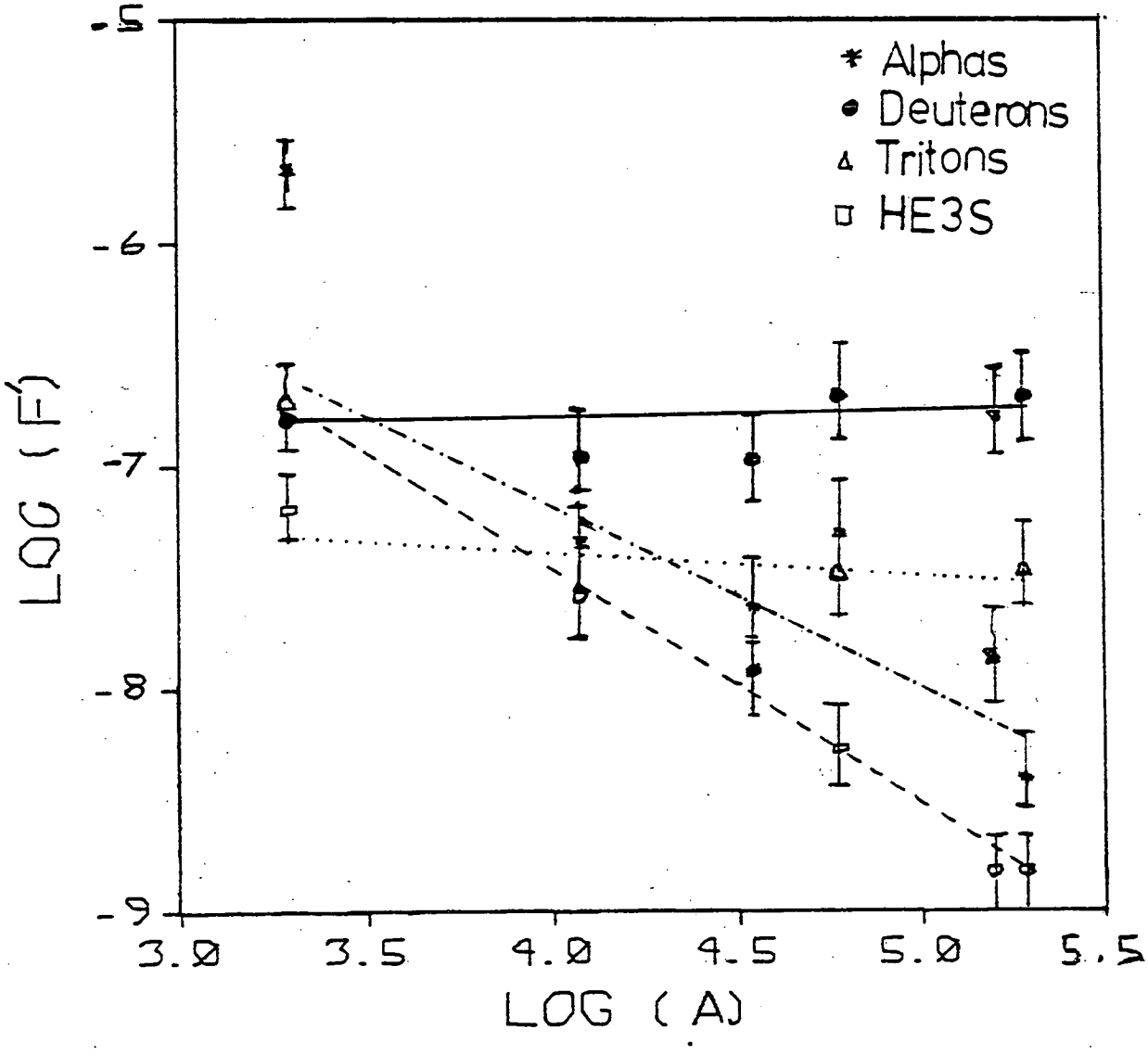

Fig. 4.11 Mass dependence of formation factors f'. Lines drawn as approximate straight line fits to the data points.

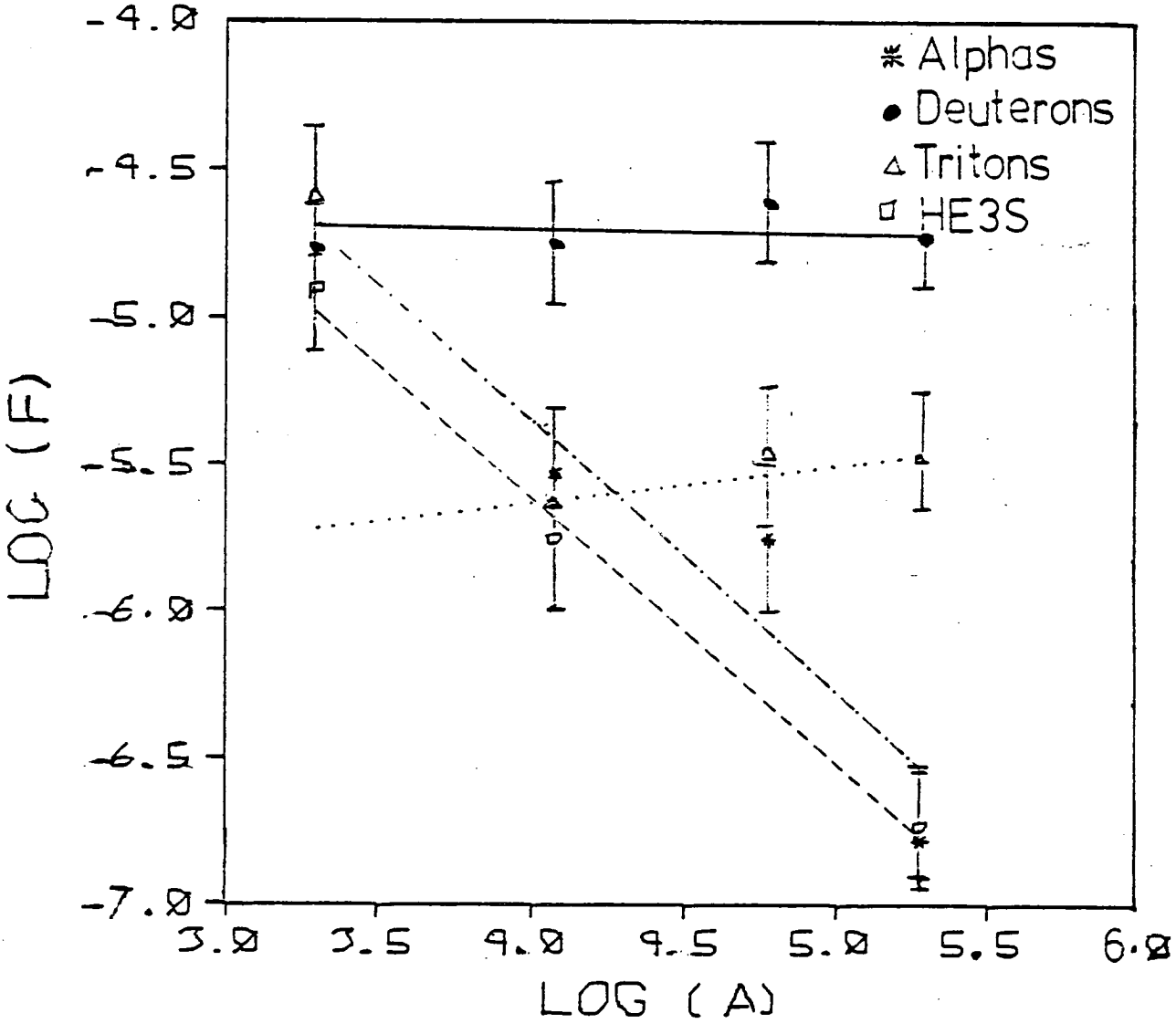

Fig. 4.12 Mass dependence of formation factors f. Lines drawn as approximate straight line fits to the data points.

of a straight line fitted by eye through the points gives the A dependence of the formation factors.

Approximate values for the A dependence of f' and f for alphas, deuterons, tritons and ^{3}He particles are given in Table 4.5.

The values of the formation factors obtained for ^{27}Aℓ are not used in calculating the values of the A dependence in the cases of alpha particles, tritons and ^{3}He particles. For ^{3}He particles the formation factor appears to be rather low in comparison with the factors calculated for the heavier nuclei. As the exciton model calculation seems to have problems in the calculation of energy spectra for ^{27}Aℓ, this value for the formation factor is disregarded. The formation factors chosen for the cases of alpha particles and tritons emitted from ^{27}Aℓ have an arbitrary value dependent on particle energy as the calculation does not predict the experimental data at any particle energy other than that chosen for the normalization.

The uncertainty associated with each of the formation factors is due to the rather arbitrary choice of particle energy at which the calculation and experimental data are normalized.

The formation factors, once they have been corrected for any angle dependence, decrease with increasing mass number for alpha particles and ^{3}He particles and are approximately independent of target mass in the case of deuterons and tritons. Formation factors calculated for use in proton induced reactions have a much greater dependence on mass number than those obtained in this thesis work for electron induced reactions as shown in Figure 4.13. A comparison between the actual values of the formation factors for proton and electron induced reactions for the target nuclei ^{27}Aℓ, Ni, Sn and ^{197}Au is given in Table 4.6. It can be seen that the two sets of formation factors are of the same order of magnitude for all the emitted complex particles. This can

TABLE 4.5

Values for the A dependence of f and f'

Emitted Particle	x for proton induced reaction	x for f'	x for f
Alphas	-1.2	-0.3	-0.8
Deuterons	-1	0	0
Tritons	-1.3	-0.1	+0.1
^{3}He's	-1.3	-1.0	-0.8

TABLE 4.6

Comparison of formation factors for proton and electron induced reactions: at $E_p \sim 62$ MeV, $E_e = 120$ MeV.

Target Nucleus	(p, α)	(e, α)	(p, d)	(e, d)
^{27}Aℓ			0.0305	0.0086
Ni	0.00932	0.00393	0.0268	0.0087
Sn	0.00228	0.00313	0.0178	0.010
^{197}Au	0.00096	0.00126	0.0139	0.0092

Target Nucleus	(p, t)	(e, t)	(p, ^{3}He)	(e, ^{3}He)
Ni	0.00919	0.0036	0.00485	0.0032
Sn	0.00398	0.0043		
^{197}Au	0.00236	0.0042	0.00076	0.0012

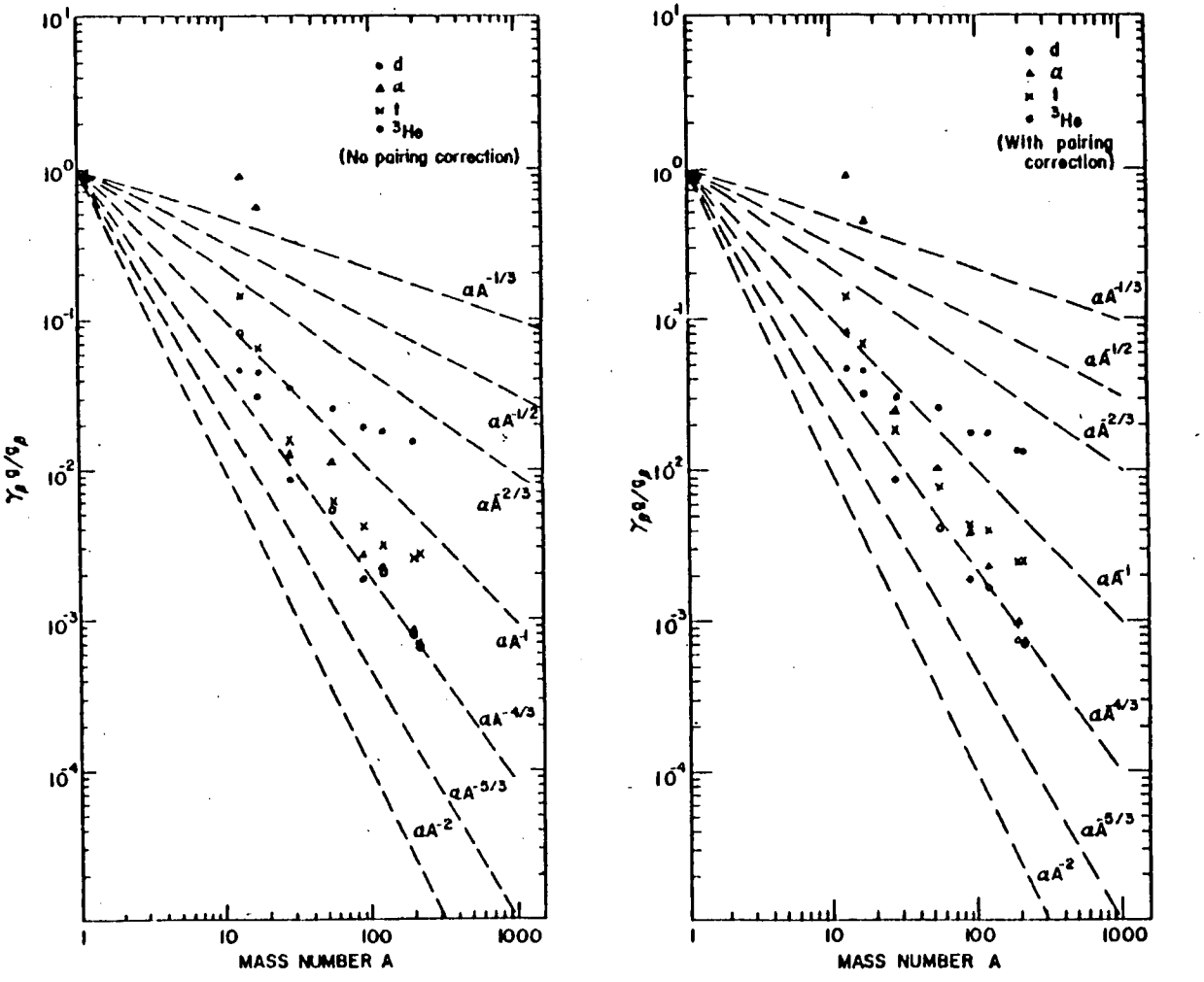

Fig. 4.13 Mass dependence of formation factors for approximately 60 MeV incident protons. Taken from Wu and Chang (ref. 82).

only be an approximate comparison as the formation factors for the electron induced reactions are calculated from data angle integrated at one particular particle energy, whilst the factors are obtained from fully angle integrated data in the case of incident protons.

The formation factors can be interpreted as parameters used to fit the calculated results to the experimental data. Thus any differences in the mass dependence of the formation factors between proton and electron induced reactions might be reflected in differences in the mass dependences of the experimental data. The mass dependence of the electron induced data obtained for this thesis is discussed in the next section.

4.1.8 Mass dependence of experimental data

The mass dependence of 17 MeV tritons, 40 MeV ^{3}He particles and both 15 and 25 MeV deuterons can be obtained from the plot of $\ell n \frac{(d^2\sigma)}{dE \cdot d\Omega}$ against $\ell n(A)$, shown in Figure 4.14. Sufficient experimental data was only available at these particular particle energies. For most targets the cross section increases with increasing mass number but not for ^{94}Mo and ^{12}C. The cross section values obtained for the Molybdenum isotopes do not agree with the systematics observed for the other nuclei. There was some uncertainty about the values given for the Mo target thicknesses, although this was thought to be only 10%. Whatever the cause for the unpredicted value of the Mo cross section, these results were ignored when calculating the A dependence of the high energy cross section for the emission of deuterons, tritons and ^{3}He particles. The cross section for tritons emitted from ^{12}C is greater by a factor of about 3 than that predicted from the systematics. Similar results for electron induced high energy alpha emission[7] show, as here, an increase

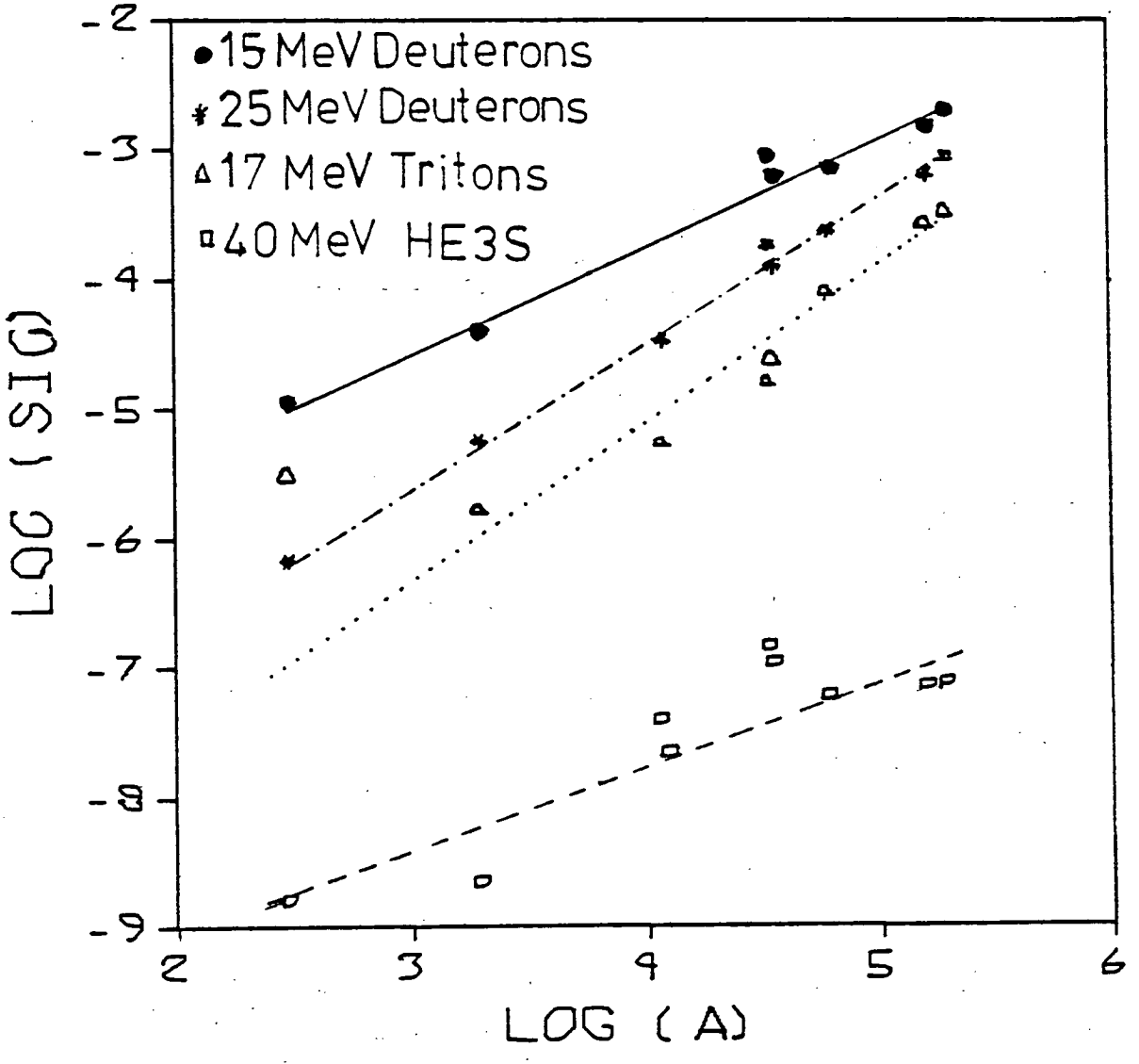

Fig. 4.14 Mass dependence of experimental data. Lines drawn as approximate straight line fits to the data.

in cross section with increasing mass number. However, the value of the cross section for high energy alpha particles emitted from ^{12}C, predicted from the systematics of Flowers et al., is about a factor of 2 less than the measured experimental value.

The large cross sections observed for the emission of alpha particles, tritons and ^{3}He particles from ^{12}C could be a result of alpha clustering within the nucleus. Brenner[121] successfully predicts yields of neutron, proton, deuteron and triton emission, following pion absorption on ^{16}O, assuming that stopped pion absorption on ^{16}O can be treated as occurring on an alpha cluster. These calculations have not yet been adapted to include the calculation of cross sections for electron induced complex particle emission assuming photon absorption onto an alpha particle.

From Figure 4.14 values for the mass dependence of the high energy cross section were obtained on the basis that the cross section follows a power law, i.e.

$$\frac{d^2\sigma}{dE \cdot d\Omega}(A) = k \cdot A^n$$

where k = a constant

and $n = 1.2$ for 17 MeV tritons

$n = 0.8$ for 15 MeV deuterons

$n = 1.1$ for 25 MeV deuterons

$n = 0.7$ for 40 MeV ^{3}He's.

Data obtained for the emission of alpha particles agree with the mass dependences reported by Flowers et al.[7], i.e. at $E_\alpha \sim 30$ MeV the (e, α) cross section varies as $A^{1.5}$ and as $A^{2.0}$ at $E_\alpha \sim 50$ MeV, with the exception of the ^{12}C data as mentioned previously.

The above values relate to the mass dependence of the cross section

above the low energy peak for all the complex particles - i.e. in the energy region where the particles are likely to be emitted due to a pre-equilibrium reaction process. The yield of low energy statistical photoalpha particles peaks at about mass 60 and then falls off rapidly with increasing A. No data is available to obtain the mass dependence for the statistical emission of photo deuterons, tritons or ^{3}He particles. However data for alpha induced complex particle emission shows a mass dependence for low energy complex particles similar to that for statistical photo alphas [79]. The high energy component of the electron induced complex particle emission spectra thus has a different mass dependence than the statistical component, indicating that a different reaction mechanism is involved.

The high energy cross section for electron induced complex particle emission shows a similar smooth increase with mass number to that for proton induced [78] and alpha induced [79] high energy complex particle emission, although the actual values of the A^n dependence are quite different. In the case of alpha induced reactions an $A^{1/3}$ dependence is observed for the emission of deuterons, tritons and ^{3}He particles, while a similar $A^{1/3}$ dependence is seen in (p, α), (p, d), (p, t) and (p,^{3}He) reactions above $A \sim 27$, for energy and angle integrated cross sections.

The $A^{1/3}$ dependence for proton and alpha particle induced reactions suggests a peripheral reaction. The quasideuteron process for photon absorption, thought to be the dominant mechanism for electron induced pre-equilibrium particle emission, has an approximately volume dependent cross section which increases almost linearly with mass number, at high photon energies. Thus, to explain the observed mass dependences of >1 a second stage A dependent reaction is necessary. The fast proton or neutron produced in the quasideuteron reaction may

initiate a cascade process of a particular mass dependence, depending on the energy of the emitted particle.

A complex particle produced by a quasideuteron reaction at the centre of a nucleus has less likelihood of being scattered or fragmented on its way out of a nucleus the higher its energy, since the mean free path of a particle increases with energy. This will result in an increase in the value of n with emitted particle energy, as observed for deuteron emission. The mean free path lengths for deuterons of 15 and 25 MeV were obtained using the expression[123]:

$$\bar{\lambda}(\varepsilon) = \frac{\hbar c}{2\omega}\left[\frac{2(\varepsilon+V)}{mc^2}\right]^{\frac{1}{2}} \qquad \varepsilon+V >> \omega$$

where V and ω are the optical model real and imaginary volume potentials, ε is the energy of the deuteron in the nucleus, relative to the top of the potential well, and $\bar{\lambda}$ is the mean free path length. Values of $\bar{\lambda}$ for E_D = 15 MeV and E_D = 25 MeV were calculated, using approximate values of the optical model parameters V = 114 MeV and ω = 19 MeV. For E_D = 15 MeV $\bar{\lambda}$ = 1.93 fm and for E_D = 25 MeV $\bar{\lambda}$ = 2.00 fm. Thus only a relatively small change in mean free path length occurs between the two deuteron energies, not enough to account for the variation in mass dependence.

Significant differences are observed between the high energy cross section mass dependence for electron and proton induced reactions. However, if the mass dependence is a result of a pre-equilibrium reaction mechanism, the exciton model calculated spectra should also show the same mass dependence calculated using mass dependent formation factors - factors which are obtained from the experimental data. All the formation factors for the proton induced reactions show a strong dependence on mass, although this is not so for electron induced reactions.

The difference in mass dependence of the high energy complex particle emission data for proton and electron induced reactions is reflected, in some way which is not fully understood, in the different mass dependences of the formation factors.

Thus, although the exciton model calculations use approximations for the transition matrix elements and assume that photon absorption is entirely on to a quasideuteron, they appear to explain well the high energy part of the experimental energy spectra for electron induced complex particle emission.

4.1.9 Data not explained by exciton or statistical model calculations

The exciton model calculated results give good fits to the experimental data, especially for high A nuclei where most of the cross section is predicted. For $^{27}A\ell$ only the very high energy parts of the deuteron and possibly ^{3}He energy spectra were predicted. Thus it seems that the calculated energy spectra show good agreement with the high energy portions of the experimental energy spectra for nuclei in the mass range 27 - 120 and predict nearly all of the cross section for the heavier nuclei.

Statistical model calculations were performed for the nuclei $^{27}A\ell$ and Sn. Good agreement with the low energy portion of the experimental spectrum was observed for the $^{27}A\ell(e, \alpha)$ and $^{27}A\ell(e, t)$ reactions but for Sn the calculated low energy peak for the emission of alpha particles did not agree either in position or magnitude with that measured experimentally. Thus a large part of the high energy spectrum for $^{27}A\ell$ is unexplained by either the statistical or exciton model calculations as is the low energy portion of the energy spectrum for Sn.

Omissions or errors in the statistical model and/or exciton model calculations, or the presence of a further reaction component, may account for the unexplained cross section. The statistical model calculation for Sn agrees with the peak positions calculated by Meneghetti and Vitale[20] within the uncertainty of the calculation. The same statistical model computer code has been used successfully to predict both the peak position and magnitude for electron induced alpha emission from ^{NAT}Ni [6]. Thus, it is thought unlikely that there are many major deficiencies in the statistical model calculations used here.

The exciton model calculation used does not include multi-chance effects. It is assumed that no other particles can be emitted from the particular state from which the particle under consideration is emitted. At high photon energies the probability that both a complex particle and a nucleon can be emitted is much greater and thus it is expected that better agreement to experimental data will be observed at low photon energies. A few-point energy spectrum for the emission of complex particles from ^{197}Au at an electron bombarding energy of 60 MeV has been measured and the data compared to exciton model calculated results. Good agreement with spectral shapes and magnitudes was observed using formation factors $\sim$ 20% less than those required for the same reactions at an electron energy of 120 MeV. A further test of the reliability of exciton model calculations at a large range of photon energies is the comparison between measured excitation functions and the exciton model calculated results discussed in Section 4.3. However the inclusion of multi chance effects will not increase the number of low energy particles which would be necessary to explain the Sn data.

There may be some error in the exciton model calculations in the region of the coulomb barrier which may account for the failure of the

calculation to predict the low energy contribution for Sn even though adequate consideration does seem to have been given to the problem of particle penetrability. A comparison of the spectral shapes produced by statistical and exciton model calculations close to the threshold energy shows that whereas the evaporation spectrum falls very rapidly to zero, the exciton model spectrum does not have such a sharp cut off. The shape of the spectra at low energies is dependent on the coulomb barrier and should thus be similar for both the theoretical calculations. The evaporation spectrum shape is consistent with a sharp fall in cross section due to particles being unable to leave the nucleus because of the height of the coulomb barrier. A better fit to the Sn data would be obtained if the exciton model spectrum had a sharper low energy cut off and this may be one reason why a good fit has not been obtained.

The failure of the exciton model calculations to explain the high energy portions of the energy spectra for $^{27}A\ell$ may be a result of the small number of nucleons available to interact within the nucleus. The worst fit to the data is found for the most complex of the emitted particles. The low probability that four particles of the correct type and momentum to be emitted as an alpha particle will be found in a particular particle hole state may make the use of the exciton model invalid for such nuclei when complex particle emission is being considered.

A quasi free scattering process or one step pick up of single nucleons or a cluster of nucleons may contribute to the reaction mechanism (as discussed in Section 4.1.1) and explain the measured energy spectra more fully. As yet there are no calculations available for these reaction mechanisms applicable to photonuclear reactions, thus the magnitude of these possible reaction components cannot be estimated at present.

4.2 Angular Distributions

4.2.1 Introduction

Angular distribution data for the emission of alpha particles, deuterons, tritons and ^{3}He particles, following electron and bremsstrahlung excitation of nuclei $12 < A < 197$, was presented in Section 3.4.2. Some of the low energy angular distributions are approximately isotropic, particularly those for the emission of low energy tritons and ^{3}He particles. Many of these distributions show structure, although this may be due to the large statistical errors associated with some of the data points. The distributions measured at high particle energies show no pronounced structure other than forward peaking - the degree of forward peaking increasing with particle energy.

A forward peaked angular distribution is indicative of a direct or pre-equilibrium reaction mechanism, while an angular distribution symmetric about 90° is expected for a compound nucleus reaction. All the angular distributions for the emission of alpha particles from ^{12}C are forward peaked. Thus it appears that even at low energies the reaction mechanism for alpha emission has a large pre-equilibrium component which becomes increasingly more dominant as the particle energy increases. The shape of the alpha energy spectrum suggests that a statistical compound nucleus reaction is dominant below about 8 MeV emission energy. (This is discussed in Section 4.1.1). The lowest alpha energy at which an angular distribution has been measured, i.e. 5 MeV, is somewhat above the peak of the energy spectrum which is at approximately 3 MeV. Although alpha particles of energy 3 MeV, i.e. in the peak, are probably emitted in a compound nucleus reaction it is likely that a pre-equilibrium reaction mechanism will begin to dominate the emission process above this energy. Thus the forward peaking of the angular distribution for the emission of 5 MeV alpha particles from ^{12}C is not particularly surprising.

Measurements for the emission of deuterons from ^{12}C show similar forward peaked angular distributions, even at low particle energies.

The lowest energy angular distributions measured for tritons and ^{3}He particles emitted from ^{12}C are approximately isotropic, consistent with particle evaporation from the nucleus. The coulomb barrier is somewhat higher for $^{27}A\ell$ than for ^{12}C and so the peaks of the energy spectra are positioned at higher particle energies. The alpha particle angular distribution taken at 5 MeV for $^{27}A\ell$ is thus sampling alpha particles from the peak of the energy spectrum. If this peak is indeed due to evaporation of alpha particles from the target nuclei, it is to be expected that the angular distribution is symmetric about 90^{o}, which is indeed the case. Similarly, the angular distribution for 2.5 MeV deuterons from $^{27}A\ell$, approximately at the peak of the energy spectrum, is very nearly isotropic.

Pre-equilibrium exciton model calculations which were used to explain the measured energy spectra cannot at present be applied to angular distribution data. The high particle energy angular distributions were, however, compared to results of a kinematic calculation of Flowers[8], which uses the basic tenets of pre-equilibrium formalism as its basis.

Angular distributions for complex particles emitted following statistical decay of a compound nucleus exhibit shapes which are characterised by the particular resonance excited in the initial real or virtual photon absorption. Legendre polynomials can be used to parameterize the data, the values of the coefficients giving an indication of which multipoles are significant in the photon absorption.

4.2.2 Low particle energy angular distributions

Some of the measured low energy angular distributions are nearly isotropic in shape, while others show some signs of structure (see Figs. 3.14 - 3.27). Both types of distribution are indicative of a compound nucleus reaction. The angular distributions were fitted with Legendre polynomials of up to fourth degree, being parameterized by the coefficients A_L:

$$\frac{d^2\sigma}{dE \cdot d\Omega} = \sum_{L=0}^{4} A_L P_L(\cos\theta)$$

Smearing effects due to the finite solid angle of the spectrometer are negligible[8] and therefore ignored. Legendre polynomial coefficients obtained from fitting angular distributions for the emission of deuterons from ^{12}C and alphas from Aℓ are shown in Fig. 4.15. For pure E1 virtual photon absorption the only non zero term, apart from A_o, is A_2 whilst for a mixture of E1 and E2 absorption, A_1 and A_3 are E1, E2 interference terms. A_4 represents E2 only and A_2 is dependent on E1 + E2. The coefficients A_1 and A_2 are the only non zero terms for the emission of particles from an M1 giant resonance[124].

For both alpha particle and deuteron emission the A_1/A_o term rises sharply from ∿ 0 at low particle energies to ∿ 1 for alpha emission, or 0.5 for deuteron emission, at high particle energies. The coefficients $\frac{A_3}{A_o}$ and $\frac{A_4}{A_o}$ are approximately zero within the experimental uncertainties at all particle energies, as is the coefficient A_2 in the case of deuteron emission. The A_2/A_o term is also zero at low energies but rises sharply above ∿ 20 MeV to a value of ∿ 0.7 at 50 MeV, for the emission of alpha particles.

Thus at low particle energies, where the reaction is more likely to proceed via compound nucleus formation, none of the coefficients have significant values and no information on the virtual photon absorption

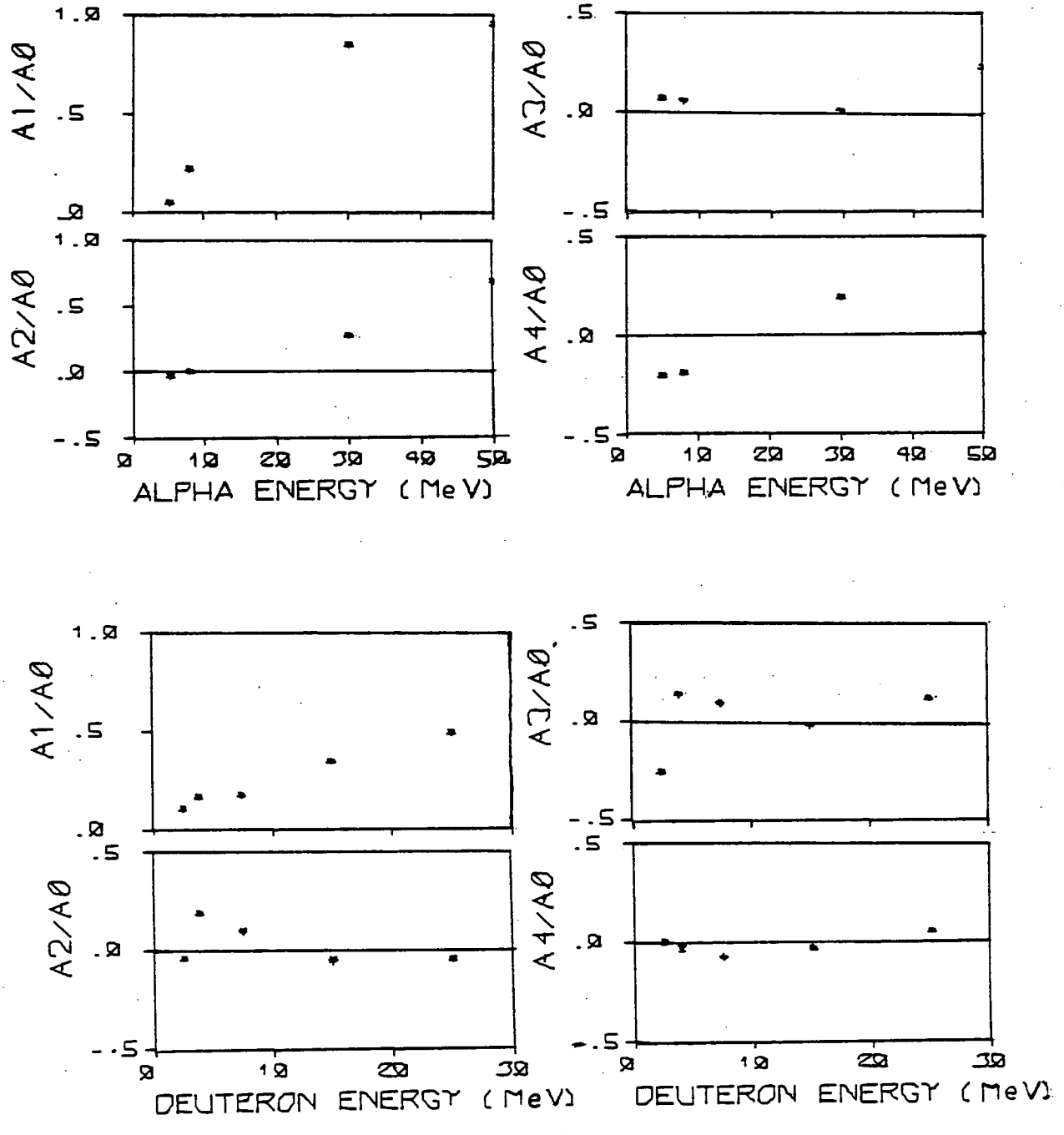

Fig. 4.15 Legendre polynomial coefficients for alphas from ^{27}Al and deuterons from ^{12}C.

can be obtained from the parameterization of the angular distributions. The $\frac{A_1}{A_o}$ term increasingly dominates the angular distributions at high particle energies, indicative of the increasing forward peaking of the experimental data. These high $\frac{A_1}{A_o}$ values may be a result of E1, E2 interference or may indicate that the emission of high energy particles is a pre-equilibrium process rather than a compound nucleus reaction, as at low energies. Measurements on the $^{56}Fe(\alpha,\gamma_o)^{60}Ni$ reaction[103] at excitation energies between 15 and 20 MeV showed an absence of interference terms. Thus the large $\frac{A_1}{A_o}$ and $\frac{A_2}{A_o}$ terms seem to indicate the inapplicability of the statistical compound nucleus model at high particle emission energies.

4.2.3 High particle energy angular distributions

High energy complex particles are likely to be emitted following absorption of high energy photons. Thus particles emitted isotropically in the centre of mass frame may have forward peaked angular distributions in the laboratory frame due to the large forward momentum of the nucleus in the centre of mass frame due to the large forward directed momentum transfer of high energy photons. Electron scattering angular distribution data exhibit very strong forward peaking, suggesting a high probability of forward momentum transfer.

Assuming that high energy alpha particles were emitted isotropically in the centre of mass frame from a compound nucleus, Flowers[8] calculated values for the ratio of the Legendre polynomial coefficients $\frac{A_1}{A_o}$ These were found to be at least a factor of 30 lower than the ratios obtained from fitting the experimental angular distributions with Legendre polynomials. Much larger ratios would be obtained if the photon momentum was assumed to be shared only by a small number of

nucleons, rather than the whole nucleus, at the time of particle emission.

Large values of $\frac{A_1}{A_o}$ are also observed for the emission of high energy deuterons, tritons and ^{3}He particles (see Table 4.7) which cannot be explained in terms of a compound nucleus reaction. Thus angular distributions for the emission of high energy particles were calculated, assuming photon absorption onto a small group of nucleons.

Assuming an isotropic distribution in the centre of mass frame, the measured, laboratory frame angular distribution, is given by:

$$\frac{d^2\sigma}{dE \cdot d\Omega}(\bar{E}, \theta) = \frac{\bar{p}}{p} \frac{d^2\sigma}{dE \cdot d\Omega}(E, \theta_o) \qquad (4.6)$$

where:

$$\bar{E} = \frac{\bar{p}^2}{2m}, \qquad E = \frac{p^2}{2m}$$

$$p = \bar{p}\Gamma\cos\theta_o \pm \sqrt{\bar{p}^2\Gamma^2\cos^2\theta_o + \bar{p}^2 - 2\Gamma\bar{p}^2\cos^2\theta}$$

$\bar{p}$ = emitted particle momentum in the laboratory frame.

θ_o = angle at which laboratory frame energy spectrum $\frac{d^2\sigma}{dE \cdot d\Omega}(E, \theta_o)$ is measured.

$$\Gamma = \frac{qm}{\bar{p} M_T}$$

m = mass of emitted particle

M_T = mass of group of nucleons sharing incident photon momentum q.

This expression is developed by Flowers[8] assuming the forward scattering approximation in which the momentum transfer between photon and nucleus is directed forward and that the photon momentum is shared between only a few nucleons at the stage for which particle emission occurs. In the virtual photon formalism the target nucleus can be excited by photons of all energies up to the electron energy, i.e.

TABLE 4.7

Values of $\frac{A_1}{A_o}$ for E_e = 120 MeV electron induced reactions.

i) Alphas

E_x (MeV)	$\frac{A_1}{A_o}$ for target nuclei: ^{12}C	^{27}Al	Ni	^{NAT}Sn	^{197}Au
5	0.36	0.04			
8	0.32	0.21			
15	0.70				
30		0.84	0.96	0.99	0.86
50	0.97	0.94		0.95	

ii) Deuterons

2.5	0.10	0.17			
4	0.16	0.08			
7.5	0.17	0.25		0.33	
15	0.34	0.34	0.41	0.54	0.60
25	0.48	0.54	0.59	0.72	0.72

iii) Tritons

5	0.23				
10		0.40	0.51	0.55	0.57
17	0.33	0.55		0.73	0.75

iv) ^3He's

6.7	0.15	0.05			
10.7	0.11	0.12			
20	0.68	0.69		0.28	
40	0.79	0.82	0.68		0.62

120 MeV in this case. At E_e = 120 MeV a reasonable upper limit to the average momentum transfer ($q = \frac{E_\gamma}{\hbar c}$) is q = 100 MeV/c. Assuming this value for q when E_e = 120 MeV angular distributions calculated using eqn. (4.6), were fitted to measured high particle energy angular distributions varying the parameter M_T. Table 4.8 lists the values obtained for M_T for the emission of alpha particles, deuterons, tritons and ^{3}He particles for E_α = 30 and 50 MeV. The calculated angular distributions are sensitive to the values of M_T as shown in Fig. 4.16 for the emission of 25 MeV deuterons from ^{NAT}Sn.

The angular distributions are calculated at particle energies for which the cross section decreases sharply for increasing particle energy. At forward angles lower values of p are sampled, yielding a higher cross section which results in a forward peaked angular distribution in the laboratory frame for a fixed laboratory frame particle energy. The value of M_T is interpreted as the average number of nucleons which share the energy of the incoming photon at the particular stage in the reaction when a particle is emitted. The value of M_T decreases with increasing mass number for all the complex particles and in the case of deuterons and tritons, lower values of M_T are necessary at the higher particle energy.

The values of M_T obtained from fitting the angular distributions of tritons emitted from ^{12}C show that this kinematic model cannot be applied here. It has already been noted (Section 4.1.8) that the yield of tritons from ^{12}C is much ($\sim$ factor of 3) greater than that predicted from systematics. This is not true for tritons emitted from ^{12}C, following either proton[78] or alpha particle[79] induced reactions. Obviously a reaction mechanism, other than pre-equilibrium emission, which appears to be the main reaction mechanism for the emission of high energy complex particles following photon absorption, dominates

TABLE 4.8

Values of M_T.

i) E_α = 30 MeV, E_D = 15 MeV, E_T = 10 MeV, E_H = 40 MeV.

Target Nucleus	α	d	t	^{3}He
^{12}C	10	10	22	9
^{27}Aℓ	-	10	11	9
^{NAT}Ni	10*	7	9	7
^{NAT}Sn	7	5	6	-
^{197}Au	8*	4	-	-

ii) E_α = 50 MeV, E_D = 25 MeV, E_T = 17 MeV.

Target Nucleus	α	d	t
^{12}C	9	7	15
^{27}Aℓ	-	7	11
^{NAT}Ni	10*	7	7
^{NAT}Sn	9	4	6
^{197}Au	8*	4	5

* Values taken from Flowers (ref. 8).

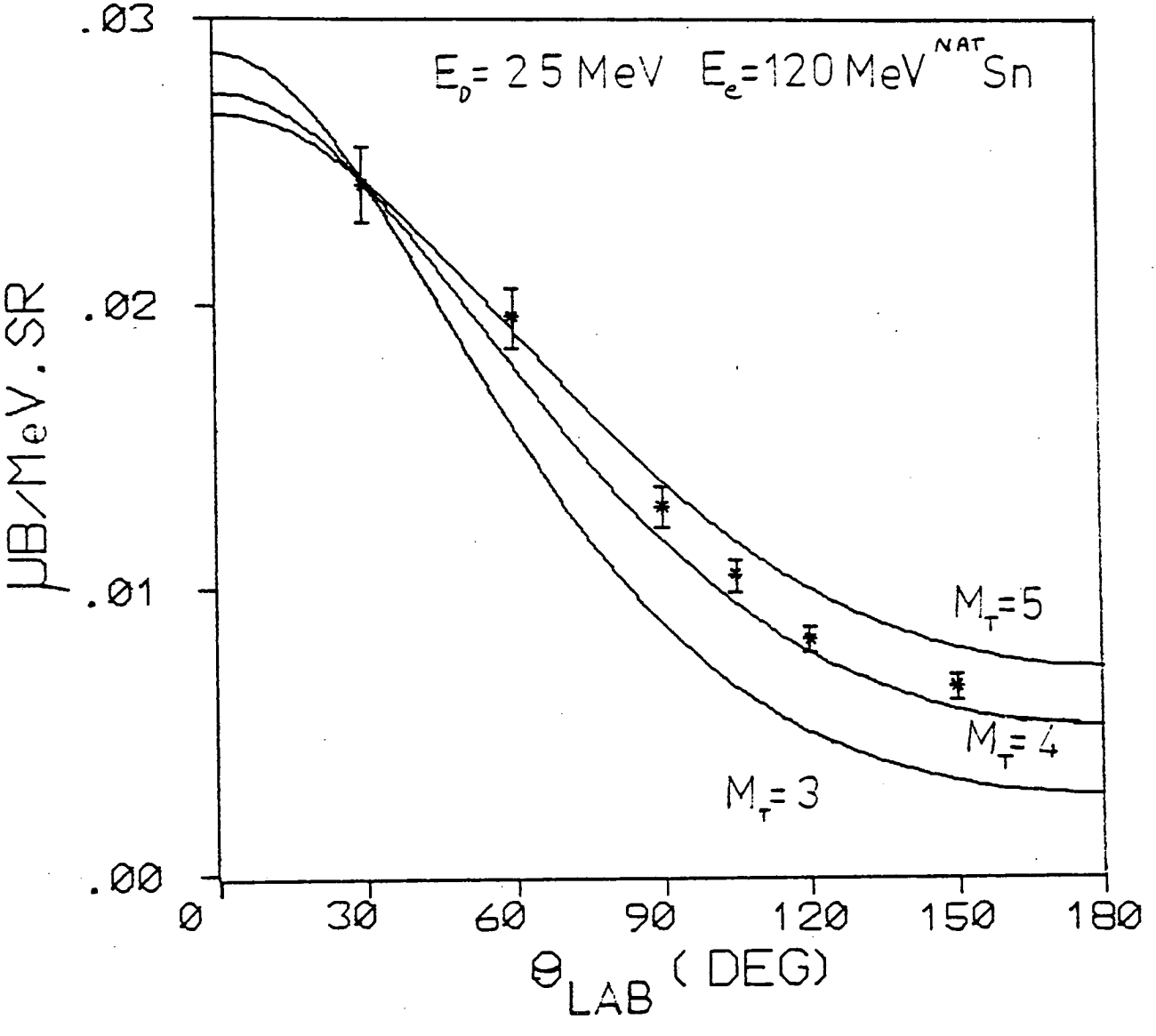

Fig. 4.16 Comparison of the measured angular distribution with the the results of the kinematic calculation for various values of M_T, for 25 MeV deuterons from ^{NAT}Sn.

the emission of tritons from ^{12}C. Such large values of M_T are obtained as the angular distributions are only slightly forward peaked, indicating a statistical mechanism where the energy of the photon is shared amongst all the nucleons in the nucleus. The large high energy tail observed in the ^{12}C triton energy spectra suggests, however, a strong pre-equilibrium or direct component. Possibly direct triton knock-out is especially important for ^{12}C, although this hypothesis cannot be investigated at present due to the lack of models applicable to the emission of complex particles from light nuclei.

Excluding the values of M_T for tritons from ^{12}C, it appears that the smallest values of M_T are required to fit the deuteron data, the values of M_T being slightly larger for both tritons and ^3He particles and largest for alpha particles. This is consistent with exciton model calculations in which high energy particles are emitted mostly during the early stages of equilibration. Thus high energy deuterons will be emitted from lower particle hole states than alpha particles as the initial photon absorption is to a 2p 2h state, i.e. absorption onto a quasideuteron.

4.2.4 A comparison of angular distributions for electron and bremsstrahlung induced reactions at E_e = 120 and 60 MeV.

Angular distributions for the emission of complex particles from ^{58}Ni and ^{60}Ni, following excitation by both electrons and photons, are shown in Figs. 3.29 - 3.36. There is little difference in the shape of the distributions for all the complex particles for the two different isotopes - the electron cross section and bremsstrahlung yield being slightly higher for ^{60}Ni. Where measurements have been made at both 60 and 120 MeV

electron and bremsstrahlung end point energies, it can be seen that both the electron and bremsstrahlung angular distributions are more forward peaked at 60 MeV than at 120 MeV. The two distributions have approximately the same shape at 60 MeV but at 120 MeV the electron distributions are more forward peaked for all the complex particles.

The ratio (bremsstrahlung yield: electron cross section) increases from $\sim$ 1.0 at 120 MeV to between 1.3 and 1.5 at 60 MeV, depending on the complex particle. The change in ratio is greatest for the highest energy particles studied, i.e. the alphas, and lowest for tritons ($E_t = \frac{1}{3}E_\alpha$).

A comparison between the bremsstrahlung spectrum incident on the target and both E1 and E2 virtual photon spectra, produced in the target at E_e = 120 MeV and 60 MeV, is shown in Figures 4.17 and 4.18 respectively for the target nucleus ^{60}Ni. At both electron energies the bremsstrahlung spectrum and virtual photon spectra are integrated above 30 MeV and the ratios of the integrated bremsstrahlung yield to both integrated E1 and E2 yields are compared to the measured angle integrated yield ratios for ^{60}Ni of particles emitted following real and virtual photon excitation. The experimental yield ratios and integrated spectrum ratios are given in Table 4.9.

Assuming that the cross section for particle emission from a nucleus is the same for both real and virtual photon absorption, the experimentally measured real to virtual photon yield ratios can be explained in terms of the bremsstrahlung to virtual photon yields. The bremsstrahlung and virtual photon spectra are integrated from 30 MeV up to the end point. The lower energy cut off is a somewhat arbitrary point chosen to approximate the photon energy range for which 10 MeV tritons, 15 MeV deuterons and 30 MeV alpha particles can be emitted from the nucleus. Thus the yield ratios obtained from integrating the spectra will only approximate the yield ratios of the real and virtual photons whose absorption actually

Fig. 4.17

Comparison of bremsstrahlung intensity with E1 and E2 virtual photon intensities for E_e = 120 MeV for ^{60}Ni.

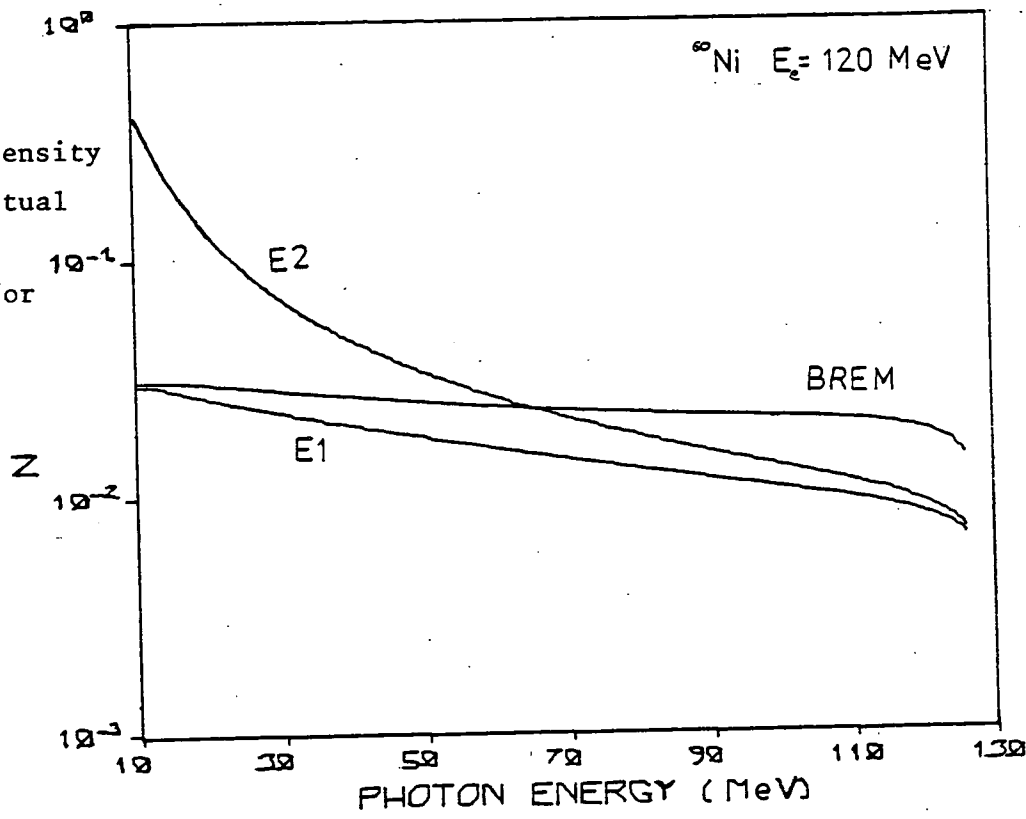

Fig. 4.18

Comparison of bremsstrahlung intensity with E1 and E2 virtual photon intensities for E_e = 60 MeV for ^{60}Ni.

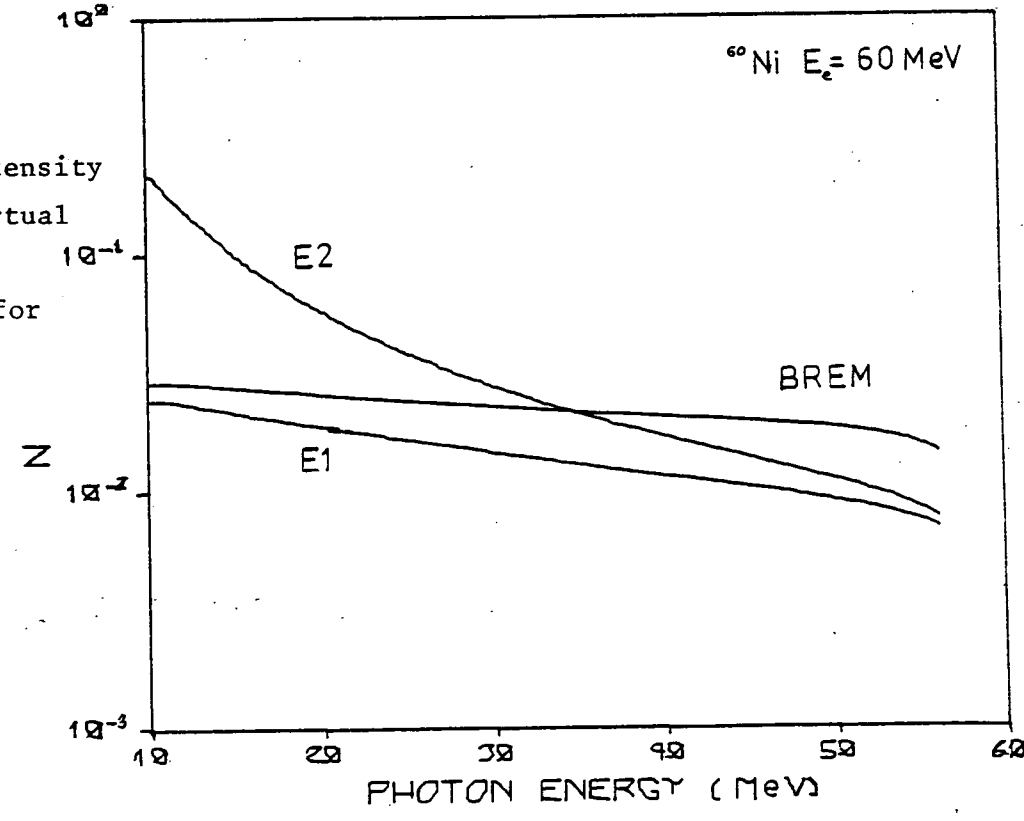

TABLE 4.9

^{60}Ni

E_e = 120 MeV

Experimental angle integrated yield ratios: photo/electro			Integrated: bremsstrahlung/E1 yield	Integrated: bremsstrahlung/E2 yield
α	d	t		
1.08	1.10	0.98	1.42	0.84
E_e = 60 MeV				
1.51	1.66	1.62	1.78	1.18
^{197}Au	E_e = 120 MeV			
0.82	0.82	0.82	1.43	0.30
E_e = 60 MeV				
0.68	0.78	0.71	1.50	0.51

caused the emission of the complex particles of these particular energies.

From Table 4.9 it can be seen that at 60 MeV electron energy pure E1 virtual photon absorption or mainly E1 with a small amount (< 20%) of E2 virtual photon absorption will account for the measured photo:electro yields. However, at the higher electron energy (120 MeV) the photo:electro yield ratio of approximately 1 can only be explained in terms of a significant ($\tilde{\sim}$ 50%) E2 virtual photon component. The magnitude of the E2 component cannot be accurately calculated due to possible interference effects between the E1 and E2 components.

Interference between the electric multipoles would result in a change in shape of the electron induced angular distribution. This is observed at 120 MeV where the electro data are more forward peaked than the equivalent photon induced angular distributions. At 60 MeV, however, both sets of angular distributions have the same shape, suggesting that the virtual photon absorption is a pure E1 process.

Similar angular distributions have been measured for the emission of complex particles from ^{197}Au, following excitation by electrons and photons at electron energies of 120 and 60 MeV, presented in Figures 3.37 - 3.39. At both electron energies the electron data is more forward peaked than the photo data and both sets of angular distributions are more forward peaked at 60 MeV than at 120 MeV. The ratio of bremsstrahlung yield:electron cross section does not change with electron energy, neither do the relative shapes of the angular distributions. From a consideration of the magnitudes of the bremsstrahlung and virtual photon spectra integrated from 30 MeV up to the end point, it seems that the virtual photon absorption is approximately 50% E1 and 50% E2 at both electron energies. At both electron energies the electro data is more forward peaked, suggesting interference between the two multipoles.

4.3 Excitation Functions

4.3.1 Introduction

Excitation functions for the emission of alpha particles, deuterons and tritons have been measured at three particle energies for electron and bremsstrahlung end point energies between 40 and 130 MeV, measurements taken at 10 MeV intervals. The data is presented in Figs. 3.40 - 3.44. The electron data is greater than the equivalent photo data at all three particle energies and for all three complex particles. In the case of alpha emission the electron curves all have the same shape as do the bremsstrahlung yield functions, with the two sets of data also having very similar slopes. This is not so in the case of the other particles; for tritons in particular the slopes vary quite considerably with particle energy.

From virtual photon theory, particle emission cross sections for nuclei excited by both electrons and real photons should be identical. Thus differences in the measured electron excitation and bremsstrahlung yield functions will result from differences between the bremsstrahlung spectrum and the relevant virtual photon spectrum. The electric dipole (E1) component is thought to dominate virtual photon absorption at the high energies considered here with electric quadrupole (E2) and electric monopole (E0) components perhaps contributing slightly.

A comparison of the E1, E2 and bremsstrahlung spectra incident on the Au target for electron energies of 120 MeV and 60 MeV, Figs. 4.19 and 4.20, shows that the E1 and bremsstrahlung spectra are quite similar in shape, with the E2 spectra considerably different. This suggests that the similarity in shape of the electro and photo curves is a result of pure E1 virtual photon absorption. Where the two slopes are not the same, this suggests that pure E2, or more likely, a mixture of E1

Fig. 4.19 Comparison of bremsstrahlung intensity with E1 and E2 virtual photon intensities for E_e = 120 MeV for ^{197}Au.

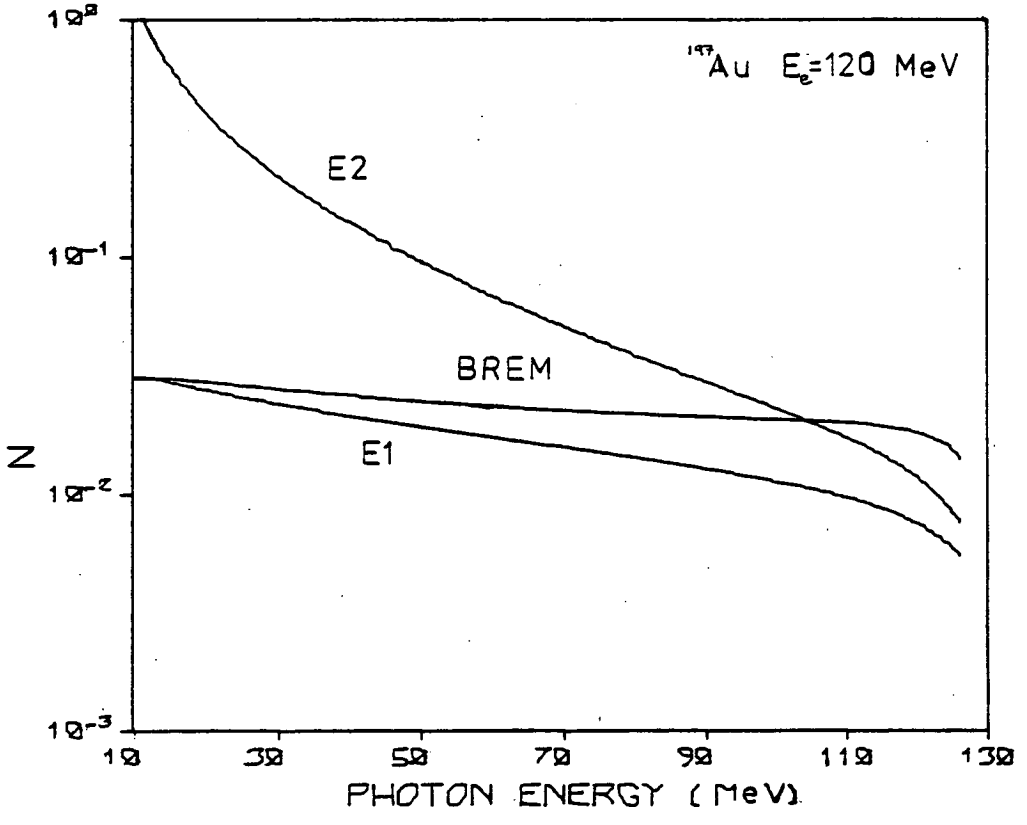

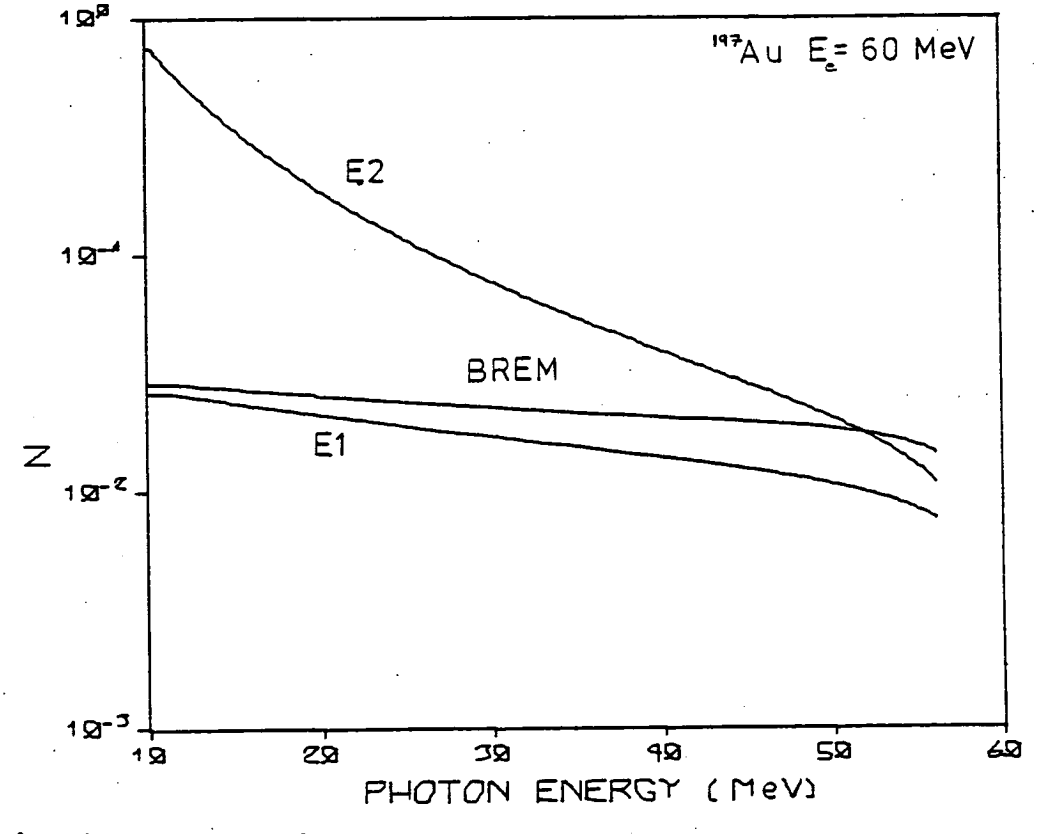

Fig. 4.20 Comparison of bremsstrahlung intensity with E1 and E2 virtual photon intensities for E_e = 60 MeV for ^{197}Au.

and E2 virtual photon absorption is required. Below about 60 MeV electron energy the electron data falls away quite rapidly in the case of alpha emission. Thus it appears that above 60 MeV the virtual photon absorption is pure E1, while below this energy multipole mixing is required. An E0 virtual photon spectrum could not be easily obtained with any accuracy and thus the possibility of E0 virtual photon absorption is not discussed.

The electron and bremsstrahlung yield functions for the emission of deuterons (Figs. 3.41 and 3.42) follow the pattern of alpha emission, having a strong similarity in shape except below 60 MeV, where the electron cross section falls away rapidly. For tritons (Figs. 3.43 and 3.44) the electron cross section does not appear to have the same shape as the bremsstrahlung yield, even at high electron energies. This is true for all three measured triton energies.

The electron cross section for 15 MeV tritons slightly exceeds that for the 11.7 MeV tritons above an electron energy of about 80 MeV. Below this energy the cross section for 15 MeV tritons falls away quite rapidly, indicating a change in energy of the peak of the triton energy spectrum from about 10 MeV at low electron energies to about 13 MeV at electron energies above 80 MeV (see also Table 3.4). One possible explanation is that there are two distinct reaction mechanisms, having different peak energies, possibly a statistical process and a pre-equilibrium process - the statistical reaction component being dominant at low electron energies and the pre-equilibrium component becoming dominant as the electron energy increases.

The bremsstrahlung yield functions have been unfolded, using a method of Flowers[8] to produce a reaction cross section which has then been folded in with a virtual photon spectrum and the result compared to the measured electron excitation functions. The statistical uncertainty

($\sim$ 10%) and large interval (10 MeV) between the data points means that great care must be taken in unfolding the yield functions.

The bremsstrahlung yield $y(E_i)$ is related to the photon absorption cross section $\sigma(E_\gamma)$

$$y(E_i) = \int_{E_o}^{E_i} dE_\gamma \sigma(E_\gamma) N(E_i, E_\gamma) \qquad i = 1,2,\ldots n$$

where E_o is the threshold energy for the reaction and $N(E_i, E_\gamma)$ is the bremsstrahlung spectrum. The yield function is not measured continuously but for a number n, of energies at intervals $E_j - E_{j-1}$. Thus assuming that $N(E_i, E_\gamma)$ is slowly varying over each energy division, the yield can be expressed[8]

$$y(E_i) \approx \sum_{j=1}^{n} \frac{2N[E_i(E_j - 1 + E_j/2)]}{E_{j-1} + E_j} \int_{E_{j-1}}^{E_j} \sigma(E_\gamma) dE_\gamma$$

which can be written

$$y(E_i) \approx \sum_{j=1}^{n} N_{ij} \bar{\sigma}_j \Delta E_j$$

where N_{ij} is the photon intensity at the centre of the energy interval, $\Delta E_j = E_j - E_{j-1}$ and $\bar{\sigma}_j$ is the average photon absorption cross section in this energy interval, i.e.

$$\bar{\sigma}_j \Delta E_j = \int_{E_{j-1}}^{E_j} \sigma(E_\gamma) dE_\gamma$$

and $$\bar{\sigma}_j = \frac{1}{\Delta E_j} \sum_{i=1}^{n} N_{ij}^{-1} \sigma_{\gamma,x}(E_i)$$

where $\sigma_{\gamma,x}(E_i)$ is the experimental cross section ($x = \alpha$, t, d, etc.)

When this expression is used to unfold excitation functions with random statistical errors on the data points, large fluctuations are

observed between neighbouring values of $\bar{\sigma}_j$. Cook[120] used a least structure method to smooth the values of $\bar{\sigma}_j$ and limit the oscillations produced in the unfolding.

Flowers follows Cook's procedure and defines a structure function $s(\bar{\sigma}_j)$ where

$$s(\bar{\sigma}_j) = \sum_{j=2}^{n-1} (\bar{\sigma}_{j+1} - 2\bar{\sigma}_j + \bar{\sigma}_{j-1})^2 \quad .$$

This function is minimised whilst satisfying the equation

$$\chi^2 = \sum_{i=1}^{n} \left(\frac{(\sum_{j=1}^{i} N_{ij}\bar{\sigma}_j) - \sigma_{\gamma,x}(E_i)}{\delta\sigma_{\gamma,x}(E_i)} \right)^2 \quad .$$

Optimum smoothing is attained when $|\chi^2 - n|$ is minimised. A smooth photo-particle spectrum is obtained from values of $\bar{\sigma}_j$ calculated by the above method for each of the unfolded cross sections. Values of the yield $y(E_i)$ are calculated from the values of $\bar{\sigma}_j$ obtained in this way by folding in the bremsstrahlung cross section and compared to the experimentally measured yields. The calculated yield functions agree very well with the measured data, indicating the validity of the unfolding technique.

4.3.2 Cross sections obtained by unfolding the excitation functions

Cross sections for the emission of alphas, deuterons and tritons from Au, at three particle energies, are obtained from the measured bremsstrahlung excitation functions, using the unfolding technique described in the previous section. The variation of these cross sections with photon energy is shown in Figures 4.21 to 4.23 for alpha particles, deuterons and tritons, respectively. The cross sections are

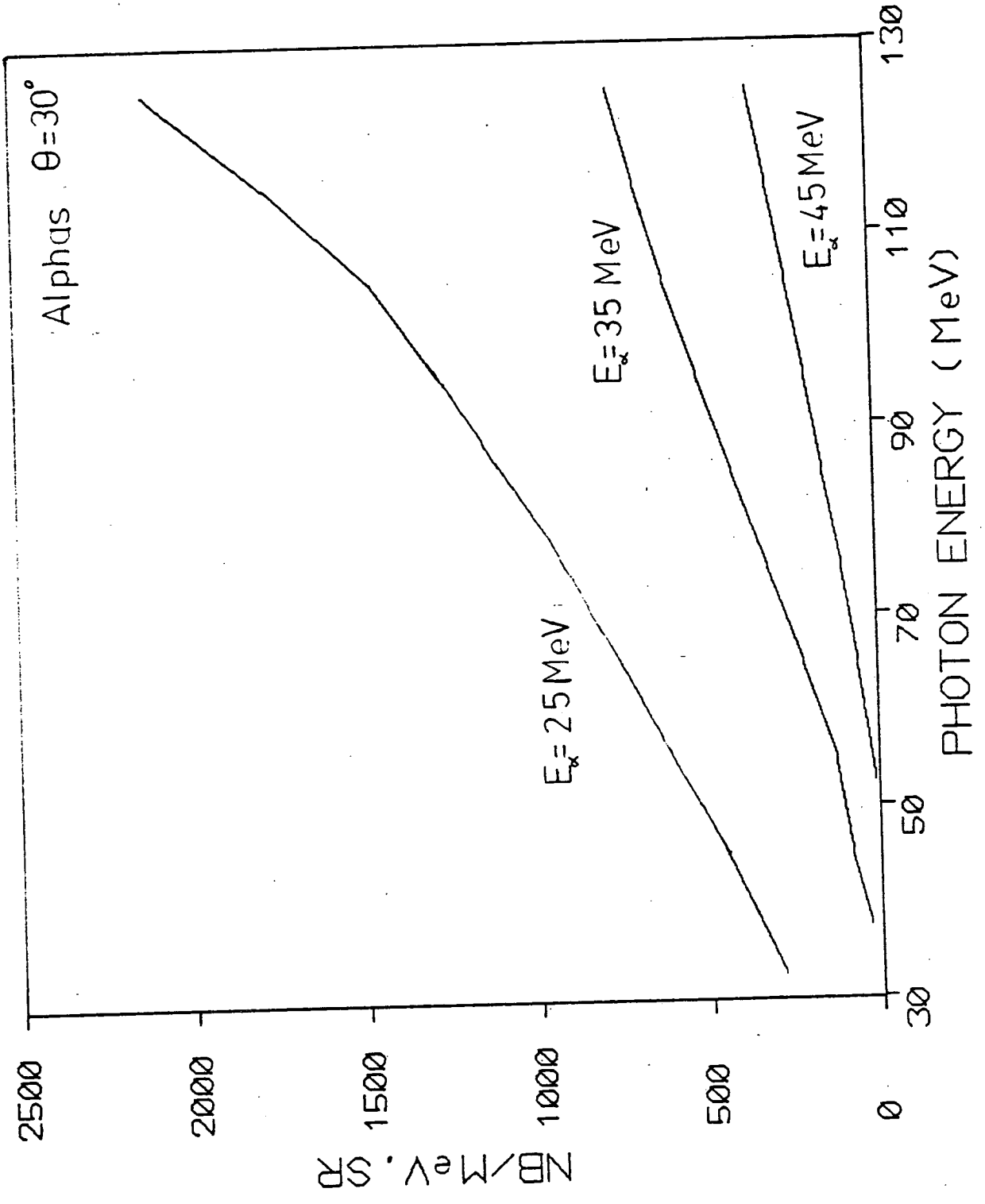

Fig. 4.21 Alpha particle emission cross sections obtained by unfolding the measured photo excitation functions for ^{197}Au.

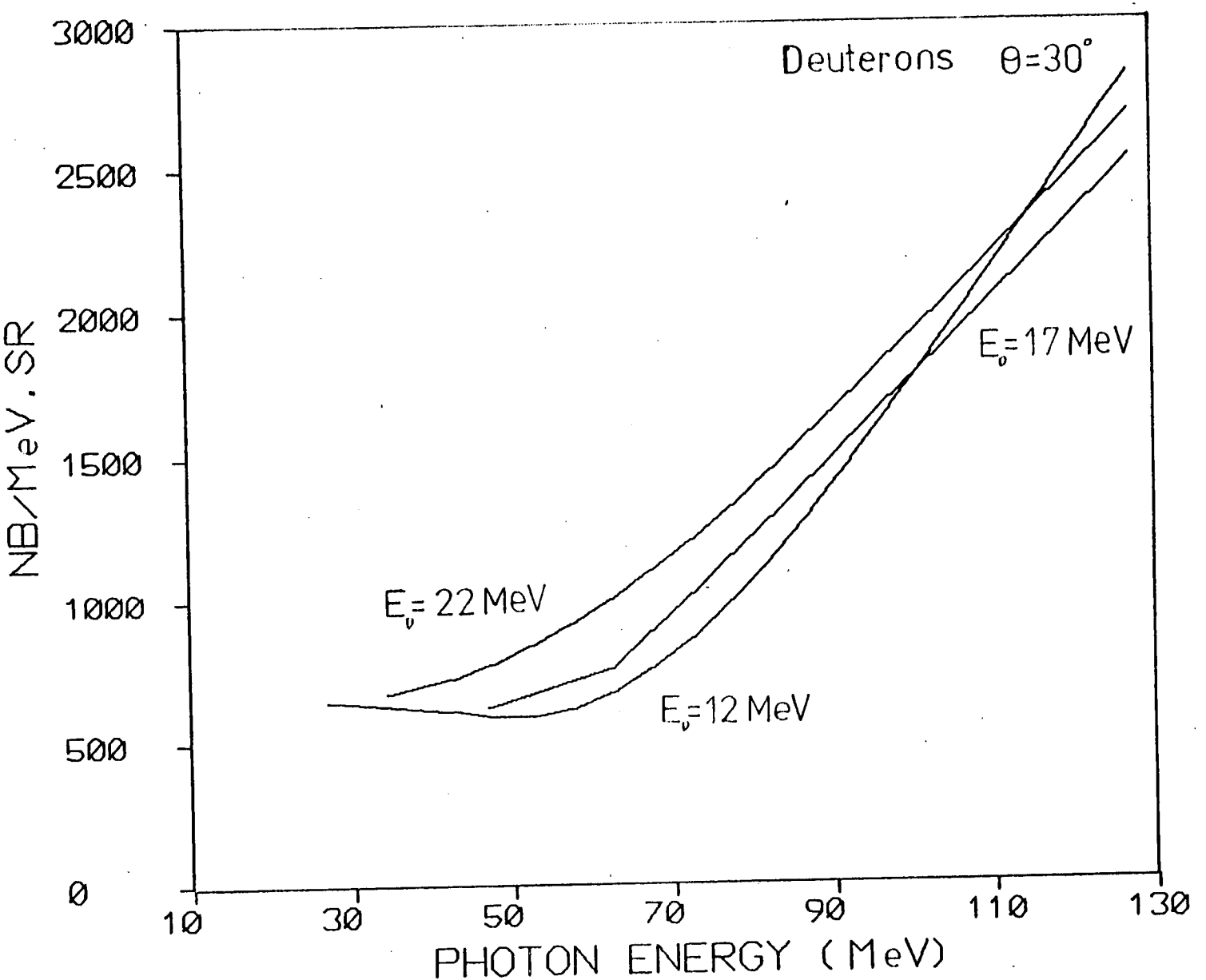

Fig. 4.22 Deuteron emission cross sections obtained by unfolding the measured photo excitation functions for ^{197}Au.

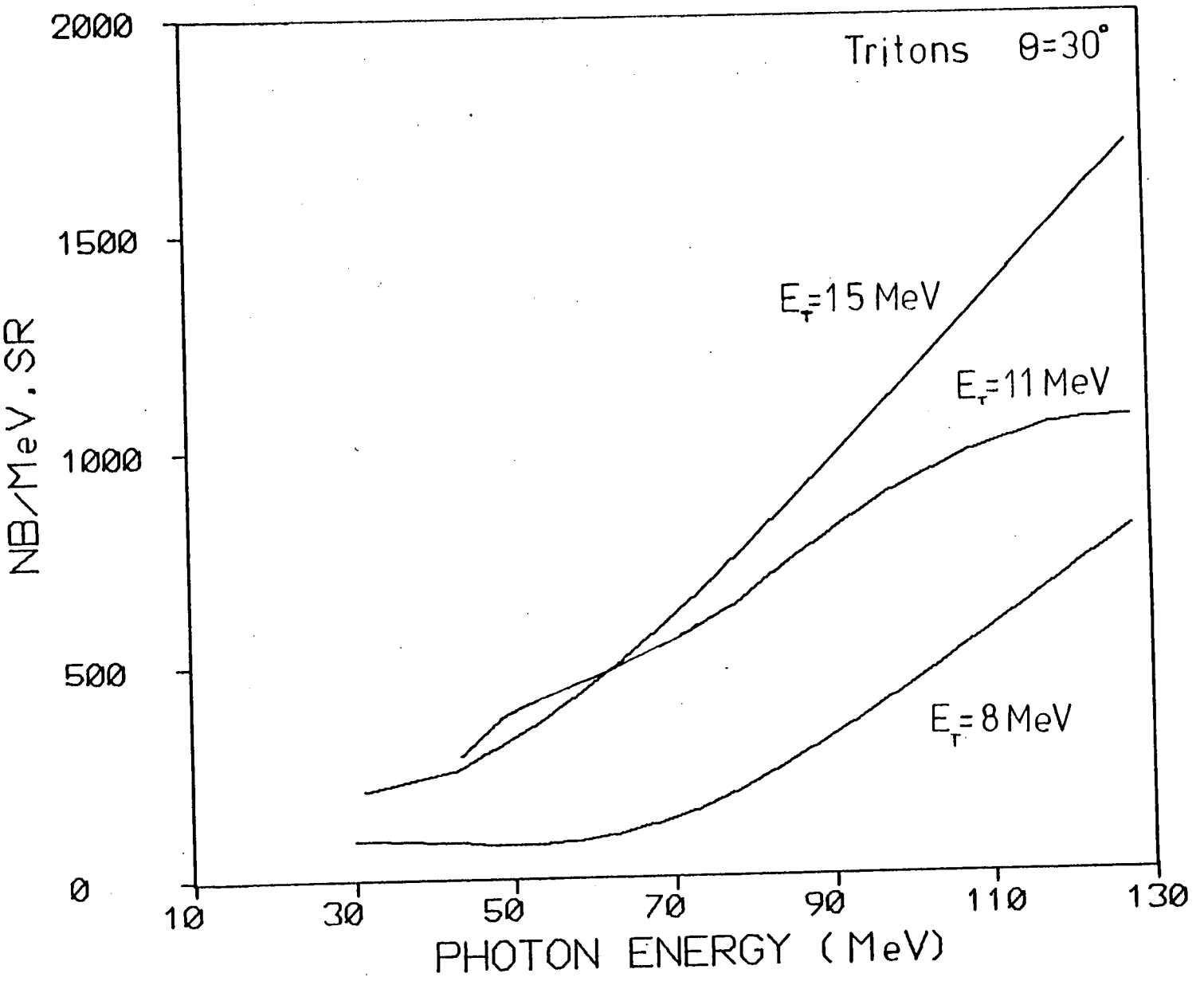

Fig. 4.23 Triton emission cross sections obtained by unfolding the measured photo excitation functions for ^{197}Au.

not angle integrated. Using values obtained from angular distributions measured at 60 and 120 MeV end point energies and interpolating between these two values, is not sufficient.

At all three alpha particle energies the cross section increases almost linearly with photon energy, the slope increasing with decreasing particle energy. The deuteron cross sections also increase almost linearly with photon energy, but only above about 70 MeV. Below this energy the cross section increases much more slowly and for 12 MeV deuterons is approximately independent of photon energy. The 17 MeV and 22 MeV cross sections have the same slope at high photon energies, while the slope for the emission of 12 MeV deuterons is somewhat steeper.

The unfolded triton emission cross sections are similar in form to the deuteron emission cross sections for the emission of 8 and 11 MeV tritons. The cross section curves can be approximated by straight lines above about 70 MeV, the slope of the 11 MeV line being the steepest. A rather different emission cross section is obtained from unfolding the excitation function for the emission of 15 MeV tritons. This cross section increases smoothly with photon energy until about 120 MeV and then appears to be constant with increasing energy.

Particle emission cross sections have been calculated for photon energies between 30 and 140 MeV, using the pre-equilibrium exciton model. A constant value of 10 mb was assumed for the photon absorption cross section in this energy region, to avoid the use of the quasideuteron model. The cross sections for the emission of complex particles from ^{197}Au, calculated using the exciton model code PREQEC, are shown in Figures 4.24 - 4.26 for alpha particles, deuterons and tritons respectively. All the cross section curves have the same basic shape - that of a broad peak, the peak position being at a higher photon energy for the higher particle energies. These calculated spectrum shapes are obviously

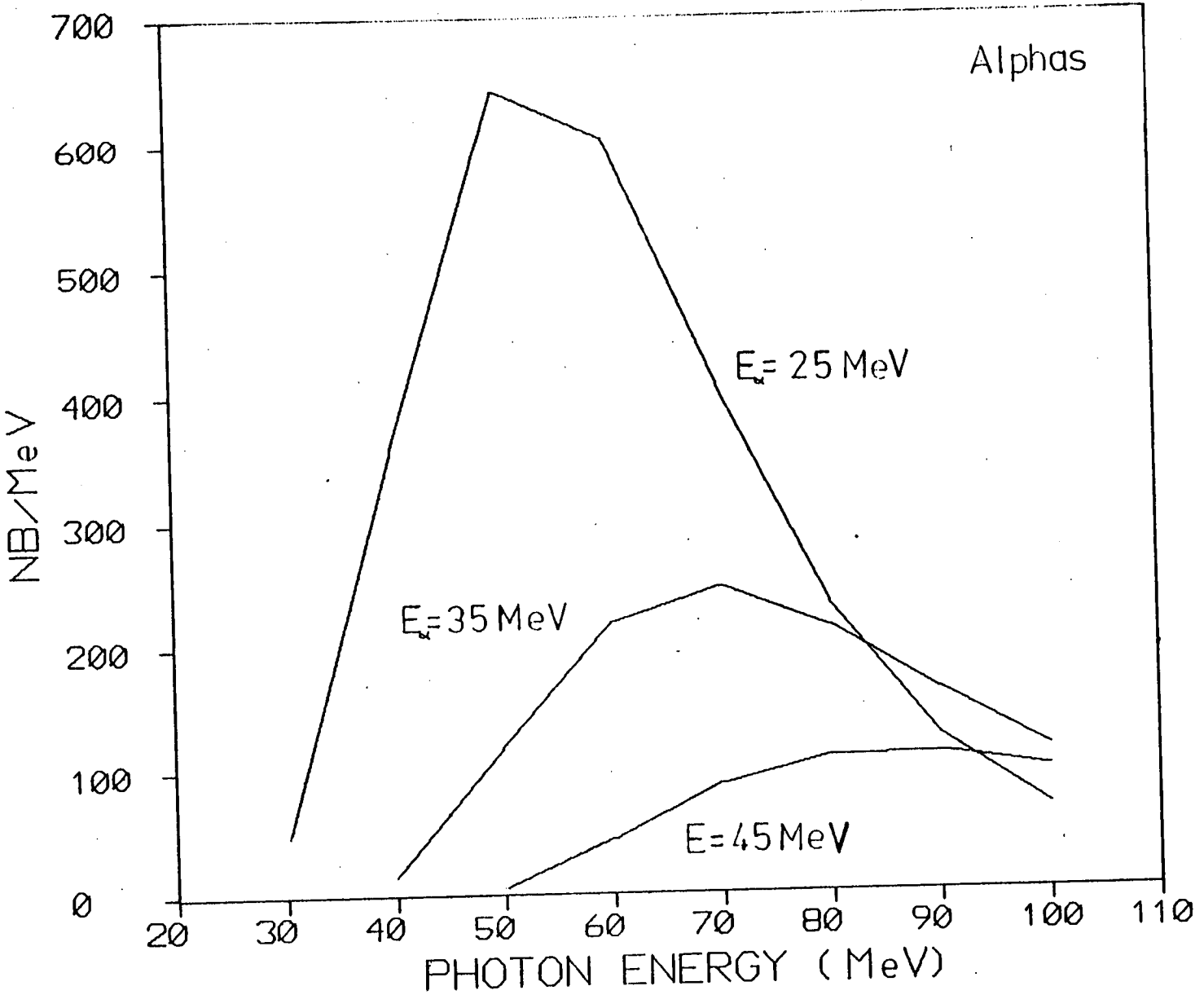

Fig. 4.24 Exciton model calculated emission spectra for alphas from ^{197}Au.

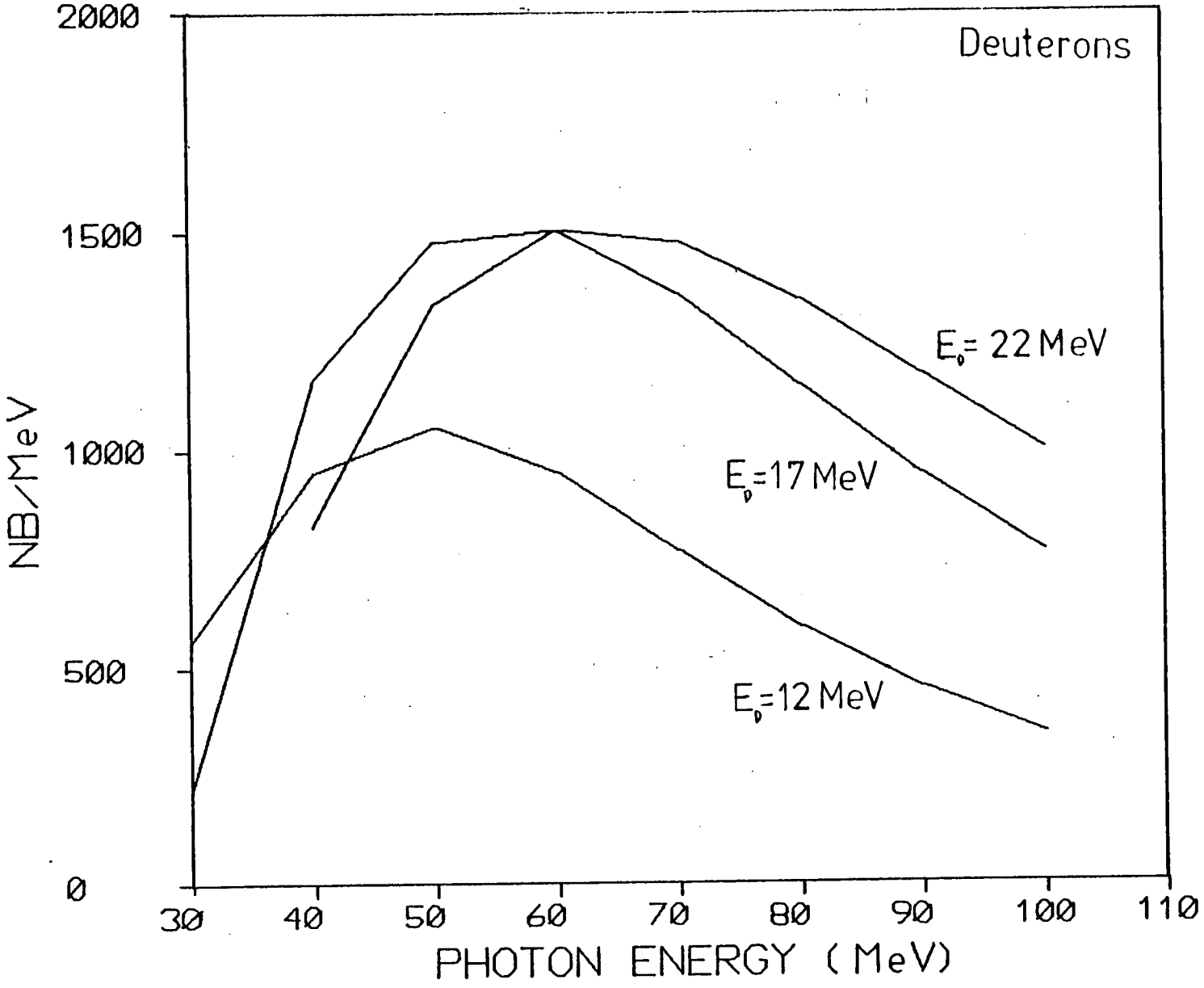

Fig. 4.25 Exciton model calculated emission spectra for deuterons from ^{197}Au.

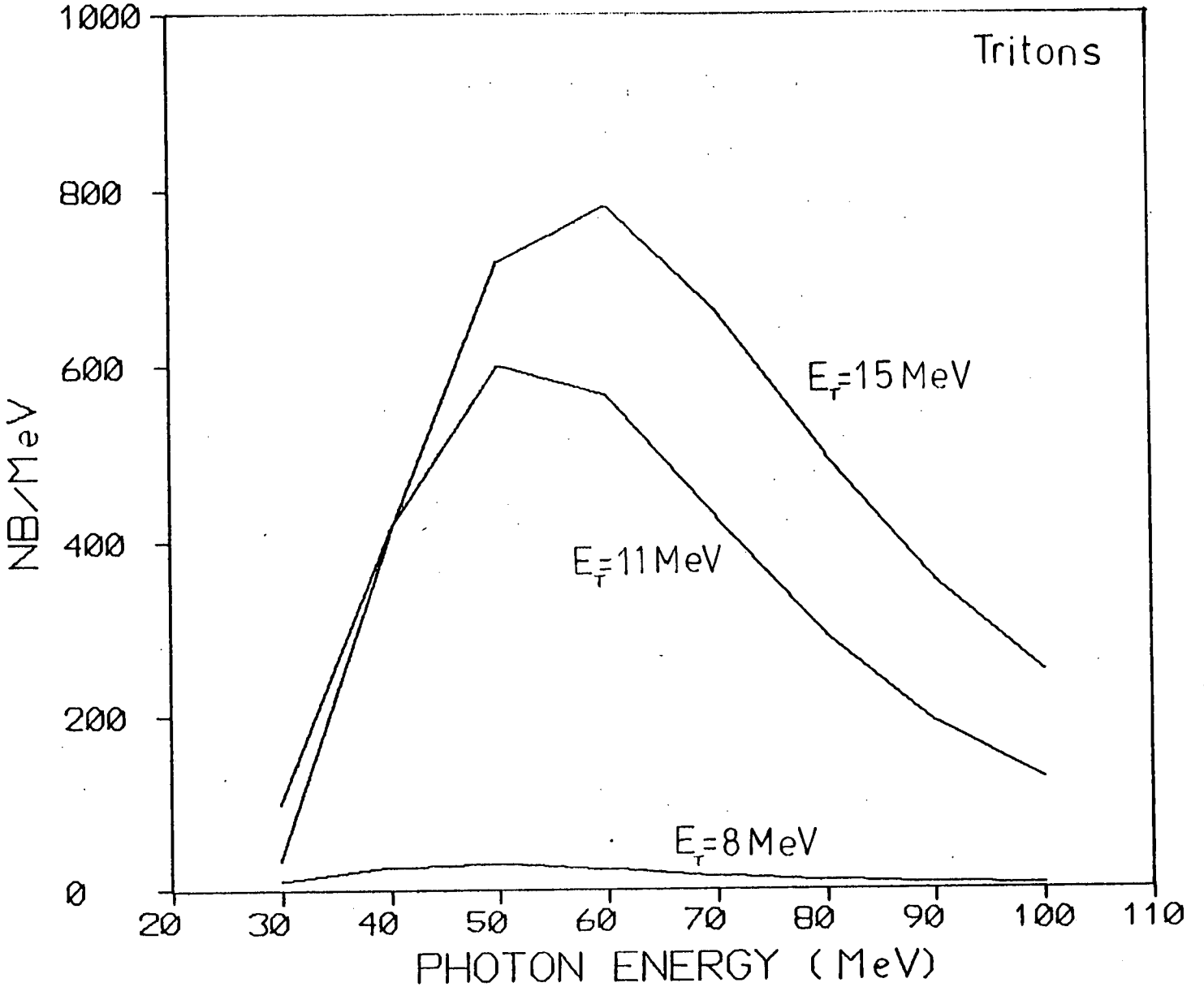

Fig. 4.26 Exciton model calculated emission spectra for tritons from ^{197}Au.

incompatible with those obtained by unfolding the bremsstrahlung excitation functions.

Complex particle energy spectra for Au measured at 120 MeV electron energy can be well explained in terms of the exciton model (see Section 4.1.7). High energy complex particles from heavy nuclei are expected to be mainly produced in a pre-equilibrium reaction, as explained previously. A calculation of the alpha particle emission cross section, based on particle evaporation from a compound nucleus, has been performed by Flowers[8] for electron energies between 40 and 140 MeV for ^{60}Ni. The calculated cross section underestimates that obtained from unfolding the data and does not reproduce the unfolded spectrum shape. Thus for Au, a nucleus much heavier than Ni, it is very unlikely that the cross section could be explained in terms of a compound nucleus reaction. There remains the possibilities of errors and or omissions in the exciton model calculation or the presence of a further reaction mechanism, as discussed in Section 4.1.9. The alteration of the exciton model calculation to include multichance effects, would not enhance the calculated spectrum at high photon energies as would be required to produce a spectrum shape similar to that obtained by unfolding the experimental data.

Thus, although the pre-equilibrium exciton model can be used successfully to explain particle energy spectra measured at a fixed electron energy, good fits to the data are not obtained for the cross sections for the emission of complex particles at particular photon energies. For measurements at a fixed electron energy, it is necessary to fold into the cross section a virtual photon spectrum which may result in a better fit to the data. Thus the more stringent test of the exciton model is a comparison with data taken at one particular electron or photon energy. By unfolding the excitation functions, cross sections at single photon energies are obtained which do not seem to be predicted by the exciton model.

4.3.3 Calculation of Electron Excitation Functions using the Unfolded Cross Sections

The particle emission cross sections for nuclei which have been excited by both electrons and bremsstrahlung radiation can be expressed as $\sigma = \sum_L N_L \sigma_L$, where σ_L is the cross section due to photon absorption of multipolarity L and N_L is the bremsstrahlung or virtual photon spectrum. In the case of electron absorption the virtual photon intensities vary with L. Thus, provided that i) the concept of virtual photon absorption is valid, ii) the unfolding technique used to obtain the cross sections is reasonably accurate and iii) there is no E0 virtual photon component as monopoles are not present in the bremsstrahlung spectrum, the electron induced excitation functions should be reproduced by folding the particle emission cross sections, obtained from the bremsstrahlung excitation functions, with the appropriate virtual photon spectra.

At electron energies between 40 and 130 MeV, the energy range considered here, electric dipole virtual photon absorption is, most probably, the dominant absorption mode, as discussed in Section 1.7. Particle emission cross sections for the emission of alpha particles, tritons and deuterons at three particle energies (E_α = 25, 35 and 45 MeV) were obtained from unfolding bremsstrahlung excitation functions

These cross sections were then folded with an E1 virtual photon spectrum and compared to the measured excitation functions. For all the complex particles and at each particle energy, the excitation functions produced in this way are about a factor of 3 lower at 120 MeV than the measured excitation functions. The measured and calculated excitation functions for the emission of 35 MeV alpha particles from ^{197}Au are shown in Fig. 4.27. The shapes of the spectra are typical of

those for the other particle energies and other complex particles. All the calculated excitation functions can be approximated by two straight lines with an increase in slope occurring at approximately 80 MeV photon energy but only the measured alpha particle data can be similarly fitted, the slopes of the straight lines being much greater in the case of the experimental data. The electron and photon induced angular distributions are somewhat different in shape, but correcting for this difference will not significantly improve the result.

In an attempt to explain the large discrepancy between the calculated and measured electron excitation functions pure E2 virtual photon absorption was assumed. The unfolded cross section for 35 MeV alphas was folded with an E2 virtual photon spectrum calculated using D.W.B.A. and applying corrections due to the finite nuclear size (see Section 1.7), to produce the electro excitation function shown in Fig. 4.27. This calculation gives a result much closer to the measured data, being lower than the experimental cross section by about 20%. The shape of the calculated excitation function differs slightly from the measured data, the slope of the curve being steeper at high photon energies. Similar results have been obtained at the other particle energies when pure E2 virtual photon absorption is assumed.

Assuming that high energy alpha emission is a result of pure E2 virtual photon absorption exhausts approximately 200% of the E2 sum rule. Most of the E2 strength is concentrated in resonances below 30 MeV, see Table 1.1, thus it seems unlikely that high energy alpha emission arises solely from E2 absorption. There is some uncertainty in the calculation of the E2 virtual photon spectrum due to the necessarily approximate treatment of the corrections due to the finite size of the nucleus, especially at high photon energies. If the multipolarity of the virtual photon spectrum is 0, representing an electric monopole, it is not likely that the electron excitation functions can

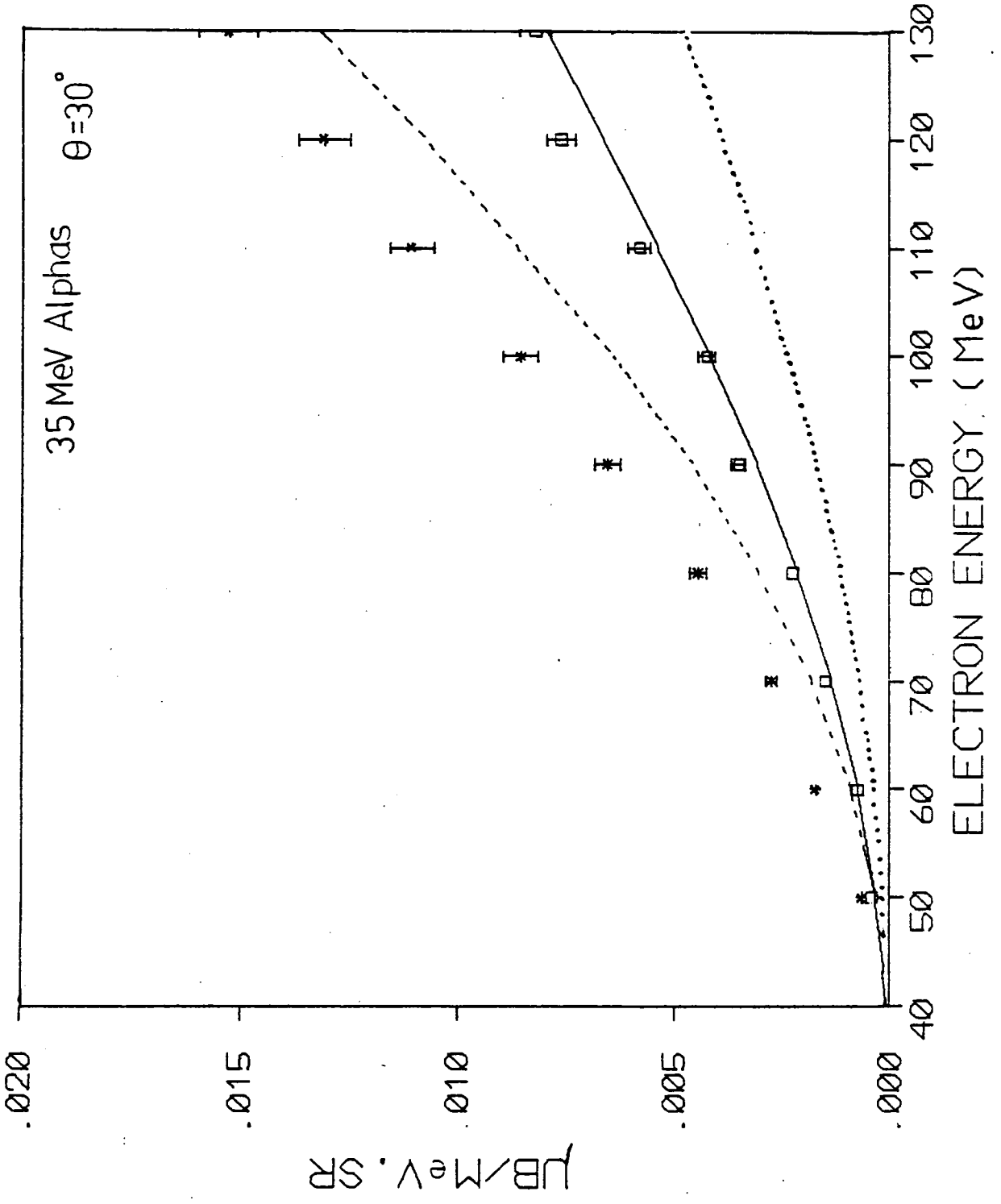

Fig. 4.27 Comparison of the measured electron (stars) and bremsstrahlung (squares) excitation functions for 35 MeV alphas from ^{197}Au and those calculated from the emission cross section obtained by unfolding the photon excitation function.. Solid line shows the emission cross section folded with a bremsstrahlung spectrum, dotted line folded with an E1 virtual photon spectrum and dashed line with an E2 virtual photon spectrum.

be reproduced. The isoscalar electric monopole strength is concentrated in a resonance at about 14 MeV[125], thus there will be little strength above 30 MeV to produce high energy complex particles. The unfolded cross sections once folded with a bremsstrahlung spectrum will reproduce the photon induced excitation functions which suggests that the unfolding technique is valid.

Thus it seems that complex particle emission from ^{197}Au following electron excitation proceeds through a combination of E1 and E2 virtual photon absorption. The amount of each multipole contribution cannot be obtained from this data since the shapes of the excitation functions, calculated using both E1 and E2 virtual photon spectra, are similar. Magnetic multipoles are assumed to be unimportant as magnetic resonances are only weakly excited in electromagnetic reactions.

Some measurements have been made on similar excitation functions for the emission of complex particles from ^{58}Ni and ^{60}Ni. Not enough data has at present been taken to allow the photon induced excitation functions to be unfolded. However, preliminary calculations show that electron excitation functions calculated on the basis of E1 virtual photon absorption are of the same order of magnitude as those measured experimentally.

CHAPTER 5

CONCLUSIONS

The systematics of electron induced complex particle emission at an electron energy of 120 MeV can be obtained from the data taken for this thesis work. Previous measurements at electron energies above the giant-resonance region and below the pion threshold have concentrated mainly on alpha particle emission. All the measured energy spectra show a low energy peak plus a high energy tail. Attempts have been made to explain the low energy peak in terms of the statistical model, at least for low and medium weight nuclei where the Coulomb barrier height will not inhibit evaporation of particles from the nucleus, and the high energy continuum in terms of the pre-equilibrium exciton model. The experimental energy spectra are well explained by combining the statistical and exciton model results except in the cases of complex particle emission from $^{27}A\ell$ and ^{Sn}Nat, where some part of the measured spectra cannot be predicted. This is thought to arise mainly from slight problems with the exciton model calculations for light nuclei and near the Coulomb barrier.

Low particle energy angular distributions are mostly symmetric about 90^{o}, consistent with statistical emission from a compound nucleus, while at higher particle energies forward peaked angular distributions are observed, the degree of forward peaking increasing with particle energy. These forward peaked angular distributions can be predicted, using kinematic considerations if the incoming photon is assumed to be absorbed by a small group of nucleons. The mass of the cluster on which the photon is absorbed increases with increasing A value of the emitted particle, in keeping with exciton model ideology.

The high particle energy mass dependence of the cross section measured at E_e = 120 MeV for the emission of complex particles from a range of nuclei, $27 < A < 197$, is significantly larger than the approximately $A^{1/3}$ dependence observed for proton induced complex particle emission[78]. This suggests that the initial photon reaction occurs within the body of the nucleus rather than at the surface as for protons. Similarly the formation factors obtained from a comparison of the exciton model calculations and measured energy spectra have mass dependences which differ slightly from the mass dependence of formation factors used in proton and alpha particle induced reactions.

Although the electron induced formation factors are corrected for angular dependence using angular distribution data taken at only one particle energy, they can be directly compared to formation factors obtained using angle integrated energy spectra, as for proton and alpha particle induced reactions. Tests showed that the formation factors once corrected for angular dependence, were not strongly dependent on particle energy. The differences observed between the mass dependence of formation factors for electron and proton or alpha particle induced reactions may be due to the presence of a direct reaction component in the emission of complex particles from nuclei excited by protons or alpha particles. Such a direct component should be calculated and subtracted from the experimental data before comparison with exciton model results to determine the formation factors. Due to the low momentum transfers involved in photon induced reactions any direct component is likely to be very small and the formation factors can be obtained from a direct comparison of the data and exciton model calculated results.

Exciton model calculated results appear to explain much of the complex particle energy spectra measured at one particular electron energy.

However exciton model calculations of particle emission spectra using monoenergetic photons do not predict the emission spectra obtained by unfolding the measured excitation functions for ^{197}Au following bremsstrahlung excitation. The reasons for this are not at present understood and require further investigation.

The measured high yield of tritons emitted from ^{12}C is an as yet unexplained result. Angular distributions of high energy tritons emitted from ^{12}C show only slight forward peaking, in contrast to the data obtained for other complex particles and for tritons from other nuclei. These results may indicate alpha clustering, or absorption of a virtual photon onto an alpha cluster in ^{12}C.

Comparisons of angular distribution measurements for ^{58}Ni, ^{60}Ni and ^{197}Au following excitation by electrons and bremsstrahlung radiation indicate that there is a significant E2 virtual photon absorption component in the emission of complex particles, particularly at high electron energies. A similar result is obtained from a comparison of measured high energy particle, electron induced, excitation functions with those calculated by folding the cross sections obtained by unfolding the bremsstrahlung induced excitation functions, with E1 and E2 virtual photon spectra. This is an interesting result as it had been assumed that particle emission in electron induced reactions follows absorption of a virtual photon onto a quasideuteron, an electric dipole process. The exciton model calculations which gave good agreement with the measured energy spectra were calculated assuming pure E1 virtual photon absorption. Calculations assuming E2 absorption have not been performed due to the long computer time required to calculate exciton model energy spectra using distorted wave, finite size corrected, E2 virtual photon spectra.

There are several further experimental measurements which may be

useful in the better understanding of electron and photon induced complex particle emission. Energy spectra and angular distribution measurements for complex particles emitted from ^{10}B may indicate whether the anomalously high yield of tritons from ^{12}C is due to alpha clustering within that nucleus. Measurements in which the emitted complex particle and scattered electron were detected in coincidence would yield information on the multipolarity of the virtual photon absorption leading to complex particle emission. Such coincidence experiments are not possible using a low duty cycle electron linear accelerator such as the University of Glasgow electron linear accelerator, used to obtain the experimental data presented in this thesis. However, such experiments should be feasible using one of the high duty factor microtrons now being developed in Europe and elsewhere, although the count rates will still be very small.

APPENDIX 1 Calibration of the Electron Beam

The momentum, and hence energy, of the electrons in the electron beam is determined from a measurement of the magnetic field in the first bending magnet of the energy analysis system made using an N.M.R. probe. The magnetic fields in this magnet are kept well below saturation and the pole gap is narrow compared to the size of the pole pieces, thus it is reasonable to assume that the magnetic field is uniform and linearly related to the N.M.R. frequency. Only one measurement of the bending magnet's field, for a known electron momentum, is therefore required to give the energy calibration.

Electrons of energy $\sim$ 100 MeV were scattered off a thin aluminium foil placed in the scattering chamber, and detected in one of the two central detectors in the focal plane of the magnetic spectrometer. The spectrometer is calibrated using 5.499 MeV alpha particles (see App. 3) which have momenta per unit charge of 101.25 MeV/c. Thus the spectrometer field setting at which alpha particles used in the spectrometer calibration are detected in the central counters will be very close to that for which the energy calibration electrons are detected. The momentum of the detected electrons (p_e') is therefore determined from the alpha calibration of the spectrometer. The electron beam momentum (p_e) is then calculated from a consideration of electron energy losses between the scattering chamber and the detectors and of the nuclear recoil correction. This calibration gives the electron momentum, p_e, in terms of the N.M.R. probe resonance frequency f, i.e. $p_e = f/k$

where $k = 233.67 \pm 0.07$ kc/s/MeV/c . (ref. 8)

The electron momentum is given in terms of the magnetic field of the first bending magnet (B) by $p_e = k'B$.

The N.M.R. probe frequency (f) and magnetic field (B) are related by

$$f = \frac{gqB}{2\pi \cdot 2m_p}$$

where g, q, m_p are the proton spin gyromagnetic ratio, charge and mass respectively.

Thus k' is given in terms of k by

$$k' = \frac{gq}{2m2m_p\, k} = 1.8199 \pm 0.0005 \quad 10^{-2} \text{ MeV/c/gauss.}$$

APPENDIX 2 Toroid Calibration

The non-intercepting beam current integrator (toroid system) used to monitor the charge delivered to the target or bremsstrahlung radiator was calibrated using a Faraday cup of 99.6% efficiency. The charge collected by both the Faraday cup and toroid system was monitored using a Brookhaven current integrator which was calibrated to give 1 logic pulse per 2×10^{-7} coulombs of charge. The ratio of logic pulses, for a given amount of charge delivered to the toroid, was measured for mean currents between 0 and 20μA, as measured by the Faraday cup. A calibration carried out in May '78 showed that the toroid was stable to within 0.5% up to ∿ 19 μa mean current. A later calibration in Sept. '79 found that the toroid was stable to within 1% up to ∿ 15 μa mean current. This change in toroid performance was probably a result of radiation damage to the preamplifier.

The toroid calibration is obtained from the ratio of integrated charge collected by the toroid (X) to that collected by the Faraday cup (0.996).

$$1 \text{ Toroid count} \equiv \frac{X}{0.996} \times 2 \times 10^{-7} \text{ coulombs.}$$

All the experimental runs were either carried out for 10^5 toroid counts or normalized to this value. Thus the number of electrons incident on the target or bremsstrahlung radiator per experimental run (N_e) is given by:

$$N_e = \frac{X}{0.996} \times 2 \times 10^{-7} \quad 10^5/E_e$$

where E_e = charge of electron = 1.6×10^{-19}C.

The values of N_e obtained for the two calibrations are

$N_e = 1.95 \pm 0.01 \times 10^{17}$ electrons May '78

$N_e = 1.86 \pm 0.02 \times 10^{17}$ electrons Sept. '79.

APPENDIX 3. Spectrometer Momentum Calibration

The calibration of the magnetic spectrometer is performed in two parts. One is the determination of the momentum of a particle at the central orbit of the spectrometer as a function of field setting, $\overline{p}(R)$, and the other is the determination of the momenta of particles incident on each detector, relative to the central detector, at a fixed magnetic field setting. The primary calibration of the spectrometer is the alpha particle calibration from which the energy analysis system is calibrated (App. 1). The alpha calibration provides one value of $\overline{p}(R)$ and gives the relative momenta at each detector. Once the energy analysis system is calibrated further calibration points can be provided by proton end points and elastic electron scattering peaks so that the functional form of $\overline{p}(R)$ can be determined.

A ^{238}Pu alpha source, which emits alphas of energies 5.4992 and 5.4565 MeV, is placed at the centre of the scattering chamber. Scalars are used to count the total number of alpha particles detected in each counter per unit time for small changes in the magnetic field in the spectrometer. A spectrum of counts against Rawson value (R) is obtained for each detector and is fitted with a function of two Gaussians such that the Rawson value $R(p_\alpha, J)$ necessary for an alpha particle of momentum p_α (E_α = mean energy of 5.4992 and 5.4565 MeV) to be incident on the centre of detector J, is obtained for each counter.

The ten detectors are mounted symmetrically on the focal plane of the spectrometer with counters $J = 4$ and $J = 5$ on either side of the optic axis. Thus the primary calibration point of $\overline{p}(R)$ can be obtained from this alpha calibration since

$$\overline{p}(R) = p(R, 4.5)$$

which is equal to $\frac{p(R, 4) + p(R, 5)}{2}$ to within an accuracy of 1 part in 10^4.

The functional form of $\bar{p}(R)$ is obtained by fitting a 3rd degree polynomial which has a zero constant term, i.e. $\bar{p}(0) = 0$ as physically required, through the values of $\bar{p}(R)$ obtained from the alpha calibration, proton end points and elastic scattering peaks,

$$\text{i.e.} \quad \bar{p}(R) = a_1 R + a_2 R^2 + a_3 R^3$$

where $\bar{p}(R)$ is the momentum of a singly charged particle on the optic axis

$$R = \text{Spectrometer field in gauss/2.}$$

The values of a_1, a_2 and a_3 are found to be:

$$a_1 = 5.2269 \times 10^{-2}$$

$$a_2 = -6.3410 \times 10^{-7}$$

$$a_3 = 1.2249 \times 10^{-10}$$

$$\text{and} \quad \bar{p}_z(R) = z\bar{p}(R)$$

where z = charge of particle detected on the optic axis. Clearly the particle momentum is only slightly non linear with respect to the magnetic field, the deviation from linearity being only $\sim 4\%$ for the highest obtainable particle momentum ($\bar{p}_\alpha = 700$ MeV/c). Thus $\bar{p}\,(R(p_\alpha, J))$ can be approximated by $cR(p_\alpha, J)$ where c is a constant from which

$$p_\alpha = p(R(p_\alpha, J), J) = cR(p_\alpha, 4.5) \qquad \text{eqn. A3.1}$$

$p(R,J)$ is related to $\bar{p}(R)$ by $F(J)$ parameters

$$p(R,J) = F(J)\,\bar{p}(R) \quad \text{where} \quad F(4.5) \text{ is defined as 1.}$$

$$\therefore F(J) = \frac{p(R(P_\alpha,J),J)}{\bar{p}(R,(p_\alpha, J))} = \frac{R(p_\alpha, 4.5)}{R(p_\alpha, J)} \qquad \text{Using (A3.1)}$$

The values of F(J) obtained in this way from the alpha calibration are:

J	F(J)
0	0.9693
1	0.9769
2	0.9839
3	0.9903
4	0.9968
5	1.0031
6	1.0092
7	1.0152
8	1.0209
9	1.0269

$\frac{\partial F}{\partial J}$ (4.5), as required in the differential cross section (Section 3.2) is taken as the differential of a fourth degree polynomial fitted to the F(J) values and is given by: $\frac{\partial f}{\partial J}$ (4.5) = 0.00621 .

APPENDIX 4 Detector Efficiencies

4.1 Relative efficiencies

The detector relative efficiencies, r_j, are obtained from a detailed study of the particle count rates measured using a target which yields smoothly decreasing energy spectra over a certain energy range. Pulse height spectra are collected for small changes in the spectrometer field setting, such that the energy ranges for neighbouring counters overlap slightly. Smoothly decreasing spectra should be observed for each complex particle, however the spectra obtained for each detector differ from each other by a normalisation factor due to the differing efficiencies. The detector relative efficiencies are calculated as factors which enable a smooth curve to be fitted through the spectra measured for each detector. A relative efficiency of 1 is assigned to the mean of the two central detectors, i.e. $r_{4.5} = 1$.

Spectra are measured for a total of N (about 10) spectrometer field settings (j = 1, N) and the counts C_{jJ} in each detector (J = 0, 9) are determined.

Taking logarithms of equation (3.2), setting $\varepsilon_J = 1$ and $D(E_J, E_{J'}) = 1$ yields:

$$\ell n\left[\frac{\dfrac{C_{jJ}}{\bar{E}_j\left(1+\dfrac{\bar{E}_j}{2m_oc^2}\right)}}{\left(1+\dfrac{\bar{E}_{jJ}}{m_oc^2}\right)}\right] = \ell n\left[\frac{d^2\sigma}{dE_{jJ}d\Omega}\right] + \ell n(r_J) + \text{constant} \qquad \text{(A4.1)}$$

$$= y_i \quad (i = 10(j-1) + J)$$

where $\bar{E}_j$ = energy of particle at J = 4.5 at field setting j

E_j = energy of particle in detector J at field setting j.

The left hand side (L.H.S.) of eqn. (A4.1) can be calculated for each detector and field setting (Sections 3.1 and 3.2), while on the R.H.S. only r_J varies as J. The r_J values are obtained by fitting an Lth degree polynomial to the measured spectra,

$$\text{i.e.} \quad \ln\left[\frac{d^2\sigma}{dE_{jJ}\, d\Omega}\right] + \ln(r_J) + \text{constant} = a_J + \sum_{n=1}^{L} a_{9+n} E_n$$

$$= \sum_{k=0}^{9+L} a_k f_k$$

where $f_k = \delta_{Jk} \qquad (k = 0, 9)$

$$= E_{jJ}^{k-9} \qquad (k = 10, 9+L)$$

the coefficients a_k are determined by minimising the quantity

$$\sum_{i=0}^{10N-1} \left[\frac{\sum_{k=1}^{9+L} a_k f_k - y_i}{\sigma_i}\right]^2,$$

where σ_i = error in y_i

$a_k (k = 10, L+9)$ do not change with J

$a_k (k = 0, 9)$ vary with J.

Thus $\ln(r_J) - \ln(r_{J'}) = a_J - a_{J'}, \qquad J, J' = 0 \to 9$

and $r_J = \dfrac{e^{a_J}}{\frac{1}{2}(e^{a_4} + e^{a_5})}$ normalised to $r_{4.5} = 1.$

Relative efficiencies were determined for all the complex particles at low and high energies and the values obtained plotted in Fig. A4.1.

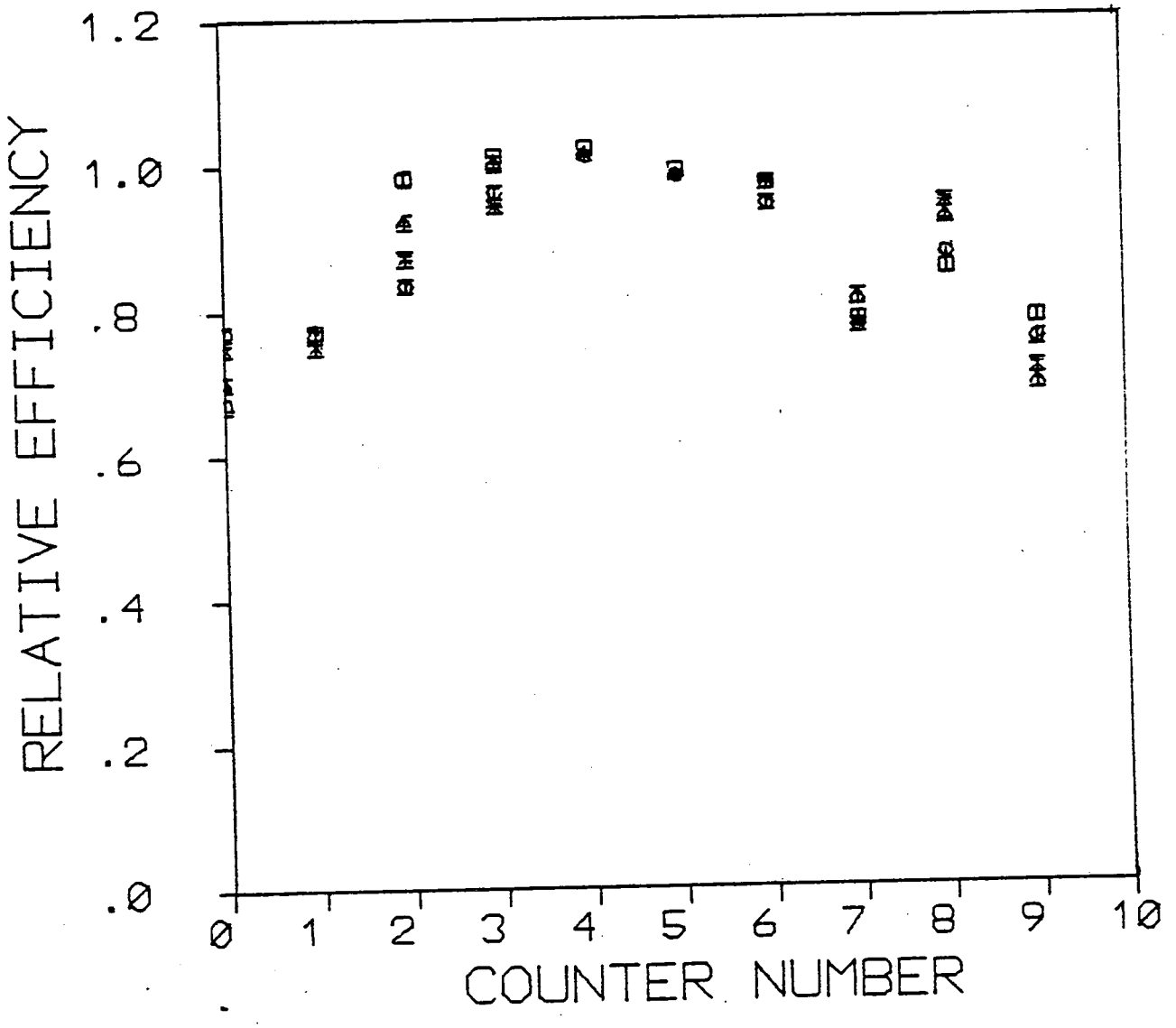

Fig. A4.1 Relative efficiencies for 8 MeV alphas (stars), 35 MeV alphas (squares), 18 MeV deuterons (circles), and 11 MeV tritons (triangles).

No systematic differences were observed with respect to particle or energy and a set of values used for all particles at all energies were estimated from the graph. Two sets of relative efficiency values for the two different detector configurations used for this thesis work are given in Table A4.1.

4.2 Absolute efficiencies

The area of the particle peak in the pulse height spectrum may be less than the total number of particles incident on the detector if the absolute efficiency of the detector is less than 100%.

Particles may lose energy in the detectors as a result of multiple scattering and inelastic nuclear interactions, resulting in a low energy tail below the peak which, during the integration process, may not be included in the peak, resulting in the loss of particles. Flowers[8] showed that the absolute efficiency of the detectors used for this thesis work with respect to alpha particles is greater than 99.4%.

Nuclear interaction losses are approximately 0.06% greater for deuterons than for alpha particles, the losses for tritons and ^{3}He particles being less than 0.3%, the value calculated for incident alpha particles. Loss of particles due to multiple scattering in the detectors varies approximately as Z^2 if Z is the charge of the incident particle. Thus multiple scattering losses for deuterons, tritons and ^{3}He particles will be the same as, or less than those for alpha particles. The absolute efficiency of the detectors will therefore be greater than 99.4% for all the complex particles detected.

TABLE A4.1

Detector Relative Efficiencies

a) May '78

Counter	r_J
0	0.74489 ± 0.00686
1	0.76434 ± 0.00731
2	0.83773 ± 0.00742
3	0.99565 ± 0.00739
4	1.00019 ± 0.00777
5	0.99981 ± 0.00810
6	0.95837 ± 0.00870
7	0.76607 ± 0.00976
8	0.85932 ± 0.00984
9	0.69408 ± 0.01096

b) September '79

Counter	r_J
0	0.95405 ± 0.01140
1	0.77645 ± 0.01147
2	0.84551 ± 0.01113
3	1.00843 ± 0.01116
4	1.00870 ± 0.00619
5	0.99130 ± 0.00630
6	0.98548 ± 0.01096
7	0.81990 ± 0.01256
8	0.88456 ± 0.01254
9	0.89591 ± 0.01686

REFERENCES

1) J. Chadwick and M. Goldhaber, Nature 134, 237 (1934).

2) L. Szilard and T.A. Chalmers, Nature 134, 494 (1934).

3) H. Hanni, V.L. Telegdi and W. Zunti, Helv. Phys. Acta 21, 203 (1948).

4) M.S. Livingstone and H.A. Bethe, Rev. Mod. Phys. 9, 351 (1936).

5) J.S. Levinger, Nuclear Photo-disintegration (Oxford University Press, 1960).

6) A.G. Flowers, A.C. Shotter, D. Branford, J.C. McGeorge and R.O. Owens, Phys. Rev. Lett. 40, 709 (1978).

7) A.G. Flowers, D. Branford, J.C. McGeorge, A.C. Shotter, P.J. Thorley, C.H. Zimmerman, R.O. Owens and J.S. Pringle, Phys. Rev. Lett. 43, 323 (1979).

8) A.G. Flowers, Ph.D. Thesis, University of Edinburgh, 1980.

9) R.N.H. Haslam and H.M. Skarsgard, Phys. Rev. 81, 479 (1951).

10) R.N.H. Haslam, L.A. Smith and J.G.V. Taylor, Phys. Rev. 84, 840 (1951).

11) R.N.H. Haslam, A.G.W. Cameron, J.A. Cooke and E.H. Crosby, Can. J. Phys. 30, 349 (1952).

12) L. Katz and A.G.W. Cameron, Can. J. Phys. 29, 518 (1951).

13) J. Blatt and V.F. Weisskopf, Theoretical Nuclear Physics, John Wiley and Sons, Inc., New York (1952).

14) M.E. Toms and J. McElhinney, Phys. Rev. 111, 561 (1958).

15) C.H. Millar, Can. J. Phys. 31, 262 (1953).

16) P. Erdös, P. Scherrer and P. Stoll, Helv. Phys. Acta 30, 639 (1957).

17) J.H. Carver, Proc. Phys. Soc. 77, 417 (1961).

18) M. Kregar and B. Povh, Nucl. Phys. 43, 170 (1963).

19) J.A. Scheer, K. Schlüpmann and F. Triantafyllidis, Nucl. Phys. 56, 113 (1964).

20) M. Meneghetti and S. Vitale, Nucl. Phys. 61, 316 (1965).

REFERENCES (Contd.)

21) H. Hoffmann, B. Prowe and H. Ullrich, Nucl. Phys. 85, 631 (1966).

22) G. Kraft, R. Kosiek, R. Mundhenke and J. Winter, Nucl. Phys. A118, 25 (1968).

23) N.A. Keller and D.B. McConnell, Can. J. Phys. 50, 1554 (1972).

24) J.J. Murphy II, H.J. Gehrhardt and D.M. Skopik, Nucl. Phys. A277, 69 (1977).

25) J.J. Murphy II, D.M. Skopik, J. Asai and J. Uegaki, Phys. Rev. C18, 736 (1978).

26) E. Wolynec, M.N. Martins and G. Moscati, Phys. Rev. Lett. 37, 585 (1976).

27) E. Wolynec, W.R. Dodge and E. Hayward, Phys. Rev. Lett. 42, 27 (1979).

28) W. Dodge, E. Hayward, G. Moscati and E. Wolynec, Phys. Rev. C18, 2435 (1978).

29) E. Wolynec, W. Dodge and E. Hayward, Private Communication (1979).

30) J.C. McGeorge, A.G. Flowers, A.C. Shotter and C.H. Zimmerman, J. Phys. G4, L145 (1978).

31) D.H. Dowell, P. Axel and L.S. Cardman, Phys. Rev. C18, 1550 (1978).

32) J.C. McGeorge, A.G. Flowers, D. Branford, C.H. Zimmerman and R.O. Owens, J. Phys. G6, L133 (1980)

33) P.R. Byerly, Jr., and W.E. Stephens, Phys. Rev. 83, 54 (1951).

34) B. Forkman, Ark. f. Fysik 11, 265 (1956).

35) B. Forkman, Nucl. Phys. 23, 269 (1961).

36) W.H. Smith and L.J. Laslett, Phys. Rev. 86, 523 (1952).

37) L.S. Ring, Jr., Phys. Rev. 99, 137 (1955).

38) V.P. Chizhov, J.E.T.P. 38, 809 (1960).

39) L. Katz and A.S. Penfold, Phys. Rev. 81, 815 (1951) and Phys. Rev. 83, 169 (1951).

40) J. Goldemberg and L. Marquez, Nucl. Phys. 7, 202 (1958).

41) V.P. Chizhov, A.P. Komar, L.A. Kulchitsky, A.V. Kulikov, E.D. Makhnovsky and Yu.M. Volkov, Nucl. Phys. 34, 562 (1962).

REFERENCES (Contd.)

42) K. Bangert, U.E.P. Berg, G. Junghams, R. Stock, K. Wienhard and H. Wolf, Nucl. Phys. A261, 149 (1976).

43) V.P. Denisov and I.Yu. Chubukov, Sov. J. Nucl. Phys. 17, 354 (1973) and Sov. J. Nucl. Phys. 22, 466 (1975).

44) Yu.P. Antuf'ev, V.L. Agranovich, V.B. Ganeko, V.S. Kuz'menko, I.I. Miroschnichenko, Sov. J. Phys. 14, 502 (1972).

45) Yu. P. Antuf'ev, V.L. Agranovich, V.B. Ganeko, U.S. Kuz'menko, I.I. Miroshnichenko, P.V. Sorokin and S.V. Shalatski, Sov. J. Phys. 15, 357 (1972).

46) D.M. Skopik, E.L. Tomusiak, E.T. Dressler, Y.M. Shin and J.J. Murphy, II, Phys. Rev. C14, 789 (1976).

47) D.M. Skopik, Y.M. Shin, J.W. Horniachek and S.K. Kundu, Nucl. Phys. A197, 185 (1972).

48) F. Heinrich and H. Wäffler, Helv. Phys. Acta 29, 232 (1956).

49) B. Wiik, Z. Phys. 189, 423 (1966).

50) A. Goldmann, P. Kniesel and H.V. Buttlar, Z. Phys. 192, 282 (1966).

51) P. Kneisel A. Goldmann and H.V. Buttlar, Z. Phys. 199, 440 (1967).

52) K. Krämer, H.V. Buttlar, A. Goldmann and B. Huber, Z. Phys. 207, 1, (1967).

53) L.A. Currie and R.H. Rodríguez-Pasques, Nucl. Phys. A157, 49 (1970).

54) D.M. Skopik and Y.M. Shin, Nucl. Phys. A223, 409 (1974).

55) J. Uegaki, J. Asai, M.K. Leung, J.J. Murphy II, Y.M. Shin and D.M. Skopik, Can. J. Phys. 57, 1059 (1979).

56) A.J.F. Siegert, Phys. Rev. 52, 787 (1937).

57) K.F. von Weizäcker, Z. Phys. 88, 54 (1934).

58) E.J. Williams, K. Danske Vidensk. Selsk., Mat.-Fys. Meddr. 13, 3, (1935)

59) K.L. Brown and R. Wilson, Phys. Rev. 93, 443 (1954).

60) D.W. Scott, A.O. Hanson and D.W. Kerst, Phys. Rev. 100, 209 (1955).

61) R.L. Hines, Phys. Rev. 105, 1534 (1957).

REFERENCES (Contd.)

62) W.C. Barber, Phys. Rev. 111, 1642 (1958).

63) W.C. Barber and T. Wiedling, Nucl. Phys. 18, 575 (1960).

64) W.R. Dodge and W.C. Barber, Phys. Rev. 127, 1746 (1962).

65) W.W. Gargaro and D.S. Onley, Phys. Rev. C4, 1032 (1971).

66) I.C. Nascimento, E. Wolynec and D.S. Onley, Nucl. Phys. A246, 210 (1975).

67) C.W. Soto Vargas, D.S. Onley and L.E. Wright, Nucl. Phys. A288, 45 (1977).

68) M.N. Martins, E. Wolynec and G. Moscati, Phys. Rev. C16, 613 (1977).

69) A.C. Shotter, J. Phys. G5, 371 (1979).

70) R.H. Helm, Phys. Rev. 104, 1466 (1956).

71) M. Rosen, R. Raphael and H. Überall, Phys. Rev. 163, 927 (1967).

72) H.W. Koch and J.W. Motz, Rev. Mod. Phys. 31, 920 (1959).

73) R.T. Deck, C.J. Mullin and C.L. Hammer, Nuovo Cim. 32, 180 (1964).

74) J.L. Matthews and R.O. Owens, Nucl. Inst. Meth. 91, 37 (1971) and Nucl. Inst. Meth. 111, 157 (1973).

75) A. Lepetre, H. Beil, R. Bergère, P. Carlos, J. Fagot, A. Veyssiere, J. Ahrens, P. Axel and U. Kneissl, Phys. Lett. 79B, 43 (1978).

76) R. Bergère, Proc. Int. Conf. on Nuclear Physics with Electromagnetic Interactions, Lecture Notes in Physics 108, 138, Springer-Verlag (1979).

77) J.S. Levinger, Phys. Rev. 84, 43 (1951).

78) F.E. Bertrand and R.W. Peele, Phys. Rev. C8, 1045 (1973).

79) J.R. Wu, C.C. Chang and H.D. Holmgren, Phys. Rev. C19, 659 (1979).

80) J.R. Wu and C.C. Chang, Phys. Rev. C16, 1812 (1977).

81) T.A. Gabriel and R.G. Alsmiller, Jr., Phys. Rev. 182, 1035 (1969).

82) J.R. Wu and C.C. Chang, Phys. Rev. C17, 1540 (1978).

83) J.J. Griffin, Phys. Rev. Lett. 17, 478 (1966).

84) M. Blann, Ann. Rev. Nucl. Sci. 25, 123 (1975).

REFERENCES (Contd.)

85) K.H. Kaiser, Ph.D. Thesis, University of Mainz, 1973, unpublished; and H. Herminghaus and K.H. Kaiser, Nuc. Inst. Meth. 113, 189 (1973).

86) S.N. Gardiner, J.L. Matthews and R.O. Owens, Nucl. Inst. Meth. 87, 285 (1970).

87) Methods of Experimental Physics, Vol. 5, (Academic Press Inc. (London) Ltd., 1961).

88) J.F. Ziegler, Helium Stopping Powers and Ranges in All Elemental Matter, Pergamon Press (1977).

89) S. Penner, N.B.S. Internal Report.

90) C.F. Williamson, J.P. Boujot and J. Picard, C.E.A. Report 3042 (1966).

91) J.B. Marion and F.C. Young, Nuclear Reaction Analysis, pub. Amsterdam (1958).

92) W.D. Myers, W.J. Swiatecki, T. Kodama, L.J. El-Jaick and E.R. Hiff, Phys. Rev. C15, 2032 (1977).

93) B.L. Berman, Rev. Mod. Phys. 47, 713 (1975).

94) T.D. Thomas, Ann. Rev. Nucl. Sci. 18, 343 (1968).

95) D. Bodansky, Ann. Rev. Nucl. Sci. 12, 79 (1962).

96) H.W. Bertini, Phys. Rev. 131, 1801 (1963) and Phys. Rev. 188, 1711 (1969).

97) V.S. Barashenkov, F.G. Gereghi, A.S. Iijinov, G.G. Jonsson and V.D. Toneev, Nucl. Phys. A231, 462 (1974).

98) W. Scobel, M. Blann and A. Mignerey, Nucl. Phys. A287, 301 (1977).

99) A. Mignerey, M. Blann and W. Scobel, Nucl. Phys. A273, 12 (1976).

100) C.B. Fulmer and J.B. Ball, Phys. Rev. 140, B330 (1965).

101) C. Kalbach, Z. Phys. A283, 401 (1977).

102) E. Gadioli, E. Gadioli Erba, L. Sajo-Bohus and G. Tagliaferri, Nuovo Cimento Riv. 6, 1 (1976).

103) G.S. Foote, Ph.D. Thesis, Australian National University, Canberra (1974).

REFERENCES (Contd.)

104) N. Shikazono and T. Terasawa, Nucl. Phys. A250, 260 (1975).

105) P.J. Dallimore, Australian National University Report No. ANU-P/512, 1970 (unpublished).

106) C.M. Perey and F.G. Perey, Atomic and Nuclear Data Tables 17, 1 (1976).

107) A. Gilbert and A.G.W. Cameron, Can. J. Phys. 43, 1446 (1965).

108) M.R. Anderson, S.R. Kennett, Z.E. Switkowski and D.G. Sargood, Nucl. Phys. A318, 471 (1979).

109) J.R. Wu, Ph.D. Thesis, University of Maryland (1977) (unpublished).

110) C.K. Cline and M. Blann, Nucl. Phys. A172, 225 (1971).

111) C.K. Cline, Nucl. Phys. A210, 590 (1973).

112) J.H. Mattauch, W. Thiele and A.H. Wapstra, Nucl. Phys. 67, 32 (1965).

113) J. Wing and P. Fong, Phys. Rev. 136, B923 (1964).

114) F.C. Williams, Jr., Nucl. Phys. A166, 31 (1971).

115) J. Garvey, B.H. Patrick, J.G. Rutherglen and I.L. Smith, Nucl. Phys. 70, 241 (1965).

116) J.S. Levinger, Phys. Lett. 82B, 181 (1979).

117) W.R. Dodge, Private Communication.

118) F. Partovi, Annals of Physics 27, 79 (1964).

119) N.N. Kaushal, E.J. Winhold, P.F. Yergin, H.A. Medicus and R.H. Auguston, Phys. Rev. 175, 1330 (1968).

120) B.C. Cook, Nucl. Inst. Meth. 24, 256 (1963).

121) D. Brenner, Ph.D. Thesis, Rutherford Report RL-79-032.

122) C. Maples, G.W. Goth and J. Cerny, Nuclear Data 2, 429 (1966).

123) M. Blann, Nucl. Phys. A213, 570 (1973).

124) S.S. Hanna, Aust. J. Phys. 29, 511 (1976).

125) H.P. Morsch, C. Sükösd, M. Rogge, P. Turek, H. Machner and C. Mayer-Böricke, Phys. Rev. C22, 489 (1980).